National Library of Canada
Bibliothèque nationale du Canada

Acquisitions and Bibliographic Services Branch
Direction des acquisitions et des services bibliographiques

395 Wellington Street
Ottawa, Ontario
K1A 0N4

395, rue Wellington
Ottawa (Ontario)
K1A 0N4

Your file Votre référence

Our file Notre référence

NOTICE

The quality of this microform is heavily dependent upon the quality of the original thesis submitted for microfilming. Every effort has been made to ensure the highest quality of reproduction possible.

If pages are missing, contact the university which granted the degree.

Some pages may have indistinct print especially if the original pages were typed with a poor typewriter ribbon or if the university sent us an inferior photocopy.

Reproduction in full or in part of this microform is governed by the Canadian Copyright Act, R.S.C. 1970, c. C-30, and subsequent amendments.

AVIS

La qualité de cette microforme dépend grandement de la qualité de la thèse soumise au microfilmage. Nous avons tout fait pour assurer une qualité supérieure de reproduction.

S'il manque des pages, veuillez communiquer avec l'université qui a conféré le grade.

La qualité d'impression de certaines pages peut laisser à désirer, surtout si les pages originales ont été dactylographiées à l'aide d'un ruban usé ou si l'université nous a fait parvenir une photocopie de qualité inférieure.

La reproduction, même partielle, de cette microforme est soumise à la Loi canadienne sur le droit d'auteur, SRC 1970, c. C-30, et ses amendements subséquents.

Canada

L'INSTITUT DE GENIE ELECTRIQUE
OTTAWA CARLETON
INSTITUTE FOR ELECTRICAL ENGINEERING

Design of an Interface Between GaAs MESFET Physical Models and the Transmission Line Matrix Method

by

Salam Francis Dindo

May 1994

Submitted to the School of Electrical Engineering
University of Ottawa

in partial fulfillment of the requirements for the degree of
Doctor of Philosophy

Salam Francis Dindo, Ottawa, Canada, 1994

Department of Electronics
Carleton University
Ottawa Canada
K1S 5B6
(613) 788-5754

Département de génie électrique/
Department of Electrical Engineering
Université d'Ottawa/
University of Ottawa
Ottawa Canada
K1N 6N5
(613) 564-8213

Department of Systems and
Computer Engineering
Carleton University
Ottawa Canada
K1S 5B6
(613) 788-5740

National Library of Canada
Bibliothèque nationale du Canada

Acquisitions and Bibliographic Services Branch
Direction des acquisitions et des services bibliographiques

395 Wellington Street
Ottawa, Ontario
K1A 0N4

395, rue Wellington
Ottawa (Ontario)
K1A 0N4

Your file Votre référence

Our file Notre référence

The author has granted an irrevocable non-exclusive licence allowing the National Library of Canada to reproduce, loan, distribute or sell copies of his/her thesis by any means and in any form or format, making this thesis available to interested persons.

L'auteur a accordé une licence irrévocable et non exclusive permettant à la Bibliothèque nationale du Canada de reproduire, prêter, distribuer ou vendre des copies de sa thèse de quelque manière et sous quelque forme que ce soit pour mettre des exemplaires de cette thèse à la disposition des personnes intéressées.

The author retains ownership of the copyright in his/her thesis. Neither the thesis nor substantial extracts from it may be printed or otherwise reproduced without his/her permission.

L'auteur conserve la propriété du droit d'auteur qui protège sa thèse. Ni la thèse ni des extraits substantiels de celle-ci ne doivent être imprimés ou autrement reproduits sans son autorisation.

ISBN 0-315-95910-X

Canada

UNIVERSITÉ D'OTTAWA
UNIVERSITY OF OTTAWA

Design of an Interface Between GaAs MESFET Physical Models and the Transmission Line Matrix Method

by

Salam Francis Dindo

May 1994

Submitted to the School of Electrical Engineering
University of Ottawa

in partial fulfillment of the requirements for the degree of
Doctor of Philosophy

Salam Francis Dindo, Ottawa, Canada, 1994

Abstract

The Transmission Line Matrix (TLM) method has been demonstrated to be capable of simulating the electromagnetic propagation in passive com‚-‿nents of monolithic microwave integrated circuits (MMICs), such as microstrip lines, air-bridges, and spiral inductors. The full simulation of MMICs by TLM is hindered by the lack of a GaAs MESFET model. Although SPICE-type lumped element models can be embedded, they are not sufficiently accurate to describe the time dependent response, and they defeat the method since TLM distinguishes itself by being capable of simulating physical structures. In addition, the TLM method cannot simulate a physics-based MESFET model since it cannot model fixed charges in the depletion region, nor can it model the highly non-linear field interactions in the conducting region. The TLM method requires a background solver to assist physics-based MESFET modelling.

This thesis presents a novel method for enabling the TLM method to simulate the active region of the MESFET. The device is treated as a two-port where the depletion region is the input, and the channel region is the output. The input of the two-port is fed electric field signals from the gate transmission line. An internal GaAs MESFET solver transforms the input electric field into a voltage waveform, and the channel current and the depletion-channel boundary profile are calculated at every time instant by consideration of the channel doping and geometry. Via suitable interface parameters, the calculated outputs are transformed by individual TLM systems filling the channel into output electric and magnetic fields.

The first part of the thesis derives a novel two-dimensional formulation of the TLM method enabling it to simulate a vertical section of the MESFET channel whose thickness is chosen small enough such that the electric field can be considered to be uniform. By controlling the TLM pulse energy, nodes conductivities, and section length, these three interface parameters enable the resultant TLM system to transform the physical characteristics of any infinitesimal section of the channel into electric and magnetic fields.

The second part of the thesis derives a numerical time-domain quasi two-

dimensional model of a GaAs MESFET with several novel aspects. Time-domain simulation is derived from non-stationary electron velocity response to the electric field. A new method is introduced, called the voltage balance method, to numerically solve the Poisson and current continuity equations at every time instant. In addition, a new time-domain treatment of the dielectric relaxation time constants of the drain and gate circuits enable the method to adopt variable time steps. When these three procedures are combined together, they result in a non-linear GaAs MESFET model which can offer sufficient accuracy and substantial time savings over other techniques.

Several practical examples are presented showing TLM computations of (i) the non-stationary carrier velocity response to applied field, (ii) the transient field response to an application of biases into the MESFET, and (iii) the field response to an applied electric field sinusoidal waveform at 10 GHZ. The thesis concludes with several recommendations for future work. The key one is to link this work with the 3-dimensional TLM method by augmenting the output channel fields with those computed by TLM for the passive field interactions in the MESFET source, gate, and drain electrodes.

TABLE OF CONTENTS

ABSTRACT i
TABLE OF CONTENTS iii
LIST OF TABLES v
LIST OF FIGURES vi
LIST OF SYMBOLS xii
ACKNOWLEDGEMENTS xx
CHAPTER 1 Introduction 1
1.1 Review of MMIC Analysis Methods 1
1.2 MMIC Modelling Tasks 4
1.2.1 Passive Structures Modeling 4
1.2.2 Active Device Modeling 6
1.2.3 Modelling the Coupling Between Passive Structures and Active Devices 11
1.3 The Objective of the Thesis 12
1.4 The Scope of the Thesis 16
1.5 References 18
CHAPTER 2 Two-Dimensional TLM Node 23
2.1 Introduction 23
2.2 TLM Node Formulation 27
2.3 TLM Node Losses 32
2.4 TLM Node Dispersion Characteristics 34
2.5 References 40
CHAPTER 3 Two-Dimensional TLM System 41
3.1 Introduction 41
3.2 Formulation of Electromagnetic Boundaries 41
3.3 Construction of the TLM Energy Sources 43
3.4 Analysis of the TLM System 44
3.5 References 65

CHAPTER 4 The GaAs MESFET Analysis Engine 66
4.1 Introduction 66
4.2 The GaAs MESFET Model 72
4.2.1 Space Discretization 77
4.2.2 GaAs MESFET Charging Time Constants 77
4.2.3 Non-stationary Electron Velocity 81
4.2.4 The Voltage Balance Method 82
4.2.5 The Conducting Channel Voltage 86
4.2.6 The Depletion Layer Voltage 87
4.2.7 The Surface Voltage 93
4.2.8 The n^+ Ohmic contacts and Buffer Regions 94
4.3 TLM Interface Parameters 95
4.4 GaAs MESFET Analysis Errors 98
4.5 References 100
CHAPTER 5 Results 102
5.1 Introduction 102
5.2 Verification of the Time-Dependent Electron Velocity 103
5.3 Verification of the New Voltage Balance Method 109
5.4 Example #1: Response of a Thin GaAs Sample to a Voltage Step 126
5.5 Example #2: GaAs MESFET Transient Response to Voltage Steps . . . 135
5.6 Example #3: GaAs MESFET Transient Response to a Sinusoidal Field . 153
5.7 References 163
CHAPTER 6 Conclusions 165
6.1 Introduction 165
6.2 Conclusions 165
6.3 Original Contributions 166
6.4 Recommendations For Future Work 166
6.5 References 168
Appendix A Monte Carlo Methods 169
Appendix B Computer Programming of the TLM MESFET Model 172

LIST OF TABLES

3.1 TLM system parameters for three examples 47

5.1 Input data parameters of two GaAs MESFETs 115

LIST OF FIGURES

1.1 Two-port model of the GaAs MESFET. 14

1.2 Block diagram of the two-port GaAs MESFET model. 15

2.1 Physical model of the MESFET conducting channel. 24

2.2 Cross-sectional view of a MESFET structure. 25

2.3 A parallel-plate structure with lossy medium between the plates and driven by a voltage source. Device dimensions are: d= the channel width, b= the height of the channel, and W= gate width. From Rao [2.1]. 26

2.4 Electric and magnetic fields between the plates for a constant voltage source. Arrows denote the electric field, the o symbols indicate the magnetic field. From Rao [2.1] 31

2.5 TLM node for MESFET analysis 32

2.6 Debye length versus GaAs channel doping 33

2.7 Loss tangent versus GaAs channel doping 35

2.8 Dispersion characteristics of the TLM node at 10^{16} atoms/cm^3 doping level. Solid lines: reference [2.5], circle, square symbols: this work. 37

2.9 Dispersion characteristics of the TLM node at 10^{17} atoms/cm^3 doping level. Solid lines: reference [2.5], circle, square symbols: this work. 38

2.10 Dispersion characteristics of the TLM node at 10^{18} atoms/cm^3 doping level. Solid lines: reference [2.5], circle, square symbols: this work. 39

3.1 Mirrored MESFET channel section and the associated electromagnetic fields. d= the channel width, b= the height of the channel, and W= gate width. Arrows: electric field, and o,x symbols: magnetic field. 43

3.2 The components of the TLM system. 45

3.3 Steady-state spatial magnetic field in uniformly conducting dielectric. Solid line: calculated results: circle symbols: TLM results. 48

3.4 Steady-state spatial electric field in uniformly conducting dielectric. Solid line:

calculated results, square symbols: TLM results. 49

3.5 Transient response of the electric field in a uniformly conducting dielectric. Dashed line= calculated results, solid line= TLM results. 50

3.6 TLM-computed transient response of $H_y(t)$. 51

3.7 TLM-computed transient response of $E_z(t)$ for the reduced length structure. . 53

3.8 TLM-computed transient response of $H_y(t)$ for the reduced length structure. . 54

3.9 Equivalent circuit of the TLM transmission line. 55

3.10 Second-order response of the TLM network. 57

3.11 Time closeup view of $H_y(t)$'s initial oscillation. 59

3.12 Steady-state spatial magnetic field in linearly-doped conducting dielectric. Solid line: calculated results, circle symbols: TLM results. 60

3.13 Steady-state spatial electric field in a linearly-doped conducting dielectric. Solid line: calculated results, square symbols: TLM results. 61

3.14 Transient response of the electric field in a linearly-doped conducting dielectric. Dashed line: calculated results, solid line: TLM results. 62

3.15 Simulation of the GaAs MESFET conducting channel by a collection of discrete TLM systems. 64

4.1 The $I_{DS}(V_{GS},V_{DS})$ characteristics of a MESFET 68

4.2 A sketch of the depletion areas in region I of the $I_{DS}(V_{GS},V_{DS})$ characteristics . 69

4.3 A sketch of the depletion areas in region II of the $I_{DS}(V_{GS},V_{DS})$ characteristics 70

4.4 A sketch of the depletion areas in region III of the $I_{DS}(V_{GS},V_{DS})$ characteristics 71

4.5 Flow-chart showing the outline of the GaAs MESFET model. 75

4.6 Flow-chart showing the outline of the Voltage Balance Method. 76

4.7 GaAs MESFET discretization scheme 78

4.8 Closeup of the discretization in the gate region 79

4.9 Steady-state mean drift velocity versus electric field for GaAs; Carnez et al. [4.9]. Solid line $N_d=1x10^{17}$ cm^{-3}; dashed line $N_d=3x10^{17}$ cm^{-3}. 83

4.10 Steady-state mean energy versus electric field; Carnez et. al [4.9]. Solid line $N_d=1x10^{17}$ cm^{-3}; dashed line $N_d=3x10^{17}$ cm^{-3} 84

4.11 Normalized steady-state electron mass versus electric field; Carnez et al. [4.9]. Solid line $N_d=1x10^{17}$ cm^{-3}; dashed line $N_d=3x10^{17}$ cm^{-3}. 85

4.12 Flow chart showing the outline of the TLM analysis. 97

5.1 Drift velocity versus time when applying an electric field pulse. Solid line: analytical formulation [5.5, 5.6]; solid dots: Monte Carlo calculations [5.5, 5.6]. 105

5.2 Drift velocity versus time when applying an electric field pulse. Solid line: analytical formulation [5.5, 5.6]; solid dots: Monte Carlo calculations [5.5, 5.6]. 106

5.3 Electron energy versus time when applying an electric field pulse. From Carnez et. al. [5.5,5.6]. 107

5.4 Steady-state electric field versus electron energy. Solid line: fitted polynomial response, x symbols: Monte Carlo results from Carnez et al. [5.5,5.6]. 108

5.5 Steady-state normalized electron effective mass versus electric field. Solid line: fitted polynomial response, x symbols: Monte Carlo results from Carnez et al. [5.5,5.6]. 110

5.6 Steady-state drift velocity versus electric field. 111

5.7 Transient drift velocity response. Solid line: response to 2/20/2 kV/cm electric field pulse with 2/2/8 pS time duration; dashed line: response to 2/40/2 kV/cm electric field pulse with 2/2/8 pS time duration. 112

5.8 Transient electron energy response. Solid line: response to 2/20/2 kV/cm electric field pulse with 2/2/8 pS time duration; dashed line: response to 2/40/2 kV/cm electric field pulse with 2/2/8 pS time duration. 113

5.9 Velocity-field relationships for MESFET #1 and MESFET #2. 117

5.10 Current-voltage characteristics of MESFET #1. Solid lines: this work, x symbols: Chang and Day [5.8], and o symbols: measured data [5.9]. 119

5.11 Electric field E_z in the channel. Solid line: this work, x symbols: Chang and Day [5.8]. 120

5.12 Electric fields in the surface region. Dashed, solid lines: E_x, E_z in this work; x,o symbols: E_x, E_z by Chang and Day [5.8]. 121

5.13 Electron concentration in the channel. Solid line: this work, x symbols: Chang and Day [5.8]. 122

5.14 Electron velocity in the channel. Solid line: this work, x symbols: Chang and Day [5.8]. 124

5.15 Current-voltage characteristics of MESFET #2. Solid lines: this work, x symbols: Chang and Day [5.8], and o symbols: measured data [5.10]. 125

5.16 Doped GaAs sample for non-stationary velocity analysis. (a) the sample enclosed between metal plates and connected to a voltage source. (b) Orientation of the fields in the sample shown with the mirrored lower half. 127

5.17 TLM energy versus time. 129

5.18 TLM node conductivity versus time. 130

5.19 TLM computed electric field E_z versus time response. 132

5.20 TLM computed magnetic field H_y versus time response. 133

5.21 Transient current versus time response. 134

5.22 Time-dependent velocity response. Solid line: response to a 2/20/2 kV/cm pulse with 2/2/6 pS time duration, dashed line: response to a 2/40/2 kV/cm pulse with 2/2/6 pS time duration. 137

5.23 Gate and drain circuits charging voltages versus time. 139

5.24 Gate and drain time constants versus time. 140

5.25 Carrier velocity at two channel sections versus time. 141

5.26 Carrier concentration in the high field section versus time. 142

5.27 TLM pulse energy versus time. 143

5.28 TLM nodes conductivity versus time. 144

5.29 Channel depth at two channel sections versus time. 145

5.30 Electric field versus time. Solid line: TLM computed, x symbols: theoretical calculations. 147

5.31 Close-up of the electric field versus time. Solid line: TLM computed, x symbols: theoretical calculations. 148

5.32 TLM computed magnetic field versus time. The TLM nodes are located at a(x=1175Å), b(x=1125Å), c(x=1075Å), d(x=1025Å), e(x=975Å), f(x=925Å), g(x=875Å), h(x=825Å), i(x=775Å), j(x=725Å), k(x=675Å), l(x=625Å), m(x=575Å), n(x=525Å), o(x=475Å), p(x=425Å), q(x=375Å), r(x=325Å), s(x=275Å), t(x=225Å), u(x=175Å), v(x=125Å), w(x=75Å). 149

5.33 Channel current versus time. Solid line: TLM computed, x symbols: theoretical calculations. 150

5.34 Electric fields versus time. Solid line: TLM computed, x symbols: theoretical calculations. 151

5.35 TLM computed magnetic field versus time. The TLM nodes are located at a(x=1175Å), b(x=1125Å), c(x=1075Å). 152

5.36 Channel current versus time. Solid line: TLM computed, x symbols: theoretical calculations. 154

5.37 The applied electric field signal E_x versus time. 155

5.38 The applied and charged gate voltage versus time. The DC components have been removed. Solid line: applied voltage, dashed line: charging voltage. . 156

5.39 The variation of the gate circuit time constant vs time. x symbols: MESFET analysis results, dashed line: fitted function. 158

5.40 The electric field versus time in the low field channel section. Solid line: theoretical analysis, x symbols: TLM computed. 159

5.41 TLM computed magnetic field versus time in the low field channel section. The TLM nodes are located at a(x=1175Å), b(x=1125Å), c(x=1075Å), d(x=1025Å), e(x=975Å), f(x=925Å), g(x=875Å), h(x=825Å), i(x=775Å), j(x=725Å), k(x=675Å), l(x=625Å), m(x=575Å), n(x=525Å), o(x=475Å), p(x=425Å), q(x=375Å), r(x=325Å), s(x=275Å), t(x=225Å), u(x=175Å), v(x=125Å), w(x=75Å). 160

5.42 The channel current versus time. Solid line: theoretical analysis, x symbols: TLM computed. 161

5.43 Comparison between time domain and steady-state computed transconductances of the same device. 162

LIST OF SYMBOLS

Chapter 2

α	Attenuation constant
e_{α}	Attenuation error
K	Boltzmann constant
σ	Conductivity
L_D	Debye length
N_D	Doping concentration
E	Electric field
q	Electron charge
Y	Equivalent transmission line admittance
Z	Equivalent transmission line impedance
R	Equivalent transmission line resistance
ω	Frequency in radians
V^i	Incident TLM impulse
H	Magnetic field
ϵ	Permittivitty
μ	permeability
ß	Phase constant
e_{β}	Phase error
γ	Propagation constant
V^r	Reflected TLM impulse

c Speed of light

T Temperature

t Time

C TLM node Capacitance

I TLM node current

L TLM node Inductance

$\Delta \ell$ TLM node-to-node spacing

r TLM node resistance

Δt TLM time step

k TLM time step number

V TLM node voltage

λ Wavelength

Chapter 3

σ Conductivity

τ Dielectric relaxation time constant

N_D Doping concentration

λ Eigenvalue of the voltage response

α Eigenvalue's real part

β Eigenvalue's imaginary part

$\mathbf{E}$ Electric field

ω Frequency in radians

$\mathbf{H}$ Magnetic field

ϵ	Permittivitty
t	Time
i	Time instantaneous current
v	Time instantaneous voltage
$\Delta\ell$	TLM node-to-node spacing
r	TLM node resistance
Δt	TLM time step
C	TLM system Capacitance per width
I	TLM system current
A	TLM system energy
b	TLM system height
L	TLM system Inductance
d	TLM system length
W	TLM system width
R	TLM system resistance per width
V	TLM system voltage

Chapter 4

R_p	Buffer layer resistance
V(t)	Charging voltage
$V_d(t)$	Charging voltage at the drain electrode
σ	Conductivity

R_c	Contact resistance
L_T	Depth of the depletion region at the high field region
h_o	Depletion/conducting-channel interface
ρ	Density of surface states
τ	Dielectric relaxation time constant
τ_g	Dielectric relaxation time constant of the gate circuit
τ_d	Dielectric relaxation time constant of the drain circuit
N_D	Doping concentration
$\mathbf{E}$	Electric field
q	Electron charge
μ	Electron drift mobility
w	Electron energy
v	Electron average drift velocity
w_o	Electron energy at thermal equilibrium
τ_w	Electron energy relaxation time constant
P	Electron momentum
τ_p	Electron momentum relaxation time constant
δ	Error term
n	Free electron concentration
V_s	Linear surface voltage
$\mathbf{H}$	Magnetic field
E_L	Maximum linear electric field

I_c MESFET channel current

V_{bi} MESFET built-in voltage

V_d MESFET drain voltage

V_g MESFET gate voltage

W MESFET gate width

V_{signal} MESFET signal voltage

$E_{surface}$ MESFET surface field

$V_{surface}$ MESFET surface voltage

R_{dc} Metallurgical ohmic resistance

m^* Normalized electron effective mass

V_{dc} Ohmic voltage drop

E_t Peak electric field above which negative differential velocity is exhibited

ϵ Permittivitty

S Seconds

$\Delta \ell$ Space discretization

ρ_1 Specific resistivity of the contact metal

v_{ss} Steady-state average drift velocity

E_{ss} Steady-state electric field

m^*_{ss} Steady-state normalized electron effective mass

V_{ss} Surface voltage contributed by surface states

a_1 Thickness of the n^+ channel

t Time

Δt Time discretization

I TLM system current

A TLM system energy

$V_{depletion}$ Voltage in the depletion layer

$V_{channel}$ Voltage in the channel layer

Chapter 5

R_p Buffer layer resistance

V(t) Charging voltage

$V_d(t)$ Charging voltage at the drain electrode

σ Conductivity

R_c Contact resistance

L_T Depth of the depletion region at the high field region

h_o Depletion/conducting-channel interface

τ_g Dielectric relaxation time constant of the gate circuit

τ_d Dielectric relaxation time constant of the drain circuit

N_D Doping concentration

E Electric field

q Electron charge

μ Electron drift mobility

w Electron energy

v Electron average drift velocity

v_s Electron average drift velocity at saturation

w_o	Electron energy at thermal equilibrium
τ_w	Electron energy relaxation time constant
P	Electron momentum
τ_p	Electron momentum relaxation time constant
n	Free electron concentration
f	Frequency
H	Magnetic field
E_L	Maximum linear electric field
I_c	MESFET channel current
V_{bi}	MESFET built-in voltage
V_d	MESFET drain voltage
V_g	MESFET gate voltage
W	MESFET gate width
V_{signal}	MESFET signal voltage
$E_{surface}$	MESFET surface field
m^*	Normalized electron effective mass
V_{dc}	Ohmic voltage drop
E_t	Peak electric field above which negative differential velocity is exhibited
ϵ	Permittivitty
E_c	Ratio of the drift mobility to the saturation velocity
S	Seconds
$\Delta \ell$	Space discretization

ρ_t Specific resistivity of the contact metal

v_{ss} Steady-state average drift velocity

E_{ss} Steady-state electric field

m^*_{ss} Steady-state normalized electron effective mass

t Time

Δt Time discretization

I TLM system current

A TLM system energy

R TLM system resistance per width

Acknowledgements

I wish to thank my research supervisors, Dr. M.M. Ney and Dr. R.G. Harrison for their support and guidance throughout the course of this work, and for the many useful suggestions they have made. I would also like to thank Dr. W.J.R. Hoefer who suggested the thesis topic, and to the members of my supervisory committee; Dr. G. Costache, Dr. B. Syrett, Dr. G. Tarr, and Dr. R. Vahldieck. In addition, I have had many useful discussions with the members of the electromagnetics group at university of Ottawa, but in particular with Ulf Mueller, presently at Duisberg University, Germany.

I am indebted to Dr. D.I. Kennedy and R.B. North of Optotek Ltd. who gave me ample experimental and practical exposure to GaAs MESFETs and MMICs technologies.

Finally I wish to thank both my family for their encouragement, and my wife, Dalida, for her patience throughout the course of this work.

CHAPTER 1

Introduction

1.1 Review of MMIC Analysis Methods

Modelling of GaAs MMICs which directly integrate passive and active components into a single semiconductor requires simulation of the amplifying MESFETs together with the surrounding passive structures, such as single and multi-coupled conductors, spiral inductors, and thin film capacitors. As more components are integrated into a single chip and the frequency of operation increases, the feature size becomes comparable to the guided wavelength and electromagnetic energy starts to couple more strongly between components. Hybrid MIC design techniques which are engineering labor intensive and based on a low volume cut and try approach cannot be used for MMICs. In hybrid MICs, a preliminary design is built by epoxying discrete passive and active components into an insulating substrate and connecting them together by wirebonding. The circuit is tested and tuned by optimizing wire bond lengths and shorting portions of resistors and transmission lines. The required specifications are achieved with following re-design and assembly iterations. This approach is not compatible with MMIC technology since they cannot be tuned after fabrication, and the associated time and costs per design and fabrication iteration are very high.

MMICs are primarily simulated either with linear and non-linear electrical-network computer-aided design (CAD) tools which offer rapid design of rough accuracy, or with full-wave numerical electromagnetic analysis which is very slow but offers high accuracy in passive device modelling. Despite the availability of these tools, research and development continue for a circuit analysis technique which offers the best compromise between, on the one hand, speed of analysis and flexibility of circuit optimization, and, on the other hand, the best possible modelling accuracy. As a result, electrical-network CAD techniques have been undergoing development for improved modelling accuracy. On the other hand numerical analysis techniques have been undergoing development for

integrating active device modelling using SPICE type equivalent circuits.

The electrical-network CAD tools, which were originally developed for the transient and steady-state analysis of electronic circuits, are pre-dominantly chosen for speed and flexibility of analysis. Linear CAD tools simulate MMICs by treating the monolithic elements as discrete components and representing them as lumped-element circuits. During steady state analysis, the elements are reduced into one of abcd, admittance, or scattering matrices which are cascaded to produce a frequency dependent output. Non-linear CAD tools, such as SPICE [1.1,1.2] and the Harmonic Balance Method (HBM) [1.3,1.4], can best model the impact of mild non-linearities of the active device on the steady state performance. In SPICE, models of nonlinear capacitors and inductors are described in terms of a state vector of capacitor voltages, inductor currents, voltages of the transmission line ports, and non-linear resistor control variables. Kirchhoff's laws are combined with the voltage-current relationships of the circuit components to produce a set of coupled differential, difference, and algebraic equations with constant coefficients. By using the results of dc analysis as the starting point, the set of equations is then solved in the time domain with a suitable integration technique, and the voltages and currents of the nodal circuit are calculated at each node for a transient time response. On the other hand, HBM is particularly useful in electric circuits that exhibit widely-separated time constants which makes it time-wise expensive for SPICE to continue to analyze until the transient response has vanished. With HBM, the circuit's steady-state response is assumed to consist of sums of sinusoids, and proceeds to find the coefficient of the sinusoids that satisfies the circuit system's differential equations. By dividing the system into two portions where the linear components are analyzed in the frequency domain, and the nonlinear elements are analyzed in the time domain, the nonlinear integro-differential equations are converted into a system of nonlinear algebraic equations whose solution-typically obtained by Newton's method-is the coefficient of the sinusoids that makes up the steady-state response. If the signals in the circuit are periodic, the discrete Fourier transform provides the needed conversion between the two domains. Hence, HBM computes the steady-state solution directly while avoiding any transients.

Full-wave electromagnetic analysis is predominantly applied to modeling passive

MMIC structures. To simulate the entire structure, lumped element models of active structures are incorporated. Though analysis of passive structures is far more accurately modelled than with electrical-network CAD tools, the analysis time is much slower. As a general rule in numerical electromagnetic analysis, the complexity of a circuit is not determined by the circuit geometry, but rather by the number of mesh points or subsections into which the structure is divided. Coarse discretization yielding approximate solutions is necessary for gains in computational speed. Though dozens of numerical electromagnetic tools [1.5] are currently in use in various laboratories, there are three commercialized frequency domain tools based on the spectral domain approach (SDA) [1.6], the method of moments (MoM) [1.7], and the finite element method (FEM) [1.8], and two commercialized time domain tools based on the finite-difference time-domain method (FDTD) [1.9], and the two-dimensional transmission line matrix method (TLM) [1.10]. The SDA method [1.11] formalizes the integral equation of the structure in the Fourier transform or spectral domain which is then solved by the Galerkin's method to yield the propagation constant and the current distribution from which the characteristic impedance is derived. This tool is numerically efficient since significant pre-processing time is required to generate the integral equation itself, but it is restricted in general to solving well-shaped planar and lossless transmission lines. MoM [1.12] is used to solve the integral equation of a MMIC structure by employing rooftop functions for the planar metallizations such as microstrip lines and pulse functions for the vertical metallizations such as vias. The number of basis functions assigned to the structure is typically optimized for speed; for example, more basis functions are utilized around microstrip discontinuities to model the current variations, and conversely, fewer basis functions are assigned away from discontinuities. This method solves the propagation constant and impedance of the electrical component and automatically accounts for the electromagnetic coupling. With FEM [1.13], the cross-section is divided into a large number of polygons where the field in each polygon is represented by a polynomial. By imposing field continuity at the polygon interfaces, the resulting matrix equations are solved for the relevant parameters of the structure. This method can solve the most complex MMIC passive structures, but at the expense of far more computer memory and

speed resources than SDA or MoM.

Numerical time domain methods, on the other hand, have the advantage over the numerical frequency domain methods by being able to account for active device transients and nonlinearities using physical-based models which also incorporate time-dependent electron transport behavior. Their disadvantage is that they are far slower since time is also discretized. FDTD [1.14] is a mathematical procedure where the time-dependent partial differential equations are replaced by a set of finite difference equations. These equations are solved iteratively at each point in the mesh placed over the structure via a volume-gridding technique. In contrast, the TLM technique [1.15] is a physical procedure where current and voltage waves propagating in two- or three-dimensional lumped element networks have direct equivalences to the electric and magnetic fields in the simulated medium. TLM lumped element networks are constructed with (i) nodes which simulate the propagation of the electromagnetic fields in an unbounded medium, and (ii) a system enclosing the nodes, boundaries, and the TLM energy sources which can simulate the various propagation modes in the bounded medium. Both FDTD and TLM have demonstrated similarities in solving the wave equation [1.16], and hence are considered as viable tools for the computation of the electromagnetic fields in waveguide and transmission line structures well into the millimeter wavelengths.

1.2 MMIC Modelling Tasks

There are three aspects of modelling tasks required for the comprehensive and accurate analysis of MMIC structures. These pertain to (i) passive structure modelling, (ii) active device modelling, and (iii) coupling between passive structures to active devices. The capabilities of electrical-network CAD tools and numerical electromagnetic methods to best model these aspects will be evaluated and assessed. The conclusions of this section will determine the objective and tasks of this thesis.

1.2.1 Passive Structures Modeling

In passive MMIC structures, the analysis of single and multiple coupled

transmission lines must take into account changes in strip width, strip bends, and strip discontinuities in multiple dielectric media, as well as the electromagnetic coupling between components. Typical structures include spiral inductors, monolithic transformers, metal-dielectric-metal capacitors, thin film resistors, and single and multi-coupled microstrips covered with single or double dielectric layers. To accurately model these structures, the electromagnetic field propagation in these structures and the appropriate boundary conditions must be taken into account. This type of analysis lends itself to numerical electromagnetic analysis as demonstrated, for example, by the simulation of spiral inductors [1.7], metal-dielectric-metal capacitors [1.17], interdigital capacitors [1.18], multi-coupled microstrip lines [1.19], and microstrip discontinuities [1.20]. The accuracy of the numerical analysis is limited by the discretization. As the mesh size approaches zero or the number of subsections approaches infinity, the numerical solution approaches the analytical prediction. Conversely, the solution of passive MMIC structures departs from full accuracy with coarser discretization.

Since electrical-network CAD tools compute electrical voltages and currents rather than the electromagnetic fields described by Maxwell equations, it has been necessary to equip them, as has happened in recent years, with some hybrid MIC models based on curve-fitting to the results of full-wave numerical methods and empirical formulae. For example, modelling of single and two coupled microstrip lines based on TEM-wave propagation in a single dielectric are provided in closed form expressions using interpolated spectral domain numerical analysis results for various substrate thicknesses, conductor widths, and dielectric constants [1.21-1.23]. Close to X-band frequencies, however, the transverse dimensions begin to represent a significant fraction of the guide wavelength and the fields begin to concentrate in the dielectric, so that the propagation departs from TEM mode. To take into account the loss of validity of the assumption of TEM propagation, a closed-form dispersion expression describing a frequency dependent effective dielectric constant has been appended to single and multiple coupled line models. Microstrip discontinuities are provided in terms of lumped elements models based on, for example, Babinet equivalence to waveguide for the microstrip slit model [1.24], and the resonator method for microstrip bends [1.25]. Lumped element models

for spiral inductors [1.26], and interdigital capacitors [1.27] based on low frequency or quasi-static approaches have also been provided. Despite these additions, electrical-network CAD tools cannot treat a large class of MMIC passive structures, for example, single and coupled microstrip transmission lines embedded in multi-dielectric media, microstrip dispersion effects in discontinuities, distributed effects in spiral inductors, and the electromagnetic coupling between structures.

1.2.2 Active Device Modeling

Analysis of GaAs MESFETs must accurately represent their operation under both small and large input signal levels. At present, the two principal methods for theoretically characterizing the operation of semiconductor devices make use of equivalent circuit models and physical device models.

Equivalent circuit models describe the electrical properties of the active device, and can be derived from theoretical considerations of the device operation or from experimental results. Device modelling in linear CAD programs is most commonly accomplished with a lumped-element circuit-type model derived from measurement of scattering parameters carried out at a group of frequencies, small RF drive level, single bias point, and with the device embedded in a fixed impedance system. Fundamental to the analysis is the assumption that the RF drive level is small enough that the MESFET remains at the bias point. In non-linear CAD tools, the same GaAs FET is simulated under large RF signal levels which causes significant voltage swings about the bias level. Thus, modelling large-signal MESFETs [1.28] consists of extraction of a large-signal model from DC measurements and optimization of a lumped element model which closely follows the actual device operation covering the saturation region, pinch-off region, and the drain-to-gate breakdown region, as well as the current-voltage characteristics in between. The advantages of the equivalent circuit models are their speed of analysis and the ease with which they can be integrated into CAD simulators. The disadvantages are several; for example, equivalent circuit models become increasingly complex and difficult to relate to the physical structure at frequencies higher than a few GHz. Also, the strong dependence of the model elements on multiple operating parameters such as bias conditions, signal

levels, and circuit impedance levels makes it very difficult to obtain a large-signal device model which accurately models the transient characteristics of the device.

Physical based GaAs MESFET modelling pertains to the description of the electron transport properties in any two-dimensional cross-section of the active channel underneath the gate electrode. Data on the device geometry, doping density, and bias conditions are used in solving the transport equations (particle, energy, and momentum conservation equations) which govern the fields in the conducting region and the Poisson equation which governs the fields in the depletion region together with a non-linear velocity-electric field relationship [1.29, 1.30]. Owing to the complexity of the two-dimensional analysis which arises from the planar placement of the electrodes, a single comprehensive analysis technique accounting for all the two-dimensional effects is not practical since it requires large computer resources. For this reason dozens of MESFET analysis techniques have been developed in the last few decades adopting various simplifying assumptions.

MESFET models can be classified into one-dimensional models, two-dimensional models, and "one and a half" or quasi two-dimensional models. A one-dimensional MESFET model is the simplest. The device's currents and voltages are expressed in a analytical closed form expressions which can be solved for quickly. This type of model, originally considered by Shockley [1.31] in the gradual channel approximation, adopts the following 8 assumptions:

- the regions are divided into fully-depleted and fully conductive layers,
- one-dimensional analysis of the Poisson equation
- one-dimensional analysis of the current continuity equation
- the source and drain contacts are rotated 90° to become perpendicular to the current flow,
- the velocity-field relationship is approximated with discrete linear segments or closed form expressions,
- the doping parameters are idealized,
- the fringing effects at either side of the gate electrode are neglected, and,
- the source and drain ohmic regions are idealized or neglected.

Despite its limitations, the gradual channel approximation was used to characterize low frequency MESFETs with long gate lengths (typically > 3um). Full two-dimensional analysis, on the other hand, is much more rigorous and cannot be formulated in a closed form, but must be carried out numerically with a finite-difference or finite-element formulation and using Monte Carlo analysis results for the electron transport properties. Since the execution speed is slow and extensive memory resources are required, this analysis technique is virtually confined to main-frame computers. In a full two-dimensional MESFET analysis, such as in the treatments of Snowden and Loret [1.32], Feng and Hintz [1.33], Ghazaly and Itoh [1.34], and Yoganathan and Banerjee [1.35], assumptions 1 to 8 are treated with the following corresponding analysis effects:

- gradual light conduction in the depletion region and a depletion/conducting channel transition region,
- two-dimensional analysis of the Poisson equation
- two-dimensional analysis of the current continuity equation to take into account the velocity rotation vector towards the drain electrode
- planar electrodes geometry
- doping dependent velocity field relationship,
- arbitrary doping and mobility dependence,
- two-dimensional analysis of the fringe region in the gate-drain region, and,
- surface and substrate effects and their influence on the ohmic region, respectively.

In addition, the following analysis effects are considered:

- gate recess,
- influence of velocity overshoot effects,
- the influence of the buffer layer, and,
- the full form of Boltzmann's transport equation which includes the effects of diffusion and temperature.

Quasi two-dimensional MESFET modeling has been widely accepted as a viable alternative since it offers optimal mix of accuracy and analysis speed. It replaces some or all of Shockley's one-dimensional assumptions with the corresponding full two-dimensional analysis, but not all the two-dimensional effects are taken into account. This type of model can therefore vary in complexity and execution speed according to the

adopted set of assumptions and analysis effects. There are two quasi two-dimensional MESFET modelling approaches, and they are based on either (1) analytical closed form expressions of the device's currents and voltages, or (2) numerical solutions. Both type of approaches offer their own execution speed versus modelling accuracy tradeoffs.

Analytical quasi two-dimensional analysis emerged as an enhanced accuracy alternative to the gradual channel approximation. Shockley's model was initially improved in the works of Grebene and Ghandi [1.29] by including the effects of velocity saturation and two-dimensional Poisson equation analysis. The works of Lehovec and Zuleeg [1.30] included the effects of interaction between the drain and gate potentials and the associated fringe regions. The accuracy of analytical modelling was further extended by including the effects of the static dipole and the formation of Gunn domain under the channel in the works Lehovec and Miller [1.36] and Shur [1.37]. Closed-form solutions for ion-implanted doping profiles were given by Taylor et al. [1.38] and Weng [1.39]. A time-dependent velocity-field relationship was included in the work of Carnez et al. [1.40] by coupling a closed-form solution of the simplified electron energy and momentum conservation equations (which excluded the effects of temperature and diffusion) to the MESFET analysis. The effects of surface states on the MESFET model were accounted for by Hariu et al. [1.41], and the effects of electrode voltages on the source and drain ohmic regions were also accounted for in the work of Byun et al. [1.42]. The velocity-field analytical form, including overshoot effects, was included in the works of Chang and Day [1.43] to formulate a versatile MESFET model for arbitrary doped channels. Finally, a doping-mobility relationship was included by Mohammad et al. [1.44] to describe heavily doped MESFET channels.

At some point, the adoption of additional analysis effects or complex MESFET structures precludes a closed form solution, and numerical formulation is the only alternative. Numerical quasi two-dimensional analysis has emerged as a less accurate but faster execution alternative to the full two-dimensional analysis which enables MESFET modeling in computer workstations. Early works in numerical modelling of MESFETs by Kennedy and O'Brien [1.45], Himsworth [1.46], Yamaguchi and Kodera [1.47], and Reiser [1.48] evaluated a solution of Poisson and current continuity equations with stationary

velocity-versus-electric-field dependence which excluded a time dependence. This type of analysis facilitated the description of a gradual depletion-to-conduction transition, two-dimensional current continuity, and velocity rotation vector. The same class of analysis was further extended by including the diffusion-field dependence by Wada and Frey [1.49]. A simplified non-stationary or time-dependent velocity-field relationship was taken into account by Curtice and Yun [1.50] by including the solution of Boltzmann's conservation equations which included temperature dependence. Higgins and Pattanayak [1.51] used a simplified non-stationary analysis by using a closed form expression for velocity of the carriers versus time, and Halkias et al. [1.52] used simplified electron energy and momentum conservation equations (which excluded diffusion and temperature to derive time-dependent velocity-versus-electric-field dependence) for time domain MESFET analysis.

Despite improvements in physical GaAs MESFET models, their use in electrical-network CAD tools and numerical electromagnetic MMIC simulators has been limited. Published results, while exactly fitting the measured transistor under study, almost always fail to predict another transistor manufactured elsewhere. The reason for this is that published results rely mainly on the reported geometrical and doping parameters to generate a model. Additional MESFET parameters crucial to the accuracy, such as the density of surface and interface states, the density of bulk and buffer traps, exact gate recess depth, metallization contact resistances, and the doping-dependent velocity-field relation, are almost always unavailable and must be assumed. These limitations, however, can be easily overcome by incorporating specialized test structures in a process-control monitor [1.53, 1.54] to characterize and extract the missing MESFET parameters.

Compared to small-signal equivalent circuit models, steady-state physics-based MESFET analysis is more compact. Compared to SPICE time domain MESFET analysis, physically-based MESFET modelling incorporating non-stationary velocity-field dependence can inherently describe the device operation under any type of circuit condition including non-linear large-signal operation.

1.2.3 Modelling the Coupling Between Passive Structures and Active Devices

The dynamic electromagnetic coupling between passive and active components must be accurately represented. For example, there are cases for which electromagnetic field high-frequency components produced by signals applied to the device, and fed to the surrounding passive structures, are coupled back to the active region. This effect has not yet been reported in the literature since it can only be taken into account by an electromagnetic treatment of MMICs which must include physics-based field modeling of MESFETs. For example, linear and non-linear electrical-network CAD tools simulate the MMIC structures as non-physical discrete equivalent circuits and therefore they cannot take the effects of dynamic coupling into account. The spectral domain based numerical electromagnetic simulator [1.6], which can calculate the effects of coupling between passive components, adopts a non-electromagnetic link to active devices for using linear or SPICE-type lumped circuit models which prevents it from simulating passive to active device coupling. In addition, the numerical finite difference time domain method is primarily used to calculate equi-potential distributions and current-voltage characteristics of MESFETs. These are used to extract a SPICE model for large signal CAD MMIC analysis. On the other hand, simulation of microwave integrated circuits is facilitated by electromagnetic field analysis since these are directly computed in passive structures. Hence the need for an electromagnetic field treatment for GaAs MESFETs in order to interface them with the non-active surrounding structures has emerged. In conclusion, the three MMIC modeling tasks can be accomplished with numerical electromagnetic time-domain analysis which must incorporate a physical based GaAs MESFET model. Two time-domain electromagnetic techniques are available which can potentially be adopted for the task of GaAs MMIC modelling: FDTD and TLM. Though FDTD can be developed to meet this objective, there are some advantages in using the TLM technique, such as insights into physical wave propagation and its efficient compatibility with Diakoptics via the John's Matrix [1.55]. Unlike FDTD, however, a TLM procedure for physical analysis of GaAs MESFETs has not yet been demonstrated. In addition, electromagnetic analysis of the MESFET active layer have yet to be developed. These two issues will form the substance of this thesis.

1.3 The Objectives of the Thesis

The objective of this thesis is to formulate a physics-based GaAs MESFET modelling technique into the TLM method. There are two types of approaches. The first is a direct modelling approach in which the TLM network is embedded within an environment consisting of wires, stubs, and lumped elements such that the behavior of the TLM medium resembles the corresponding physical system. This type of formulation must first be explored.

Let us examine first the MESFET's depletion region. After the gate metallization is deposited on the lightly-doped GaAs channel, electrons diffuse from the bulk of the semiconductor and form a dense layer of mobile carriers at the interface leaving behind uncovered positive fixed charges. Eventually, their population will build up to the point where the field they set up will counteract the diffusion current. Within the depletion region, no mobile electrons exist, and a normal electric field exists. This field is a maximum at the metal-semiconductor interface and linearly decays to zero at the interface between the depletion layer and the conducting channel. Application of a negative bias will increase the width of the space charge layer since the field across the junction is increased. More fixed charges will be exposed retarding the diffusion current until a balance is reached. The TLM method cannot model the depletion region principally because it cannot simulate fixed charges. It is, though, possible to conceive of an implementation where the entire nodes are considered as energy sources which emulate fixed charges, and some of the boundaries would be non-stationary. An algorithm can be embedded such that in response to the boundary conditions, the energy sources would launch pulses of various magnitudes and polarities and the volume of the region would expand or contract such that the Poisson equation is satisfied. However, MESFET operation also involves the behavior of mobile electrons in the conducting channel. This must be investigated. The field interactions there are highly non-linear since (i) the carrier velocity does not respond instantly or linearly to the applied field and (ii) the electron concentration in various parts of the channel undergoes accumulation and partial depletion in the high field region. The TLM method can not model these complex interactions either. There are also other limitations in the TLM method which make direct

physical GaAs MESFET modelling impractical. Let's suppose that a new two-dimensional TLM formulation of the MESFET active region has been realized by supplanting the nodes with the necessary additional hardware and algorithms. We are not concerned with how the method has been arrived at, but we would like to determine the time required for a MESFET response, for example, to a 10-GHz signal. Suppose that the MESFET has a gate length of 0.7 μm, source-drain spacing of 5 μm, and a channel depth of 1200 Å. Typically, high field conditions reduce the channel opening to roughly 10% of the channel depth, and at least 10 nodes are required to simulate the region with reasonable accuracy. This requires a space discretization of 10 Å, and the active area is filled with 600,000 nodes. Space and time discretization are related by the speed of light in the medium, and hence $\Delta t = 1.2 \times 10^{-17}$ seconds. Assuming that a computer is available which can execute the TLM scattering matrix of more than half a million nodes at a rate of 5 times a second, the same computer will need 19 days to execute 8.3 million time steps covering only one cycle of the signal. Using a non-uniform space mesh has been reported to improve the computer run time for certain class of problems by 80%. Under present conditions, dense meshing would be required for the high field region whose area is a time variable and can extend roughly by 150% of the gate length. Using the reported percentage time reduction, the run time of this problem reduces to 4 days. This figure deteriorates quickly for power GaAs MESFETs which use much wider source-drain spacings and deeper channels. This discussion shows another limitation. The linkage of the TLM time step to the space discretization severely restricts its scope. In GaAs MESFETs, when the voltages are applied to both electrodes, the gate-source and drain-source circuits charge according to their R-C time constants. The drain time constant is the lower one and is typically in the order of $\tau_d \approx 10^{-14}$ seconds. The time domain response can be adequately characterized choosing Δt between $0.01\tau_d$ to $0.1\tau_d$. In contrast, the TLM method presets Δt between $1 \times 10^{-5}\tau_d$ to $1 \times 10^{-4}\tau_d$ resulting in excessively large run times. It becomes clear from this discussion that the direct approach to physical TLM formulation of GaAs MESFETs is neither possible nor practical.

The second type of approach is novel, and presents an indirect physical TLM formulation for GaAs MESFETs. In this approach, the MESFET is treated as a two-port

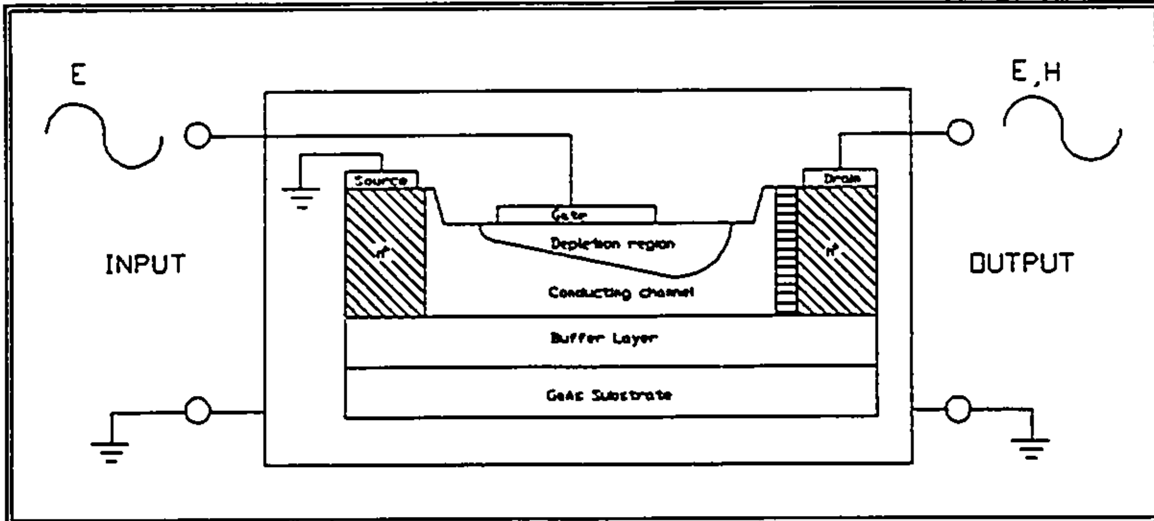

Figure 1.1: Two-port model of the GaAs MESFET.

structure shown in Figure 1.1 where the depletion region is the input. The output consists of the conducting channel at the vicinity of the drain electrode which is shown as the horizontally shaded region in Figure 1.1. However, the parameters of the entire conducting channel can also be computed if needed. The electric field is treated as the input signal to the gate electrode, and the output electric and magnetic field emerging from the drain electrode is computed. The rationale of this type of indirect implementation is that in MMIC analysis, an electromagnetic wave propagating at the MESFET's gate electrode stimulates after a time delay another wave at the drain electrode. One is therefore less concerned with TLM simulation of the depletion region. However, the TLM simulation of the channel behavior and particularly that part in the vicinity of the drain electrode is more important since it shapes the output response. TLM formulation proceeds in two steps as shown in Figure 1.2. In the first step, a non-TLM, numerical GaAs MESFET analysis engine is implemented which responds to the electrode voltages and the electric field signal at the gate electrode, and computes the output channel current and the profiles of the depletion and conducting regions at every time step. The solving method is based on the solution of the Poisson and current continuity equations under a non-stationary carrier velocity. In the second step, the output of the analysis engine is transformed into the electromagnetic response in the channel by a new TLM

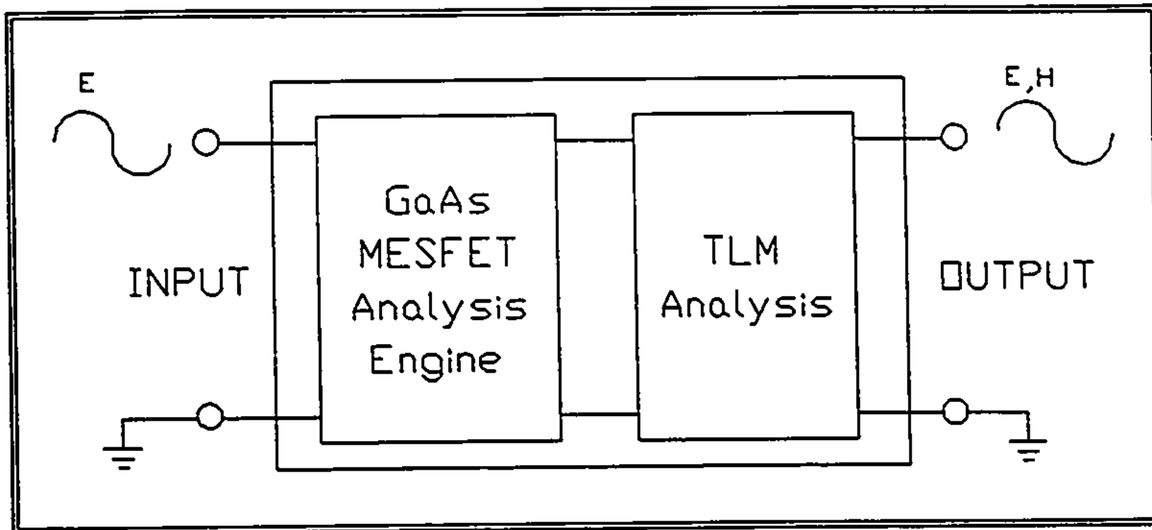

Figure 1.2: Block diagram of the two-port GaAs MESFET model.

formulation. The simulation by TLM is achieved by discretizing the channel into vertical sections small enough in width such that the electric field can be considered uniform within any section. Using the channel current, conductivity, and the length of the channel sections obtained by the GaAs MESFET analysis engine at every time step, the new TLM formulation transforms this output into an electromagnetic field response at any linearized section.

Interfacing a physical GaAs MESFET model into TLM using the indirect approach of this thesis offers several possibilities. For example, the GaAs MESFET analysis engine allows decoupling the time step and space discretization linkage, and enables the time step to be chosen more efficiently. Also, the engine allows non-uniform space discretization within the two axes and in different regions such that high field regions can be finely meshed while low field regions can be coarsely gridded. The combination of larger time steps and non-uniform discretizations greatly speeds computer run time and enhances the accuracy of the results. In addition, two unique possibilities are presented here. 1) Since the engine's time step can be coarser than that of the corresponding TLM network, this necessitates that the interface parameters, (i) the channel current, (ii) conductivity, and (iii) the length of the channel sections obtained by the GaAs MESFET analysis engine at every time step must be interpolated to fit the time step of the TLM

network; and 2) the TLM network simulating a particular conducting channel section can also be coarser than that simulated by the engine, and hence the interface parameters must also be spatially interpolated. Finally, much time saving is also obtained by confining the TLM simulation into the portion of the conducting channel in close vicinity to the drain electrode.

1.4 The Scope of the Thesis

This thesis will develop the two components of Figure 1.2, the GaAs MESFET analysis engine and the TLM network which simulates the conducting channel. This will result in an interface between the active portion of the GaAs MESFET and the two dimensional TLM method. The MESFET model encompasses any two-dimensional cross-section of the semiconductor along the gate width and underneath the gate electrode. The gate, drain, and source metallizations are not taken into account since their analysis must be taken in the context of a future three-dimensional analysis.

The thesis is organized as follows. Chapter 2 outlines a novel TLM formulation capable of modeling the local conductivity at any point in a MESFET channel with arbitrary doping profile. A two-dimensional shunt node previously used for simulating diffusion phenomena [1.56] has been re-formulated and adapted, for the first time, to simulate the wave propagation in the semiconductor medium, taking the local conductivity into account. Both the TLM node characteristics and the errors will be analyzed.

Chapter 3 derives an appropriate TLM system which can simulate a conducting channel section. It also derives interfacing parameters which enables the TLM system to transform the channel current, conductivity, and channel section length (computed by the GaAs MESFET analysis engine) into an electromagnetic field response. Unlike the predominant methods of using lumped elements and stubs to modify the wave propagation, a novel approach is used where the required response is obtained by modulating (i) the TLM energy sources, (ii) the TLM node conductivity, and (iii) the TLM system length. Several examples will be investigated. These will demonstrate the agreement of both the transient and the steady state responses produced by the TLM system with theoretical predictions.

Chapter 4 describes the theory behind the GaAs MESFET analysis engine. A numerical, physically based, and quasi-two-dimensional time-domain analysis is utilized. The time response is derived from non-stationary carrier velocity dependence coupled with the semiconductor's dielectric relaxation time constants. Poisson and current continuity equations and the carrier velocity dependence are solved at every time step using a novel voltage balance method (VBM). The chapter concludes with a discussion of the sources of errors in the MESFET model.

Chapter 5 is divided into two sections. The first section is devoted to verifying the GaAs MESFET analysis engine. The time domain velocity response is first verified against Monte Carlo results, and the VBM method is verified against two experimentally measured MESFETs reported in the literature. In the second section, three examples are presented showing TLM computations of (i) the non-stationary carrier velocity response to an applied field, (ii) the transient field response to an application of biases to the MESFET, and (iii) the field response to an applied electric field sinusoidal waveform at 10 GHz.

The thesis concludes in Chapter 6 with several recommendations for future work. The key one is to link this work with the 3-dimensional TLM method by augmenting the output channel fields with those computed by TLM for the passive field interactions in the MESFET source, gate, and drain electrodes.

1.5 References

1.1 L.W. Nagel, "SPICE2: A Computer Program to Simulate Semiconductor Circuits," Electronic Research Laboratory, University of California-Berkeley, Memo ERL-M520, 1975.

1.2 V. Rizzoli and A. Neri, "State of the Art and Present Trends in Nonlinear Microwave CAD Techniques," IEEE Trans. Microwave Theory Tech., Vol. 36, No. 2, pp. 343-365, February 1988.

1.3 J. Lindenlaub, "An Approach for Finding the Sinusoidal Steady-State Response of Non-Linear Systems," Proc. 7th Allerton Conf. Circuit Syst. Theory (University of Illinois, Chicago), 1969.

1.4 M. Nakhla and J. Vlach, "A Piecewise Harmonic-Balance Technique For Determination of Periodic Response of Non-Linear Systems," IEEE Trans. Circuits Syst., vol. CAS-23, pp. 85-91, Feb. 1976.

1.5 T. Itoh, "An Overview on Numerical Techniques for Modelling 3-Dimensional Passive Components," in Proc. 15th European Microwave Conf. (Paris), pp. 1059-1063, 1985.

1.6 R. H. Jansen, "LINMIC: A CAD Package For the Layout-Oriented Design of Single- and Multi-Layer of Single-and Multi-Layer MICs/MMICs up to mm-Wave Frequencies," Microwave Journal, pp. 151-161, February 1986.

1.7 M. Stubbs, L. Chow, and G. Howard, "Simulation Tool Accurately Models MMIC Passive Elements," Microwaves & RF, vol. 27, no. 1, pp. 75-79, January 1988.

1.8 EMAS, The MacNeal-Schwendler Corp., 815 Colorado Blvd., Los Angeles, Ca.

1.9 EM WAVETRACER, Wavetracer, 289 Great Rd., Acton, MA 01720.

1.10 W. Hoefer and P. So, The Electromagnetic Wave Simulator, John Wiley & Sons Ltd., 1991.

1.11 R.H. Jansen, "The Spectral Domain Approach for Microwave Integrated Circuits," IEEE Trans. Microwave Theory Tech., Vol. 33, No. 10, pp. 1043-1056, October 1985.

1.12 M.M. Ney, "Method of Moments as Applied to Electromagnetic Problems," IEEE Trans. Microwave Theory Tech., Vol. 33, No. 10, pp. 972-980, October 1985.

1.13 J.B. Davies, "The Finite Element Method", Chapter 2 of "Numerical Techniques For Passive Microwave and Millimeter-Wave Structures", edited by T. Itoh, John Wiley & Sons, New York, pp. 33-132, 1989.

1.14 K. Yee, "Numerical Solution of Initial Boundary Value Problem Involving Maxwell's Equations," IEEE. Trans. on Antennas and Propagation, Vol. AP-14, No. 3, pp. 302-307, May 1966.

1.15 P.B. Johns and R.L. Beurle, "Numerical Solution of 2-Dimensional Scattering Problems Using a Transmission Line Matrix," Proc. Inst. Elec. Eng., Vol. 118, No. 9, pp. 1203-1208, September 1971.

1.16 P.B. Johns, "On the Relation Between TLM Method and Finite Difference Methods for Maxwell's Equations," IEEE Trans. Microwave Theory Tech., Vol. 35, No. 1, pp. 60-61, January 1987.

1.17 J.C. Rautio, "Reviewing Available EM Simulation Tools," Microwaves & RF, vol. 30, no. 6, pp. 16-20, June 1991.

1.18 D.W. Esfandiara and M. Siracusa, "Design of Interdigital Capacitors and Their Application to GaAs Monolithic Filters," IEEE Microwave Symposium Digest, Vol. 1, pp. 295-298, 1987.

1.19 G.E. Mariki and C. Yeh, "Dynamic 3-Dimensional TLM Analysis of Microstriplines on Anisotropic Substrate," IEEE Trans. Microwave Theory Tech., Vol. 33, No. 9, pp. 789-799, September 1985.

1.20 J.H. Thompson and T.R. Apel, "Simplified Microstrip Discontinuity Modeling Using the TLM Method Interfaced to Microwave CAD," Microwave Journal, pp. 79-88, July 1990.

1.21 E.O. Hammerstad, "Equations For Microstrip Circuit Design," Proc. EMC, PP. 268-272, 1975.

1.22 R.H. Jansen and M. Kirschning, " Arguments and an Accurate Model For the Power-Current Formulation of Microstrip Characteristic Impedance," Artech. Elek. Übertragung, Vol. 37, pp. 108-112, 1983.

1.23 M. Kirschning and R.H. Jansen, "Accurate Wide-Range Design Equations For the Frequency-Dependent Characteristics of Parallel Coupled Microstrip Lines," IEEE Trans. Microwave Theory Tech., Vol. 27, No. 1, pp. 83-89, January 1984.

1.24 W.J.R. Hoefer, "Equivalent Series Inductivity of a Narrow Transverse Slit in Microstrip," IEEE Trans. Microwave Theory Tech., Vol. 15, pp. 822-824, October

1977.

1.25 M. Kirschning, R.H. Jansen, and N.L. Koster, "Measurement and CAD Modeling of Microstrip Discontinuities By an Improved Resonator Method," IEEE MTT-S Symposium Digest, pp. 495-497, May 1983.

1.26 H.M. Greenhouse, "Design of Planar Rectangular Microelectronic Inductors," IEEE Trans. Parts, Hybrids, and Packaging, Vol. 10, No. 2, pp. 101-109, June 1974.

1.27 G. Alley, "Interdigital Capacitors and Their Application to Lumped-Element Microwave Integrated Circuits," IEEE Trans. Microwave Theory Tech., Vol. 18, pp. 1028-1033, December 1970.

1.28 W.R. Curtice, "GaAs MESFET Modeling and Nonlinear CAD," IEEE Trans. Microwave Theory Tech., Vol. 36, No. 2, pp. 220-230, February 1988.

1.29 A.B. Grebene and S.K. Ghandi, "General Theory for Pinched Operation of the Junction-Gate FET," Solid State Electronics, Vol. 12, pp. 573-589, 1969

1.30 K. Lehovec and R. Zuleeg, "Voltage-Current Characteristics of GaAs J-FETs in the Hot Electron Range," Solid State Electronics, Vol. 13, pp. 1415-1426, 1970

1.31 W. Shockley, "A Unipolar Field Effect Transistor," Proc. IRE, vol. 40, pp. 1365-1377, November 1952.

1.32 C. Snowden and D. Loret, "Two-Dimensional Hot-Electron Models for Short Gate Length GaAs MESFETs," IEEE Trans. Electron Devices, Vol. 34, No. 2, pp. 212-223 February 1987.

1.33 Y. Feng and A. Hitz "Simulation of Submicrometer GaAs MESFETs Using a Full Dynamic Transport Model," IEEE Trans. Electron Devices, Vol. 35, No. 9, pp. 1419-1431 September 1988.

1.34 S. El-Ghazaly and T. Itoh, "Two-Dimensional Numerical Simulation of Short Gate Length GaAs MESFETs and Application to the Travelling Gunn Domain Phenomenon," International Journal of Numerical Modeling, Vol. 1, pp. 19-30, 1988.

1.35 S. Yoganathan, and S. Banerjee, "A New Decoupled Algorithm for Non-stationary Transient Simulation of GaAs MESFETs," IEEE Trans. Electron Devices, Vol. 39, No. 7, pp. 1578-1587, July 1992.

1.36 K. Lehovec and R. Miller, "Field Distribution in JFETs at Large Drain Voltages," IEEE Trans. Electron Devices, Vol. 22, No. 5, pp. 273-281, May 1975.

1.37 M. Shur, "Analytical Models of GaAs MESFETs," IEEE Trans. Electron Devices, Vol. 25, No. 6, pp. 612-618, June 1978.

1.38 G. Taylor, H. Darley, R. Frye, and P. Chatterjee, "A Device Model For an Ion-Implanted MESFET," IEEE Trans. Electron Devices, Vol. 26, No. 3, pp. 172-182, March 1979.

1.39 T. Weng, "I-V Characteristics of MESFETs With Nonuniform Carrier Distribution," IEEE Trans. Electron Devices, Vol. 29, No. 10, pp. 1641-1643, October 1982.

1.40 B. Carnez, A. Cappy, A. Kaszynski, E. Constant, and G. Salmer, "Modeling of a Submicrometer Gate FET Including Effects of Non-stationary Electron Dynamics," J. Appl. Phys. Vol. 51, No. 1, pp. 784-790, January 1980.

1.41 T. Hariu, K. Takahashi, and Y. Shibata, "New Modelling of GaAs MESFETs," IEEE Trans. Electron Devices, Vol. 30, No. 12, pp. 1743-1749, December 1983.

1.42 Y. Byun, M. Shur, A. Peczalski, and F. Schuermeyer, "Gate-Voltage Dependence of Source and Drain Series Resistances and Effective Gate Length in GaAs MESFETs," IEEE Trans. Electron Devices, Vol. 35, No. 8, pp. 1241-1245, August 1988.

1.43 C. Chang and D. Day, "Analytic Theory for Current-Voltage Characteristic and Field Distribution of GaAs MESFET's," IEEE Trans. Electron Devices, Vol. 36, No. 2, pp. 269-280, February 1989.

1.44 S. Mohammad, M. Patil, G. Gao, and H. Markoc, "Analytical Model for I-V Characteristics of Ion-Implanted MESFETs with Heavily Doped Channels," IEEE Trans. Electron Devices, Vol. 37, No. 1, pp. 11-19, January 1990.

1.45 D. Kennedy and R. O'Brien, "Computer-Aided Two-dimensional Analysis of the JFET," IBM J. Res. Develop., Vol. 14, pp. 95-116, 1970.

1.46 B. Himsworth, "A Two-Dimensional Analysis of GaAs JFETs With Long and Short Channels," Solid State Electronics, Vol. 15, pp. 1353-1361, 1972.

1.47 K. Yamaguchi and H. Kodera, "Drain Conductance of JFETs in the Hot Electron Range," IEEE Trans. Electron Devices, Vol. 23, No. 6, pp. 545-553, June 1976.

1.48 M. Reiser, "A Two-Dimensional Numerical FET Model for DC, AC, and Large-Signal Analysis," IEEE Trans. Electron Devices, Vol. 20, No. 1, pp. 35-45, April 1978.

1.49 T. Wada and J. Frey, "Physical Basis of Short Channel MESFET Operation," IEEE Trans. Electron Devices, Vol. 26, No. 4, pp. 476-488, April 1979.

1.50 W. Curtice and Y. Yun, "A Temperature Model For the GaAs MESFET," IEEE Trans. Electron Devices, Vol. 28, No. 8, pp. 954-962, August 1981.

1.51 J. Higgins and D. Pattanayak, "A Numerical Approach to Modeling the Ultrashort Gate MESFET," IEEE Trans. Electron Devices, Vol. 29, No. 2, pp. 179-183, February 1982.

1.52 G. Halkias, H. Gerard, Y. Crosnier, and G. Salmer, "A New Approach to the RF Power Operation of MESFETs," IEEE Trans. Electron Devices, Vol. 37, No. 5, pp. 817-825, May 1989.

1.53 A.A. Immorlica, D.R. Decker, and W.A. Hill, "A Diagnostic Pattern for GaAs FET Material Development and Process Monitoring," IEEE Trans. Electron Devices, Vol. 27, No. 12, pp. 2285-2291, December 1980.

1.54 S.M. Baier, M.S. Shur, K. Lee, N.C. Cirillo, and S.A. Hanka "FET Characterization Using Gated-TLM Structure," IEEE Trans. Electron Devices, Vol. 32, No. 12, pp. 2824-2829, December 1985.

1.55 P.B. Johns and S. Akhtarzad, " The Use of Time Domain Diakoptics in Time Discrete Models of Fields," Int. J. Numer. Methods Eng., Vol. 17, pp. 1-14, 1981.

1.56 S. Pulko, A. Mallik, and P.B. Johns, "Application of TLM to Thermal Diffusion in Bodies of Complex Geometry", International Journal for Numerical Methods in Engineering, Vol. 23, 2303-2312, 1986.

CHAPTER 2

Two-Dimensional TLM Node

2.1 Introduction

As explained in the first chapter, the proposed GaAs MESFET to TLM interface necessitates the treatment of the active device as a two-port network where the input port is the depletion region, and the output port is the conducting channel. This is a logical model since the applied electric field signal at the gate electrode is not amplified, but rather the flowing current and the associated magnetic field in the conducting channel are modulated by the rapid expansion and contraction of the depletion region and as a result they adopt the characteristics of the signal. The GaAs MESFET to TLM interface is concerned with formulating a TLM network which can model the conducting channel characteristics.

The GaAs MESFET conducting channel is a region with time-dependent and spatially non-uniform conductivity coupled with moving boundaries. Figure 2.1 shows a physical model of the MESFET conducting channel. It is bounded by the n^+ source and drain contacts, the channel-substrate interface at the bottom, the free recessed surface denoted by paths a-b and c-d, and the conducting channel-depletion interface denoted by the path b-c. The boundary conditions are fixed voltages at the electrode contacts, an abrupt conductive to semi-insulating transition at the channel-substrate interface, and electric fields due to electronic states at the surface. The electrons originate from the source metal electrode-n^+ contact and get collected at the n^+ contact-drain electrode. When a high frequency signal is applied to the gate, the path b-c becomes mobile. The vertices b and c can move sideways along the z-direction, and the path in between moves up and down along the x-axis, as well as sideways along z. Under the general conditions that the voltages are fixed at the source and drain electrodes, the electric field increases rapidly underneath the depletion layer. The deeper the depletion layer penetration, the higher the electric field rises. Under these condition, the conductivity

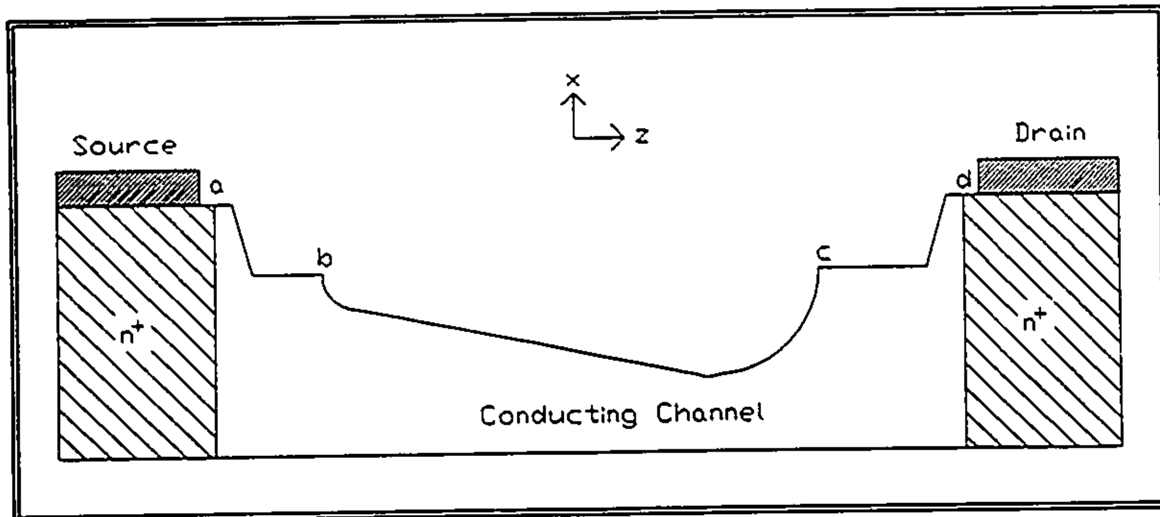

Figure 2.1: Physical model of the MESFET conducting channel.

versus electric field relationship is linear in the low field region, but the relationship becomes highly nonlinear well into the depletion layer because current continuity is maintained.

Let us consider that we are given at some time step $t=t_0$ the structure in Figure 2.1 with known doping conditions, fixed voltages, and fixed boundaries. The requirement is to develop a TLM network to simulate the entire conducting channel. If we properly translate the boundaries to electromagnetic equivalents, apply Maxwell equations of the lossy medium to the node formulation, and launch energy pulses at the source contact, we quickly find that the TLM system cannot simulate the intended structure since (i) the voltage-current characteristics between the source and drain are not ohmic, (ii) the conductivity must be allowed to vary according to both the electric field distribution and its time history, and (iii) there is no mechanism capable of enforcing current continuity. Clearly any TLM formulation must take into account (i) through (iii) above.

We thus consider the channel as sub-divided into a collection of segments whose voltage-current characteristics are ohmic, and we segment the channel into rectangular sections of single node width $\Delta\ell$, and length b(z,x) as shown in Figure 2.2. The section width $\Delta\ell$, is chosen such that the electric field variations

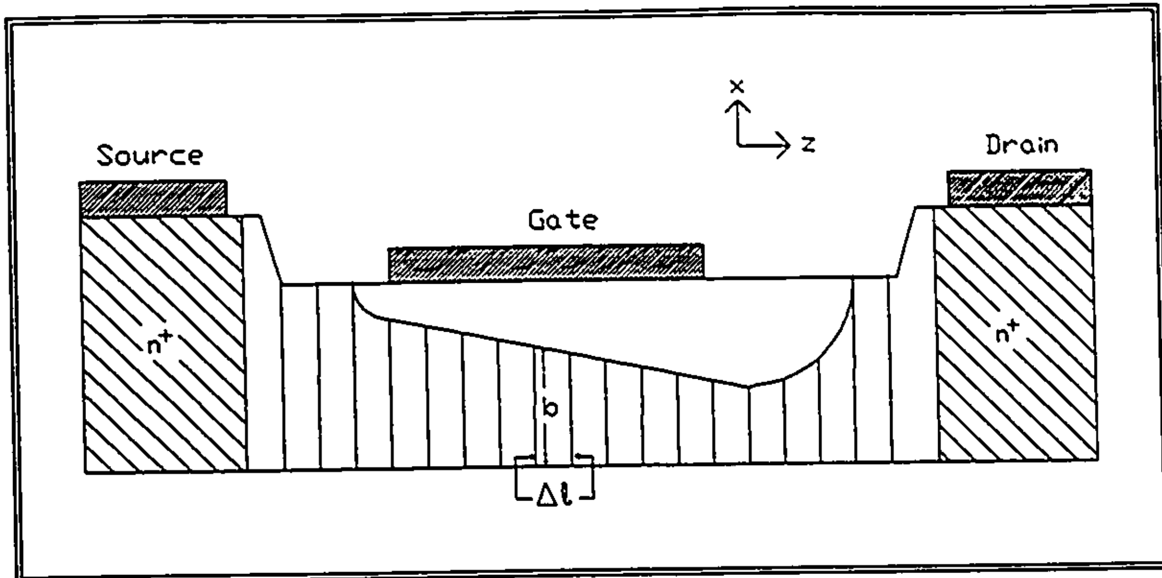

Figure 2.2: Cross-sectional view of a MESFET structure.

$$\frac{\partial E}{\partial z} = 0$$

are small enough to be considered uniform. Within each section the current-voltage relationship is ohmic, and the electric and magnetic fields are inter-related by the local conductivity and section length. In addition, we simplify the task of formulating the TLM network by requiring that we know in advance both the conductivity distribution and the channel current. Therefore, if a TLM network simulating such a discrete channel section can be formulated, then the MESFET's conducting channel can be modelled by TLM networks fitting the entire channel cross-section.

Prior to this work, such a TLM network had not been formulated. However, the electromagnetic field distribution within a discrete section of the MESFET conducting channel where the electric field is uniform and the current-voltage relationship is ohmic has been investigated by N.N. Rao [2.1] as a parallel-plate structure with a lossy medium between the plates and driven by a voltage source, as shown in Figure 2.3. The two-dimensional curl Maxwell equations in the structure are:

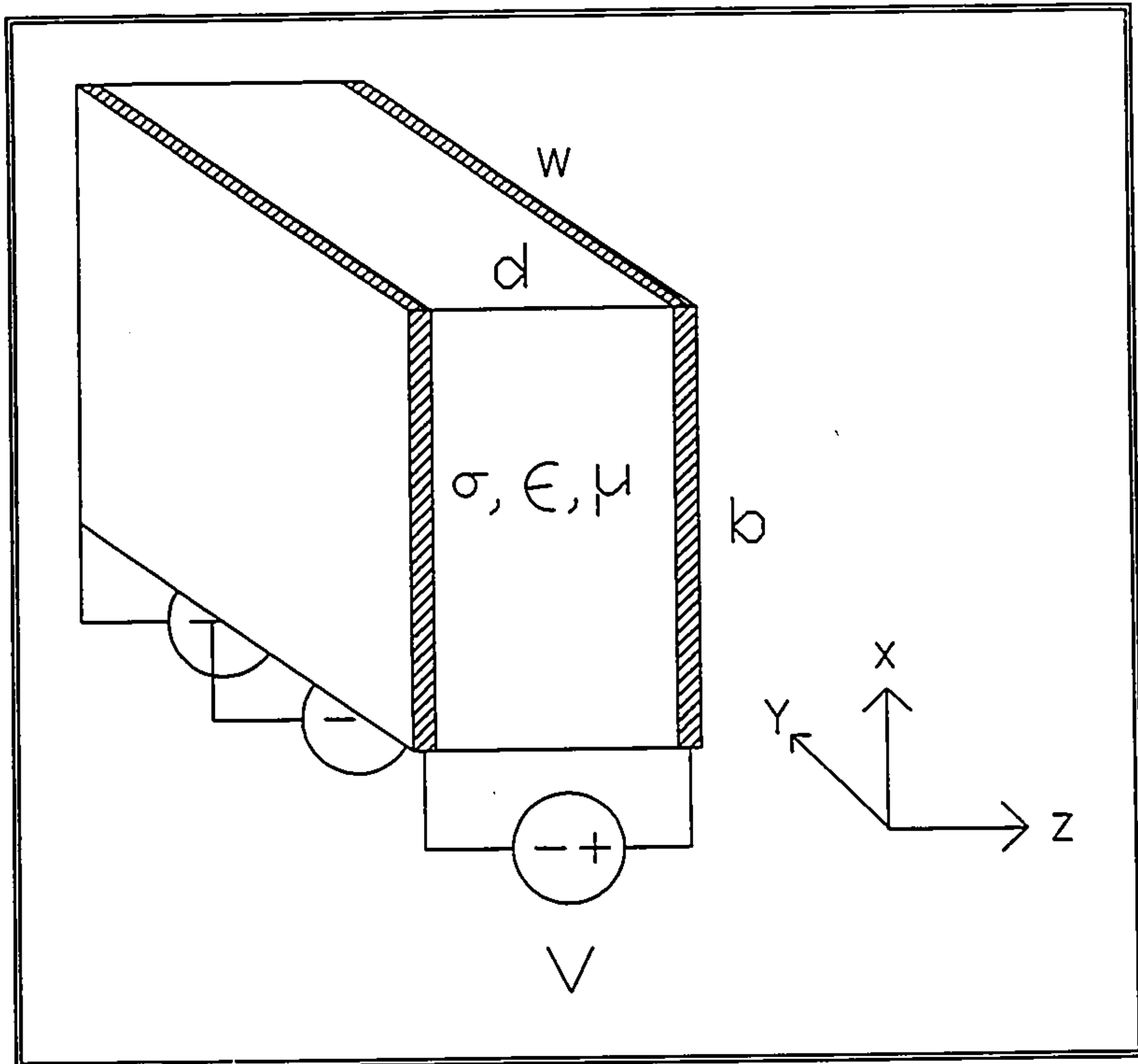

Figure 2.3: A parallel-plate structure with lossy medium between the plates and driven by a voltage source. Device dimensions are: d= the channel width, b= the height of the channel, and W= gate width. From Rao [2.1].

$$\frac{\partial H_y}{\partial x} = -\epsilon \frac{\partial E_z}{\partial t} - \sigma E_z \tag{2.1}$$

$$\frac{\partial H_y}{\partial z} = +\epsilon \frac{\partial E_x}{\partial t} + \sigma E_x \tag{2.2}$$

$$\frac{\partial E_z}{\partial x} - \frac{\partial E_x}{\partial z} = - \mu \frac{\partial H_y}{\partial t} . \tag{2.3}$$

The electric and magnetic fields between the plates for a constant voltage source have been calculated and are shown in Figure 2.4. The electric field is uniform along the width of the section, whereas the current density is zero at the depletion-conducting channel interface and rises to maximum at the base of the channel. At the various sections in the conducting channel, the magnitudes of the electric and magnetic fields vary but follow the same general distribution shown in Figure 2.4. The work in this and the next chapter is devoted to the derivation of a TLM network which can model this structure.

The TLM simulation of any structure requires both a TLM node which simulates the wave propagation in an unbounded homogeneous and lossy medium, and a TLM system which simulates the wave propagation in the medium bounded by electromagnetic walls and embedded with calibrated energy sources. A two-dimensional shunt node previously used for simulating diffusion phenomena has been re-formulated in this work and adapted, for the first time, to simulate the wave propagation in the semiconductor medium taking the local conductivity into account. This chapter begins with a formulation of the TLM node. This includes the assignment of the two-dimensional fields to the node and the resulting scattering parameters. In addition, both the associated errors and dispersion will be analyzed. The next chapter completes the TLM network formulation by deriving the required TLM system.

2.2 TLM Node Formulation

A TLM node can be synthesized by directly linking the voltages and currents of a suitable lumped element network to the MESFET electric and magnetic fields [2.2, 2.3]. Consider the two-dimensional shunt TLM node in Figure 2.5, originally used for modelling carrier diffusion [2.4]. Its transmission-line partial differential equations are found by applying Kirchhoff's law:

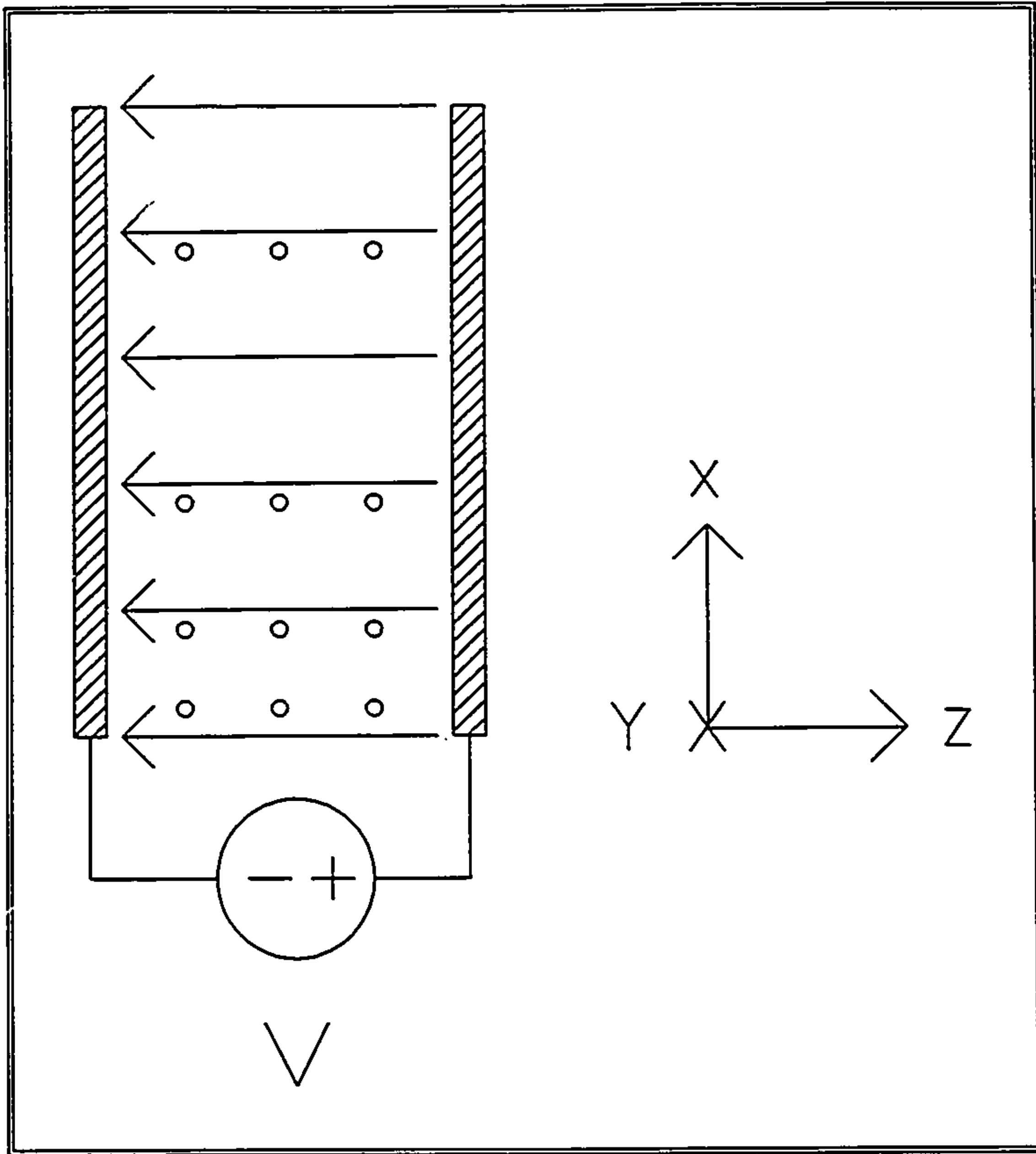

Figure 2.4: Electric and magnetic fields between the plates for a constant voltage source. Arrows denote the electric field, the o symbols indicate the magnetic field. From Rao [2.1].

$$\frac{\partial V_y}{\partial x} = -L\frac{\partial I_z}{\partial t} - rI_z \qquad (2.4)$$

$$\frac{\partial V_y}{\partial z} = - L\frac{\partial I_z}{\partial t} - rI_z \qquad (2.5)$$

$$\frac{\partial I_z}{\partial z} + \frac{\partial I_x}{\partial x} = - 2C\frac{\partial V_y}{\partial t} \ . \qquad (2.6)$$

The field terms and constants of (2.1-2.3) and the voltage-current terms and constants of (2.4-2.6) are linked by using the following correspondences:

(a) the node current, I_z, simulates the MESFET's electric field, $-E_x$,

(b) the node current, I_x, simulates the MESFET's electric field, E_z,

(c) the node voltage, V_y, simulates the longitudinal magnetic field, H_y,

(d) the node resistance, r, simulates the local conductivity, σ,

(e) the node inductance, L, simulates the MESFET's dielectric constant, $\epsilon_r\epsilon_o$, and,

(f) the node capacitance, C, simulates the MESFET's permeability, $\mu_r\,\mu_o$.

By using the above correspondences and eliminating the electric field in (2.1-2.3), one obtains a 2-D wave equation for **H**:

$$\frac{\partial^2 H_y}{\partial x^2} + \frac{\partial^2 H_y}{\partial z^2} - \mu\epsilon\,\frac{\partial^2 H_y}{\partial t^2} - \mu\sigma\,\frac{\partial H_y}{\partial t} = 0 \qquad (2.7)$$

which is the wave equation governing the magnetic field in a conducting medium. The incident and reflected voltage and current impulses at every node in a TLM mesh in the x-z plane are given by [2.4]:

$${}_{k-1}V_l^r = \left[\frac{Z}{R+Z}\right]\,{}_k\Phi + \left[\frac{R-Z}{R+Z}\right]\,{}_kV_l^i \qquad l = 1...4 \qquad (2.8)$$

where

$$ {}_k\Phi = \left[\frac{ {}_kV_1^i + {}_kV_2^i + {}_kV_3^i + {}_kV_4^i }{2} \right] , \tag{2.9} $$

k is the time step, the number subscripts in the voltage terms refer to the branch numbers of the TLM node, as shown in Figure 2.5, and the i and r superscripts refer to the incident and reflected voltages, respectively. Z is the impedance, which consists of the shunt capacitance and the series inductance of any branch of the TLM node, simulating the lossless medium's characteristic admittance. Finally, R is the TLM node resistance that simulates the medium's conductivity. Hence,

$$ Z = \frac{1}{\eta_o} \sqrt{\frac{\epsilon_r}{\mu_r}} \tag{2.10} $$

$$ R = \frac{\sigma \, \Delta \ell}{2} \; . \tag{2.11} $$

Since the MESFET's dielectric constant and permeability are assumed not to change inside the medium, the reflected impulses simply become incident impulses on the neighboring nodes:

$$ {}_{k-1}V_1^i(z,x) = {}_{k-1}V_3^r(z,x-1) \tag{2.12} $$

$$ {}_{k-1}V_2^i(z,x) = {}_{k-1}V_4^r(z-1,x) \tag{2.13} $$

$$ {}_{k-1}V_3^i(z,x) = {}_{k-1}V_1^r(z,x+1) \tag{2.14} $$

$$ {}_{k-1}V_4^i(z,x) = {}_{k-1}V_2^r(z+1,x) \; . \tag{2.15} $$

Using the correspondences written before, the field components in the MESFET are

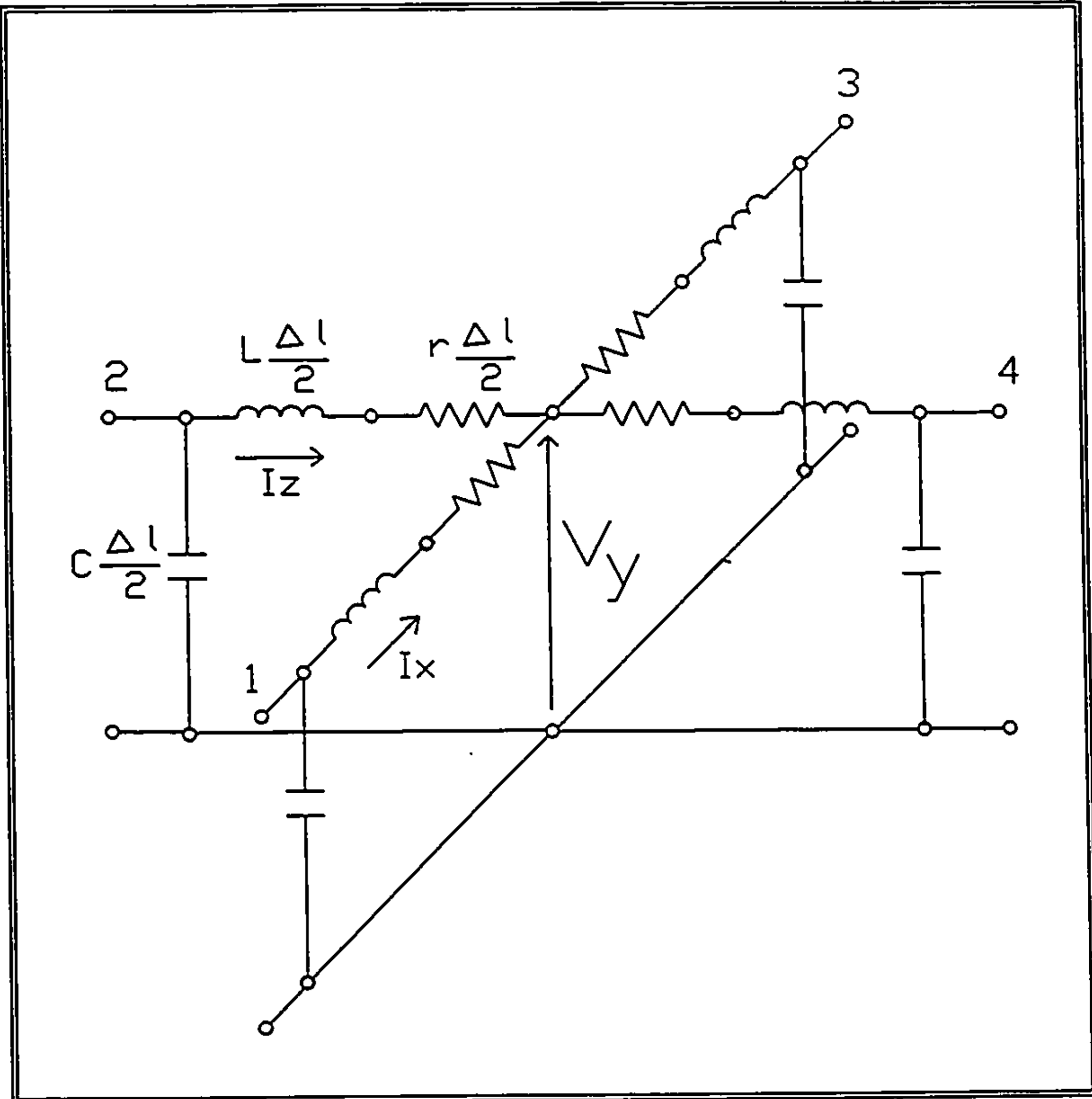

Figure 2.5: TLM node for MESFET analysis.

calculated from the TLM node voltages and currents as follows:

$$ {}_kV_y \equiv {}_kH_y = \frac{Y}{2}\sum_{m=1}^{4} {}_kV_m^i \qquad (2.16)$$

$$ {}_kI_x \equiv {}_kE_z = {}_kV_1^i - {}_kV_3^i \tag{2.17} $$

$$ -{}_kI_z \equiv {}_kE_x = {}_kV_2^i - {}_kV_4^i \ . \tag{2.18} $$

where Y is the reciprocal of Z. Finally, the single time step is determined by the node-to-node spacing:

$$ \Delta t = \frac{\Delta \ell \sqrt{\epsilon_r \mu_r}}{c} \ , \tag{2.19} $$

where c is the speed of light in vacuum.

2.3 TLM Node Losses

The losses at each point in the physical semiconductor space are shared by the node's branch resistors, and, therefore are properly localized. There are, however, three important considerations related to the size of the localized losses:

(1) The Debye length L_D, which is the mean carrier distance for semiconductor analysis in a cloud of particles, must be the upper limit for the node-to-node spacing, $\Delta\ell$:

$$ L_D = \sqrt{\frac{\epsilon KT}{q^2 N_D}} \ . \tag{2.20} $$

The Debye length is displayed graphically in Figure 2.6. For typical GaAs MESFET doping concentrations ranging between 10^{17} to 10^{18} atoms/cm^3, the Debye length varies between 150 to 50 Angstroms.

(2) Considering (2.8), the TLM system will undergo oscillations if the reflection coefficient is non-negative [2.5]. Hence R must be maintained much less than (Z/2). Using (2.10) and (2.11) the following condition must be enforced:

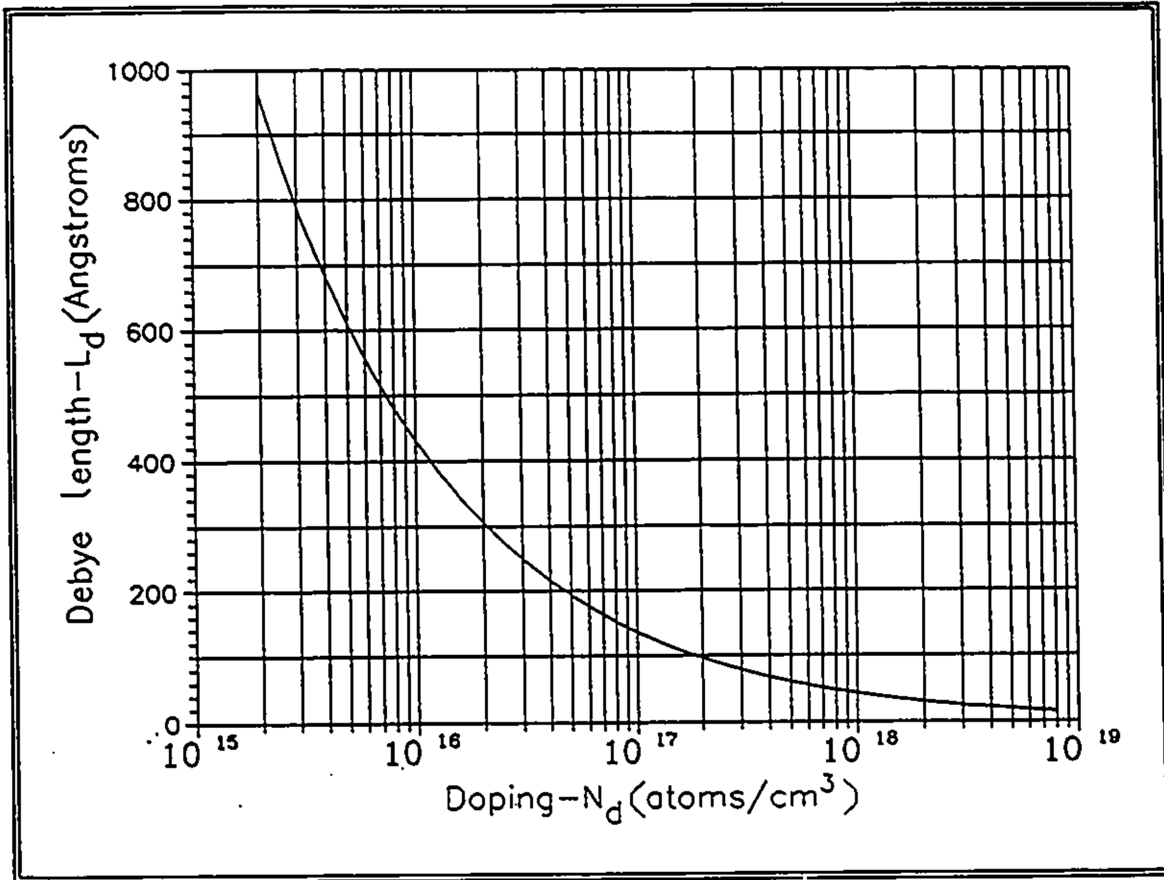

Figure 2.6: Debye length versus GaAs channel doping.

$$\sigma \Delta \ell \ll \frac{1}{\eta_o} \sqrt{\frac{\epsilon_r}{\mu_r}} \ . \tag{2.21}$$

However, using the Debye length as the node-to-node spacing, it can be readily verified that R remains at least an order of magnitude smaller than (Z/2) for all practical doping levels.

(3) To ensure that the conduction current losses do not distort the shape of the TLM impulses, the loss tangent should be kept well below unity. This is achieved by maintaining the Debye length, L_d, as the upper limit of the node-to-node spacing $\Delta\ell$:

$$\frac{\sigma\,\Delta\ell}{\omega\,\epsilon} \leq \frac{\sigma\,L_d}{\omega\,\epsilon} \ll 1 \qquad (2.22)$$

The relation of the Debye length to doping in GaAs, as shown in Figure 2.6, is used to calculate the loss tangent at 30 GHz. Figure 2.7 shows that the loss tangent is well below unity for standard doping levels.

2.4 TLM Node Dispersion Characteristics

Maximum dispersion is introduced by axial propagation of a simulated wavefront, that is, along the x- or z- direction. It is evaluated by plotting the ratio of the attenuation (α_ℓ) and phase ($\beta_\ell = \beta_o\sqrt{(\epsilon_r\,\mu_r)}$) constants of the mesh line, to the ones simulated by the TLM network's α_n and β_n as a function of the normalized frequency ($\Delta\ell/\lambda$). The wave propagation over a distance of one node in a periodic mesh structure results in the following transmission (ABCD) matrix:

$$\begin{bmatrix} V_i \\ I_i \end{bmatrix} = \begin{bmatrix} e^{\gamma_n \Delta\ell} & 0 \\ 0 & e^{\gamma_n \Delta\ell} \end{bmatrix} \begin{bmatrix} V_{i-1} \\ I_{i-1} \end{bmatrix} \qquad (2.23)$$

where the propagation constant of the simulated wave is

$$\gamma_n = \alpha_n + j\beta_n\ . \qquad (2.24)$$

The propagation constant in the mesh lines is obtained by calculating the transmission matrix of the TLM node in Figure 2.5 relating the input-output voltages and currents of branches 2 and 4. Branches 1 and 3 are terminated by electric walls and, according to the present TLM node formulation, they are treated as open circuited stubs of length $\Delta\ell/2$. The circuit complexity of this node necessitates the use of a circuit analysis program to generate the ABCD matrix which is then equated with (2.23). The attenuation and phase dispersion at 10 GHz for resistance values corresponding to the following doping levels: 10^{16}, 10^{17}, and 10^{18} atoms/cm^3 are calculated and shown in Figures 2.8, 2.9, and 2.10

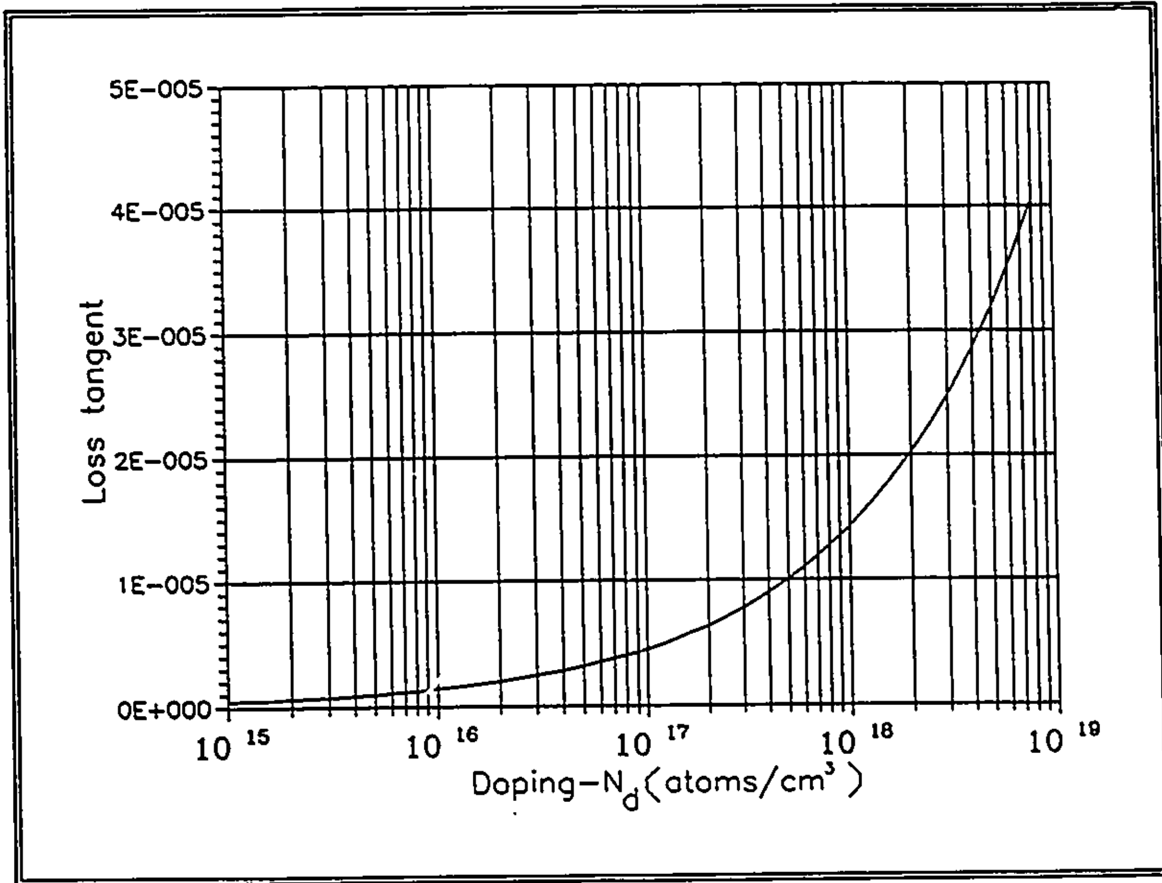

Figure 2.7: Loss tangent versus GaAs channel doping.

respectively. The errors in attenuation and phase are given as [2.5]:

$$e_{\alpha} = \frac{1}{\sqrt{2}} \frac{\alpha_n}{\alpha_t} - 1 \tag{2.25a}$$

$$e_{\beta} = \frac{1}{\sqrt{2}} \frac{\beta_n}{\beta_t} - 1 \tag{2.25b}$$

In contrast to the TLM simulation of passive structures, which are typically discretized such that $\Delta\ell$ is one tenth to one hundredth of a wavelength, in a GaAs MESFET the channel must be discretized such that $\Delta\ell$ is at least six orders of magnitude smaller than

the wavelength. The maximum attenuation dispersion error of the semiconductor node when adhering to the Debye length is less than 0.05 % and 0.16% at 10^{16} and 10^{18} atoms/cm^3 doping levels respectively. Under the same conditions, the maximum phase dispersion error is less than 0.007 % and 0.2% respectively.

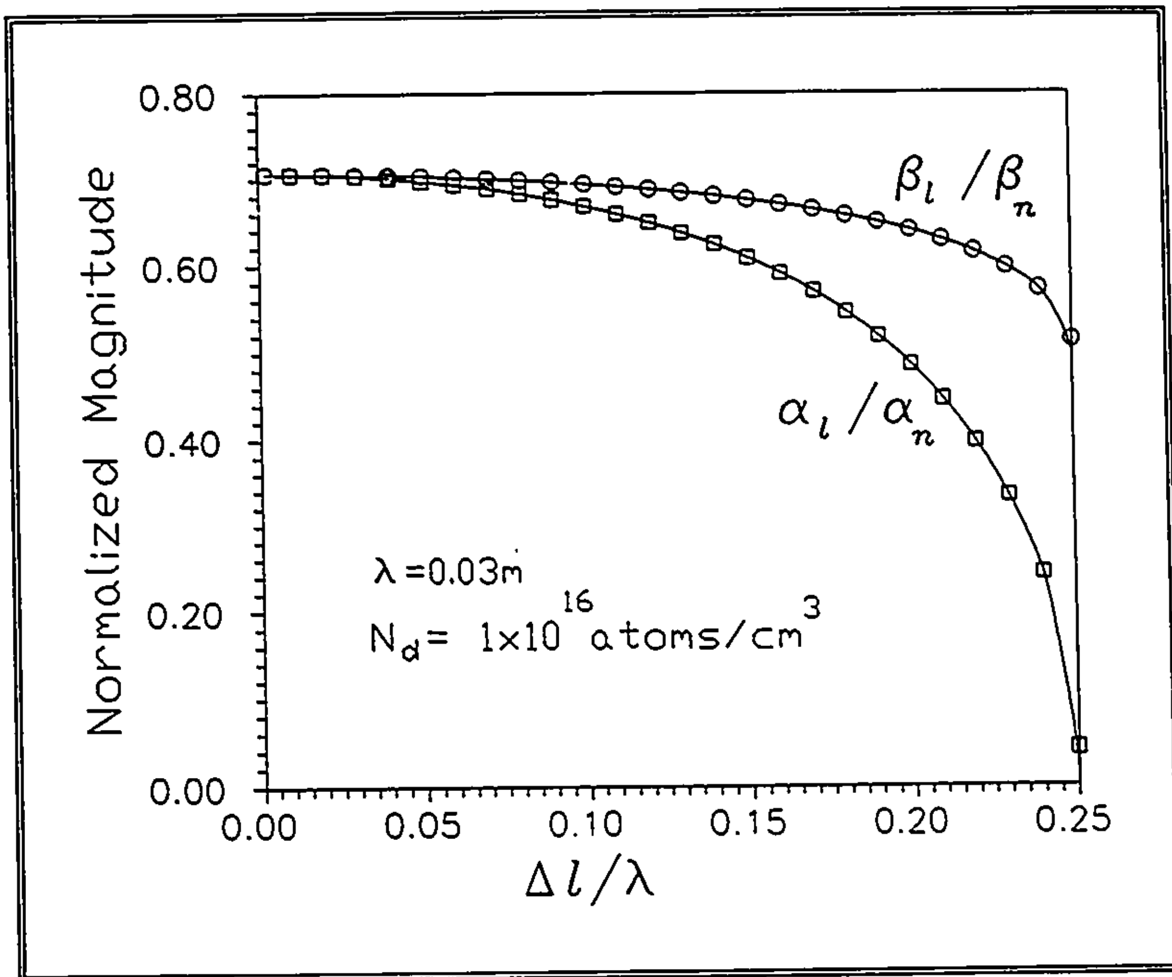

Figure 2.8: Dispersion characteristics of the TLM node at 10^{16} atoms/cm^3 doping level. Solid lines: reference [2.5], circle, square symbols: this work.

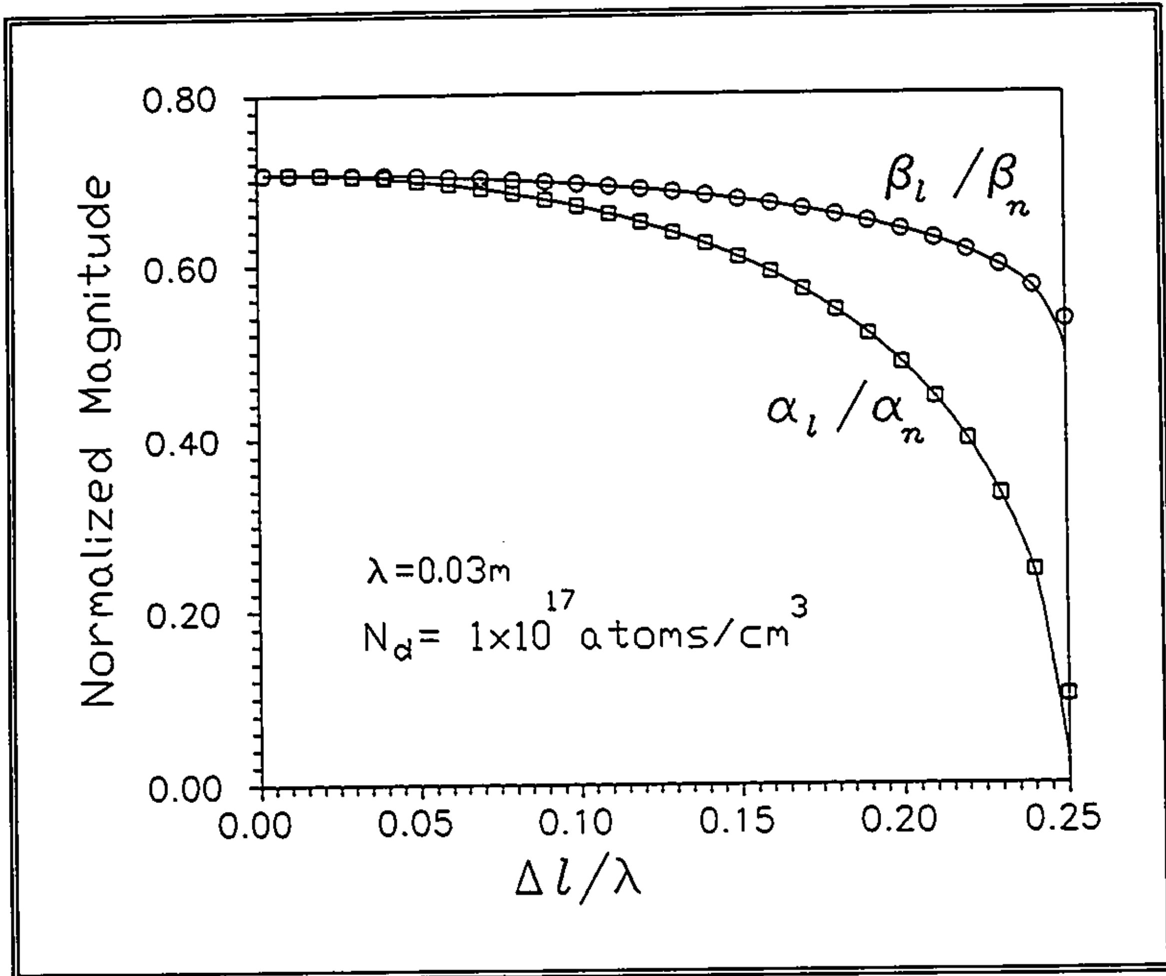

Figure 2.9: Dispersion characteristics of the TLM node at 10^{17} atoms/cm^3 doping level. Solid lines: reference [2.5], circle, square symbols: this work.

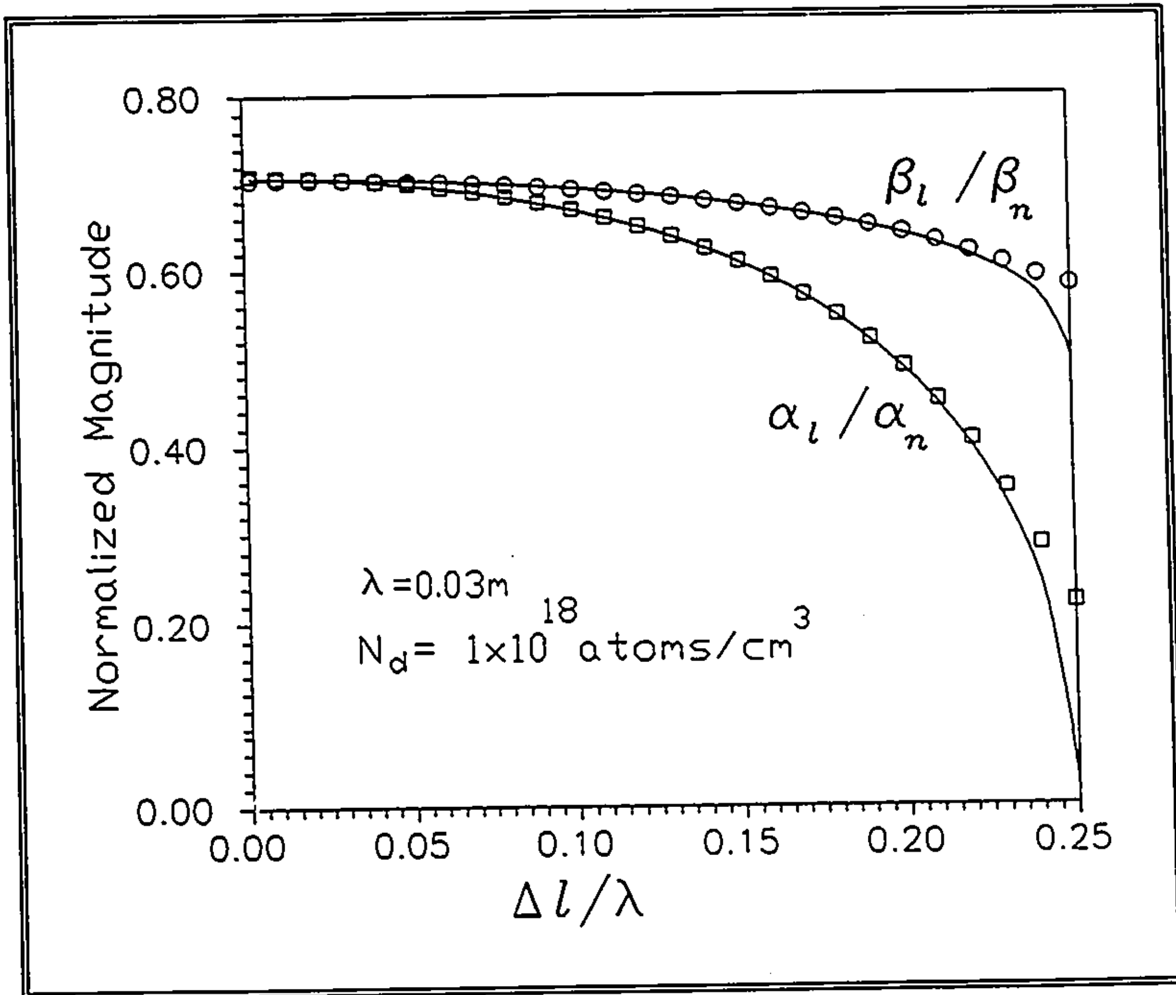

Figure 2.10: Dispersion characteristics of the TLM node at 10^{18} atoms/cm^3 doping level. Solid lines: reference [2.5], circle, square symbols: this work.

2.5 References

2.1 N.N. Rao, Elements of Engineering Electromagnetics, Prentice-Hall, Inc. 1977. pp. 357-364.

2.2 S.F. Dindo and M.M. Ney, "Two-Dimensional Transmission Line Matrix (TLM) Simulation of the Electromagnetic Fields in a Rectangular Section of a Discretized GaAs MESFET Channel With Arbitrary Doping Profile," IEEE MTT-S International Microwave Symposium, Atlanta, 1455-1458, (1993).

2.3 S.F. Dindo, M.M. Ney, and R.G. Harrison, "A New Two-Dimensional Transmission Line Matrix (TLM) Node Formulation For Thin Semiconductor Samples," Submitted for publication to the International Journal For Numerical Modelling.

2.4 S. Pulko, A. Mallik, and P.B. Johns, "Application of TLM to Thermal Diffusion in Bodies of Complex Geometry", International Journal for Numerical Methods in Engineering, Vol. 23, 2303-2312 (1986)

2.5 W.J.R. Hoefer, "The Transmission Line Matrix Method - Theory and Application", IEEE Trans. on Microwave Theory and Techniques, Vol. 23, pp. 882-893 October 1985.

CHAPTER 3

Two-Dimensional TLM System

3.1 Introduction

In the previous chapter, we set the objective of formulating a TLM network capable of simulating the GaAs MESFET conducting channel, given that at any time instant, the following parameters are known in advance:

- the voltages and fields at the boundaries
- the boundary profile of the channel.

In addition, we divided the channel into discrete vertical sections where the width is small enough such that the local current-voltage relationship is ohmic, and we required to know in advance both the conductivity distribution and the channel current. A TLM node was then formulated to describe the electromagnetic fields propagation in an unbounded semiconductor medium. In this chapter a TLM system, which is defined as a medium bounded by electromagnetic walls and embedded with calibrated energy sources, is formulated to describe the electromagnetic fields in a rectangular section of a discretized MESFET channel, such as those described in Figures 2.3-2.4. The issues investigated are the translation of the conducting channel's physical boundaries into an electromagnetic equivalent, and the translation of the electrical current into a TLM energy source (or sources). The calibration of the TLM energy source(s) will also be investigated in three examples. These are chosen to represent general MESFET conducting channel conditions, such as, varying doping profiles and channel heights. Based on these results, the TLM model will be completed.

3.2 Formulation of Electromagnetic Boundaries

The parameters of the TLM system enclosure are obtained by translating the physical boundaries of the MESFET channel into magnetic or electric walls [3.1, 3.2]. An electric wall requires the tangential electric field $\mathbf{E}_t$, and the normal magnetic field $\mathbf{H}_n$, to

be zero:

$$
\begin{aligned}
n \times E &= 0 \rightarrow E_t = 0 \ , \ E_n \neq 0 \\
n \cdot H &= 0 \rightarrow H_n = 0 \ , \ H_t \neq 0
\end{aligned}
\tag{3.1}
$$

while a magnetic wall requires the tangential magnetic field, H_t, and the normal electric field, E_n, to vanish:

$$
\begin{aligned}
n \cdot E &= 0 \rightarrow E_n = 0 \ , \ E_t \neq 0 \\
n \times H &= 0 \rightarrow H_t = 0 \ , \ H_n \neq 0
\end{aligned}
\tag{3.2}
$$

In our two-port MESFET model, we implied that the channel is to be divided into two distinct regions. The depletion region is carrier free, and the conducting channel is charge free. To satisfy these conditions, it is required that in the depletion layer and at the conducting channel boundary, both H_y and E_x are zero [3.3, 3.4] and the boundary is a magnetic wall. The vertical or constant-z boundaries in the channel are translated into electric walls since E_x and H_z are zero. A complication arises when attempting to model the base of the channel at the channel/semi-insulating interface where E_z and H_y are both non-zero, and hence have no electromagnetic equivalent. This complication is avoided by mirroring the structure at the channel/semi-insulating interface. Thus, in a rectangular section of the MESFET channel, the vertical boundaries become perfect electric walls, and the horizontal boundaries become perfect magnetic walls. To attain the maximum magnetic field at the bottom of the MESFET channel the DC voltage is applied at a single point half-way between the metal plates. With this formulation, modeling an infinitesimal MESFET channel section of Figure 2.3 and the associated electromagnetic field of Figure 2.4 are transformed into the mirrored structure depicted in Figure 3.1. The electromagnetic fields of the mirrored structure were calculated by following the work of Rao [3.3].

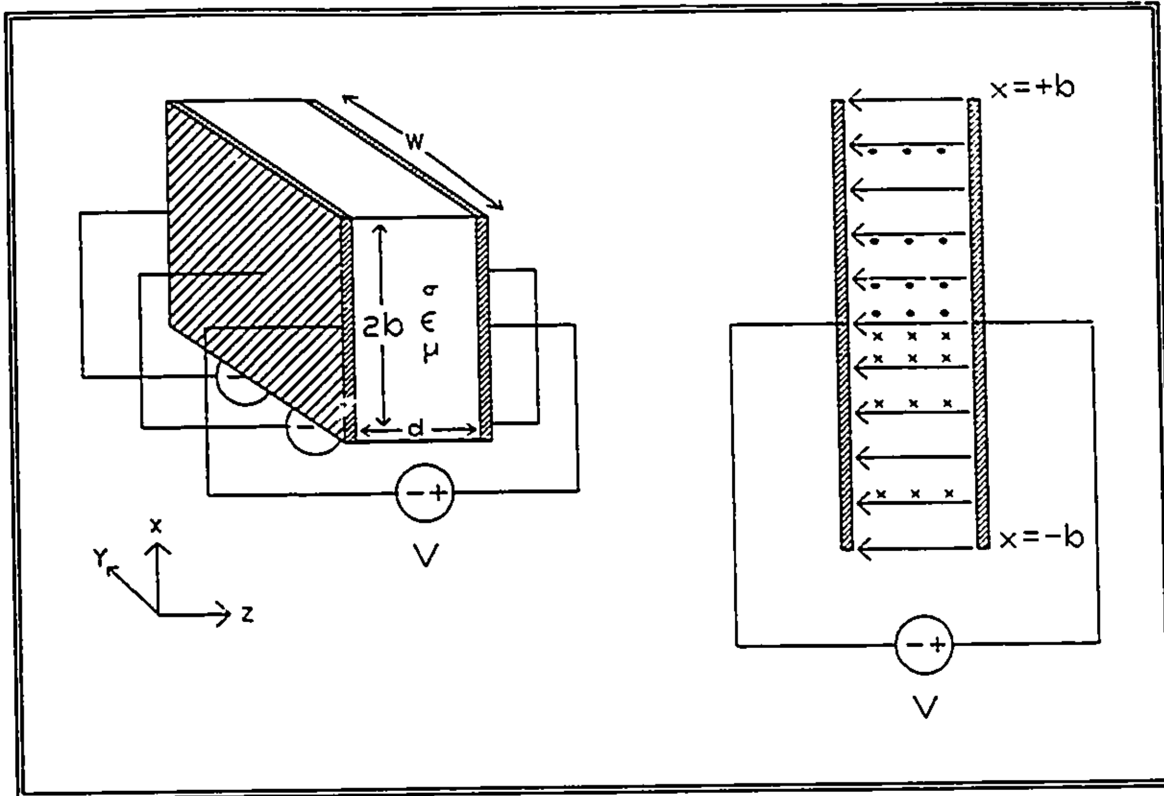

Figure 3.1: Mirrored MESFET channel section and the associated electromagnetic fields. d= the channel width, b= the height of the channel, and W= gate width. Arrows: electric field, and o,x symbols: magnetic field.

3.3 Construction of the TLM Energy Sources

It remains to determine the distribution of the electromagnetic energy sources and the locations of the nodes where they are to be positioned within the TLM system, so that the electromagnetic fields of Figure 3.1 can be simulated. Some experimentation is necessary to arrive at the proper configuration. This process, however, is facilitated by having the TLM system mimic the physical system. For example, since a point voltage is applied at the center of the structure half-way between the magnetic walls, a single-point energy injection is applied at the point where the battery is connected. Also, the time-continuous nature of the electron current is implemented as a time-continuous pulse injection, in other words, a square waveform of infinite time duration. Finally, by injecting the energy pulses into a single branch of the TLM node, which is oriented in the same

direction as the current flow in the physical system, this results in the desired response.

Figure 3.2 depicts the TLM system which shows terminology used by the TLM simulator. In the system, the dielectric box encloses TLM nodes which describe the dielectric constant and conductivity. It is bounded by the magnetic and electric walls which are located half-way between nodes. Since the physical wall boundaries are located half-way between nodes, the exact point where the DC voltage is applied is inaccessible. Hence the input energy sources must be located at two nodes about the center of the box.

3.4 Analysis of the TLM System

Thus far, we have formulated a TLM system by modelling the physical boundaries, the voltage source, and the characteristics of the MESFET's conducting channel medium. We still do not know how the TLM energy sources are related to the channel current. The relationship will be investigated in this section by theoretical analysis of the TLM system and comparison with several computational examples. We begin first by deriving the electromagnetic fields of the mirrored structure of Figure 3.1 for the general case of arbitrary conductivity distribution $\sigma(x)$. Let the width of the channel section be $\Delta\ell$. The steady-state electric field is one-dimensional and uniform at any point along z according to the applied constant voltage:

$$E_z = -\frac{V}{\Delta\ell} \,. \tag{3.3}$$

The steady-state magnetic field arising from the conduction current density is:

$$\frac{\partial H_y}{\partial x} = -\sigma(x)\,E_z \tag{3.4}$$

which upon integration and enforcement of the boundary conditions that the current density on the horizontal boundaries must be zero leads to:

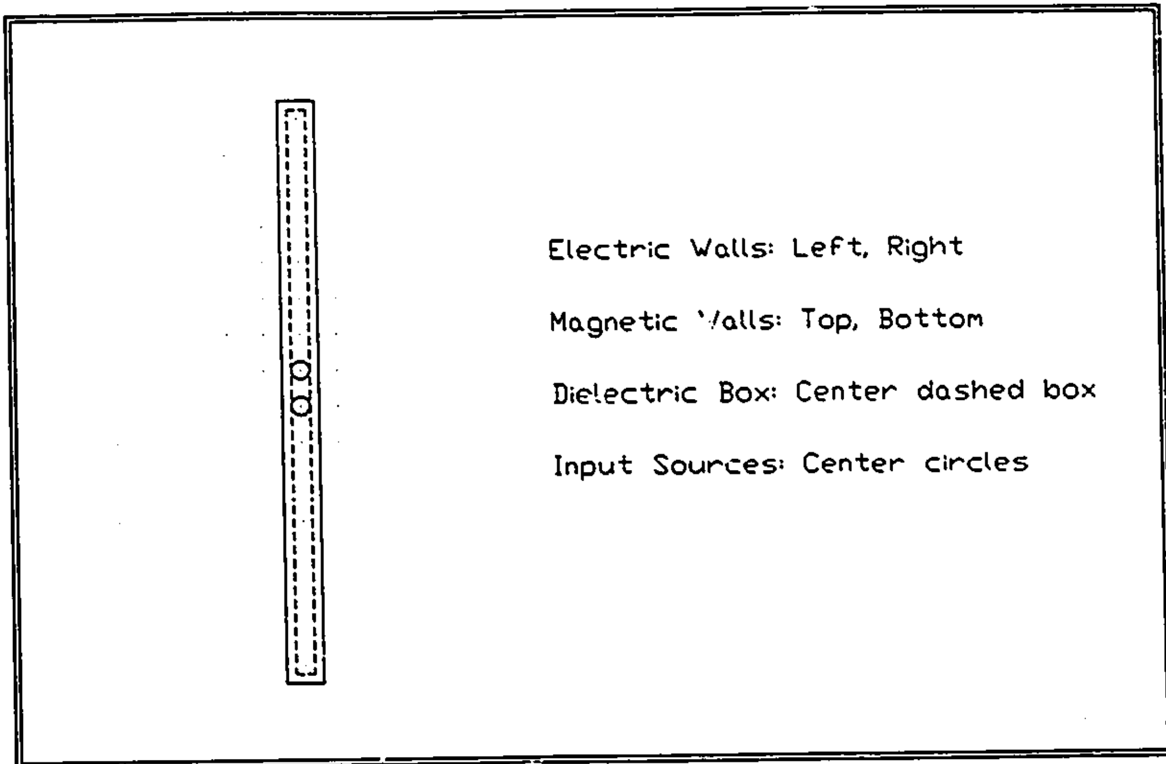

Figure 3.2: The components of the TLM system.

$$H_y = -E_z \int_{x=-b}^{x=0} \sigma(x)\, dx = \frac{V}{\Delta \ell} \int_{x=-b}^{x=0} \sigma(x)\, dx \qquad for\ x < 0 \tag{3.5}$$

$$H_y = -E_z \int_{x=0}^{x=b} \sigma(x)\, dx = \frac{V}{\Delta \ell} \int_{x=0}^{x=b} \sigma(x)\, dx \qquad for\ x > 0\ . \tag{3.6}$$

The transient field responses, on the other hand, are obtained by treating the MESFET channel as a constant-current source. The rectangular section can equivalently be also modeled as a constant-current source feeding a lossy dielectric represented by a parallel resistor-capacitor network. The electric field response can be shown to be:

$$E_z(t) = \frac{V}{\Delta \ell}\left[1 - e^{-\left(\frac{t}{\tau}\right)}\right]\ . \tag{3.7}$$

The time constant is obtained in terms of the resistance and capacitance per width:

$$\tau = R\,C = \frac{\Delta\ell}{2\,\sigma_{ave}\,b}\,\frac{2\,\epsilon\,b}{\Delta\ell} = \frac{\epsilon}{\sigma_{ave}} \tag{3.8}$$

where σ_{ave} is the average conductivity:

$$\sigma_{ave} = \frac{\int_{x=-b}^{x=b} \sigma(x)\,dx}{2b} \, . \tag{3.9}$$

The theoretical and experimental responses of three TLM systems to an identical DC current step simulated by a time continuous impulse energy excitation are next presented. The parameters of the infinitesimal MESFET channel segments being simulated in these examples are listed in Table 3.1. Example 1 describes a uniformly-doped section. The theoretical and numerical steady-state spatial magnetic and electric field responses to the energy excitation in Figures 3.3 and 3.4 show virtually exact agreement. The magnitude of the magnetic field increases linearly to a maximum at the center of the rectangle where the point voltage is applied, while the electric field is spatially constant. The linear distribution of the magnetic field arises from the integration of constant conductivity. The measured electric field transient response in Figure 3.5, on the other hand, exhibits a first-order response superimposed on decaying second-order oscillations. The transient magnetic field response which otherwise should be constant also exhibits oscillatory disturbances, as shown in Figure 3.6 for the spatial point $x=0.5\Delta\ell$. When the high-frequency components of these ripples are filtered from the transient electric field, the entire calculated response, including its time constant, agrees with the theoretical response.

The period of each of the second-order oscillations in the electric field response are directly correlated to the distance between the energy sources and the magnetic wall boundaries. In the limit when this distance is reduced to a single node, the second order

TLM System Parameter	Example 1	Example 2	Example 3
Conductivity, σ [/ Ω-m]	10800	10800	σ= 10.8 x (x in [Å])
b [Å]	1000	50	1000
TLM Distance Step, $\Delta\ell$ [Å]	50	50	50
TLM time step, Δt [S]	6.0×10^{-17}	6.0×10^{-17}	6.0×10^{-17}
Pulse energy magnitude, A	$1.0 \times 10^{+6}$	$1.0 \times 10^{+6}$	$1.0 \times 10^{+6}$

TABLE 3.1: TLM system parameters for three examples

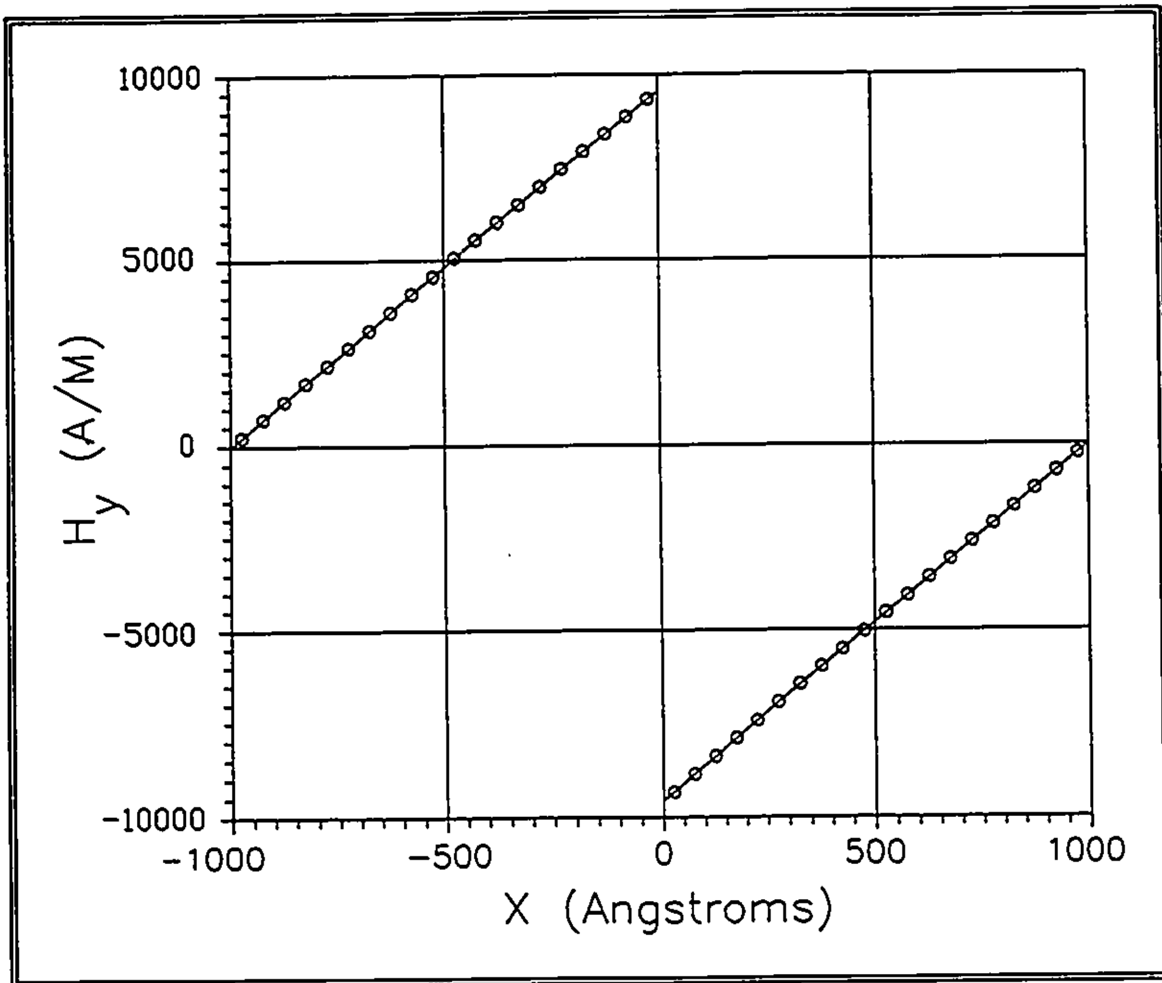

Figure 3.3: Steady-state spatial magnetic field in uniformly conducting dielectric. Solid line: calculated results, circle symbols: TLM results.

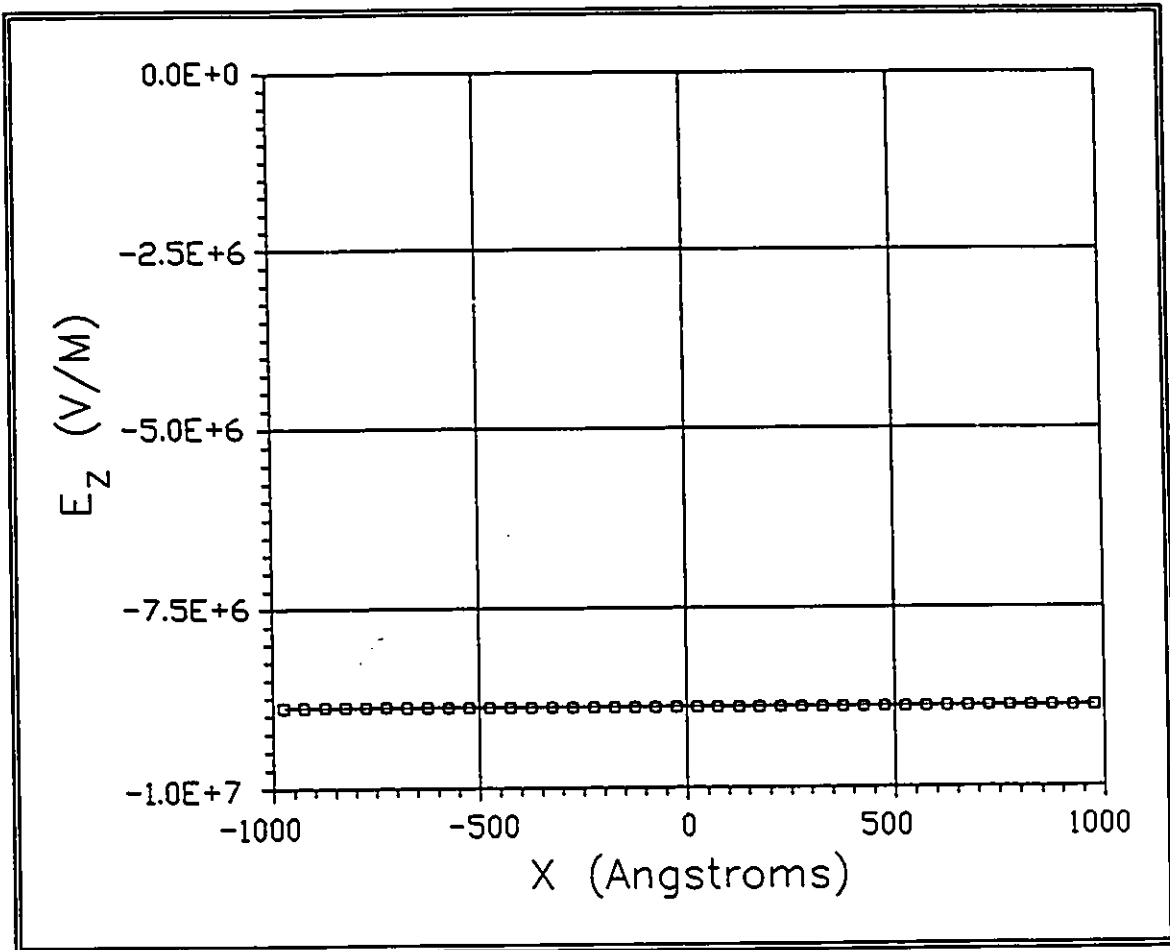

Figure 3.4: Steady-state spatial electric field in uniformly conducting dielectric. Solid line: calculated results, square symbols: TLM results.

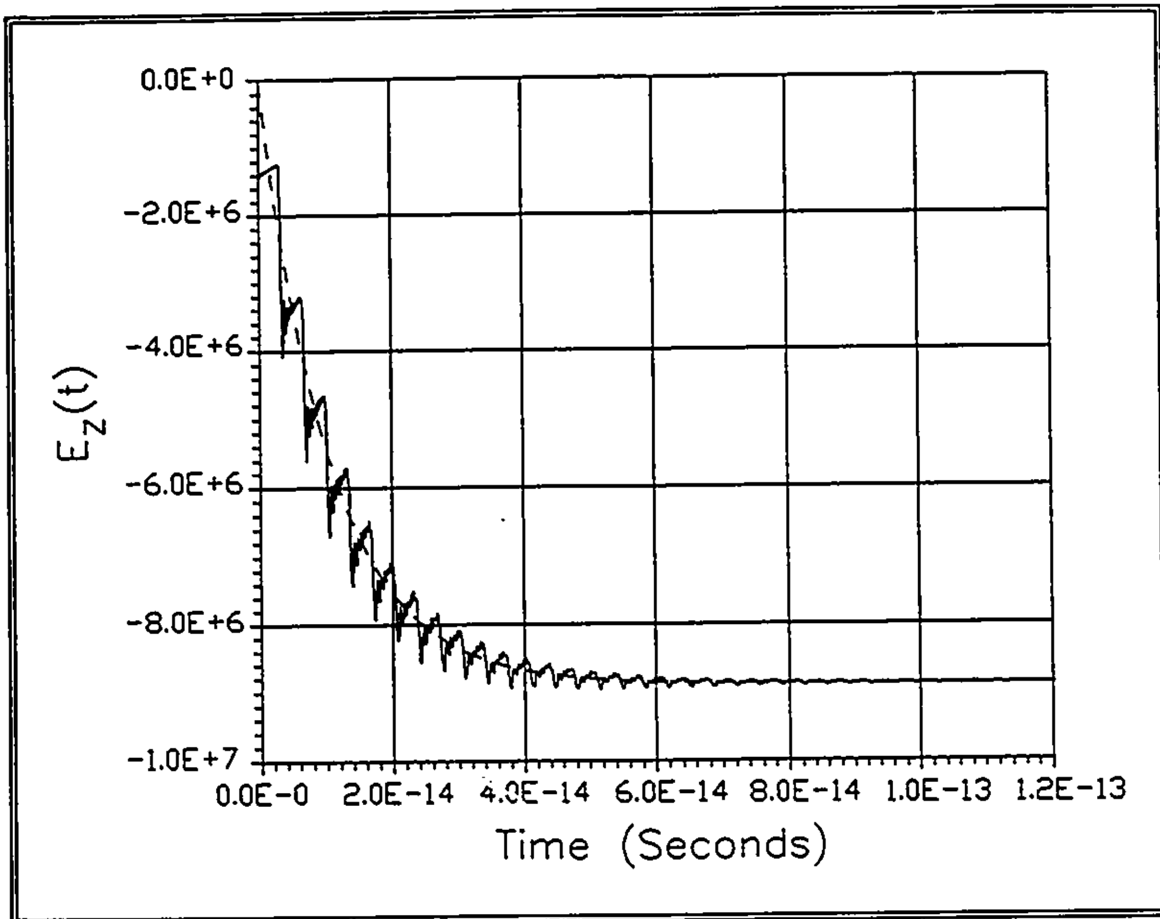

Figure 3.5: Transient response of the electric field in a uniformly conducting dielectric. Dashed line: calculated results, solid line: TLM results.

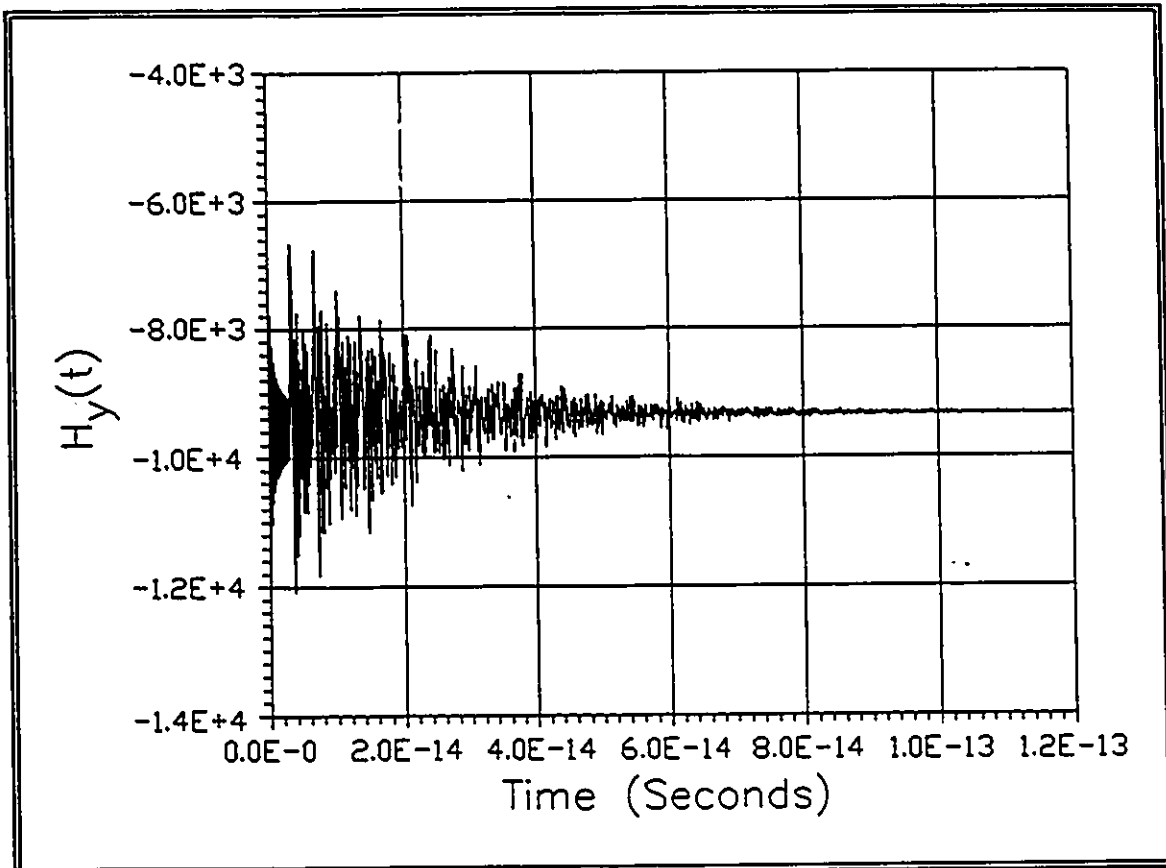

Figure 3.6: TLM-computed transient response of $H_y(t)$.

oscillations in the electric field should vanish. Thus, the simulated MESFET channel section is reduced in length to a single node in Example 2. The resulting transient electric field response, as obtained by TLM and shown in Figure 3.7, is indeed much smoother and is free of second-order oscillations. On the other hand, the magnetic field response, as calculated by TLM and shown in Figure 3.8, is a single second-order oscillation decaying sinusoid oscillating about the steady state.

The evolution of the decaying oscillations in Example 1 can be traced by examining the TLM node circuit. Closer examination of the distribution of the pulses in the TLM node branches reveals that their magnitude after any time step equals the externally applied pulse, since all the scattered pulses cancel. Hence, the equivalent circuit of the TLM node is that of a step pulse injection at time t=0 into the RLC network shown in Figure 3.9. The voltage time response v(t) across the capacitor is proportional to the magnetic field described in (2.16). Consider the voltage time response v(t), in the RLC network to an applied step of magnitude V. The differential equations of the left-hand RLC circuit are:

$$\frac{dv}{dt} = \frac{1}{C\,\Delta\ell}\, i \tag{3.10}$$

$$\frac{di}{dt} = -\frac{2}{L\,\Delta\ell}\, v - \frac{r}{L}\, i + \frac{2\,V}{L\,\Delta\ell}\ . \tag{3.11}$$

The eigenvalues of the voltage response are:

$$\lambda_1 = -\frac{r}{2\,L} + j\sqrt{\left(\frac{r}{2\,L}\right)^2 - \frac{2}{L\,C\,(\Delta\ell)^2}} = -\alpha + j\,\beta \tag{3.12}$$

$$\lambda_2 = -\frac{r}{2\,L} - j\sqrt{\left(\frac{r}{2\,L}\right)^2 - \frac{2}{L\,C\,(\Delta\ell)^2}} = -\alpha - j\,\beta\ \cdot \tag{3.13}$$

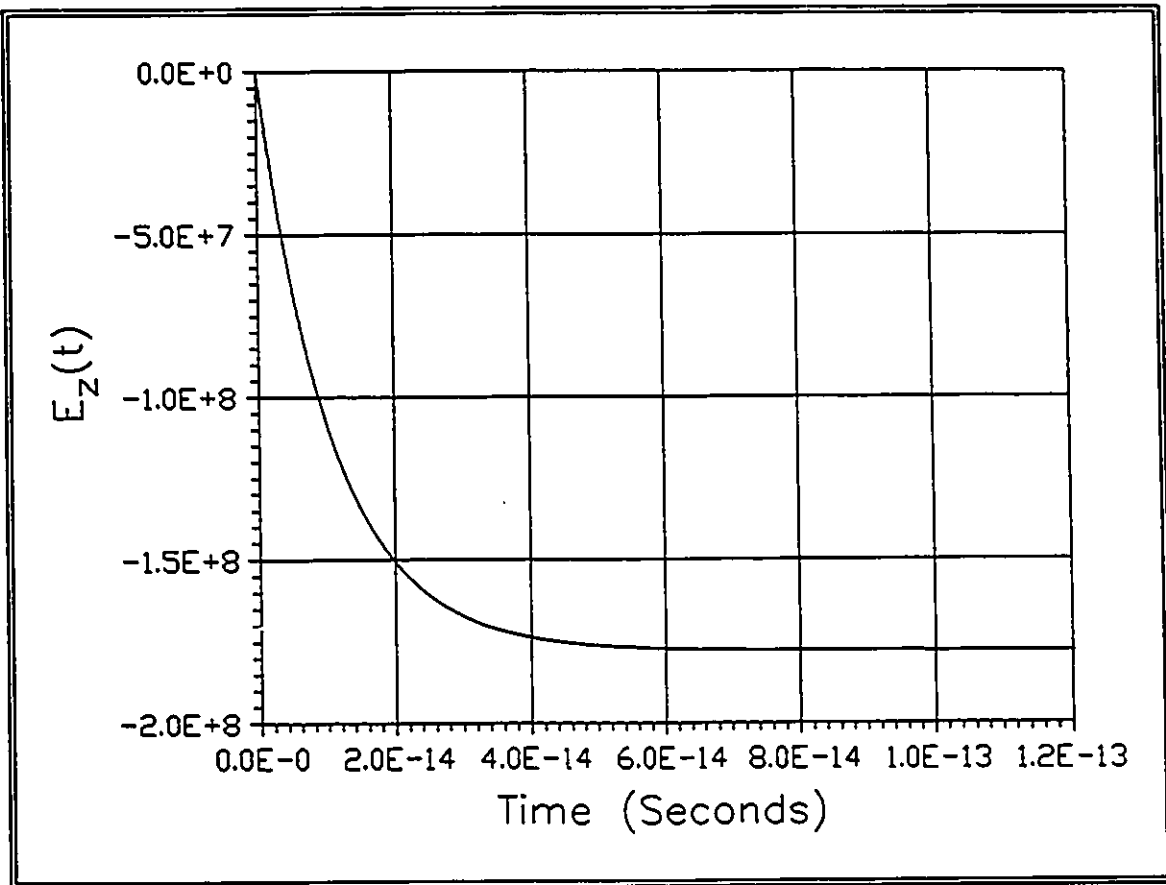

Figure 3.7: TLM-computed transient response of $E_z(t)$ for the reduced length structure.

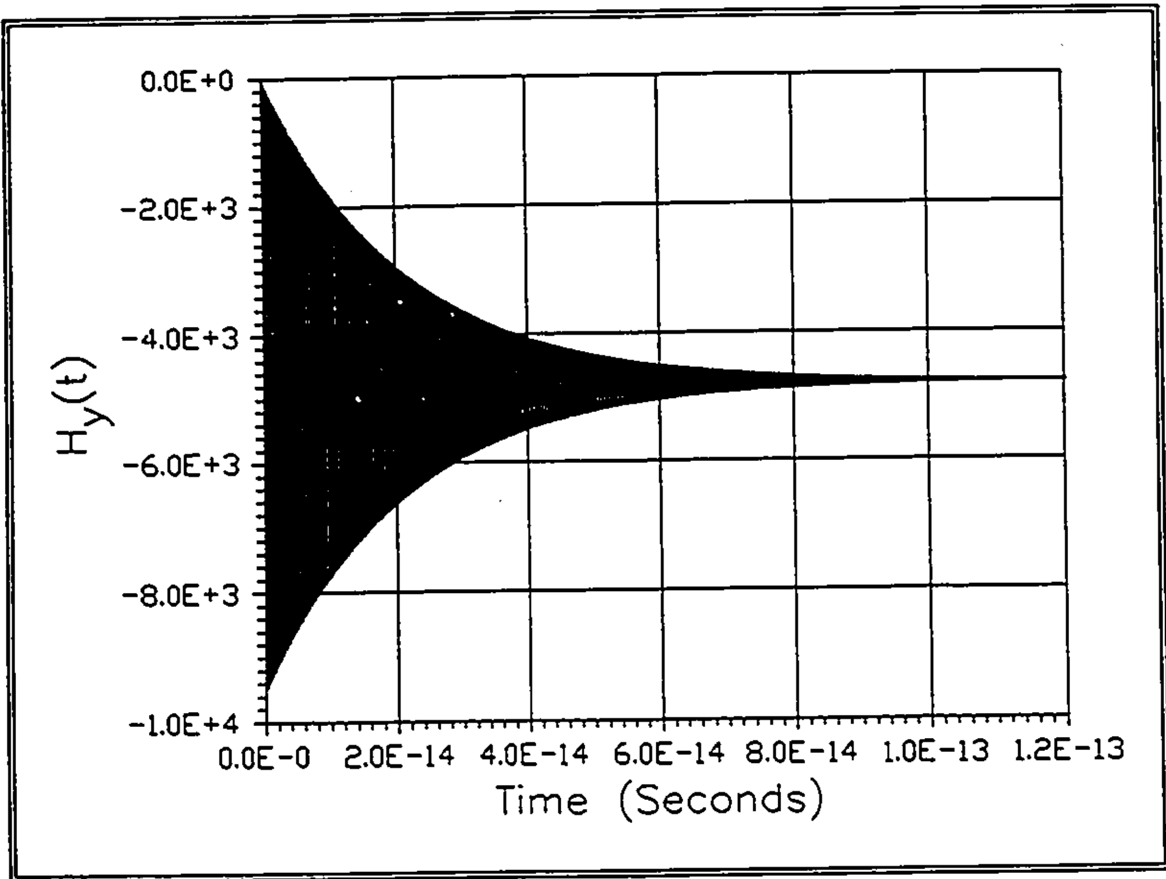

Figure 3.8: TLM-computed transient response of $H_y(t)$ for the reduced length structure.

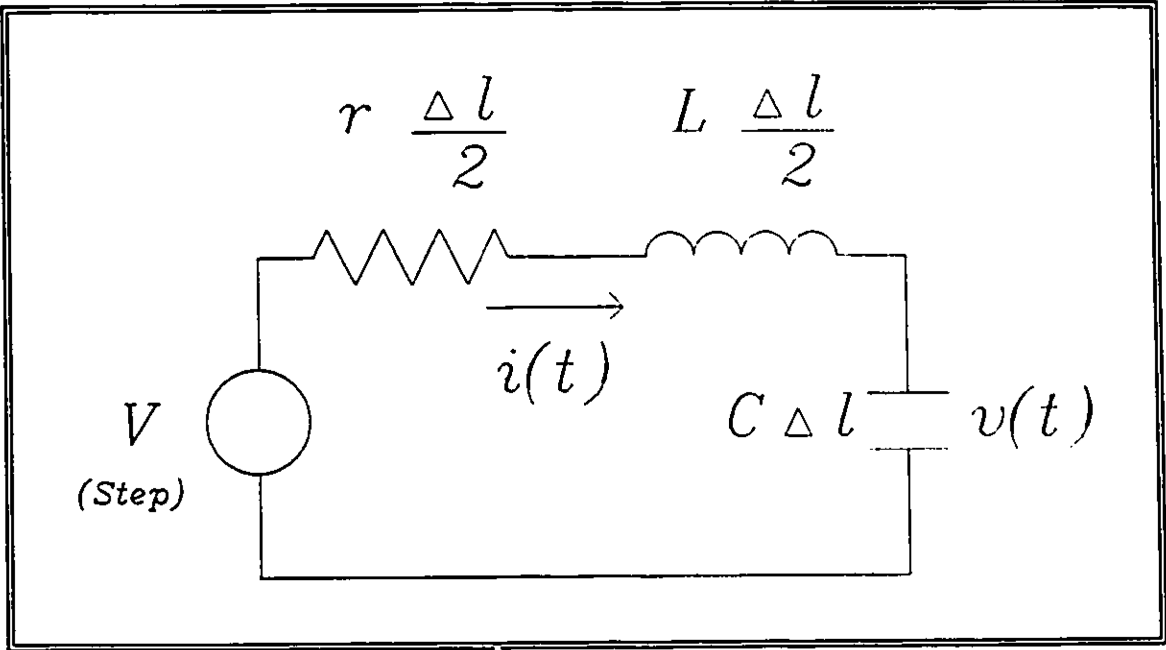

Figure 3.9: Equivalent circuit of the TLM transmission line.

The circuit is underdamped since from (2.11) and (2.21):

$$R < \frac{2\sqrt{2}}{\Delta\ell} \sqrt{\frac{L}{C}} \tag{3.14}$$

and the voltage response to the impulse excitation is:

$$v(t) = V \left[1 - \frac{1}{\sqrt{1 - \frac{C r^2}{4 L}}} e^{-\alpha t} \sin\left(\beta t + \tan^{-1}\left(\frac{\beta}{\alpha} \right) \right) \right] \tag{3.15}$$

The function v(t) sketched in Figure 3.10 shows an initial overshoot and a decaying sinusoid around the steady-state value. The frequency of oscillations is:

$$\omega = \sqrt{\frac{2}{L\, C\, (\Delta\ell)^2}} , \tag{3.16}$$

and the time constant of the envelop is:

$$\tau = \frac{2 L}{r} . \tag{3.17}$$

The maxima occur at:

$$v(t) = V\,(1 + e^{-\alpha t_m}) \quad where \quad t_m = (2n+1)\,\frac{\pi}{\beta} \quad for \quad n = 0, 1, 2, \ldots \tag{3.18}$$

Using the following values for the TLM node from the correspondences (e-f) in Section 2.2:

r= 10800 Ω/M

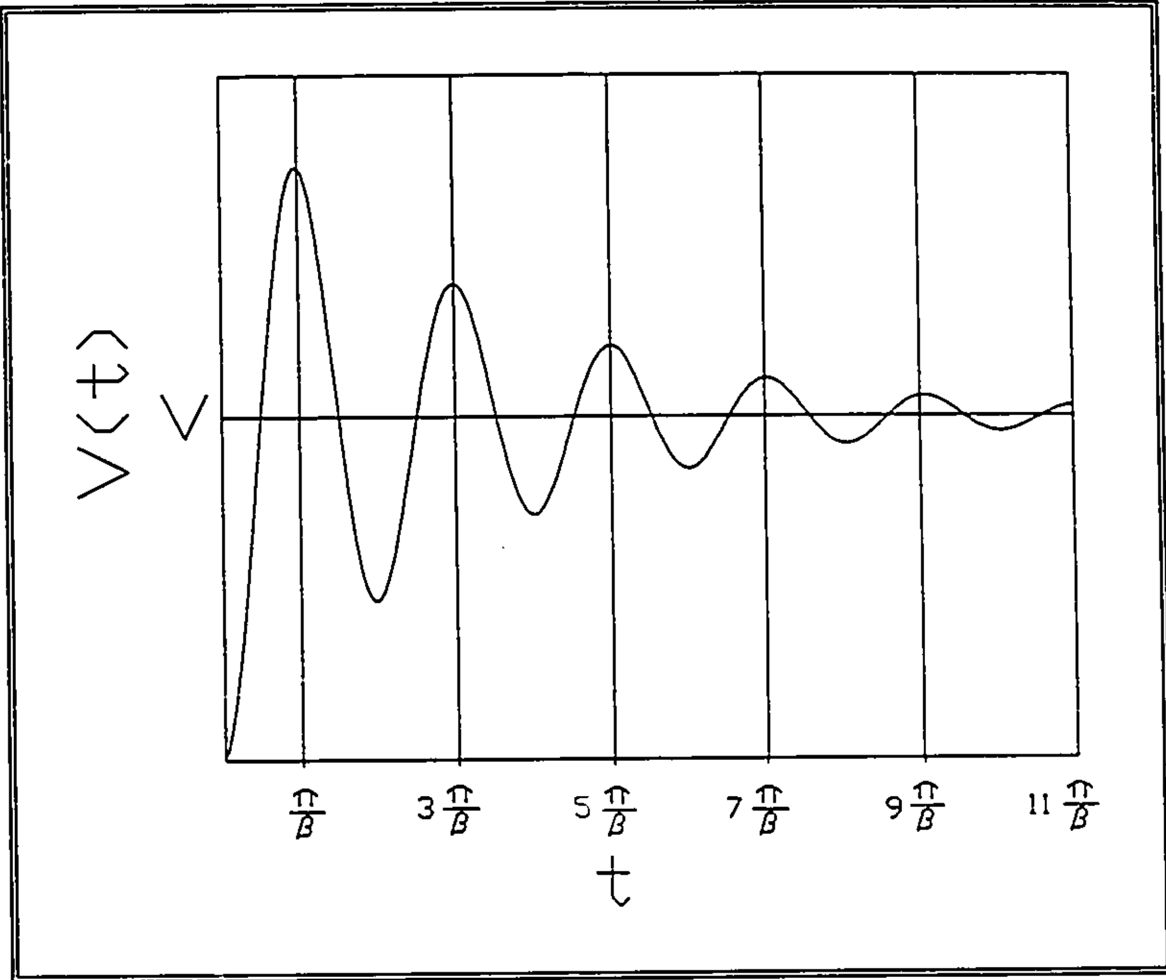

Figure 3.10: Second-order response of the TLM network.

$$C = 4\pi 10^{-7} \text{ F/M}$$

$$L = 13 \times 8.854\times10^{-12} \text{ H/M}$$

the following decaying sinusoid parameters are calculated:

$$\alpha = 2.35\times10^{+13}$$

$$\beta = 2.35\times10^{+16}$$

$$\omega = 2.35\times10^{+16} \text{ rad/seconds}$$

$$\tau \text{ (envelope)} = 2.13\times10^{-14} \text{ seconds}$$

$$(2n+1)\pi/\beta = 1.34\times10^{-16},\ 4.00\times10^{-16},\ 6.70\times10^{-16} \text{ seconds.}$$

By inspection, the predicted time constant of the envelope agrees with the TLM response of Figure 3.8. Also, as shown by Figure 3.11, in which a close-up view of the first few TLM time iterations is displayed, it can be seen that the peaks in the magnetic field response show close agreement with the calculated values.

In Example 1, the pulse energy magnitude at the source nodes is constant until the energy pulses return to the source nodes from the first reflection at the boundaries. At that point in time, new second order oscillations are generated which add to the previous ones. Hence, the magnetic field response of Figure 3.6, which initially exhibits a single second order response, also shows increasing disorder with increasing number of time iterations after the first reflection at the boundaries after 40 time steps.

Consider now Example 3, which is the case of a linearly, doped MESFET channel with the parameters shown in Table 3.1. The theoretical and numerical steady-state spatial magnetic and electric field responses in Figures 3.12 and 3.13 also show virtually exact agreement. In this case, the magnitude of the magnetic field increases quadratically to a maximum at the center of the slab while the electric field remains spatially constant. The quadratic distribution of the magnetic field arises from the integration of a linearly-increasing conductivity. The analytical and numerical electric field transient response to a constant current is shown in Figure 3.14. Good agreement can be seen, considering that the superimposed second-order sinusoids have relatively low amplitude and can be easily filtered out.

We have discussed how TLM produces decaying second-order oscillations, but not how they originated. TLM, being a physical modelling tool has in fact computed the

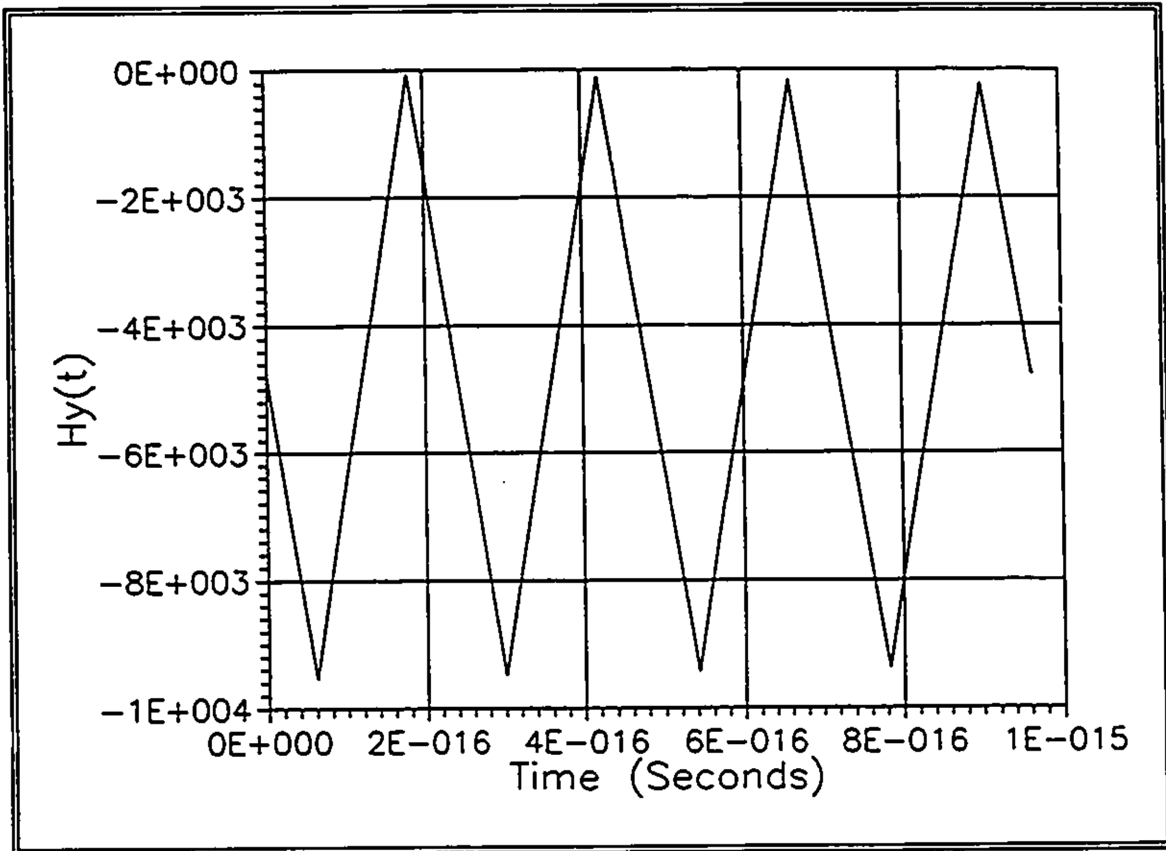

Figure 3.11: Time closeup view of $H_y(t)$'s initial oscillation.

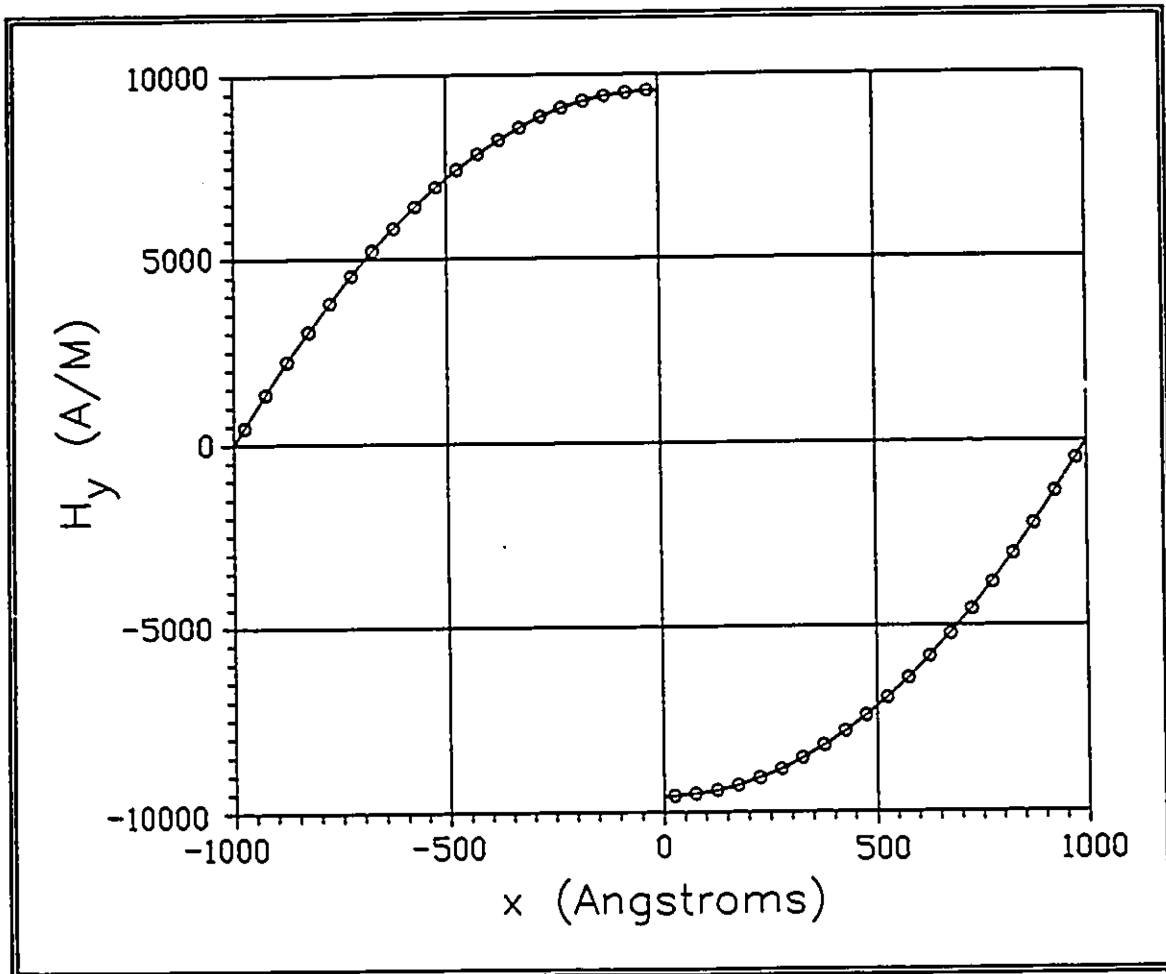

Figure 3.12: Steady-state spatial magnetic field in linearly-doped conducting dielectric. Solid line: calculated results, circle symbols: TLM results.

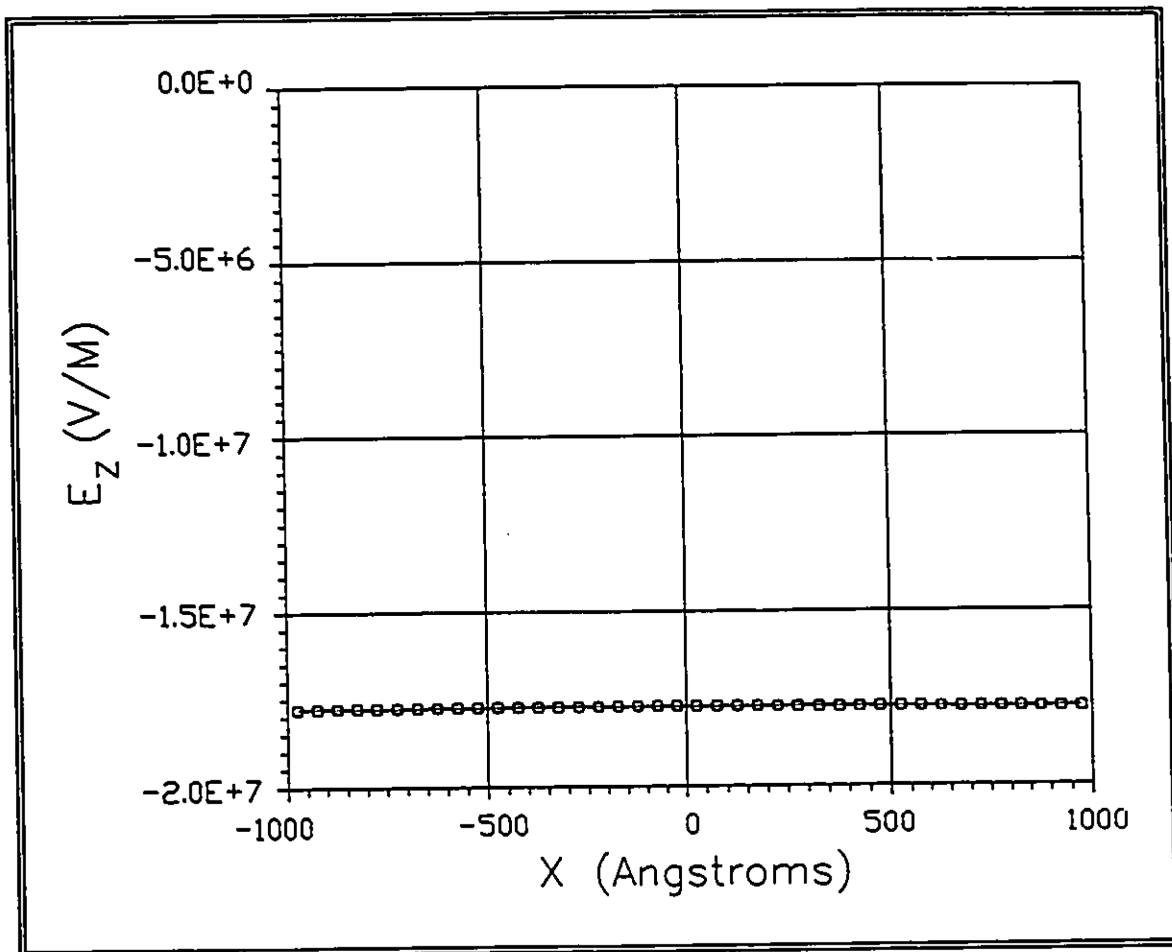

Figure 3.13: Steady-state spatial electric field in a linearly-doped conducting dielectric. Solid line: calculated results, square symbols: TLM results.

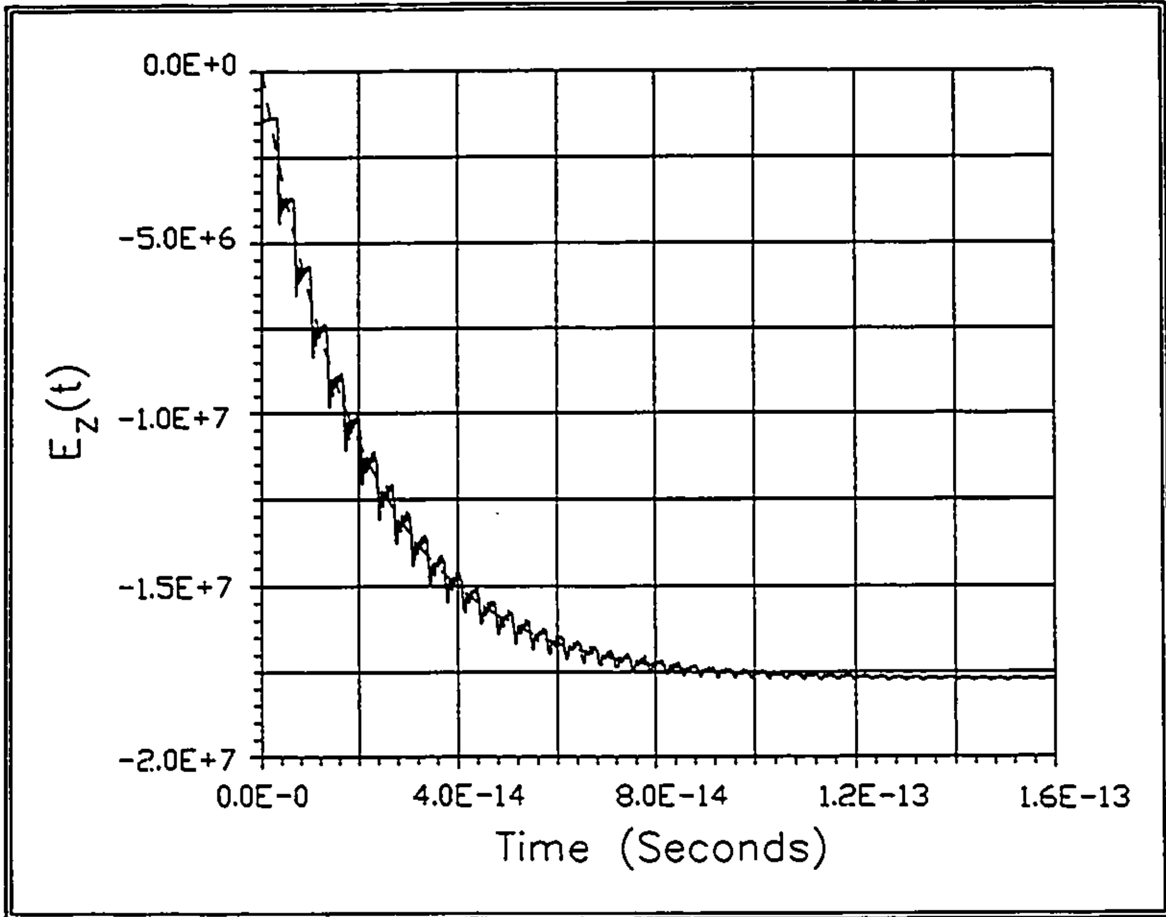

Figure 3.14: Transient response of the electric field in a linearly-doped conducting dielectric. Dashed line: calculated results, solid line: TLM results.

expected response for the type of non-physical excitation used in these examples. We have applied ideal current steps instantly rising to the steady-state level. In real situations, the TLM system would charge to the steady-state according to its dielectric relaxation time constant derived in (3.8). In Chapter 5, several examples will be presented to show the TLM response to excitations where the dielectric relaxation time constant is used to simulate the behavior of physical device. In these cases, the TLM responses will be seen to be free from second-order oscillations.

In the three examples of this Chapter, the injected current, which is computed from the magnetic field at x=0, is found to be constant and independent of the section's conductivity distribution and length. In these examples, and using the values of the magnetic field at x=0, the injected current is related to the TLM energy magnitude A, the gate width W, and the relative dielectric constant ϵ_r, by the following expression:

$$I = 2.65 \times 10^{-3} A \; W \sqrt{\epsilon_r} \quad . \tag{3.19}$$

This relationship can be used to determine the amount of TLM energy necessary to simulate the channel current in a TLM system. It can also be used to enforce current continuity at any point in the MESFET channel since (3.19) is independent of the conductivity distribution and channel height.

The formulation of a TLM network to simulate the GaAs MESFET conducting channel of Figure 2.1 is now complete. By having the GaAs MESFET analysis engine (which will be described next in Chapter 4) make available the following conducting channel parameters at every time instant:

- the profile of paths a to d in Figure 2.1,
- the conductivity at every point in the conducting channel space, and,
- the channel current,

then in Figure 3.15, the TLM sections' lengths, TLM nodes' conductivity distributions, and the TLM energies, are all injected into the TLM systems and the electromagnetic responses can then be computed. We have effectively used TLM to transform the current-voltage characteristics produced by the GaAs MESFET analysis engine into

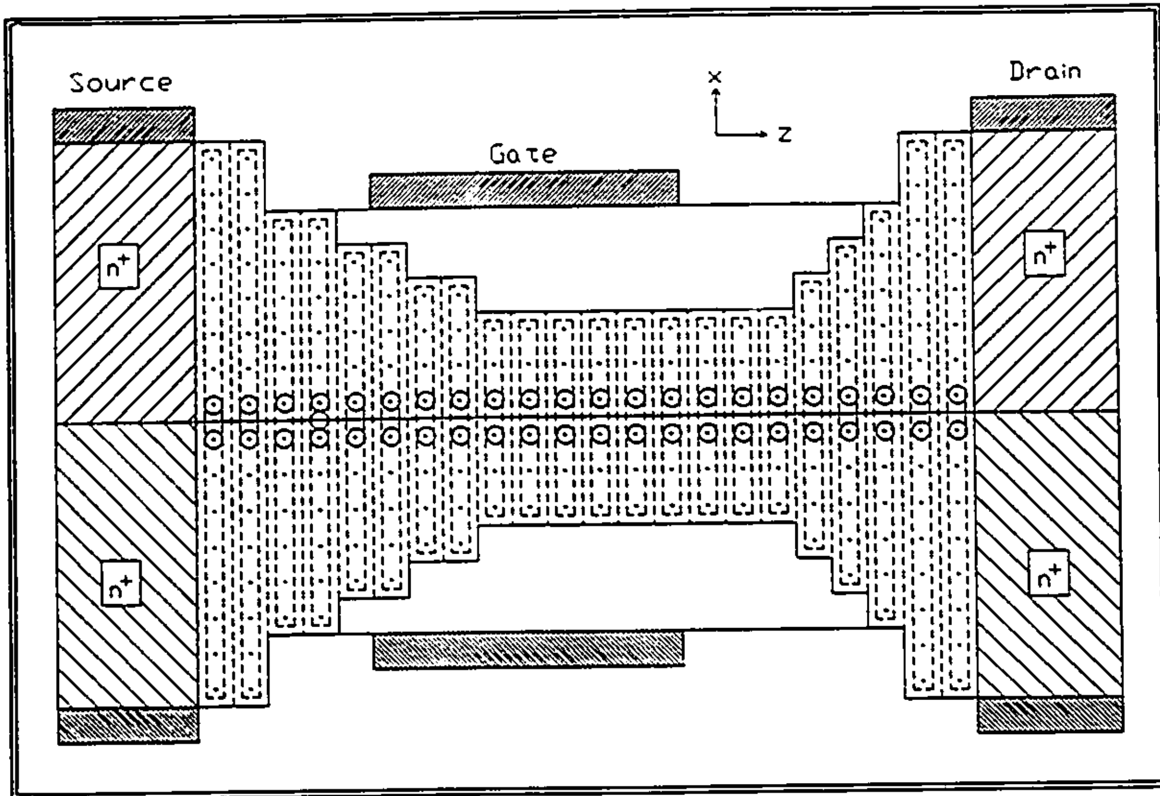

Figure 3.15: Simulation of the GaAs MESFET conducting channel by a collection of discrete TLM systems.

electromagnetic tıelds.

3.5 References

3.1 S.F. Dindo and M.M. Ney, "Two-Dimensional Transmission Line Matrix (TLM) Simulation of the Electromagnetic Fields in a Rectangular Section of a Discretized GaAs MESFET Channel With Arbitrary Doping Profile," IEEE MTT-S International Microwave Symposium, Atlanta, 1455-1458, (1993).

3.2 S.F. Dindo, M.M. Ney, and R.G. Harrison, "A New Two-Dimensional Transmission Line Matrix (TLM) Node Formulation For Thin Semiconductor Samples," Submitted for publication to the International Journal For Numerical Modelling.

3.3 N.N. Rao, Elements of Engineering Electromagnetics, Prentice-Hall, Inc. 1977. pp. 357-364.

3.4 C. Chang and D. Day, "Analytical Theory for Current-Voltage Characteristics and Field Distribution of GaAs MESFET's", IEEE Trans. Electron Devices, vol. 36, No. 2, pp. 269-280 February 1989.

CHAPTER 4

The GaAs MESFET Analysis Engine

4.1 Introduction

The function of the GaAs MESFET analysis engine is to supply the interface parameters discussed in Chapter 3. These parameters enable the TLM network to simulate the electromagnetic fields in the conducting channel. The analysis engine embodies a numerical, physically based, non-stationary, quasi two-dimensional time-domain model which has several major merits. Firstly, being a physically based model, it enables the engine to predict the nonlinear response to large signals for a wide class of MESFET structures. Secondly, the response can be characterized as a function of geometry, material doping, and bias levels. Thirdly, adopting non-stationary analysis, where the velocity/time history of the carriers in addition to their field dependence are considered, allows a true transient time analysis of sub-micron gate length structures. And fourthly, it is capable of predicting more accurately high frequency transconductance and gain than steady-state methods.

Before launching into the model derivation, it is useful to examine the effects of the drain-to-source voltage V_{DS}, and gate-to-source voltage V_{GS} on the properties of the active layer at a time t at which the transient velocity has achieved steady state. The active layer, which contains both the depletion and the conducting channel regions, undergoes modulation due to the drain current characteristics, $I_{DS}(V_{GS},V_{DS})$. Analysis of the MESFET behavior consists of resolving the precise interface between the two regions under the gate electrode by the self-consistent solution of (i) the two-dimensional Poisson equation which yields the height of the depletion region, (ii) the two-dimensional time-space relationship between electron velocity in the channel to the applied field, and (iii) the continuity of the current density equation in the conducting channel. The effects of the surface states are also taken into account to resolve the interface in the ohmic access regions of the channel. In the process of resolving the interface, all other parameters,

such as the channel current, channel voltage, and the electric field, are also computed.

The $I_{DS}(V_{GS},V_{DS})$ characteristics are sketched in Figure 4.1 for a single fixed V_{GS}. Three regions are identified which affect the active region differently: region I, or the ohmic region, where the MESFET behaves like a resistor; region II, or the knee region, where the drain current begins to saturate; and region III, or the saturation region, where the current increases slowly with V_{DS}.

REGION I Figure 4.2 sketches the MESFET cross-section showing the interface profile, represented by the path cdfh, between the depleted regions and the conducting channel. The device is biased for ohmic operation where the electron velocity is linearly proportional to the applied field. The surface states are considered to be have been caused during layer growth and device fabrication and are non-variant with applied biases; therefore, the depletion layer maintains the same height at the source and drain contacts. The ohmic depletion regions are defined by the polygons 1 and 3. It is the region under the gate defined by the polygon 2 which undergoes modulation by the applied biases. In this case, the channel voltage adds to the gate voltage to increase the height of the depletion region at f further than d. In the entire channel, $E_z \leq E_L$, where E_z is the electric field at any point in the channel, and E_L is defined as the maximum electric field above which the velocity-field relationship is no longer linear.

REGION II In Figure 4.3, the drain voltage is increased to the knee region, where the electron velocity increasingly saturates with applied field. There are now two regions under the gate: polygon 2 where $E_z \leq E_L$, and polygon 3 where $E_z \leq E_T$. E_T is defined as the peak electric field above which negative differential velocity is exhibited. The electric field is E_L along the segment ef. The interface between the depletion and conducting channel regions along the segment fh is no longer linear. This reflects the saturating velocity-field dependence.

REGION III In Figure 4.4, the drain voltage is further increased well into the saturation region. The electron velocity is now fully saturated, and does not vary with increased field. Polygon 2 defines the region where $E_z \leq E_L$, polygon 3 defines the region where $E_z \leq E_T$, and polygons 4 and 5 define the high-field regions where $E_z \geq E_T$. The field is E_L along the segment ef, and E_T along the segment gh, at which the velocity peaks.

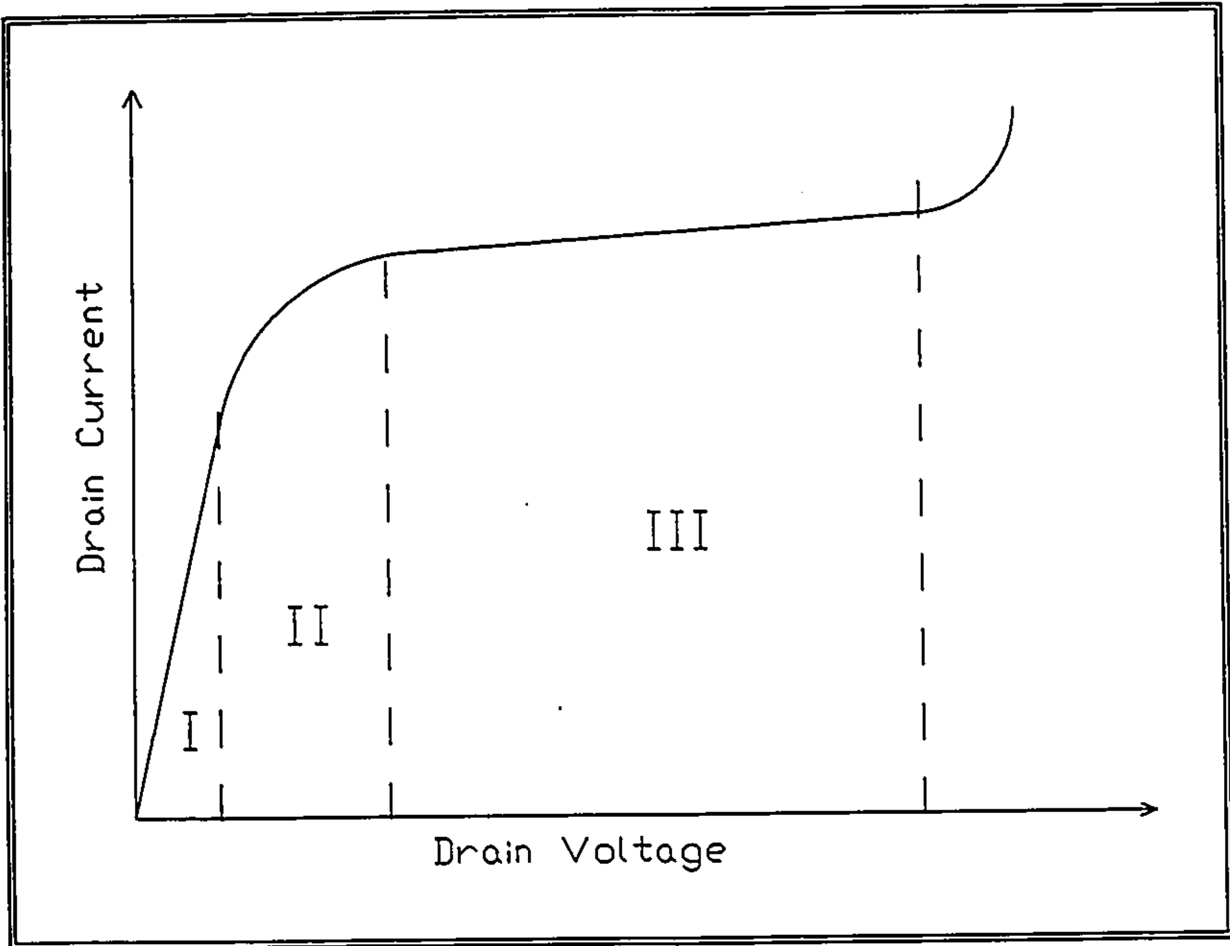

Figure 4.1: The $I_{DS}(V_{GS},V_{DS})$ characteristics of a MESFET

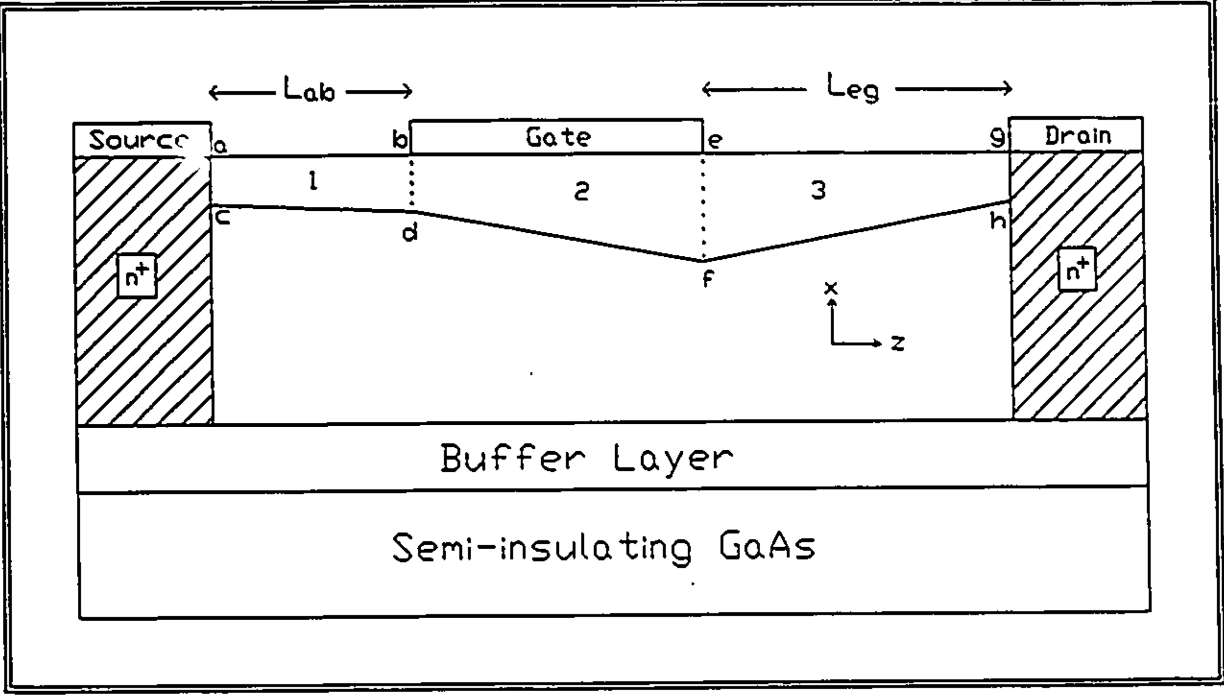

Figure 4.2: A sketch of the depletion areas in region I of the $I_{DS}(V_{GS},V_{DS})$ characteristics

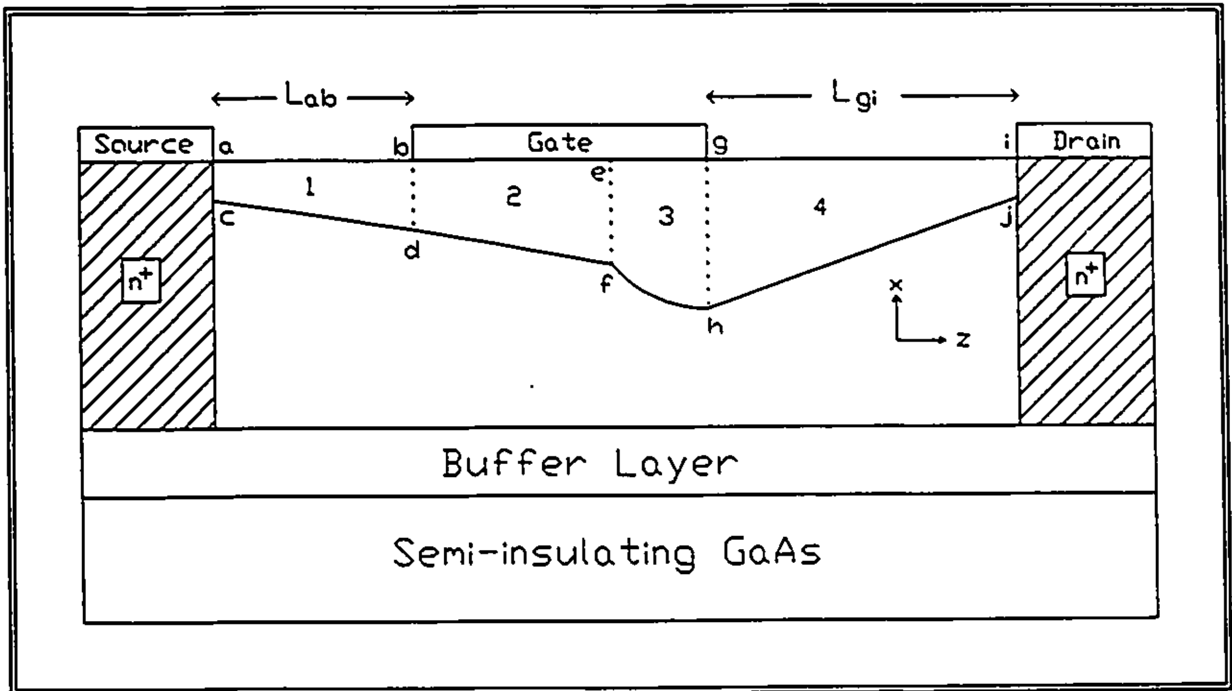

Figure 4.3: A sketch of the depletion areas in region II of the $I_{DS}(V_{GS},V_{DS})$ characteristics

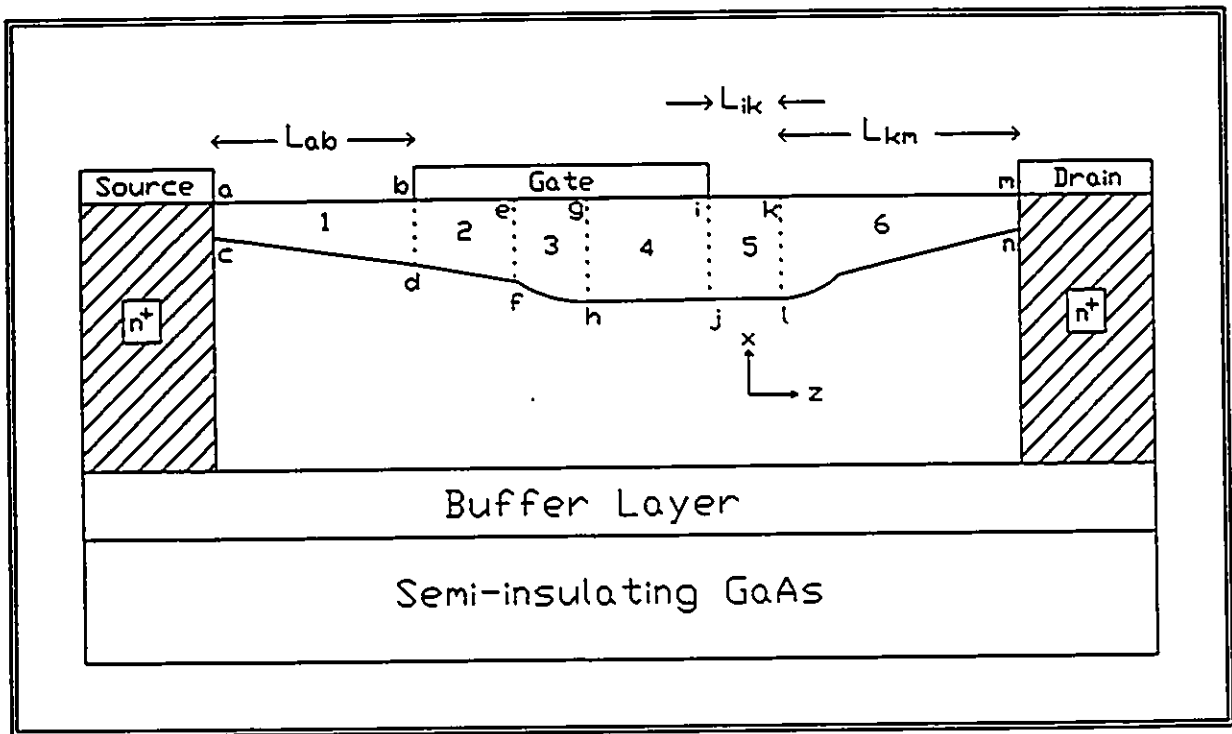

Figure 4.4: A sketch of the depletion areas in region III of the $I_{DS}(V_{GS},V_{DS})$ characteristics

In the high-field regions, the depth of the depletion region is substantially constant, and the electron velocity relaxes to a saturated value. Current continuity is maintained by electron accumulation in polygons 4 and part of 5, to be balanced by partial electron depletion in the rest of region 5. At the segment kl, the field drops back to E_T, at which the electron velocity peaks again. Further inside polygon 6, the field drops as the distance from the gate increases, and the velocity decreases again. The depleted part of the channel can be approximated by the one-dimensional Poisson equation whenever $E_z < E_T$. In the high field region, an additional field component extending from the drain to the source is taken into account by two-dimensional treatment of the Poisson equation.

At greater drain-source voltages outside the saturation region, the high-field region extends further from the gate and approaches the drain electrode. In addition, the high-field region extends to encompass most of the gate region. If sufficiently large negative gate-source bias is also applied, the depth of the depletion region extends further into the conducting channel. In all these cases, large currents flow and device breakdown becomes imminent.

The MESFET model implemented in this thesis describes the operation of the device in the ohmic, knee, and saturation regions of the current-voltage characteristics. The operation boundaries are defined by the onset of the drain and gate voltages sufficient to initiate the process of leakage drain currents prior to device breakdown.

4.2 The GaAs MESFET Model

The MESFET model amalgamates two separate components. The first model component extracts the time dependence by computing both the carrier velocities across the channel and the charging voltages at the gate and drain electrodes. The second model component receives these results at each time step and computes the TLM interface parameters: (i) the channel current I_c, (ii) the channel conductivity $\sigma(z,x)$, and (iii) the depletion/conducting-channel interface profile $h_o(z,x)$. Non-stationary electron dynamics and their effects on velocity are accounted for by the self-consistent solution of the electron-energy and momentum-balance equations using published results of

relaxation effects derived from Monte Carlo[1] calculations. Voltage-charging effects are obtained by calculating the resistance-capacitance time constants τ_d and τ_g, of the MESFET drain and gate equivalent circuits, respectively. The time step is chosen to be a constant fraction of the lower of τ_d and τ_g. But since the two time constants are time-varying, the model features a variable time step, which is a unique treatment. The second model component utilizes the time-dependent velocities and charging voltages and numerically solves the Poisson and current continuity-equations in the channel using a new Voltage Balance Method.

The model adopts several assumptions. Some are dictated by the TLM network, and others are chosen to avoid excessive computer time and memory. The basic assumptions used for the construction of the model are:

- the depleted regions are carrier free
- the conductive channel contains no fixed charges
- There is negligible residual diffusion current after the drift-diffusion mechanisms have settled
- room temperature analysis.

The first two assumptions arise since the TLM system modelled after the work of Rao [4.1] imposes an abrupt depletion to conducting region transition. In actual devices, the transition is gradual and is of the order of one to three Debye lengths [4.2]. The related error is minimal in MESFETs whose gate lengths are greater than their channel depth [4.3, 4.4]. The third assumption is adopted on the premise that the material is substantially free of traps and is operating in a dark environment at room temperature so that the residual diffusion current in the depletion-conducting channel interface is negligible. The MESFET model is capable of adopting the following analysis effects by virtue of the Voltage Balance Method:

- two-dimensional analysis of the Poisson equation,

---

[1] Turn to Appendix A for a brief introduction into Monte Carlo Methods.

- arbitrary doping and mobility dependence in the x-direction,
- multiple doping profiles in the z-direction,
- two-dimensional analysis of the fringe region in the gate-drain region,
- surface states and their influence on the ohmic region,
- gate recess,
- influence of velocity overshoot effects, and,
- the influence of the buffer layer and the n^+ contacts.

The entire MESFET model can be outlined in the process flow chart shown in Figure 4.5. The process begins with the definition of the geometry and doping of the test structure followed by spatial discretization of the active layer into a mesh of nodes. The initial conditions, such as starting voltages and input signal, are evaluated. The starting conditions most commonly consist of ground or zero biases at the drain and gate electrodes. The device is then transitioned into bias conditions chosen for system usage. Following the evaluation of the drain and gate time constants, the time step is chosen, and they are all used to evaluate the charging voltages and the two dimensional non-stationary velocities. The new Voltage Balance Method is then used to obtain the channel current and conductivity as well as the depletion/conducting-channel profile. At this point, the TLM interface parameters for the entire MESFET channel are evaluated. The new time constants are then re-evaluated and the process cycle repeats until the final time is reached.

The Voltage Balance Method is outlined in the process flow chart shown in Figure 4.6 [4.5]. This new technique combines numerical computations with analytical formulations to obtain quasi two-dimensional analysis which is optimized for high computational speeds and good accuracy. In this method, the region between the source and drain contacts is segmented into rectangular sections each of single node thickness, and each section in turn is discretized into nodes. For given gate and drain voltages at any time t, a trial current, I_x, is applied to all the segments. The interface boundary between the depletion layer and the conducting channel, $h_o(z,x)$, for each segment is

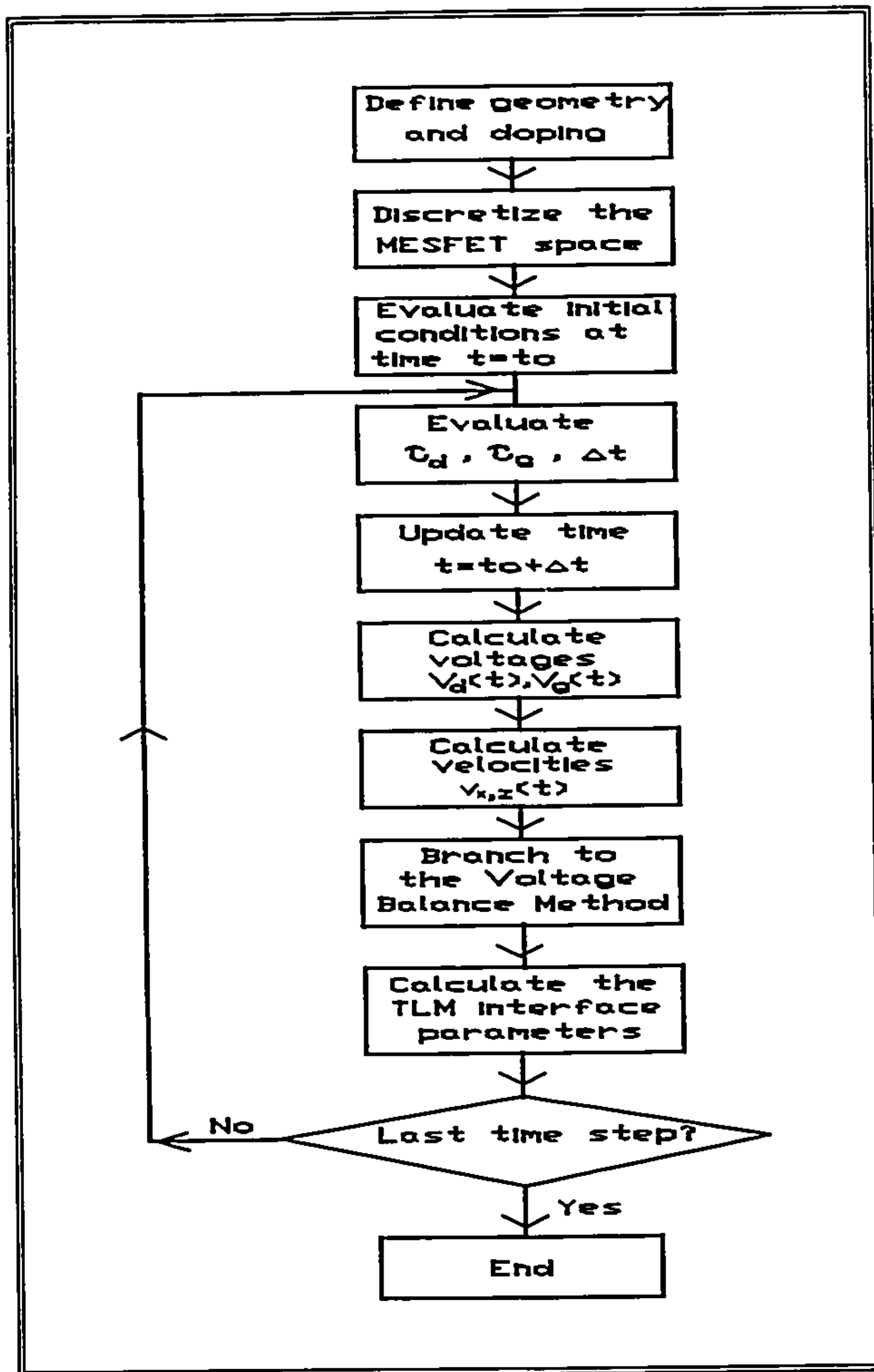

Figure 4.5: Flow-chart showing the outline of the GaAs MESFET model.

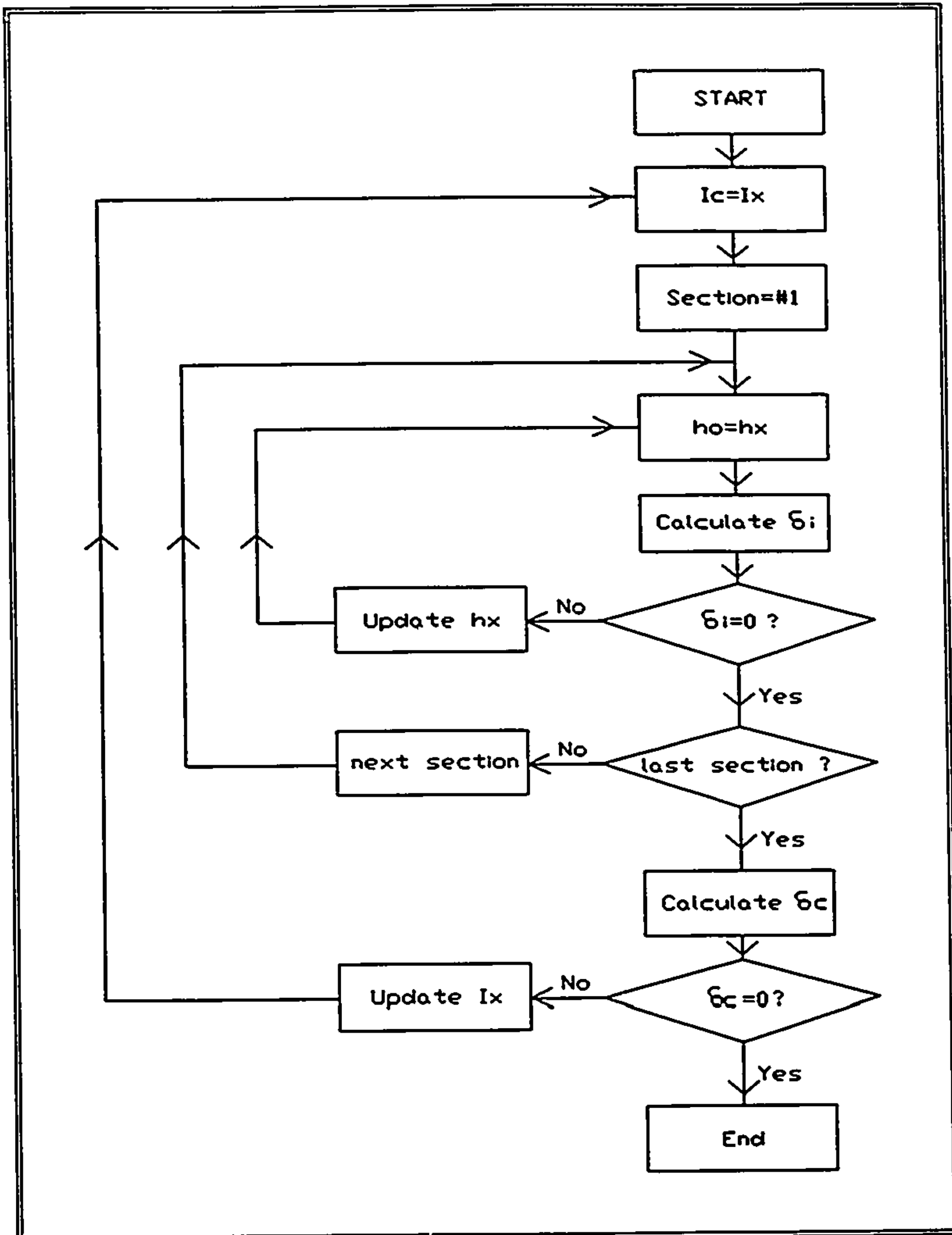

Figure 4.6: Flow chart showing the outline of the Voltage Balance Method.

obtained by solving the voltage equation arising from the Poisson and current continuity equations and the surface voltage for each channel section at h_x. Newton's method is used to minimize the ensuing error functions $\delta_i(x,z)$ for each section. Using I_x and $h_x(z,x)$, the channel voltage at the drain contact, $V_{channel}$, is calculated and compared with the charging drain voltage, $V_d(t)$. This time, the bisection method is used to minimize the other ensuing error function, δ_c. Upon minimization of $\delta_i(x,z)$ and δ_c the MESFET voltages are balanced and the solutions for I_c and $h_o(z,x)$ are reached.

4.2.1 Space Discretization

The present MESFET model allows non-uniform space discretization, and as in TLM, it requires the maximum node-to-node space not to exceed the Debye length. The active region can be meshed, for example, differently along the x- and z-axes, or non-uniformly along a given axis. However, in the case where the GaAs MESFET analysis engine is to be synchronized with the TLM analysis, then the general discretization rule that the physical boundaries are located halfway between nodes must be applied. For example, Figure 3.15 shows a general sub-sectioning of the MESFET channel into a collection of discrete TLM systems. The components of any one system is described in Figure 3.2. Each system encloses a vertical line of nodes and is completely enclosed with electromagnetic boundaries halfway between nodes. Figure 4.7 shows a practical discretization arrangement for the MESFET analysis engine which is also compatible with the TLM descritization scheme of Figure 3.15. The high-field region is meshed with a finer x-z grid than the low field regions. The close-up of the gate region in Figure 4.8 shows that, in addition, the x grid is finer than the z grid in both the low and the high field regions. The size of the grids are typically chosen to be a compromise between computer memory limitations and execution speed. It is noted that in the current MESFET analysis, the buffer and the n^+ contact regions are not meshed since their effects are included in the analysis as bulk effects. This will be discussed in Section 4.2.8.

4.2.2 GaAs MESFET Charging Time Constants

When a semiconductor is subjected to an electric field, the conductivity responds

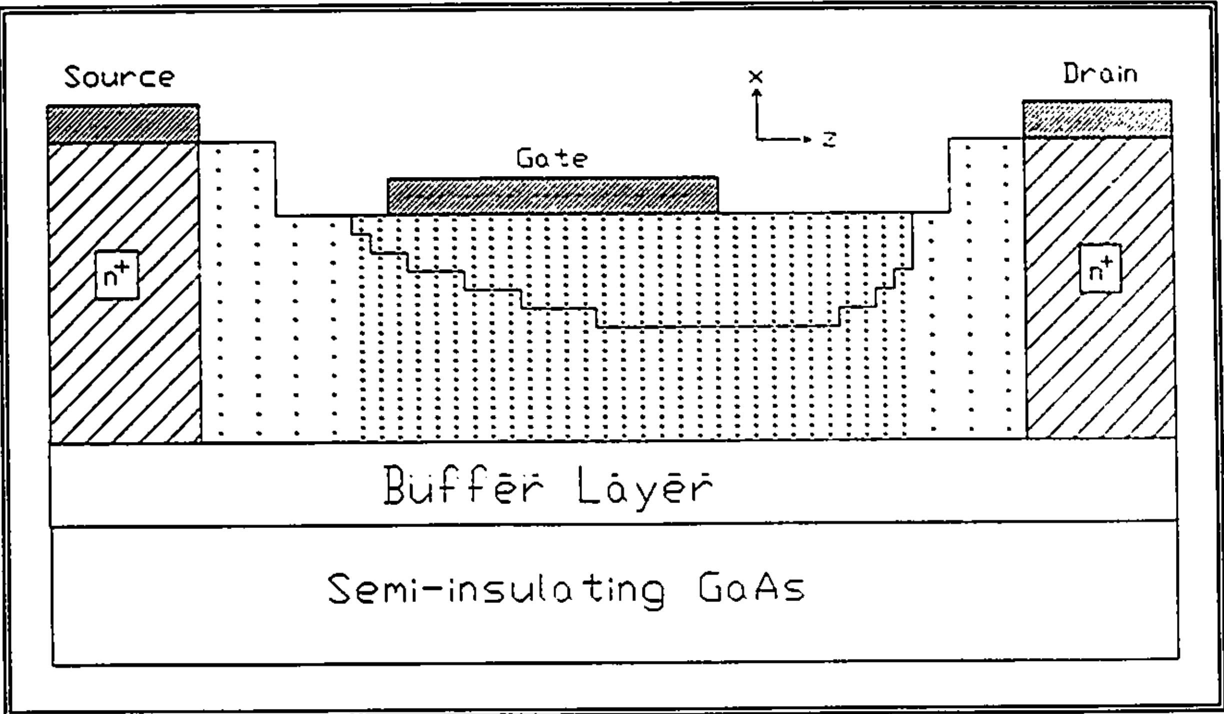

Figure 4.7: GaAs MESFET discretization scheme

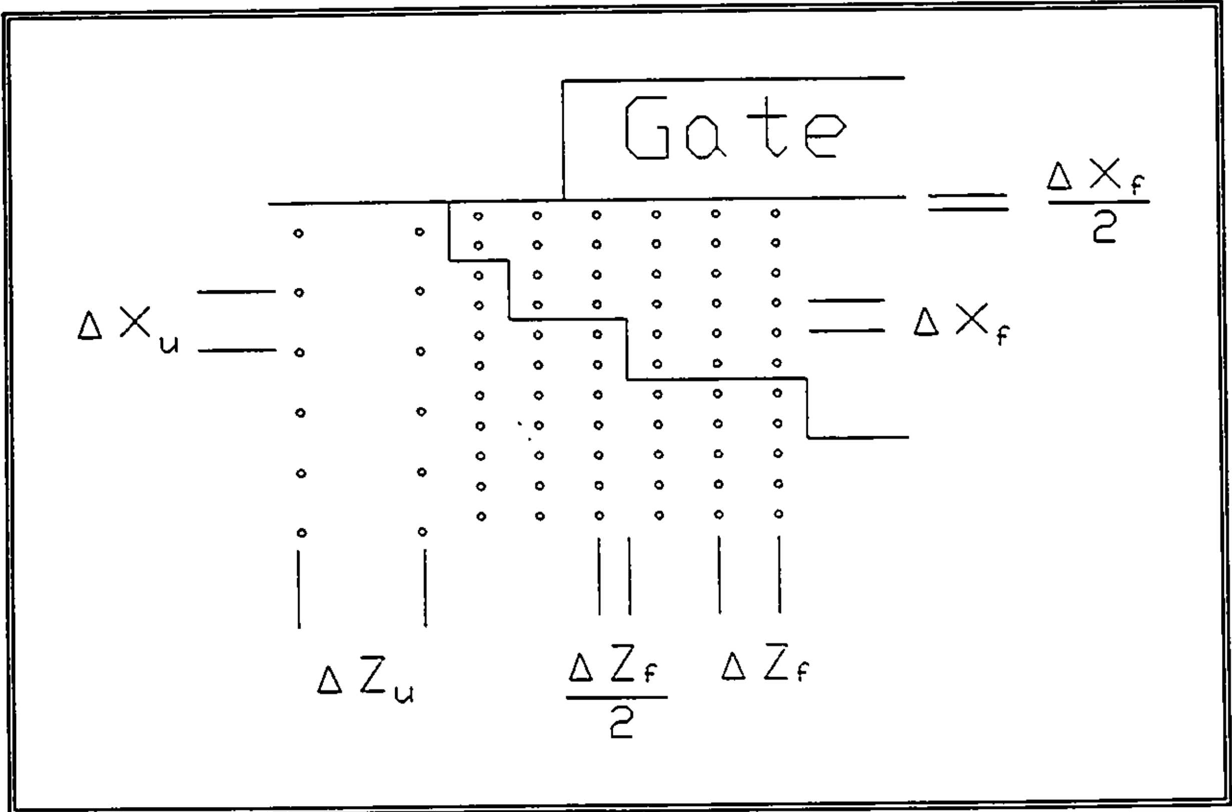

Figure 4.8: Closeup of the discretization in the gate region

in a finite time dictated by a dielectric relaxation time constant [4.6] given as:

$$\tau_R = \frac{\epsilon}{\sigma} \, . \tag{4.1}$$

This can be represented by an RC equivalent circuit of a lossy medium. In a GaAs MESFET, two dielectric relaxation time constants dictate the charging time behavior: τ_g and τ_d. τ_g is given by the product of the capacitance of the depletion region under the gate electrode and the resistance of the channel in the linear region [4.7]. τ_d is the product of the drain-to-source capacitance and resistance of the enclosed conducting channel sections. In the present MESFET model, once the time constants are calculated, the time step is chosen to be a fraction of the lesser of the two, typically .025τ to .05τ. The charging drain and gate voltages are then calculated by discretizing the differential equation of an applied voltage, V_{ap}, charging an RC network. The charging voltage[2], V(t), can be shown to be:

$$V_i(t) = V_{i(ap)}(t)\left(1 - e^{-\frac{\Delta t}{\tau}}\right) + V_{i-1}(t)\left(e^{-\frac{\Delta t}{\tau}}\right) \tag{4.2}$$

where Δt is the time discretization and the subscripts i and i-1 refer to the present and previous time iterations. The time step is directly dependent on the dynamic gate and drain time constants τ_g and τ_d. Since τ_d in the active region is at least an order of magnitude smaller than τ_g, the device charges to the drain voltage faster than to the gate voltage. Hence, before the drain voltage charges to 98% of the final voltage, Δt is chosen as a fraction (typically one tenth to one twentieth) of τ_d, and thereafter, Δt is chosen as a fraction of τ_g.

[2] The MESFET model outlined in this thesis distinguishes between the applied and charging voltages. The applied voltage is the source voltage feeding an equivalent series RC network, and the charging voltage is that measured across the capacitor.

4.2.3 Non-stationary Electron Velocity

Non-stationary electron dynamics in submicron gate length GaAs MESFETs are necessary to account for rapid changes in the electric fields and their effects on the material's conductivity. For example, when a voltage or electric field step is applied to a GaAs sample, the electron energy w, and electron momentum P, do not follow the applied field instantly, and the conductivity is no longer constant [4.8]. Instead, the system reaches equilibrium or steady-state conditions after a time determined by the electron energy relaxation time constant, $\tau_w(w)$, the momentum relaxation time constant, $\tau_p(w)$, and the energy and momentum conservation equations:

$$\frac{dw}{dt} = qE\frac{dx}{dt} - \frac{w - w_o}{\tau_w(w)} \tag{4.3}$$

$$\frac{dP}{dt} = qE - \frac{P}{\tau_p(w)} \tag{4.4}$$

where w_o is the thermal-equilibrium energy. $\tau_w(w)$ and $\tau_p(w)$ are found by considering steady-state conditions by setting each of the left-hand sides of (4.3) and (4.4) to zero:

$$\tau_w(w) = \frac{w - w_o}{qE_{ss}(w)\,v_{ss}(w)} \tag{4.5}$$

$$\tau_p(w) = \frac{P_{ss}(w)}{qE_{ss}(w)} \tag{4.6}$$

where the ss subscripts in the velocity, energy, and momentum terms denote steady-state quantities. The electron momentum is related to the velocity by the normalized effective electron mass $m^*_{ss}(w)$:

$$P_{ss}(w) = m^*_{ss}(w)\,v_{ss}(w) \ . \tag{4.7}$$

The average drift velocity, electron energy, and electron effective mass as a function of the steady-state electric field have been calculated by Carnez et al. [4.9] using Monte Carlo simulations, for carrier doping concentrations ranging from 1×10^{17} to 3×10^{17} atoms/cm^3. The relationships are displayed graphically in Figures 4.9, 4.10, and 4.11 respectively. For a given electric field in the MESFET channel, $\tau_w(w)$ and $\tau_p(w)$ can be calculated form (4.5) and (4.6) using Figures 4.9 to 4.11, and the velocity at any time instant becomes the only unknown in (4.3) and (4.4) which can then be solved for and determined.

4.2.4 The Voltage Balance Method

The Voltage Balance Method, outlined in the flow-chart of Figure 4.6, utilizes two different optimizers to balance two MESFET voltage systems and obtain the solutions for I_c, $\sigma(z,x)$, and $h_o(z,x)$ [4.5]. The MESFET active layer shown in Figure 4.4 is considered to be divided between the source and drain n^+ contacts into i sub-sections normal to the z-direction, and each section is meshed in the same manner as in Figure 4.7. The dimensions of any section j are $z=\Delta\ell_j$ and $x=a$, where a is the channel depth which extends from the surface to the base of the channel. The method begins by selecting a trial channel current, I_x. The first MESFET system voltages to be balanced are along $h_o(z,x)$. This consists of finding the depletion depth at every z such that the voltages at h are balanced:

$$V_{depletion} = V_{channel} \quad . \tag{4.8}$$

The depletion layer potential $V_{depletion}$, is found from the solution of the Poisson equation taking into account the surface voltage $V_{surface}$. The channel voltage $V_{channel}$, at any section z is the product of the channel current I_x and the sum of the resistances of the conducting channel sections from the source contact to z. The surface voltage includes the free surface potential as well as the gate electrode voltage. Because of the discretization, the precise value of h_o is not realized, and instead the error terms:

$$\delta_i = V_{depletion} - V_{channel} \tag{4.9}$$

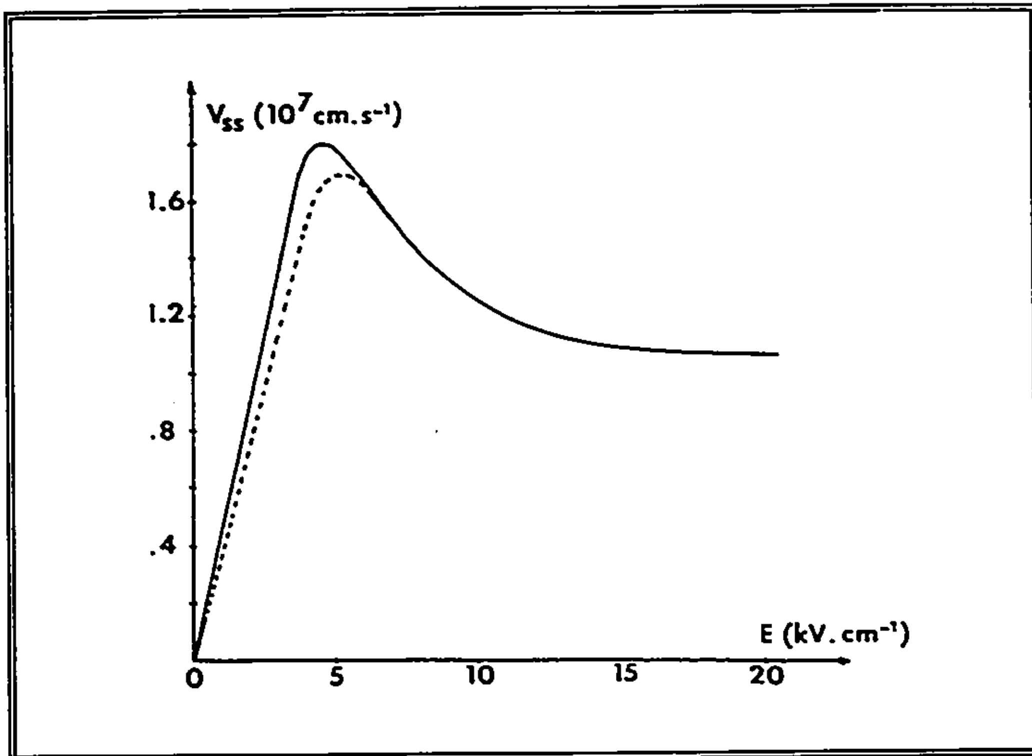

Figure 4.9: Steady-state mean drift velocity versus electric field for GaAs; Carnez et al. [4.9]. Solid line $N_d=1\times10^{17}$ cm^{-3}; dashed line $N_d=3\times10^{17}$ cm^{-3}.

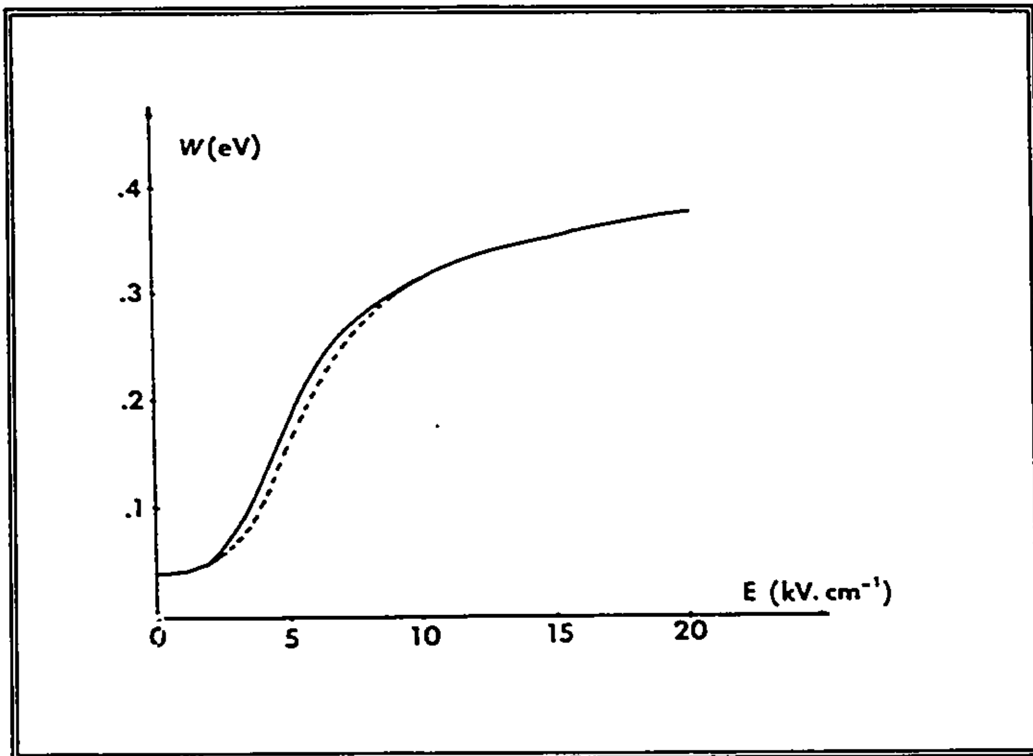

Figure 4.10: Steady-state mean energy versus electric field; Carnez et al. [4.9]. Solid line $N_d=1x10^{17}$ cm^{-3}; dashed line $N_d=3x10^{17}$ cm^{-3}.

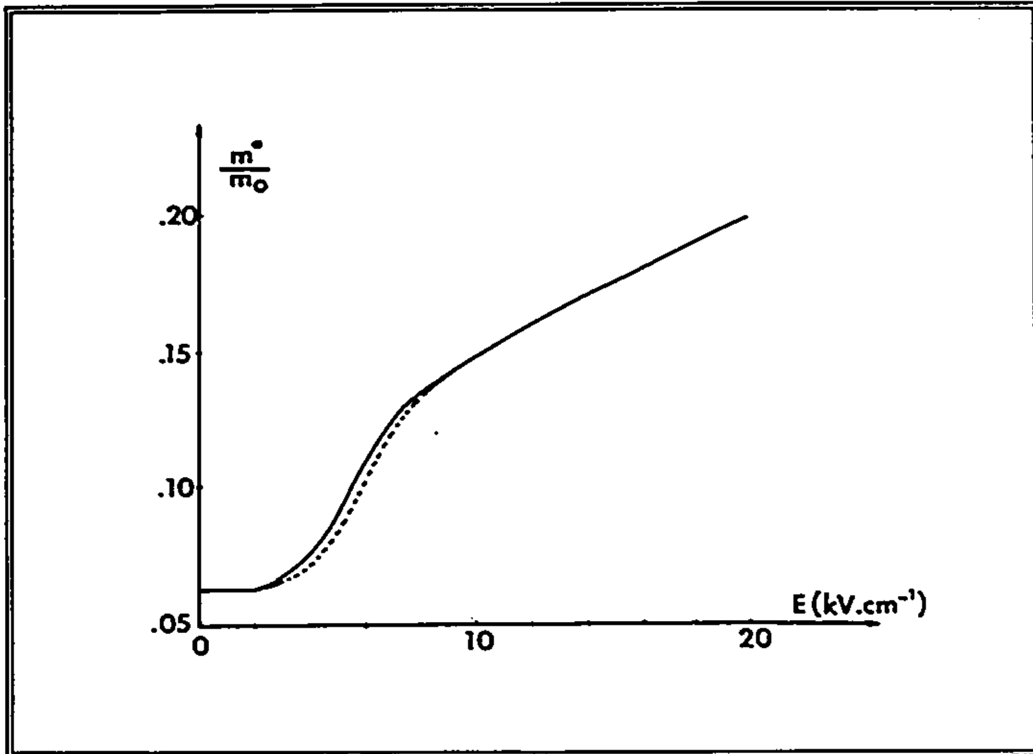

Figure 4.11: Normalized steady-state electron mass versus electric field; Carnez et al. [4.9]. Solid line $N_d=1\times10^{17}$ cm^{-3}; dashed line $N_d=3\times10^{17}$ cm^{-3}.

are minimized for all the i sections. The second MESFET system voltages are then balanced:

$$V_{channel} = V_d(t) \qquad (4.10)$$

where $V_{channel}$ is the channel voltage at section i, and $V_d(t)$ is the charging voltage at the drain electrode at time t. If not balanced, the entire procedure is repeated by choosing different values of I_x until the following error function is minimized:

$$\delta_c = V_d(t) - V_{channel} \; . \qquad (4.11)$$

The minimization of δ_i and δ_c terms can be carried out using any optimization technique. In this work, δ_i and δ_c minimizations are conveniently carried out using Newton's method and the Bisection method, respectively. The expressions for the conducting channel voltage $V_{channel}$, depletion layer voltage $V_{depletion}$, and the surface voltage $V_{surface}$, are evaluated in the following sections.

4.2.5 The Conducting Channel Voltage

The channel potential $V_{channel}$ at any section k is the product of the channel current I_c, and the sum of the conducting channel resistances of the first k sections:

$$V_{channel} = \sum_{j=1}^{k} \left(\frac{I_c \, \Delta \ell_j}{\sigma_j \, W} \right) \qquad (4.12)$$

where W is the gate width. σ_j at section j is:

$$\sigma_j = \int_0^{h_o} \frac{q \; v(z,x) \; n(x)}{E_j} dx \qquad (4.13)$$

where E_j is the electric field at section j. v(z,x) are the non-stationary velocities in the channel, and n(x) is obtained from the solution of the Poisson equation at h_o:

$$n(x) = N_D(x) + \frac{\epsilon}{q}\frac{\partial^2 V_{Depletion}}{\partial z^2} . \tag{4.14}$$

Expressions (4.12) and (4.13) are valid for any point in the channel, and they take into account arbitrary doping and mobility dependencies.

4.2.6 The Depletion Layer Voltage

The general two-dimensional form of the Poisson equation[3] is:

$$\frac{\partial^2 V_{Depletion}}{\partial z^2} + \frac{\partial^2 V_{Depletion}}{\partial x^2} = -\frac{q N_D}{\epsilon} . \tag{4.15}$$

When operating in the ohmic and knee regions, E_z exhibits much smaller variations along z compared with E_x variations along x, and the depletion regions are treated by the one-dimensional Poisson equation. Hence the depletion regions in Figures 4.2 and 4.3, as well as the regions 1, 2, 3, and 6 of Figure 4.4 can be described by the one-dimensional Poisson equation:

$$\frac{\partial^2 V}{\partial x^2} = -\frac{q N_D(x)}{\epsilon} . \tag{4.16}$$

By integrating from the surface to any point x within the depletion region, the transverse field is obtained:

$$E_x = -\frac{\partial V}{\partial x} = \frac{q}{\epsilon}\int_0^x N_D(x)\, dx + C \tag{4.17}$$

[3] To be consistent with the outline of the Voltage Balance Method, the voltage notation rather than the electrostatic potential notation is used for the Poisson equation solution. The model derived in this thesis is applicable to a common source MESFET operation, and hence the source electrode is always considered at ground potential.

where the constant C is obtained from the boundary condition that $E_x=0$ at the abrupt depletion/conducting-channel interface $x=h_o$. Equation (4.17) becomes:

$$E_x = -\frac{\partial V}{\partial x} = \frac{q}{\epsilon}\left[\int_0^x N_D(x)\, dx - \int_0^{h_o} N_D(x)\, dx \right] \tag{4.18}$$

Integrating again for the voltage at any point in the depletion region and including the boundary condition that the voltage at the surface is $V_{surface}$, the following expression is obtained:

$$V(x) = \frac{q}{\epsilon}\left[-\int_0^x \int_0^x N_D(x)\, dx\, dx + x \int_0^{h_o} N_D(x)\, dx \right] + V_{surface} \tag{4.19}$$

The depletion layer voltage at the depletion/conducting-channel interface $x=h_o$ is:

$$V_{depletion}(h_o) = \frac{q}{\epsilon}\left[-\int_0^{h_o} \int_0^{h_o} N_D(x)\, dx\, dx + h_o \int_0^{h_o} N_D(x)\, dx \right] + V_{surface} \, . \tag{4.20}$$

In regions 4 and 5 of Figure 4.4, E_z exhibits large variations with z, and hence the two-dimensional Poisson equation must be solved. The general form of Poisson's equation is solved by defining a new voltage function W(z,x) [4.10]:

$$W(z,x) = V(z,x) + \frac{q}{\epsilon} \int_0^x \int_0^x N_d(x)\, dx\, dx \tag{4.21}$$

The general solution of the resulting Laplace equation is:

$$W(z,x) = \left[k_1 e^{kz} + k_2 e^{-kz}\right]\left[k_3 \cos(kx) + k_4 \sin(kx)\right] + k_5\,(z^3 - 3zx^2) +$$

$$+ k_6(x^3 - 3z^2x) + k_7(z^2 - x^2) + k_8 zx + k_9 z + k_{10} x + k_{11} \, . \tag{4.22}$$

The constants k, and k_1 to k_{11} are obtained by satisfying the boundary conditions. The z- and x-directed electric fields can be obtained by taking the derivatives of W(z,x) as a function of z and x respectively:

$$\frac{\partial W(z,x)}{\partial z} = \left[k_1 k e^{kz} - k_2 k e^{-kz}\right]\left[k_3 \cos(kx) + k_4 \sin(kx)\right] +$$

$$k_5(3z^2 - 3x^2) + k_6(x^3 - 6zx) + k_7(2z - x^2) + k_8 x + k_9 \tag{4.23}$$

$$\frac{\partial W(z,x)}{\partial x} = \left[k_1 e^{kz} + k_2 e^{-kz}\right]\left[-k_3 k \sin(kx) + k_4 k \cos(kx)\right] +$$

$$k_5(z^3 - 6zx) + k_6(3x^2 - 3z^2) + k_7(z^2 - 2x) + k_8 z + k_{10} \tag{4.24}$$

Consider first region 4 of Figure 4.4. Let h_o and L_T be length of the segments gh and hj respectively. The boundary conditions are:

(i) along segment gi: $V = V_{surface}$

(ii) along segment gh: $V = V_{surface} + \frac{qx}{\epsilon}\int_0^{h_o} N_D(x)\,dx - \frac{q}{\epsilon}\int_0^x\int_0^x N_D(x)\,dx\,dx$

(iii) along segment hj: $E_x = 0$

(iv) at h: $E_z = E_T$

For convenience of analysis, the axes reference point (0,0) is shifted to the point i. The application of (i) into (4.22) results in:

$$k_3 = k_5 = k_7 = k_9 = 0 \text{ , and } k_{11} = V_{surface} \text{ .}$$

Also, (4.22) satisfies boundary condition (ii) provided that

$$k_6 = 0 \text{ , and, } k_{10} = \frac{q}{\epsilon} \int_0^{h_o} N_D(x)\, dx \ .$$

Since the sin term cannot be zero, the boundary condition can be satisfied provided that the exponential terms are transformed into a hyperbolic expression such that the expression for W(z,x) becomes:

$$W(z,x) = k_{12} \sinh(k(z+L_T)) \sin(kx) + k_8 zx + \frac{qx}{\epsilon} \int_0^{h_o} N_D(x)\, dx + V_{surface} \tag{4.25}$$

where k_{12} is a new constant. Next, the application of boundary condition (iii) into (4.24) and (4.25) leads to:

$$k_8 = 0 \text{ , and, } k = \frac{\pi}{2h_o} \ .$$

The final boundary condition (iv) determines k_{12}:

$$k_{12} = \frac{2E_T h_o}{\pi} \ .$$

Thus, the expression for the depletion voltage at any point within the depletion region is:

$$V(z,x) = \frac{2E_T h_o}{\pi} \sinh\left(\frac{\pi(z+L_T)}{2h_o}\right) \sin\left(\frac{\pi x}{2h_o}\right) +$$

$$+ \frac{qx}{\epsilon} \int_0^{h_o} N_D(x)\, dx - \frac{q}{\epsilon} \int_0^x \int_0^x N_D(x)\, dx\, dx + V_{surface} \ . \tag{4.26}$$

The depletion voltage at $x=h_o$ is:

$$V_{depletion}(z,h_o) = \frac{2E_T h_o}{\pi}\sinh\left(\frac{\pi(z+L_T)}{2h_o}\right) +$$

$$+ \frac{q h_o}{\epsilon}\int_0^{h_o} N_D(x)\,dx - \frac{q}{\epsilon}\int_0^{h_o}\int_0^{h_o} N_D(x)\,dx\,dx + V_{surface} \,. \qquad (4.27)$$

Consider now the boundary conditions in region 5 of Figure 4.4:

(i) segment ij: $V_{(region\ 4)} = V_{(region\ 5)}$

(ii) segment jl: $E_x = 0$

(iii) at i: $E_z = E_x + E_{surface}$

(iv) at j: $E_{z(region\ 4)} = E_{z(region\ 5)}$

where $E_{Surface}$ is the electric field due to exposed surface states. Application of boundary condition (i) into (4.22) leads to:

$$k_3 = k_6 = k_7 = 0 \ , \ k_{11} = V_{surface} \ , \ k_{10} = \frac{q}{\epsilon}\int_0^{h_o} N_D(x)\,dx \ , \ k = \frac{\pi}{2h_o} \text{ , and,}$$

$$(k_1 + k_2)\,k_4 = \frac{2\,E_T\,h_o}{\pi}\sinh\left[\frac{\pi\,L_T}{2\,h_o}\right] \,.$$

The application of the second boundary condition leads to:

$$k_8 = 6k_5 h_o \ ,$$

and the third boundary condition determines k_9:

$$k_9 = E_T \sinh\left[\frac{\pi\,L_T}{2\,h_o}\right] + \frac{q}{\epsilon}\int_0^{h_o} N_D(x)\,dx + E_{surface} \,.$$

The fourth boundary condition determines k_5:

$$k_5 = \frac{E_T \cosh\left[\frac{\pi L_T}{2h_o}\right] - \frac{q}{\epsilon}\int_0^{h_o} N_D(x)\, dx - E_{surface}}{3h_o^2} .$$

Thus, the expression for the depletion voltage at any point within the depletion region is:

$$V(z,x) = \frac{2E_T h_o}{\pi} \sinh\left(\frac{\pi L_T}{2h_o}\right) e^{\left[-\frac{\pi z}{2h_o}\right]} \sin\left(\frac{\pi x}{2h_o}\right) + \frac{qx}{\epsilon}\int_0^{h_o} N_D(x)\, dx - \frac{q}{\epsilon}\int_0^{x}\int_0^{x} N_D(x)\, dx\, dx +$$

$$\left[\frac{E_T \cosh\left[\frac{\pi L_T}{2h_o}\right] - \frac{q}{\epsilon}\int_0^{h_o} N_D(x)\, dx - E_{surface}}{3h_o^2}\right](z^3 - 3zx^2 + 6h_o zx) +$$

$$(E_T \sinh\left[\frac{\pi L_T}{2h_o}\right] + \frac{q}{\epsilon}\int_0^{h_o} N_D(x)\, dx + E_{surface})z + V_{surface} \qquad (4.28)$$

The depletion voltage at $x=h_o$ is:

$$V_{depletion}(z,h_o) = \frac{2E_T h_o}{\pi} \sinh\left(\frac{\pi L_T}{2h_o}\right) e^{\left[-\frac{\pi z}{2h_o}\right]} + \frac{q h_o}{\epsilon}\int_0^{h_o} N_D(x)\, dx - \frac{q}{\epsilon}\int_0^{h_o}\int_0^{h_o} N_D(x)\, dx\, dx +$$

$$\left[\frac{E_T \cosh\left[\frac{\pi L_T}{2h_o}\right] - \frac{q}{\epsilon}\int_0^{h_o} N_D(x)\, dx - E_{surface}}{3h_o^2}\right](z^3 + 3zh_o^2) +$$

$$+ \left(E_T \sinh\left[\frac{\pi L_T}{2h_o}\right] + \frac{q}{\epsilon}\int_0^{h_o} N_D(x)\, dx + E_{surface}\right) z + V_{surface} \tag{4.29}$$

4.2.7 The Surface Voltage

The surface voltage at any point along (z,0) must take into account the boundary conditions at both of the metallized surface-air regions. The voltages at the metallized regions are:

(i) source electrode: $V_{source} = 0$

(ii) gate electrode: $V_{gate} = V_G - V_{bi} + V_{signal}$

(iii) drain electrode: $V_{drain} = V_D$

where V_{bi} is the built-in voltage, V_{signal} is the applied signal voltage. The voltages at the surface-air region arise from two components [4.11, 4.12]:

$$V_{surface} = V_{ss} + V_s. \tag{4.30}$$

The first component, V_{ss}, is contributed by the density of surface states $\rho_{surface}$, which in turn generates a surface field $E_{surface}$. The second component, V_s, is influenced by the voltages at the electrodes and varies linearly with distance from the source and the drain. Consider first the source-gate region. Let L_{ab} be the length of the segment ab in any of Figures 4.2, 4.3, or 4.4. V_s is given as:

$$V_s(z) = \frac{V_{gate}}{L_{ab}} z \ . \tag{4.31}$$

Consider next the gate-drain region. Let L_{eg} be the length of segment eg in Figure 4.2. V_s is given as:

$$V_s(z) = \frac{V_{Drain} - V_{Gate}}{L_{eg}} z + V_{Gate} \ . \tag{4.32}$$

Next let L_{gi} be the length of the segment gi in Figure 4.3. V_s is given as:

$$V_s(z) = \frac{V_{Drain} - V_{Gate}}{L_{gi}} z + V_{Gate} \ . \tag{4.33}$$

In Figure 4.4, let L_{ik} and L_{km} be the length of the segments ik and km respectively. V_s along L_{ik} is obtained from (4.28):

$$V_s(z) = \frac{z^3 \left[E_T \cosh\left[\frac{\pi L_T}{2 h_o}\right] - E_{surface} \right]}{3 h_o^2} + \left(E_T \sinh\left[\frac{\pi L_T}{2 h_o}\right] + E_{surface} \right) z + V_{gate} \tag{4.34}$$

V_s along L_{km} is:

$$V_s(z) = \frac{V_{Drain} - V_k}{L_{km}} z + V_k \tag{4.35}$$

where V_k is obtained by substituting the position of z=k in (4.34).

4.2.8 The n$^+$ Ohmic contacts and Buffer Regions

The metallurgical ohmic resistances, R_{dc}, of the drain and source regions are obtained by the standard treatment given by Fukui [4.13]:

$$R_{dc} = \frac{1}{W}\sqrt{\left[\frac{R_c \rho_1}{a_1}\right]} \tag{4.36}$$

where ρ_1 is the specific resistivity of the contact metal/N-doped-GaAs alloy, a_1 is the thickness of the n^+ channel, and R_c is the contact resistance. Both ρ_1 and R_c are functions of doping:

$$\rho_1 = 0.11\, N_d^{-0.82} \quad \Omega\text{-}cm \tag{4.37}$$

where N_d in (4.37) is valid in the range of 10^{15} to 10^{19} cm^{-3}.

$$R_c = 4\, N_d^{-0.5} \quad (10^{-5}\ \Omega\text{-}cm) \tag{4.38}$$

where N_d in (4.38) is valid in the range of 3×10^{16} to 10^{19} cm^{-3}.

The source metal resistance introduces an ohmic voltage drop:

$$V_{dc} = I_c\, R_{dc} \tag{4.39}$$

which adds to the channel potential at the first section in the flow-chart of Figure 4.7. The drain metal resistance is added to the channel potential of the last MESFET section prior to being compared to the charging drain voltage. The effect of the buffer layer is introduced as a leakage resistance R_p which can be derived from the depth and doping of the layer. After the channel current I_x is determined, the following correction is introduced [4.10]:

$$I_c = I_x + \frac{V_{channel}}{R_p}\ . \tag{4.40}$$

4.3 TLM Interface Parameters

The TLM interface parameters I_c, $\sigma(z,x)$, and $h_o(z,x)$ generated by the GaAs MESFET analysis engine must be adapted for TLM analysis. First, I_c is converted to TLM

energy A, via (3.19):

$$A = \frac{I_c}{2.65 \ x \ 10^{-3} \ W \sqrt{\epsilon_r}} \tag{4.41}$$

Second, σ which is calculated from (4.13) can be calculated at any point z,x in the channel since the velocity profile v(z,x) and the carrier concentration n(x) from (4.14) are known:

$$\sigma_j = \frac{q \ v(z,x) \ n(x)}{E_z} \tag{4.42}$$

Third, $h_o(z,x)$ provides location at time t of the magnetic boundaries of the TLM systems fitting the MESFET channel as illustrated in Figure 3.15.

In linking the GaAs MESFET analysis engine to the TLM analysis, two complications must be considered. First, the node locations in the TLM system can be different from those calculated by the GaAs MESFET analysis engine. In this case, the conductivity of the TLM nodes must be obtained from spatial interpolation of v(z,x) and n(x) and using (4.42). $h_o(z,x)$ must also be rounded off to the nearest TLM length unit. Second, the time step in the TLM system is most often much smaller than that used by the GaAs MESFET analysis engine. In this case, the three interface parameters must also be interpolated in time to generate the required TLM time steps.

There are two methods for linking the MESFET analysis engine to the TLM analysis. One method is to perform the spatial and time interpolation of the TLM interface parameters after the MESFET analysis engine has proceeded one time step. This enables the TLM analysis to catch up with its own smaller time steps. The second method is to operate the TLM analysis as a post processor. After the entire MESFET transient behavior is evaluated by the analysis engine, the TLM interface parameters are converted by interpolation into look-up tables. The TLM analysis can then proceed as shown in Figure 4.12 using the values of the pulse energy, nodes conductivity, and TLM system heights

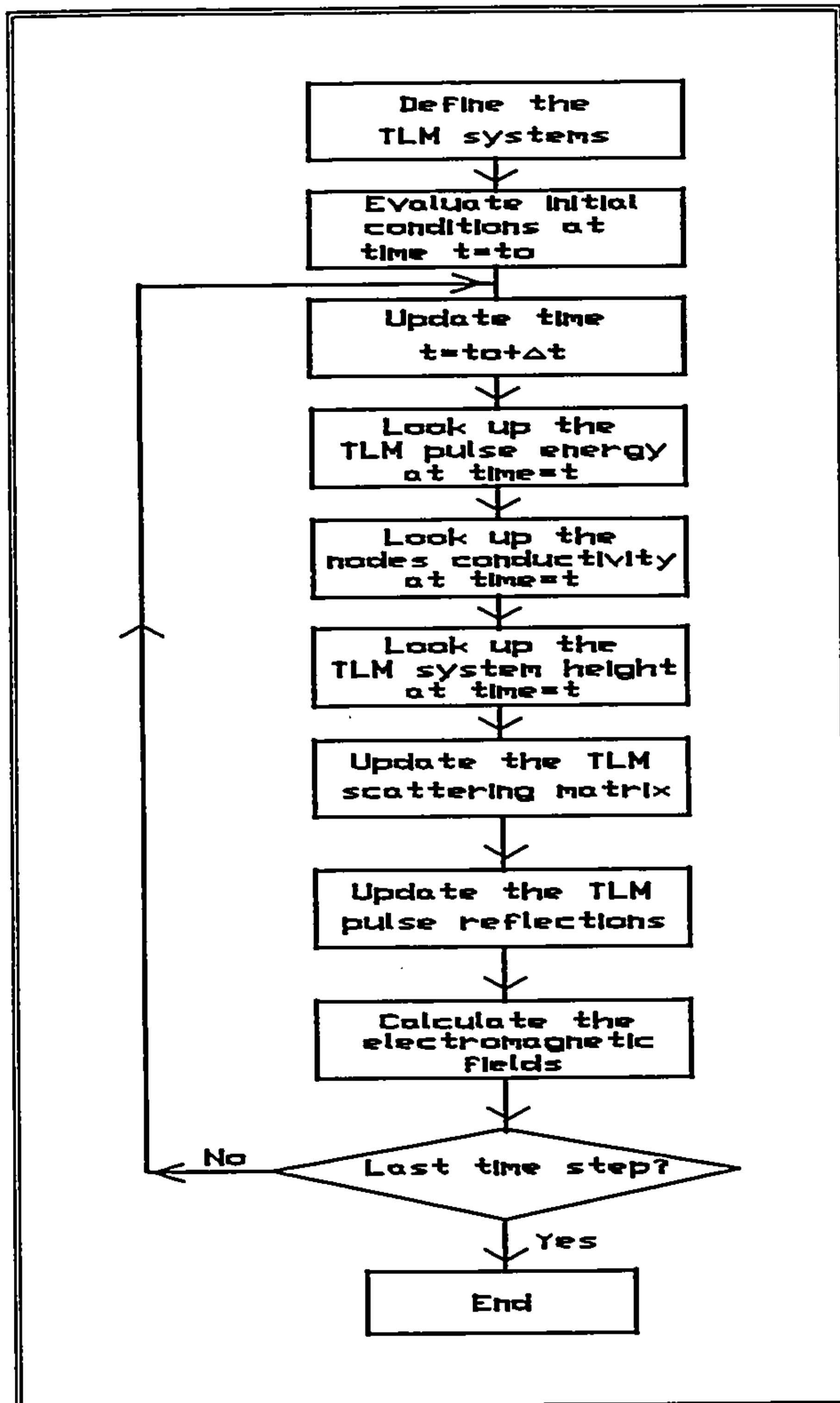

Figure 4.12: Flow chart showing the outline of the TLM analysis.

from the look-up tables at every TLM time step.

4.4 GaAs MESFET Analysis Errors

There are three sources of error incurred by this MESFET analysis approach. They arise from (i) space discretization, (ii) time discretization, and (iii) spatial and time interpolation of the MESFET-to-TLM interface parameters. The space discretization errors manifest themselves during MESFET analysis by obtaining varying minima for the error functions δ_i and δ_c. X-axis discretization causes most of the inaccuracies in the calculation of $h_o(z,x)$, while z-axis discretization causes in most of the inaccuracies in I_c. Time discretization directly impacts the accuracy of the charging voltages and the non-stationary carrier velocities. If the time step is not fine enough, the time variations of the applied signal would not be followed. This would manifest itself in the apparent attenuation of the charging voltages. On the other hand, the velocity profiles would appear too coarse. The spatial interpolation errors of the MESFET-TLM interface parameters arise if the TLM mesh size is coarser than that of the MESFET analysis engine and manifest themselves in the apparent attenuation of the computed electric field and channel current. On the other hand, the time interpolation errors of the MESFET-TLM interface parameters are related to the interpolation functions used to fill in the required TLM time steps. The further apart the time steps in MESFET analysis are, the larger the interpolation errors become.

In a highly non-linear device such as the GaAs MESFET, quantizing the impact of the individual errors is difficult. Characterization of the errors in a device is influenced by a host of parameters, for example, the type of doping, surface states, gate recess, geometry, and operating conditions, as well as by the highly nonlinear interactions of the fields. Error characterization must therefore be undertaken for the particular device under study. However, some guidelines for minimizing the errors can be drawn from practical work with the simulator, as well as considerations of available computer resources such as memory and required speed of analysis. For example, vertical meshing of the high-field region must insure that there are enough nodes in the thin conducting channel region where the opening is typically 10% of the channel thickness. At least 10 to 20

nodes are needed in this region. On the other hand, such a rule of thumb cannot be applied to horizontal meshing. The horizontal mesh must still be dense enough to account for rapid field variations. To obtain a suitable horizontal grid, an initial guess is tried and the electric field profile is examined. If the profile appears to be too coarse, then a denser grid is applied. The process is repeated until no further change of profile is obtained. As to the time step, it cannot be set to be too low since little variations in the MESFET-TLM interface parameters would be obtained due to spatial discretization. If finer time discretization is required, then the spatial meshing must correspondingly become denser. On the other extreme, choosing a coarse time step results in excessive time interpolation errors in the TLM network. Finally, minimizing the spatial interpolation errors caused by the MESFET-TLM interface can be achieved by choosing finer TLM mesh and paying the time penalty. Several TLM mesh grids must be tried by the operator to determine the range of acceptable results.

4.8 References

4.1 N.N. Rao, Elements of Engineering Electromagnetics, Prentice-Hall, Inc. 1977. pp. 357-364.

4.2 R.A. Warriner, "Distribution Function Relaxation Times in GaAs," IEE J. Solid State Electron Devices, Vol. 1, pp. 92-96, 1977.

4.3 C. Kim and E. Yang, "An Analysis of Current Saturation Mechanism of Junction FETs," IEEE Trans. Electron Devices, Vol. 17, No. 2, pp. 120-127 February 1970.

4.4 J.R. Hauser, "Characteristics of Junction FETs With Small Channel to Width Ratios," State Electronics, Vol. 10, pp. 577-587, 1967

4.5 S.F. Dindo, M.M. Ney, and R.G. Harrison, "A New Steady-State Formulation For Current-Voltage Characteristics of GaAs MESFETs Using the Voltage Balance Method," Submitted for publication to the IEEE Trans. Electron Devices.

4.6 S.M.Sze, Physics of Semiconductor Devices, John Wiley & Sons, New York, p. 639, 1981.

4.7 D. Pavilidis, J. Cazaux, and J. Graffeuil, "The Influence of Ion-Implanted Profiles on the Performance of GaAs MESFETs and MMIC Amplifiers," IEEE Trans. Electron Devices, Vol. 36, No. 4, pp. 642-652, April 1988.

4.8 C.M. Snowden and D. Loret, "Two-Dimensional Hot-Electron Model for Short Gate-Length GaAs MESFETs," IEEE Trans. Electron Devices, Vol. 34, No. 2, pp. 212-223, February 1987.

4.9 B. Carnez, A. Cappy, A. Kaszynski, E. Constant, and G. Salmer, "Modeling of a Submicrometer gate FET Including Effects of Non-Stationary Electron Dynamics," J. Appl. Phys. 51(1), January 1980, pp. 784-790.

4.10 C. Chang and D. Day, "Analytic Theory for Current-Voltage Characteristic and Field Distribution of GaAs MESFET's," IEEE Trans. Electron Devices, Vol. 36, No. 2, pp. 269-280, February 1989.

4.11 J. Baek, M. Shur, K. Lee, and T. Vu, "Current-Voltage Characteristics of Ungated GaAs FET's," IEEE Trans. Electron Devices, Vol. 32, No. 11, pp. 2426-2430, Nov. 1985.

4.12 C. Chen and K. Wise, "Transconductance Compression in Sub-micrometer GaAs MESFET's," IEEE Electron Devices Lett., Vol. 4, pp. 341-343, Oct. 1983.

4.13 H. Fukui, "Determination of the Basic Device Parameters of a GaAs MESFET," Bell Systems Technical Journal, Vol. 58, No.3 pp. 771-796, March 1979.

CHAPTER 5

Results

5.1 Introduction

At this stage in this work, we have formulated both the TLM analysis for modelling the conducting channel and the GaAs MESFET analysis engine. We have also defined the interface parameters which link the two systems together. We are therefore at the point where we can run simulations to compute for the first time in TLM the transient electromagnetic response of the GaAs MESFET to input operating DC biases and electric field signals. But prior to conducting these simulations, we must verify the GaAs MESFET analysis engine model, which consists of validating the transient response to applied operating DC biases.

The verification of time domain GaAs MESFET analysis represents a challenge. Present high frequency recording devices, such as, automatic network analyzers and spectrum analyzers only capture the steady state gain and frequency spectrum characteristics in response to applied signal. The typical transient time of a MESFET is in the order of few picoseconds, and no recording device is presently available which is fast enough to sample the channel current with a resolution in the order of femtoseconds. To circumvent this difficulty, prominent workers in this field, for example, Snowden and Loret [5.1], Feng and Hintz [5.2], El-Ghazaly and Itoh [5.3], and Yoganathan and Banerjee [5.4], all adopt two validation criteria of the GaAs MESFET transient response: (1) using experimental results of the electron energy and momentum relaxation time constants, carrier mobility, and diffusion coefficients from Monte Carlo simulations to validate the transient velocity response, and (2) using the solution of Poisson and current continuity equations with the results of the transient electron velocity to validate the channel current at any one given time instant. In this thesis we will follow these same two validation criteria. We will first subject a sample of doped GaAs to two voltage pulses and monitor the time dependent velocity response. The results will be compared with

published results of other investigators. We will then investigate the validity of the new Voltage Balance Method in solving the Poisson and current continuity for the channel current calculations using the carrier velocities at a pre-specified time step. By choosing the velocity-field dependence a long time after the biases are applied, the process essentially becomes an investigation of the voltage balance method to characterize MESFET current-voltage characteristics at steady-state. This is a natural choice since extensive work has been published and verified against experimentally measured devices. Thus, the second process of verification ensures that the solution for the channel current by the consistent application of Poisson's equation, current continuity, and the velocity-field function agree with the published work of other investigators. This will necessitate adopting the fitting parameters which they used to match their models to the measured devices. Following the GaAs MESFET model verification, three simulation examples will be presented. The first example will demonstrate the TLM computation of the electromagnetic fields in a thin GaAs sample when subjected to a voltage step. The second example will demonstrate the computation of the MESFET transient response when subjected to gate and drain voltage steps. In the third example, a sinusoidal electric field will be impressed upon the gate electrode, and the electromagnetic response will be computed. The first example is chosen to demonstrate for the first time the simulation of non-stationary electron dynamics by the TLM method. In the last two examples, the GaAs MESFET analysis engine and the link with the TLM analysis will be also demonstrated.

5.2 Verification of the Time-Dependent Electron Velocity

In the work of Carnez et al. [5.5, 5.6], non-stationary electron dynamics are derived by conducting Monte Carlo calculations and fitting analytical formulations into the results. The analytical formulations were described in equations (4.3) to (4.7). The relaxation effects $\tau_w(w)$ and $\tau_p(w)$, are derived from the dependencies of E_{ss}, v_{ss}, and m^*_{ss} upon the electron energy w. These were also shown in Figures 4.9 to 4.11 for carrier doping concentrations ranging from 1×10^{17} to 3×10^{17} atoms/cm^{-3}. The Monte Carlo experiments of Carnez et al. consisted of subjecting 2/20/2 kV/cm and 2/40/2 kV/cm electric field pulses with 2/2/8 pS durations, respectively into a thin doped GaAs sample, and

monitoring the observed carrier velocity as a function of time. The results are reproduced here in Figures 5.1 and 5.2 respectively. In addition, the transient electron energy response for the 2/20/2 kV/cm pulse is presented and reproduced in Figure 5.3. The selection of the pulses was intended to show the velocity response for various applied steps. For example, the 0/2 kV/cm step subjects the sample to a field E which is below the peak field E_T, and therefore shows the carriers response before velocity saturation; the 2/20 kV/cm and 2/40 kV/cm steps subject the sample to $E>E_T$ and therefore show the velocity overshoot levels which can be attained; and the 20/2 kV/cm and 40/2 kV/cm steps show the velocity relaxation behavior of the carriers from high fields to below E_T. Figures 5.1 and 5.2 show velocity overshoot as the applied field exceeds E_T, and velocity undershoot as the field abruptly dips below E_T. In both cases, their analytical formulations show excellent agreement with the Monte Carlo calculations.

Implementing their results into the MESFET analysis engine begins by discretizing the energy balance equations into a Finite Difference Time Domain (FDTD) scheme:

$$w_i - w_{i-1} = q \cdot \Delta t \left[E_i v_i - E_{ss}(w_i)\, v_{ss}(w_i)\right] \tag{5.1}$$

$$m^*_{ss}(w_i)\, v_i - m^*_{ss}(w_{i-1})\, v_{i-1} = q\, \Delta t \left[E_i - \frac{v_i E_{ss}(w_i)}{v_{ss}(w_i)}\right] \tag{5.2}$$

where the dependencies of $E_{ss}(w)$, and $m^*_{ss}(w)$ are provided by fitting the graphical results of Figures 4.9 to 4.11 with polynomial equations. The following set of polynomial equations are used to fit $E_{ss}(w)$ at 1×10^{17} atoms/cm^{-3} doping level, and both are compared in Figure 5.4:

$E_{ss}(w) = -14.85 + 364.01w$ $\qquad 0.04 \le w \le 0.045$

$E_{ss}(w) = 0.46 + 35.44w - 59.50w^2$ $\qquad 0.045 \le w \le 0.2$

$E_{ss}(w) = 38.99 - 618.36w + 4094.74w^2 - 11919.10w^3 + 13431.20w^4$ $\qquad 0.2 < w \le 0.38$

$E_{ss}(w) = -112.79 + 354.65w$ $\qquad w > 0.38$

The following set of polynomial equations is used to fit $m^*_{ss}(E_{ss}(w))$ at the same doping

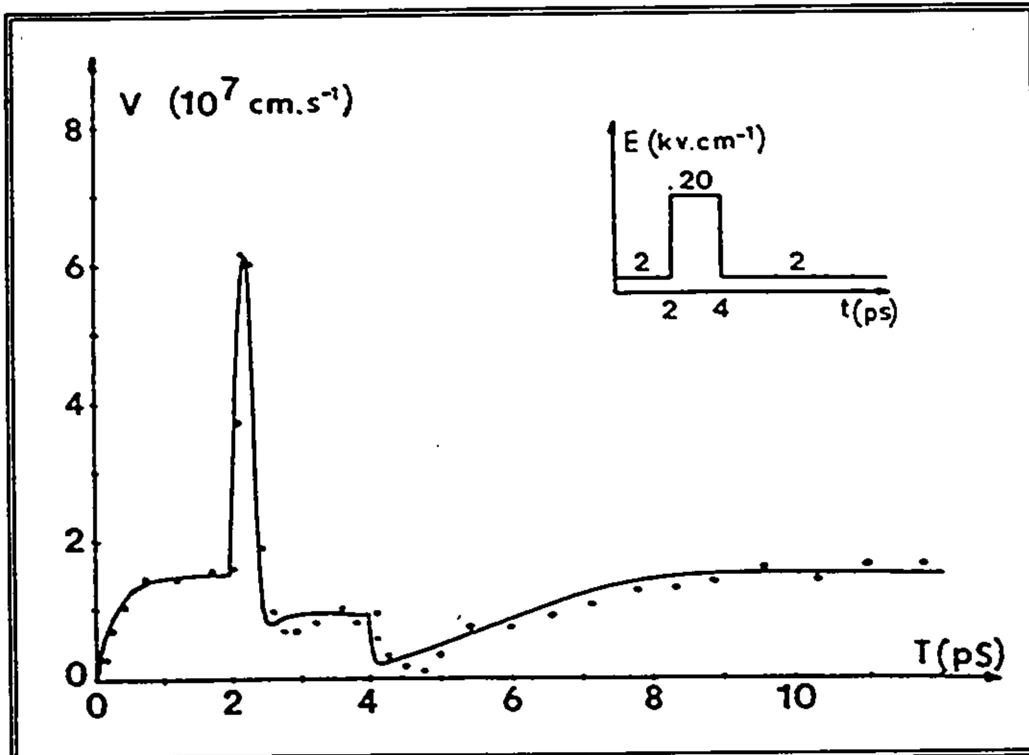

Figure 5.1: Drift velocity versus time when applying an electric field pulse. Solid line: analytical formulation [5.5, 5.6]; solid dots: Monte Carlo calculations [5.5, 5.6].

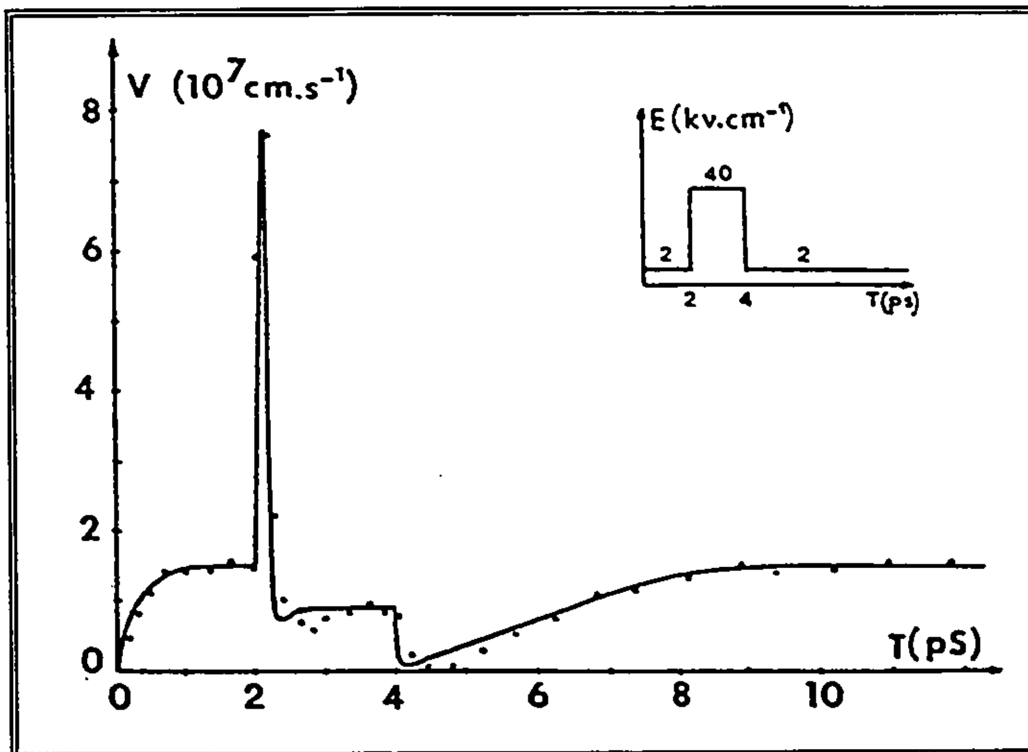

Figure 5.2: Drift velocity versus time when applying an electric field pulse. Solid line: analytical formulation [5.5, 5.6]; solid dots: Monte Carlo calculations [5.5, 5.6].

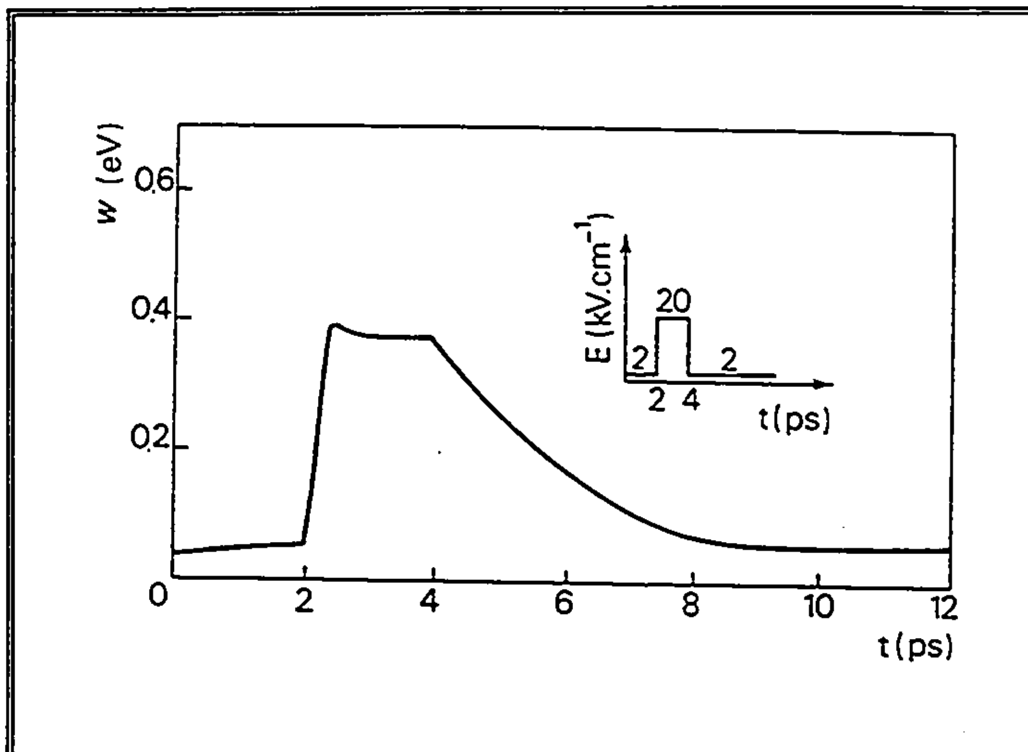

Figure 5.3: Electron energy versus time when applying an electric field pulse. From Carnez et al. [5.5,5.6].

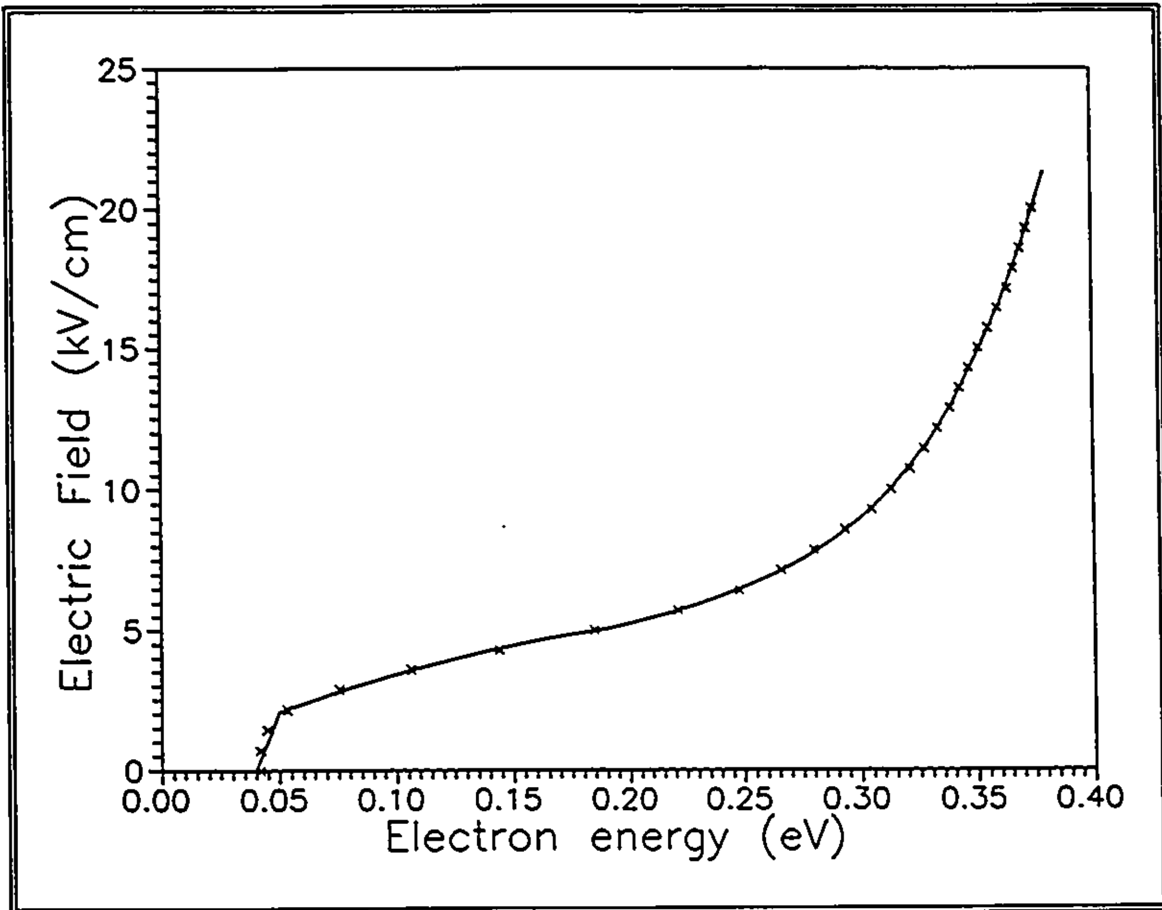

Figure 5.4: Steady-state electric field versus electron energy. Solid line: fitted polynomial response, x symbols: Monte Carlo results from Carnez et al. [5.5,5.6].

level, and both are compared in Figure 5.5:

$m^*_{ss}(E_{ss}(w)) = 0.063 \qquad E_{ss}(w) \leq 2$

$m^*_{ss}(E_{ss}(w)) = 0.070 - 0.0082\, E_{ss}(w) + 0.0025\, E_{ss}^2(w) \qquad 2 < E_{ss}(w) \leq 6$

$m^*_{ss}(E_{ss}(w)) = -0.018 + 0.029\, E_{ss}(w) - 0.0012\, E_{ss}^2(w) \qquad 6 < E_{ss}(w) \leq 10$

$m^*_{ss}(E_{ss}(w)) = 0.10 + 0.0050\, E_{ss}(w) \qquad E_{ss}(w) > 10$

In these equations, the units for the electric field and the electron energy are kV/cm and eV respectively. The effective electron mass is normalized to the mass at the thermal equilibrium energy w_o. The steady-state electron drift velocity $v_{ss}(w)$, can be deduced from Figures 5.1 and 5.2. For example, Carnez et al. used saturation velocity $v_s \approx 1 \times 10^7$ cm/sec, low field mobility $\mu \approx 7500$ cm^2/V-Sec, and a peak field $E_T = 32.50$ kV/cm; the v_{ss} versus E_{ss} relationship is displayed in Figure 5.6. Using the same sample of GaAs with 1×10^{17} atoms/cm^{-3}, a time step $\Delta t=0.01$pSec, 1200 iterations, equations (5.1) and (5.2) are solved for the transient drift velocity and electron energy. The response of the drift velocity, shown in Figure 5.7 for the two electric field pulses, exhibits excellent agreement with Carnez et al. results in Figures 5.1 and 5.2. Aspects such as peak velocity overshoot and its duration, undershoot characteristics, low field response, and the steady state behavior are all reproduced. The response of the electron energy, shown in Figure 5.8, also exhibits excellent agreement with Figure 5.3. The agreement with the Monte Carlo results of Carnez et al. shows that the adoption of their energy balance equations and the fittings to the energy and momentum relaxation functions in this work verifies the time-dependent carrier velocity behavior.

5.3 Verification of the New Voltage Balance Method

In this section the capability of the new Voltage Balance Method [5.7] to characterize GaAs MESFET current-voltage characteristics at steady-state will be validated by choosing the velocity-field dependence a long time after the biases are applied, and verifying the results against published work of other investigators. This necessitates adopting the input data parameters used by these workers to fit their models to their measured devices. For a given velocity-field dependence, the current-voltage characteristics can be completely and uniquely determined by specifying the following

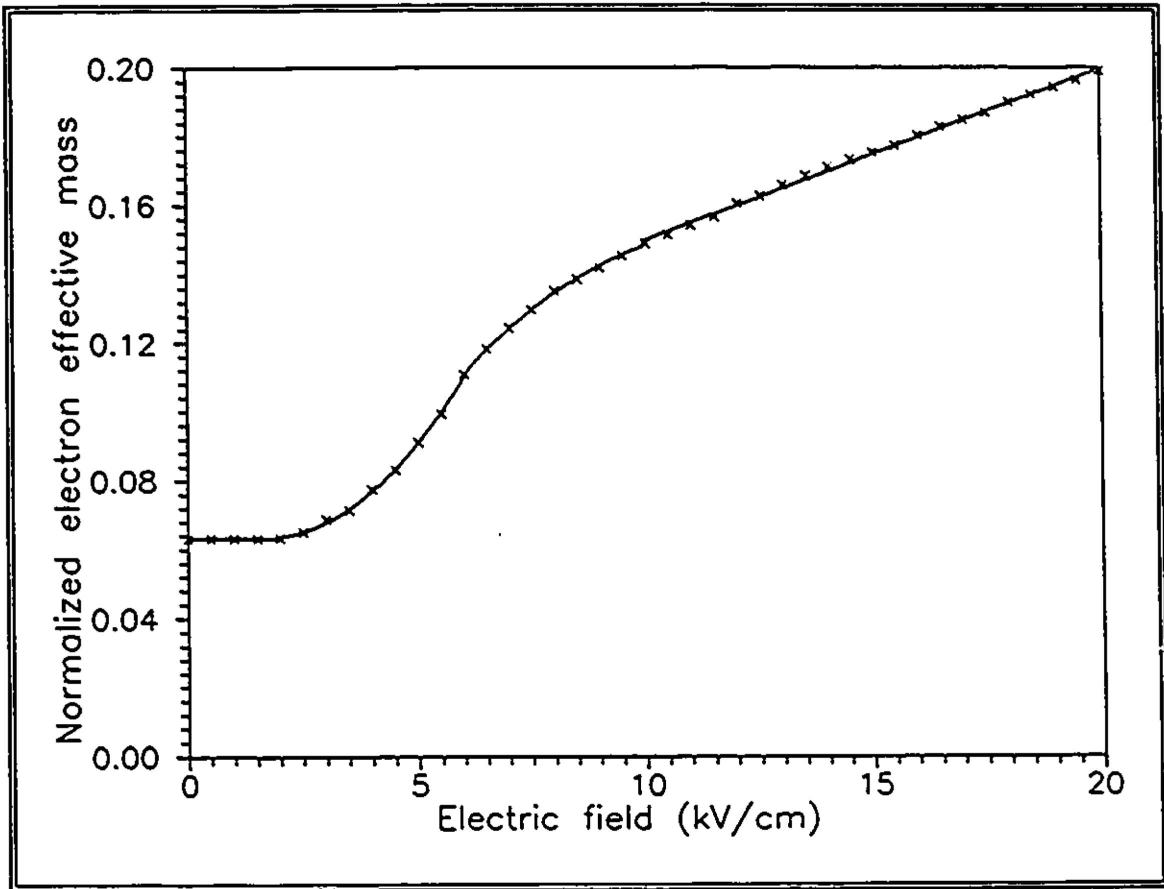

Figure 5.5: Steady-state normalized electron effective mass versus electric field. Solid line: fitted polynomial response, x symbols: Monte Carlo results from Carnez et al. [5.5,5.6].

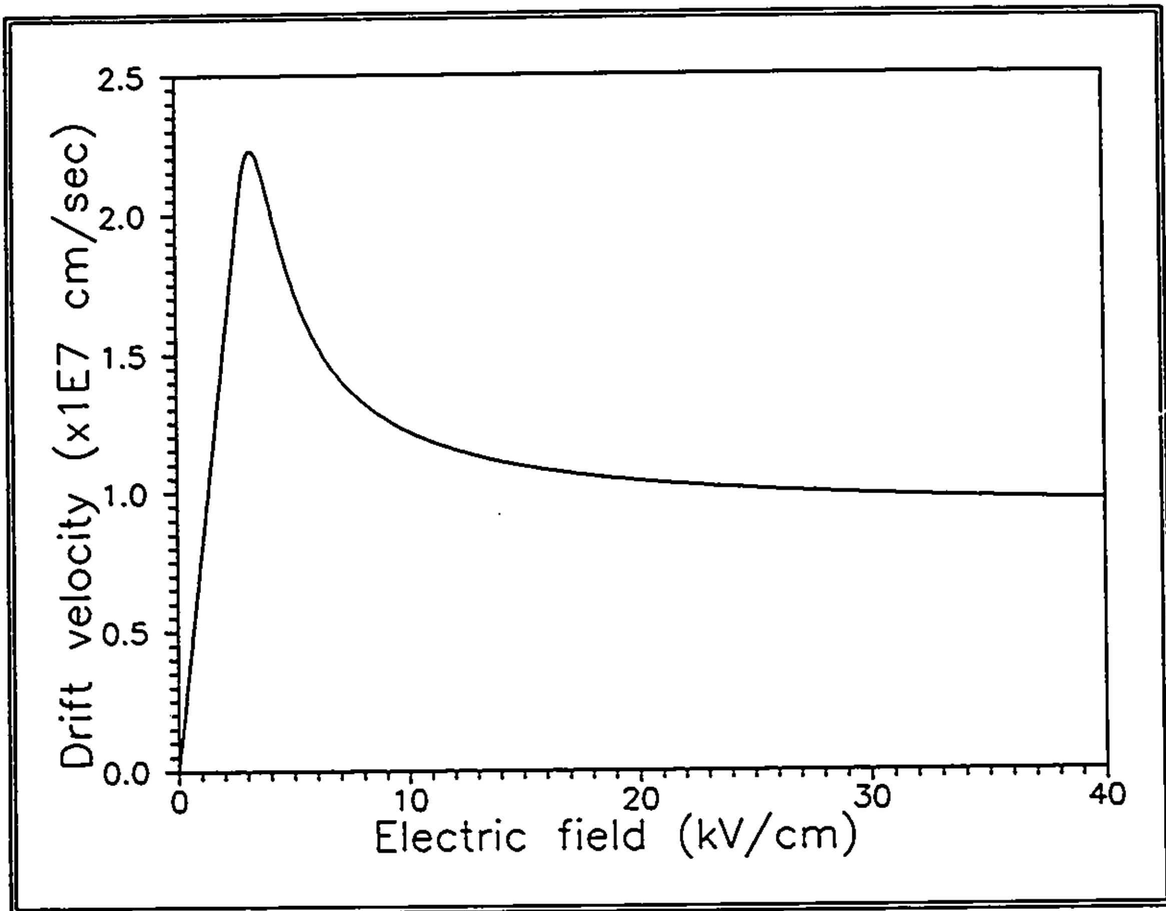

Figure 5.6: Steady-state drift velocity versus electric field.

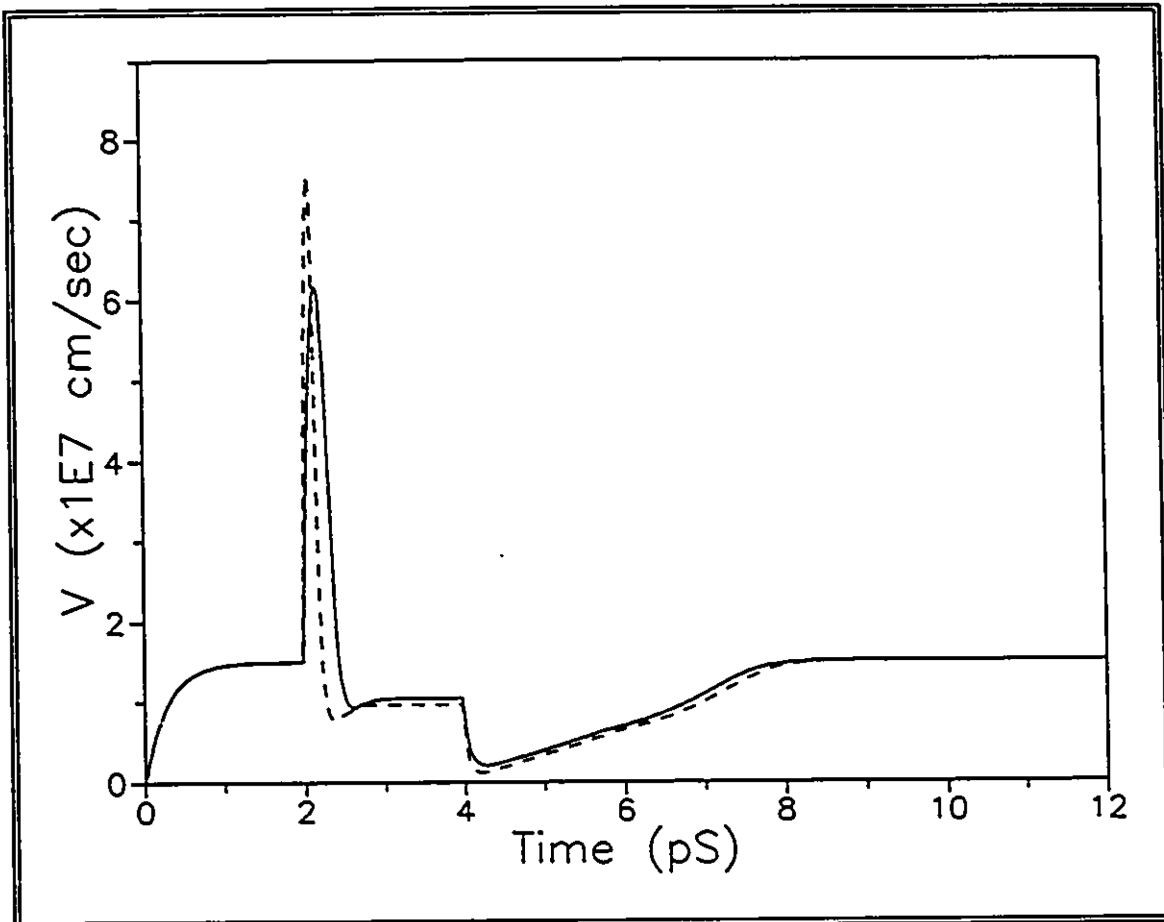

Figure 5.7: Transient drift velocity response. Solid line: response to 2/20/2 kV/cm electric field pulse with 2/2/8 pS time duration; dashed line: response to 2/40/2 kV/cm electric field pulse with 2/2/8 pS time duration.

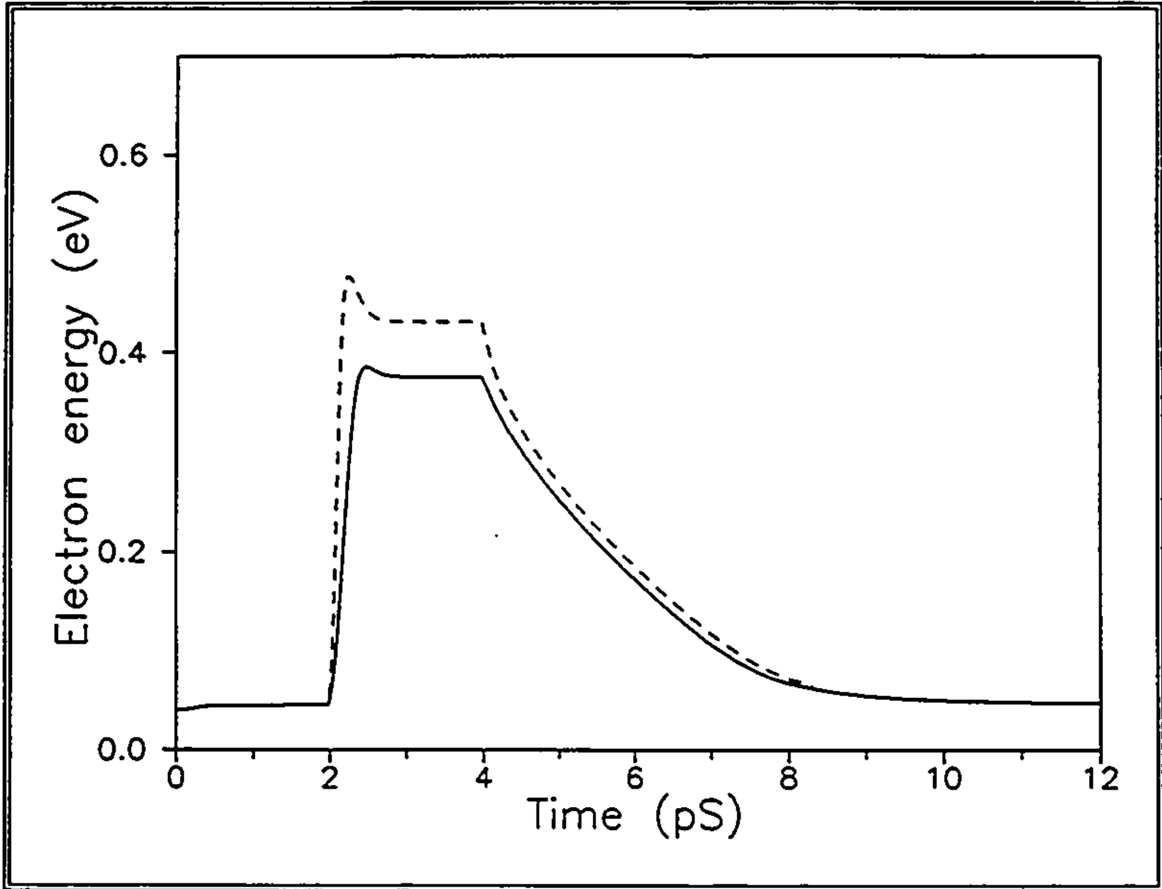

Figure 5.8: Transient electron energy response. Solid line: response to 2/20/2 kV/cm electric field pulse with 2/2/8 pS time duration; dashed line: response to 2/40/2 kV/cm electric field pulse with 2/2/8 pS time duration.

input data parameters: (1) doping, (2) mobility, (3) saturation velocity, (4) peak electric field, (5) surface field, (6) built-in voltage, (7) channel thickness, (8) recess dimensions, (9) gate length, (10) gate width, (11) source-gate spacing, (12) drain-source spacing, (13) ohmic contact resistances, and (14) buffer layer resistance. When all these input parameters are adopted into two solving methods, differences in results can then be attributed to the modelling methods and assumptions. On the other hand, such a comparison may not be valid if any of the input parameters are omitted or approximated. Of the published literature on GaAs MESFET work which show comparison between the fit of models to experimentally measured devices, almost none report the full input data parameters listed above. Reproducing such work becomes difficult.

One exception is the work of Chang and Day [5.8], which derives a closed-form solution to a quasi two-dimensional GaAs MESFET model. They compared their model with experimental data of two measured MESFET current-voltage characteristics, and they provided the complete sets of input data parameters for each transistor. These are shown in Table 5.1. The first device, labeled as MESFET #1, was reported previously by Pucel et al. [5.9]. Its gate length is one micron, and its width is 500μm. The conducting channel is epitaxial of 6.5x10^{16} atoms/cm^{-3} doping and 3400Å in thickness. It is formed on an unintentionally doped buffer layer, which presents a shunt resistance of 2000Ω to the channel. The ohmic contacts are formed by a gold-germanium alloy, while the Schottky contact is formed by an aluminum metal which introduces a barrier of 0.75V. The second device, labeled in Table 5.1 as MESFET #2, was reported previously by Morkoç et al. [5.10]. Its gate length is 0.7μm, and its width is 150μm. The conducting channel is epitaxial with 2.2x10^{17} atoms/cm^{-3} doping and 1200Å in thickness. It is formed on a lightly-doped buffer layer which presents a shunt resistance of 1000Ω to the channel. The ohmic contacts are formed by a gold-germanium alloy, while the Schottky contact is formed with layered titanium-tungsten-gold metals which introduce a barrier of 0.89V. No data on gate recess depth is reported. The two devices contrast with respect to the application. The first is intended for medium power applications since the doping is relatively light, the channel is thick, and the gate is relatively wide in order to deliver the required RF power. The second device is intended for low noise and low power applications since the doping

Data Parameter	MESFET #1	MESFET #2
Doping N_D, [cm^{-3}]	6.5×10^{16}	2.2×10^{17}
Mobility μ, [cm^2/V.S]	4600	3800
$N_D(x)$ and $\mu(x)$ Profiles	Uniform	Uniform
Saturation Velocity v_s, [cm/sec]	7×10^6	7×10^6
Peak Field E_T, [kV/cm]	3.6	4.6
Surface States $E_{surface}$, [kV/cm]	0	0
Built-in Voltage V_{bi}, [V]	0.75	0.89
Channel Thickness a, [Å]	3400	1200
Gate Length L_G, [μm]	1.0	0.7
Gate Width W, [μm]	500	250
Source-Gate Spacing L_{SG}, [μm]	4.8	1.8
Gate-Drain Spacing L_{DG}, [μm]	4.8	1.8
Extracted contact Resistance R_c, [Ω]	0.56	0.17
Buffer Layer Resistance R_p, [Ω]	1000	2000

Table 5.1: Input data parameters of two GaAs MESFETs.

is relatively high and the channel thickness is thin.

Chang and Day's model adopts the same set of assumptions as those described in Section 4.2. Compared to the MESFET analysis effects described in Section 4.2, they use an analytical closed-form solution of the two-dimensional Poisson equation, and follow the same treatment for the buffer layer. In their model, they use a continuous steady-state velocity field relationship which includes velocity overshoot with the following expressions:

$$v = \mu E , \qquad E \le E_L \tag{5.3a}$$

$$v = \frac{\mu E}{\sqrt{1 + \left(\frac{E - E_L}{E_c} \right)^2}} , \qquad E \ge E_L \tag{5.3b}$$

where E_L represents the maximum field value above which the velocity-field relationship is no longer linear, and E_c relates the carrier mobility and the drift velocity at saturation such that:

$$E_c = \frac{v_s}{\mu} . \tag{5.4}$$

The maximum velocity attained in (5.3b) occurs at the peak field, E_T. It follows that by specifying μ, E_T, and v_s, the entire velocity-field curve can be fully defined using (5.3a) and (5.3b). These three parameters are particular to the manufacturing process and the epitaxial layer. In their work, Morkoç et al. [5.10] and Pucel et al. [5.9] measured and reported the low field mobility, but did not report on the recess depth and surface fields of both devices. Chang and Day therefore assumed them to be zero, and instead chose suitable E_T and v_s to best fit the reported I-V characteristics. The velocity-field characteristics of the two devices are shown in Figure 5.9, and are used in the Voltage

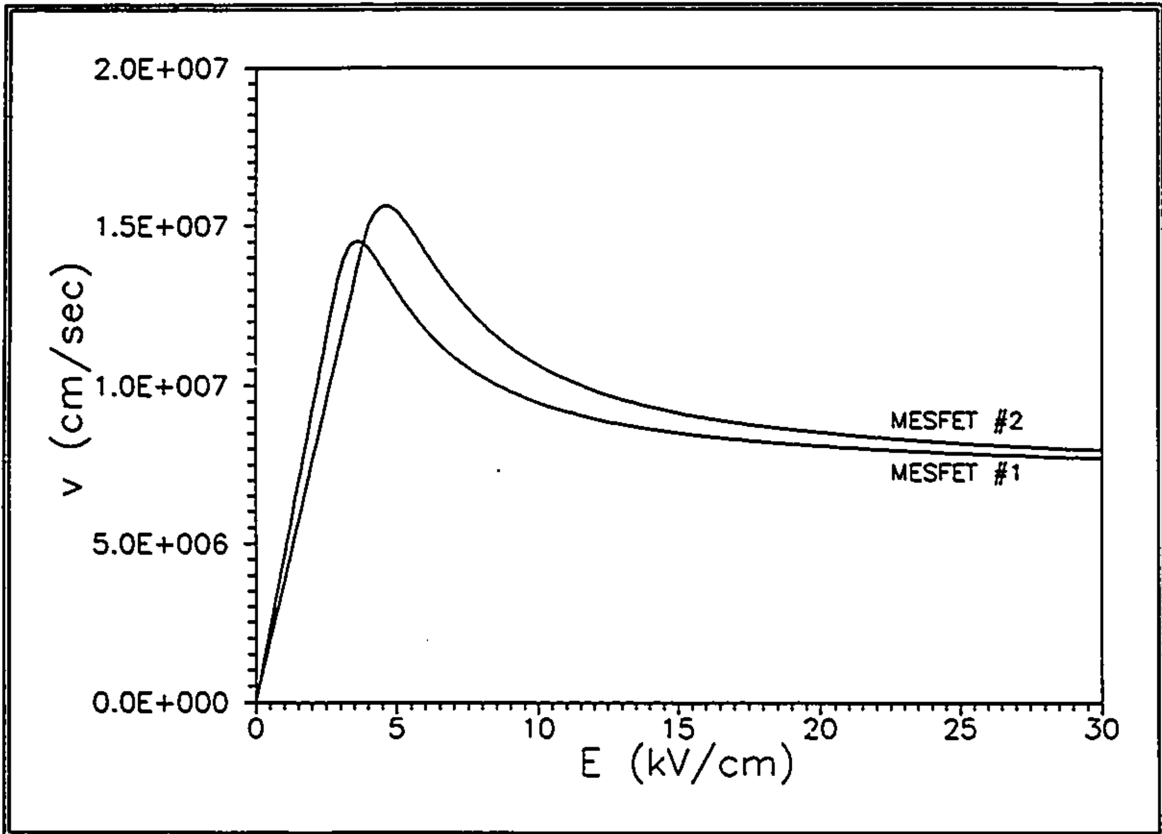

Figure 5.9: Velocity-field relationships for MESFET #1 and MESFET #2.

Balance Method for the comparison.

Chang and Day's method, however, departs from this work in the crucial treatment of the ohmic and fringe regions. Unlike the more complete treatment in this work, they approximated the ohmic regions as two distinct sections. The first section contains the metallization contact resistance R_{dc} and an inactive and completely undepleted region which extends part of the distance from the ohmic metal edge to the gate. The second section contains the gate fringe region which they approximate as a square region whose length is proportional to the depleted height at the gate source edge. The proportionality factor is provided by an adjustable fitting factor, s, which they used to improve the model fit. Their ohmic region model exhibits (i) equal source and drain ohmic resistances, (ii) highest error at the drain ohmic region, and (iii) increased ohmic-contact-to-gate spacings to reflect undepleted ohmic regions. Hence the adjustable factor is crucial in order to obtain the best fit to the current-voltage characteristics. This type of ohmic region modelling is inexact, but it allows their analysis to be given in a set of closed form equations. To apply their results to this analysis, the metallization contact resistance R_{dc} is extracted from the physical-ohmic-contact-to-gate spacings and the stated ohmic resistances and are shown in Table 5.1.

The current-voltage characteristics of MESFET #1 computed by the Voltage Balance Method is shown in Figure 5.10 where they are compared with those calculated in [5.8] and the experimental data from [5.9]. The calculated curves in this work show good agreement with the method of Chang and Day. It also unintentionally exhibits a somewhat better fit to the experimental data. The discretization used for the MESFET active layer in our calculation is $\Delta x=10Å$ and $\Delta z=100Å$. Chang and Day also reported on the electric fields, free carrier concentration, and drift velocity profiles at $V_D=15V$ and $V_G=-2V$. Figure 5.11 shows good agreement in the computation of E_z in the channel between this work and [5.8]. In the Figure, the origin of the z-axis is taken to be at the gate metal edge at the drain side. Figure 5.12 shows the comparison between E_z and E_x in the surface region. Again, the fields demonstrate excellent agreement. Figure 5.13 shows the comparison of the electron concentration in the channel. It exhibits accumulation underneath the gate and partial depletion at some distance into the drain. Good

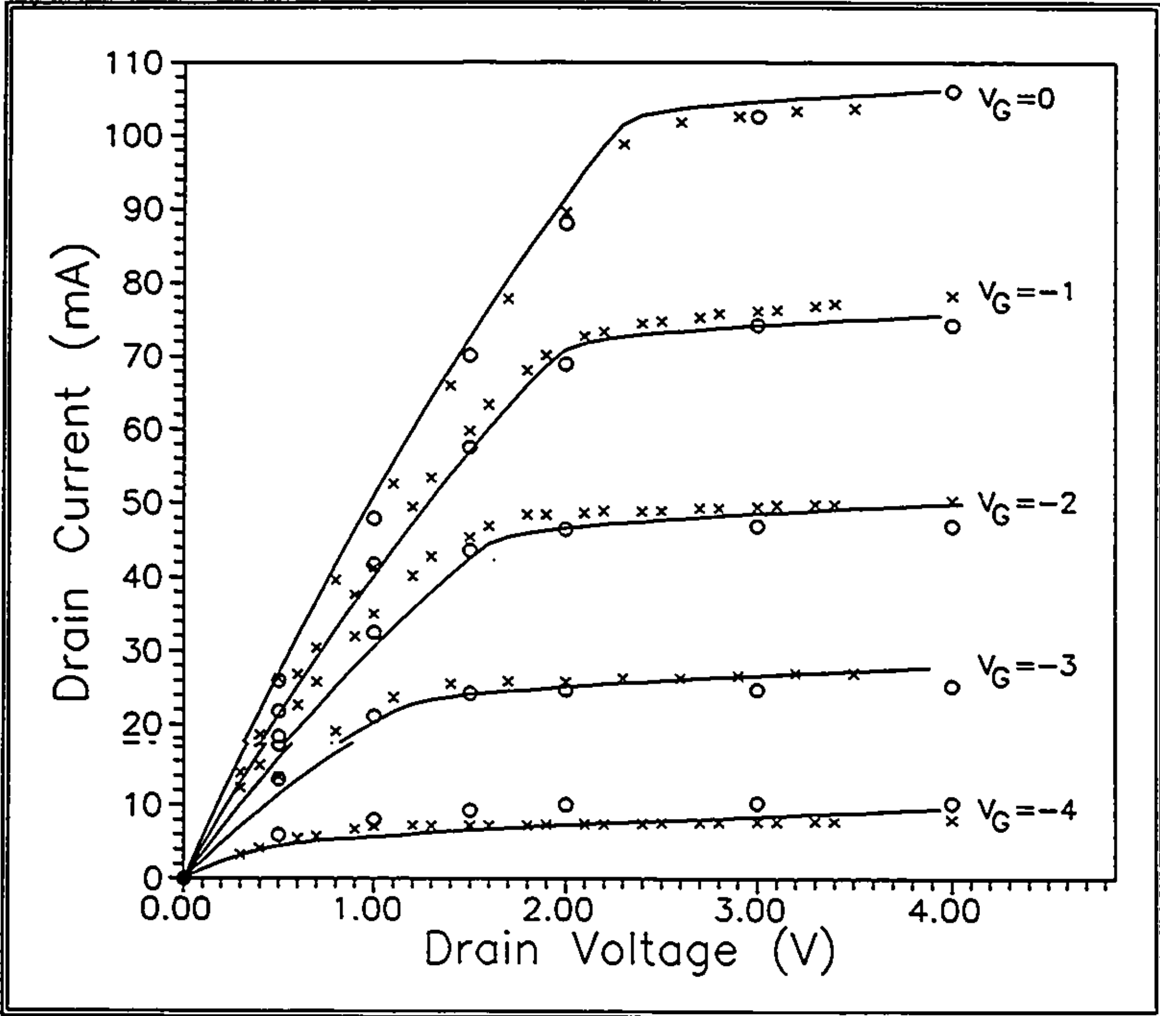

Figure 5.10: Current-voltage characteristics of MESFET #1. Solid lines: this work, x symbols: Chang and Day [5.8], and o symbols: measured data [5.9].

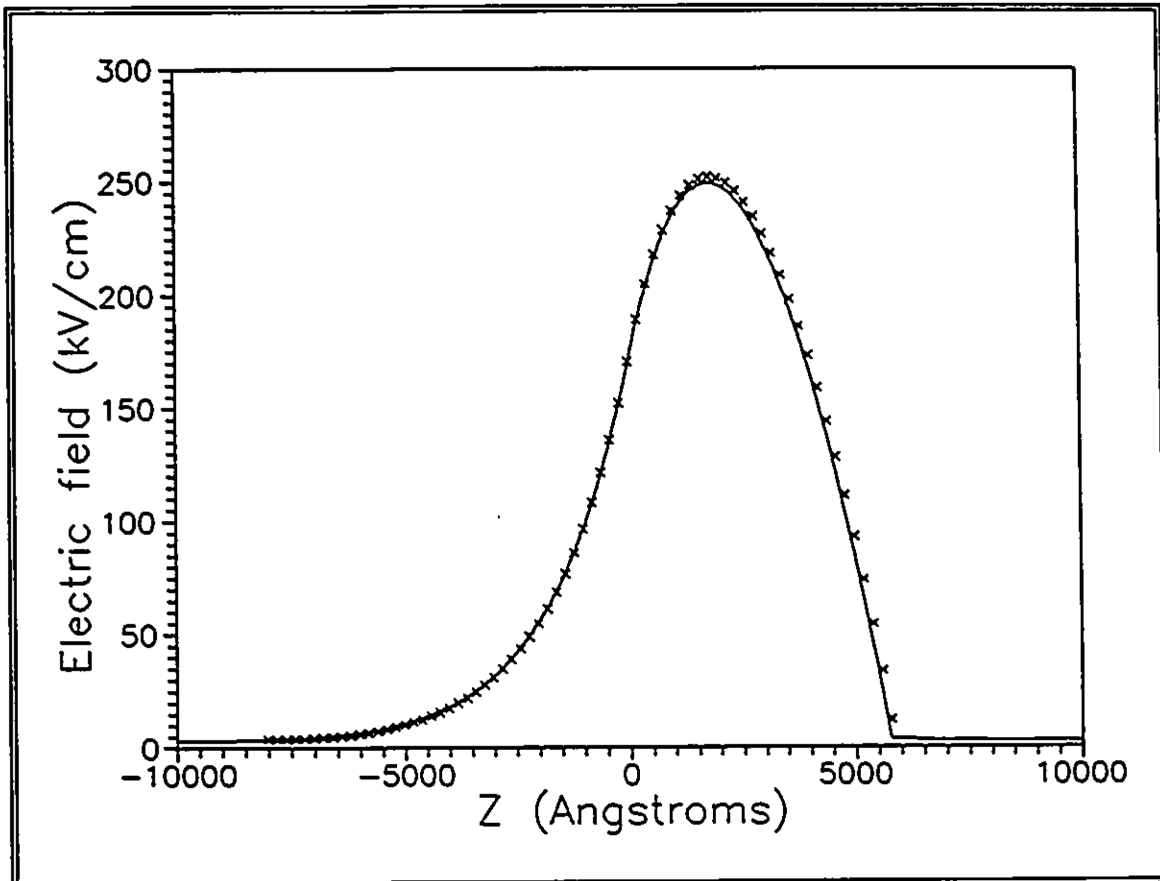

Figure 5.11: Electric field E_z in the channel. Solid line: this work, x symbols: Chang and Day [5.8].

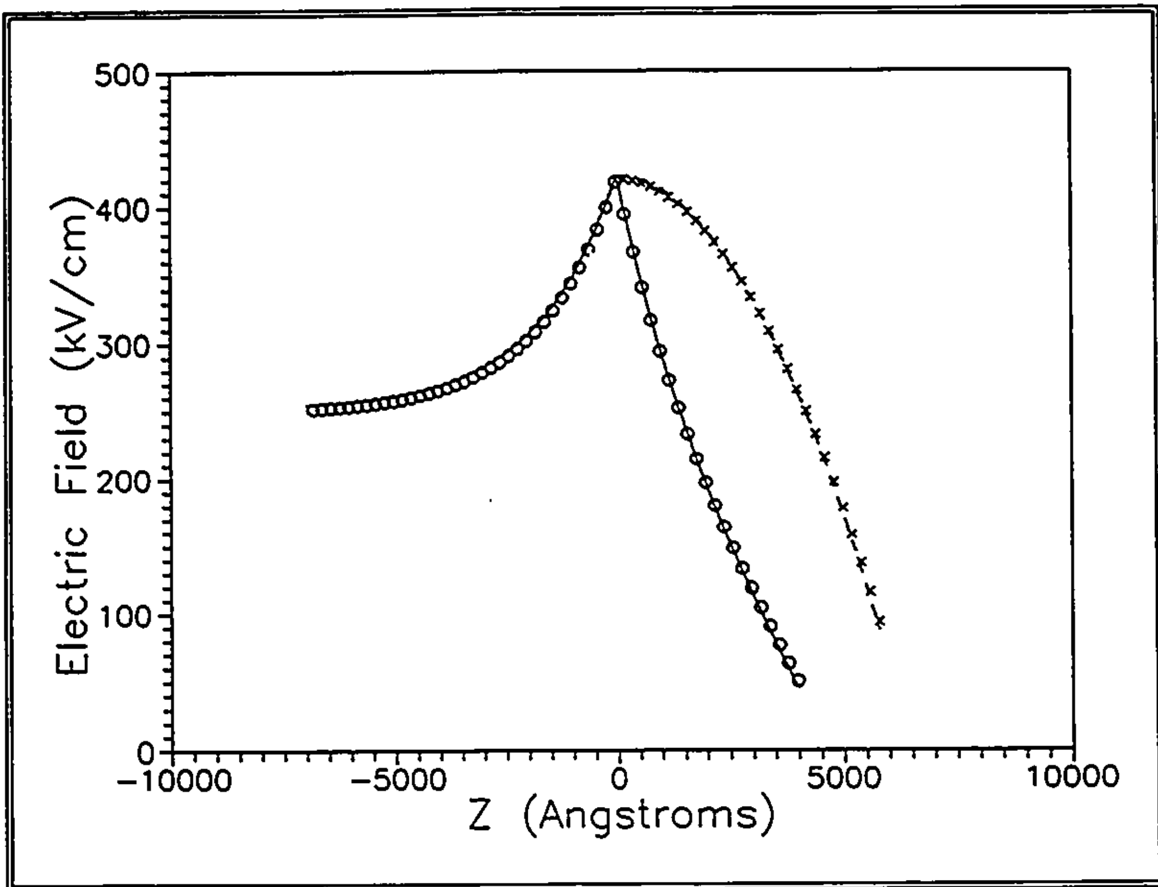

Figure 5.12: Electric fields in the surface region. Dashed, solid lines: E_x, E_z in this work; x,o symbols: E_x, E_z by Chang and Day [5.8].

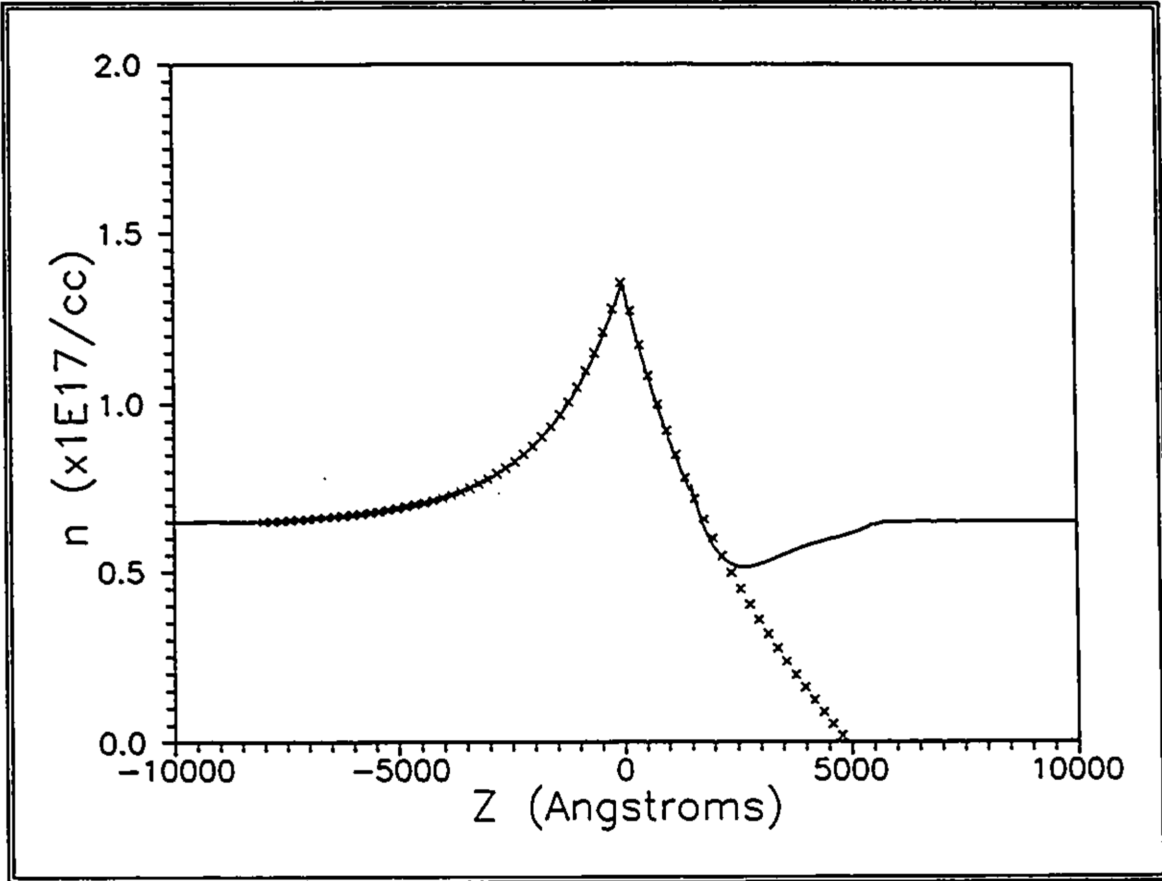

Figure 5.13: Electron concentration in the channel. Solid line: this work, x symbols: Chang and Day [5.8].

agreement is demonstrated until the tail of the gate-drain high field region is reached where in [5.8] the electron concentration continues to decrease, whereas in the Voltage Balance Method the electron concentration returns to the doping levels of the channel in the low field region. The behavior of the electron carrier concentration according to [5.8] is incorrect in the tail end of the high field region since an analytical expression is used which is not valid outside that region. On the other hand, the Voltage Balance Method properly accounts for the carrier concentration using (4.14) and the behavior of the electric field in the channel shown in Figure 5.11. Finally, Figure 5.14 shows the comparison between the carrier velocity in the high field regions. The double velocity peaks are demonstrated in both methods since the peak field is approached twice.

The current-voltage characteristics of MESFET #2 computed in this work, compared with those calculated in [5.8] and the experimental data from [5.10], are shown in Figure 5.15. The discretization used for the MESFET active layer in our calculation is $\Delta x=4Å$ and $\Delta z=20Å$. The calculated curves in this work show fairly close agreement with the method of Chang and Day. Their method also exhibits fair agreement with the experimental data. The difference between the two theoretical methods in this case is attributed to larger discrepancies in the ohmic region modelling which was compounded by their use of larger adjustable fit factors for this region. The difference between their theoretical method and the measured device is attributed to the limitations in using E_T and v_s as fitting factors to compensate for the unknown recess depth and surface fields.

The comparisons of the current-voltage characteristics and the high field region parameters of the two devices has demonstrated that the Voltage Balance Method is capable of simulating MESFETs given a carrier velocity dependence at a time t long after the biases are applied. When combined with the non-stationary velocity analysis demonstrated in the previous section, we have in effect validated and obtained a method which is capable of simulating non-stationary time domain GaAs MESFET behavior. Next, the methods developed in this thesis will be demonstrated with three examples.

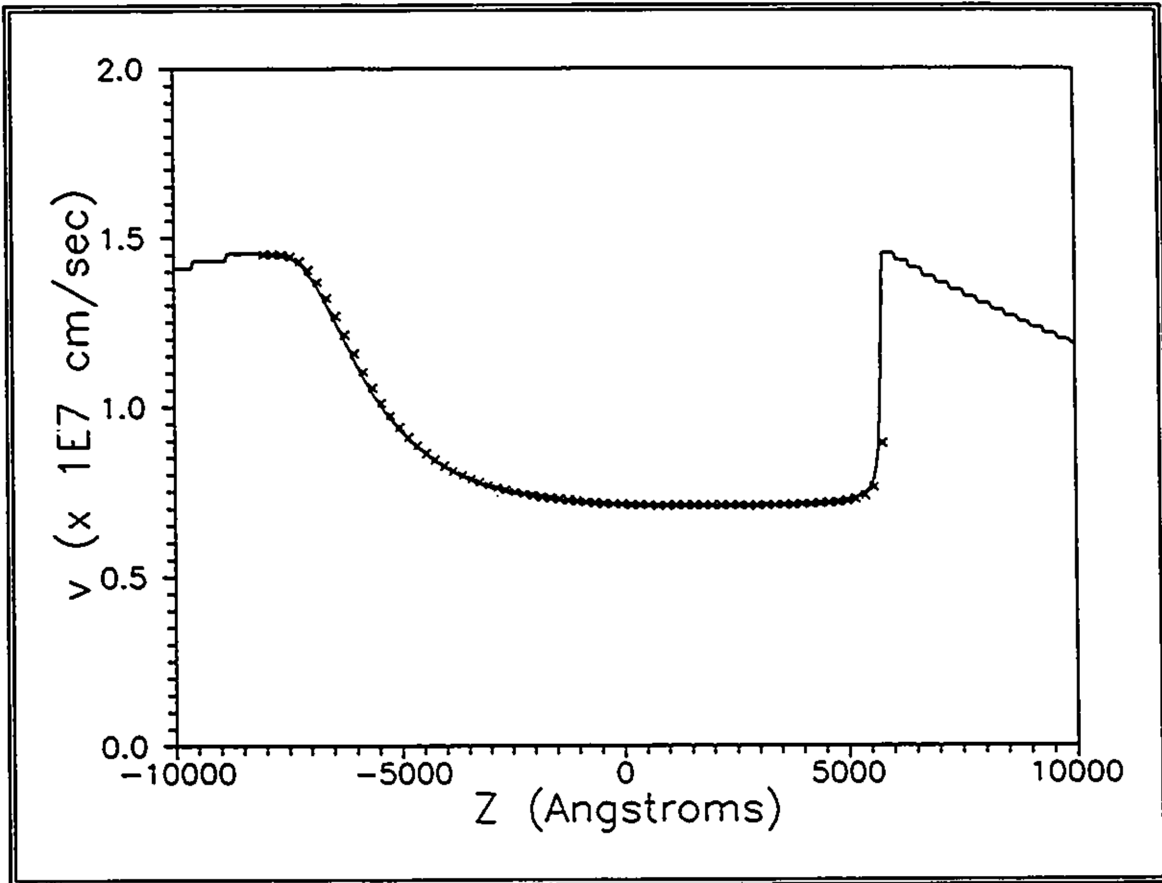

Figure 5.14: Electron velocity in the channel. Solid line: this work, x symbols: Chang and Day [5.8].

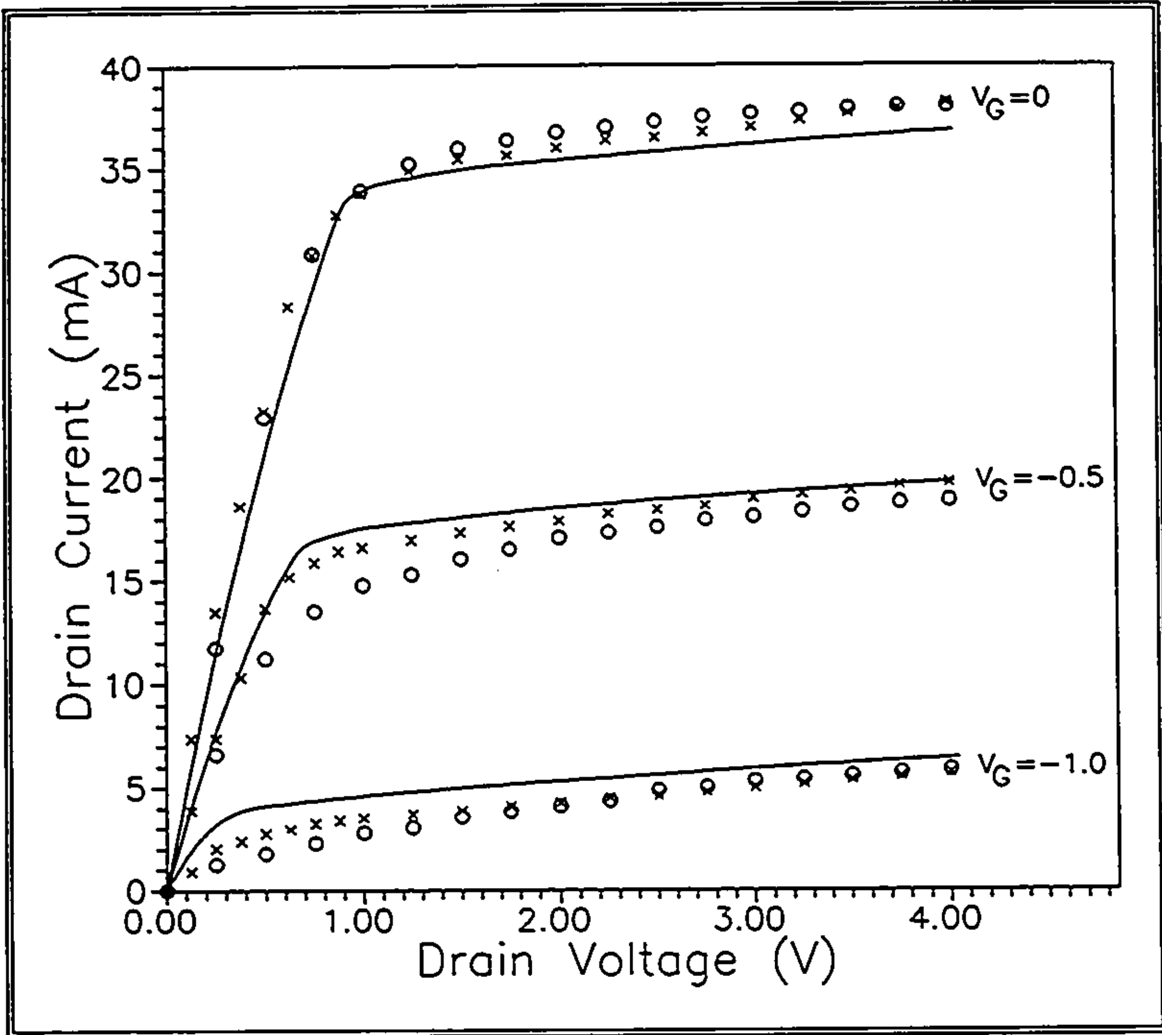

Figure 5.15: Current-voltage characteristics of MESFET #2. Solid lines: this work, x symbols: Chang and Day [5.8], and o symbols: measured data [5.10].

5.4 Example #1: Response of a Thin GaAs Sample to a Voltage Step

This example is intended to demonstrate the TLM simulation of non-stationary and time-dependent velocity [5.11, 5.12]. The GaAs sample shown in Figure 5.16a is subjected to a fast voltage pulse. The length, height, and width of the sample are 100Å, 500Å, and 250μm respectively. The doping and voltage parameters used are chosen to match those of Figure 5.1: the doping used is 1x10^{17} cm^{-3}, low field mobility μ=7500 [cm^2/V-Sec], conductivity σ= 12000 [1/Ω-m]. The overall low-field resistance becomes 0.067 Ω. To subject the sample to the same 2/20/2 kV/cm electric field pulse, the applied voltage must be a 0.002/0.02/0.002 V pulse with the same time durations. Also, the voltage polarity must be as shown in Figure 5.16 to maintain the sense of the applied electric field.

The discretization of the physical GaAs sample of Figure 5.16a and adapting it into a TLM system imposes several requirements: (i) the step size $\Delta\ell$, must be equal or smaller than Debye's length L_d. For convenience, the step size is chosen to be the same as the sample's length $\Delta\ell$= 100Å, and it is noted in Figure 2.6 that this is well below L_d≈135Å. Hence the errors associated with the TLM coarseness, conductivity and dispersion are negligible; (ii) the structure must be mirrored at the point where the voltage is connected as shown in Figure 5.16b. The addition of the mirrored structure is required in order to conform to the boundary conditions of the TLM method discussed in Chapter 3. Its existence does not require the scaling of the voltages and fields, and hence the results for lower half can be ignored after the completion of TLM analysis. The sample is filled with 10 nodes located at the following co-ordinates: (50Å,450Å), (50Å,350Å), (50Å,250Å), (50Å,150Å), (50Å,50Å), (50Å,-50Å), (50Å,-150Å), (50Å,-250Å), (50Å,-350Å), and (50Å,-450Å); and (iii) the polarity of the applied voltage results in the steady-state field orientations shown in Figure 5.16b: E_z is positive and constant across the sample, and H_y is positive and rises linearly from zero at the upper edge of the sample (x=5$\Delta\ell$) to maximum at the center where the voltage is applied (x=0).

The TLM system computes the electric and magnetic fields in the GaAs sample and at the same time accounts for the non-stationary electron velocity by controlling both the injection energy and the losses of the individual nodes at every time step. These two

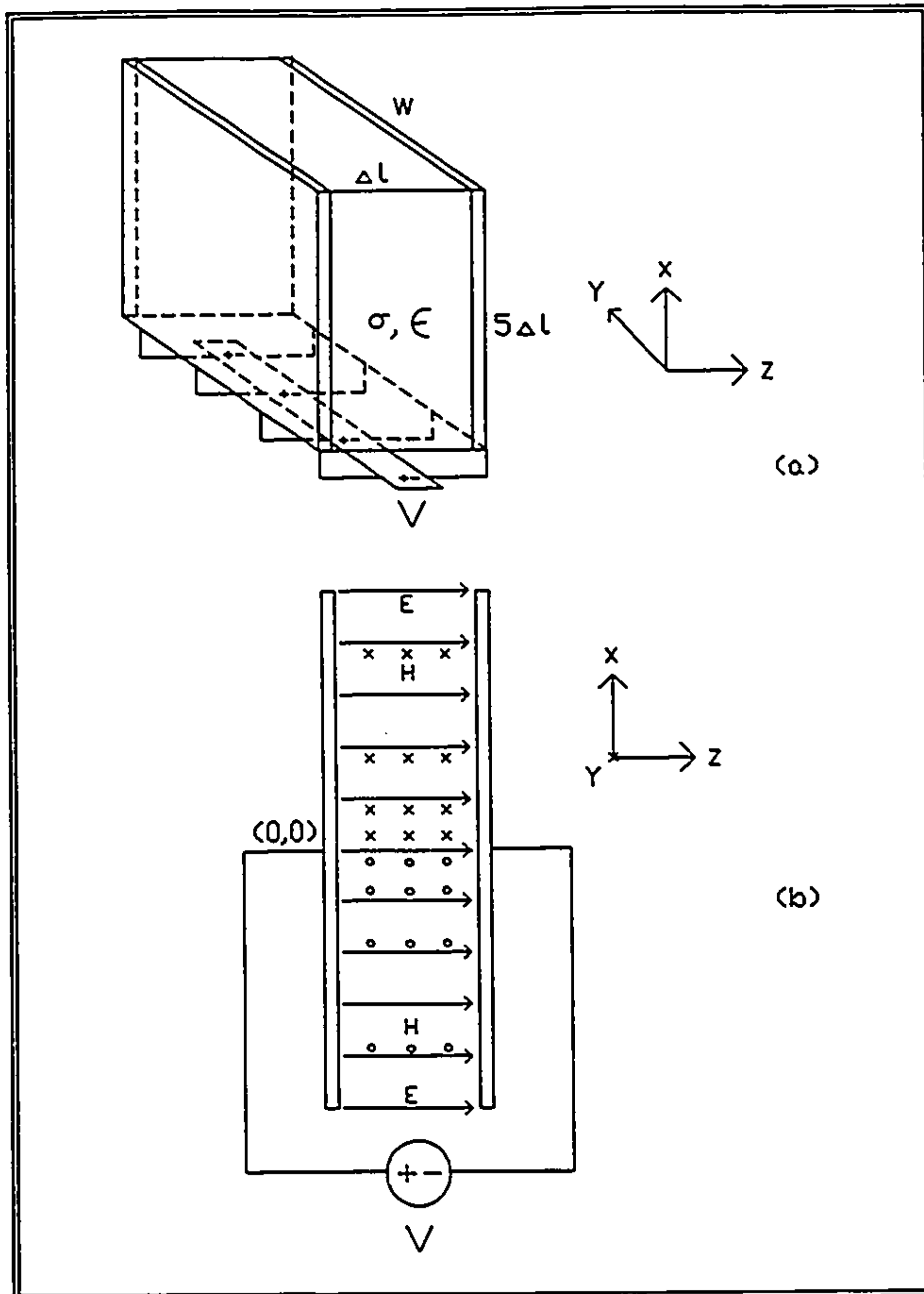

Figure 5.16: Doped GaAs sample for non-stationary velocity analysis. (a) the sample enclosed between metal plates and connected to a voltage source. (b) Orientation of the fields in the sample shown with the mirrored lower half.

controlling quantities can be treated as interface parameters. A novel approach is undertaken whereby FDTD is used to calculate the non-stationary electron dynamics and the results are interfaced into TLM. The conductivities of the TLM nodes are computed at each time iteration by synchronizing the time step Δt in (5.1) and (5.2) to that of the TLM system. Following the computation of the incident and reflected TLM impulses at every node by (2.8) and (2.9) and at the electromagnetic boundaries, the resistance R of the TLM node in (2.11) is updated using the following conductivity definition:

$$ {}_{k}\sigma = \frac{q\, v_i\, n}{{}_{k}E} \tag{5.5} $$

where the k subscript denotes the TLM time step number. Then the amount of TLM energy A is computed at each time step using relation (3.19):

$$ A_i = \frac{I_i}{2.65 \ x \ 10^{-3} \ W \sqrt{\epsilon_r}} \tag{5.6} $$

where I_i is the current at time step i which can be obtained from the applied voltage and the sample's resistance. The sample responds to the applied pulse in a finite time dictated by the dielectric relaxation time constant given in (4.1). At any time step, the sample charges to the voltage V_i in response to the applied voltage $V_{i(ap)}$ as given in (4.2). Since the conductivity changes with every time step, the resistance R_i becomes:

$$ R_i = \frac{\Delta\ell}{\sigma_i W 5 \Delta\ell} \ . \tag{5.7} $$

Both (5.7) and the pulse information are used to compute the current, which in turn is used in (5.6) to calculate the TLM energy at each time step.

The TLM response for the first 10pS is calculated. With a time step $\Delta t = 1.2\mathrm{x}10^{-16}$ seconds (computed from (2.19)), 83,148 time iterations are required. The TLM energy and the conductivity of the nodes are shown in Figures 5.17, and 5.18 respectively. It is noted

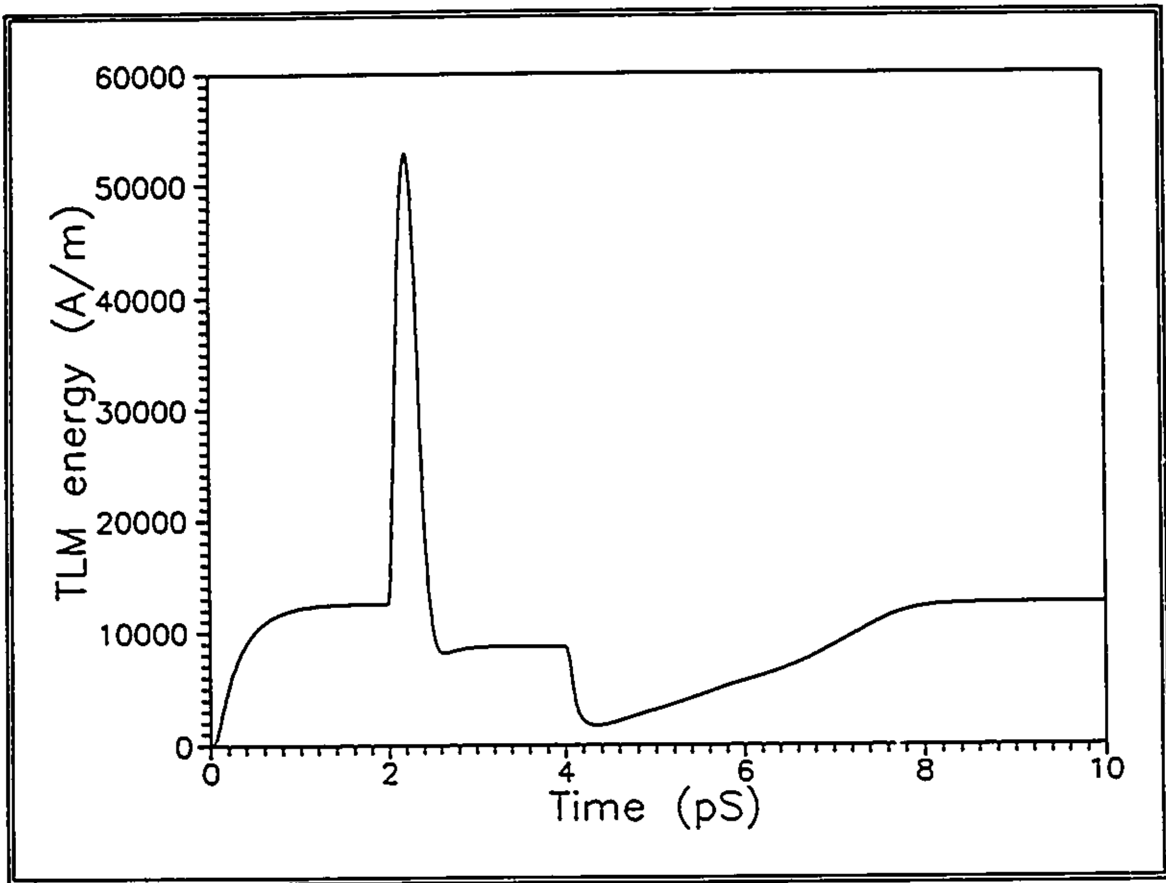

Figure 5.17: TLM energy versus time.

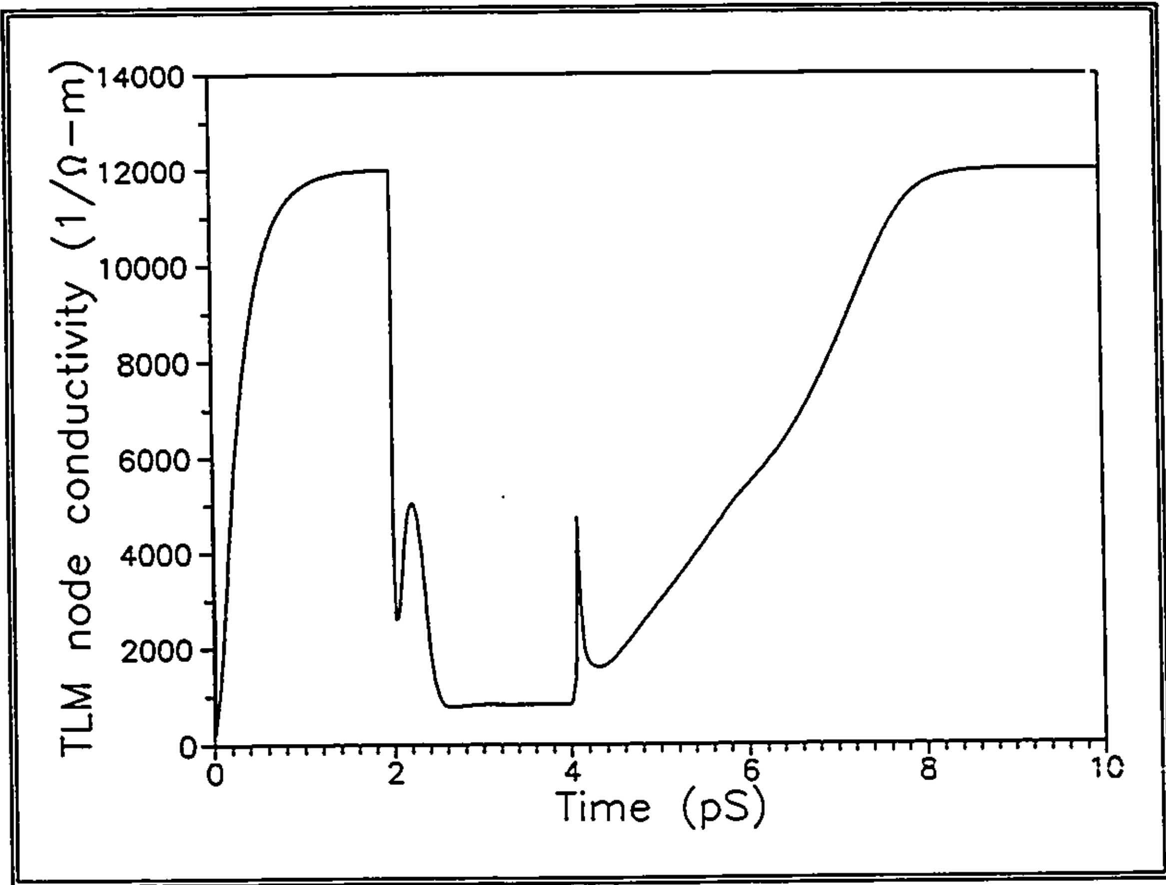

Figure 5.18: TLM node conductivity versus time.

that since the doping profile in the sample is uniform, then the same conductivity versus time dependence applies for all the TLM nodes. The TLM computed electric field E_z is shown in Figure 5.19. E_z is positive and identical in each of the samples' TLM nodes. Furthermore, the steady-state values of the 2/20/2 kV/cm pulse are identical to that used by Carnez et al. (Figure 5.1). The inclusion of the dielectric relaxation time constant and voltage charging effects are shown to give rise to fast exponentially rising and falling field steps, as opposed to being ideal and abrupt. It can be concluded that the TLM computed electric field lags behind the applied field by the sample's dielectric relaxation time constant. The TLM computed magnetic field H_y in Figure 5.20 shows five distinct traces: a at (50Å,450Å), b at (50Å,350Å), c at (50Å,250Å), d at (50Å,150Å), and e at (50Å,50Å). It is clear that H_y is smallest at the TLM node located half a TLM step away from the free edge of the sample, and largest at the node located half a step from the edge of the sample which is connected to the voltage source. Also, the spatial distribution at any time is linear since the doping is uniform. It is easier to familiarize ourselves with the magnetic field by showing the transient current. The electrical current in the sample is proportional to the maximum magnetic field:

$$I = H_{y(max)}\, W. \tag{5.8}$$

It is noted that the edges of the sample are not located at a TLM node, and hence $H_{y(max)}$ must be obtained by extrapolating the magnetic field to the point where the voltage supply is connected. Figure 5.21 shows the transient electric current through the sample. The low field (2 kV/cm) steady-state current is 0.03 Amperes, which agrees with the ratio of the voltage pulse at 0.002 V to the low field resistance of 0.0667 Ω calculated at the beginning of this section. It is interesting to observe that non-stationary velocity shows that the sample experiences a current spike 4 times larger than the steady-state value.

It is important to note the impact of using the dielectric relaxation time constant in the computation of the TLM energy supplied to the system. In this example, the TLM pulses fed start from zero and rise quickly to their steady-state values. In contrast, the TLM pulses applied to the examples in Chapter 3 were constant in amplitude and non-zero at time t=0. In the latter case, the electric and magnetic fields experienced decaying second-order oscillations, which are notably absent in the example of this section. The

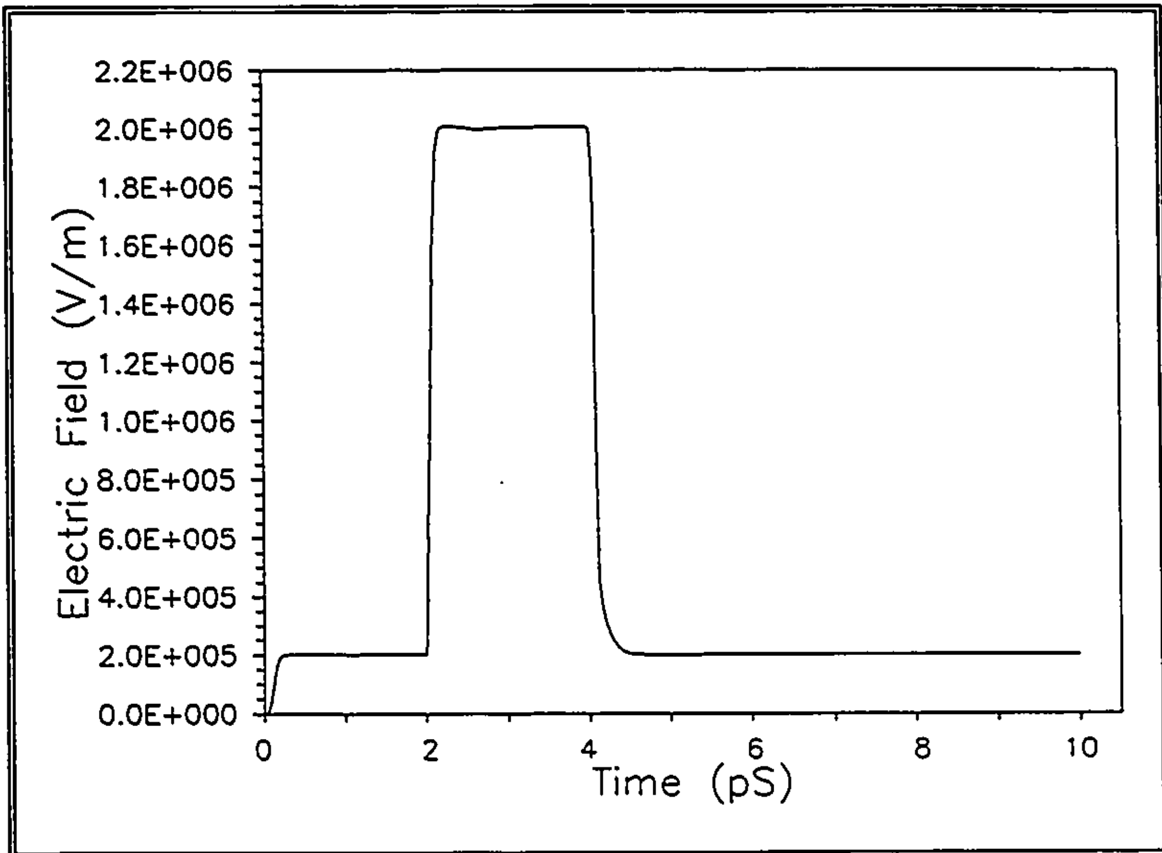

Figure 5.19: TLM computed electric field E_z versus time response.

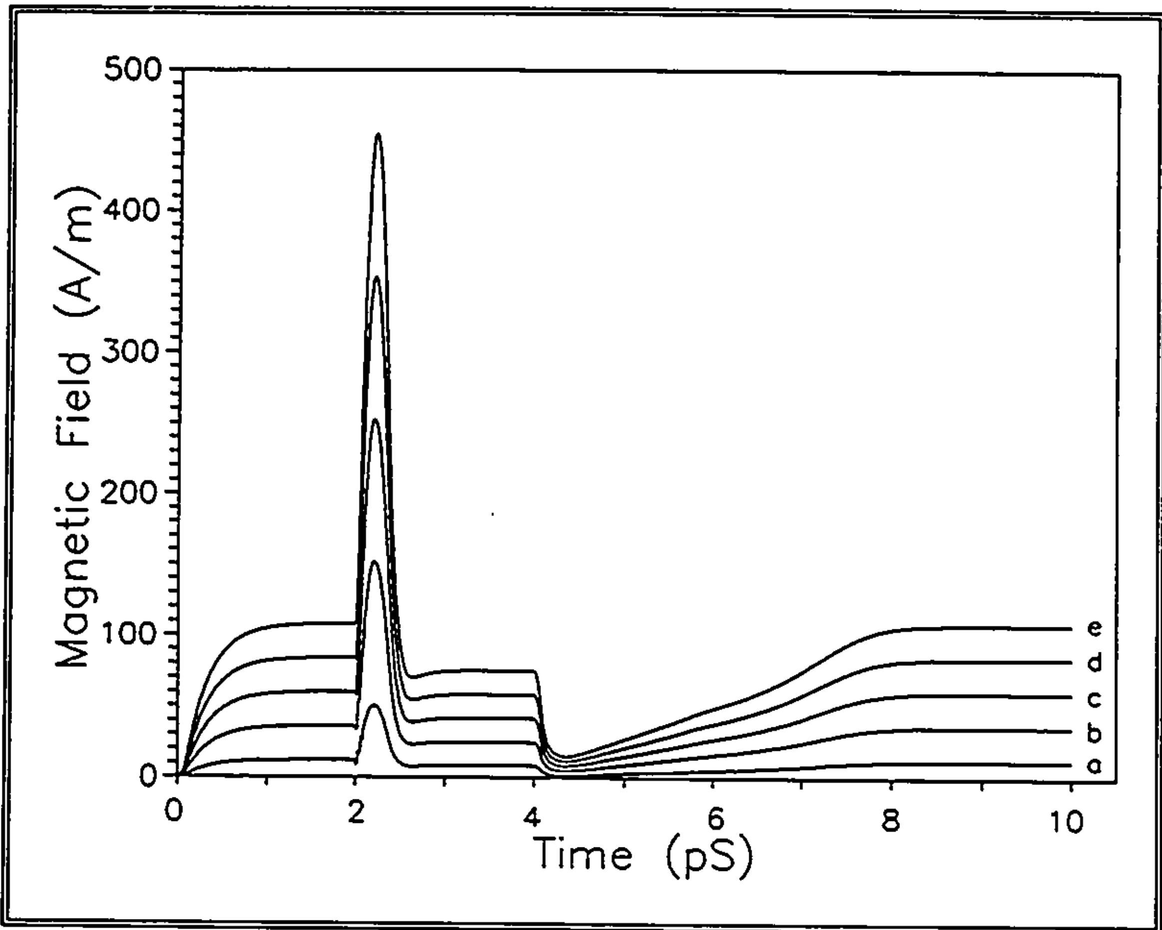

Figure 5.20: TLM computed magnetic field H_y versus time response.

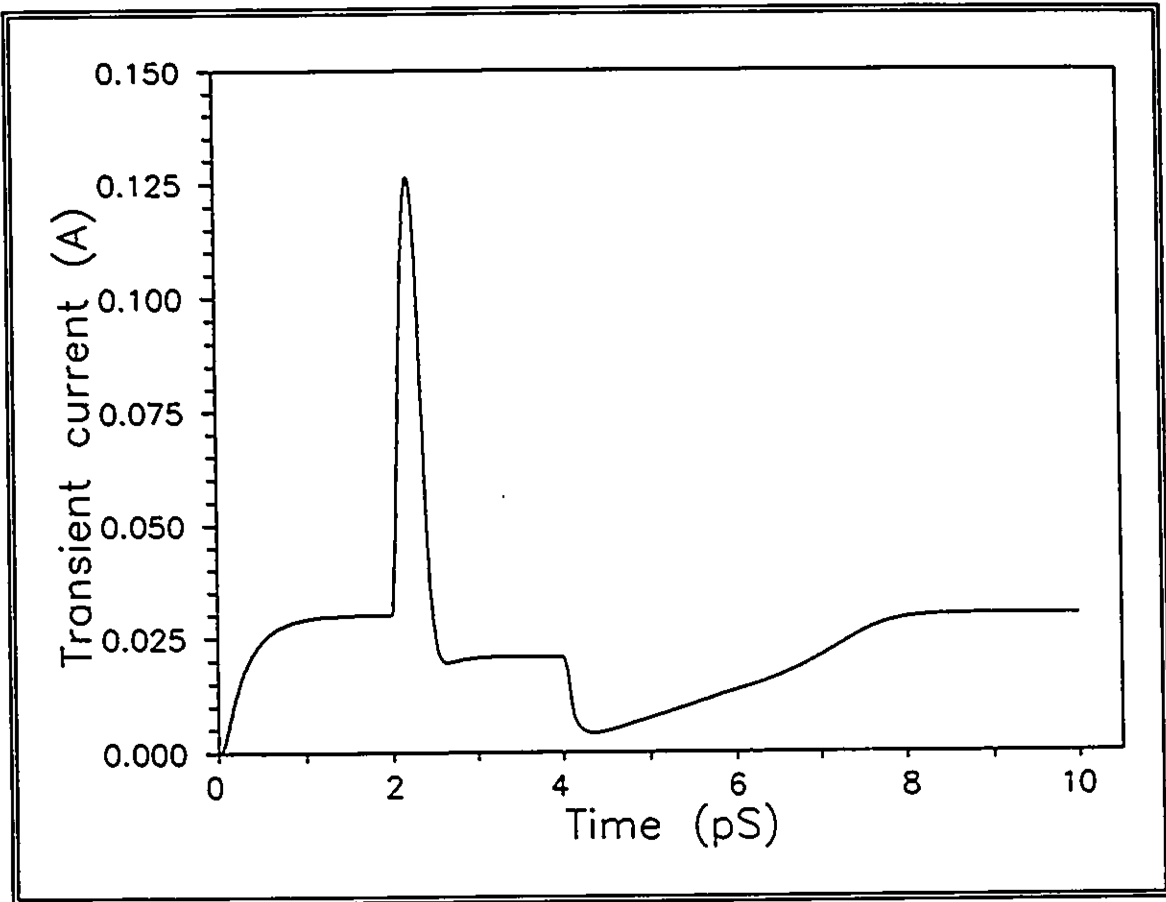

Figure 5.21: Transient current versus time response.

reason for this is that ideal steps are non-physical and are not encountered in practice. However, the TLM network computes the proper response to the non-physical stimulus. The use of the TLM system's dielectric relaxation time constant provides smooth and more realistic response. In addition, the need for filtering out second-order oscillations superimposed on the system's response is no longer required.

5.5 Examples #2: GaAs MESFET Transient Response to Voltage Steps

This example demonstrates the current and electromagnetic transient responses of a GaAs MESFET to the simultaneous application of drain and gate voltage steps. The device reported by Morkoç et al. [5.10], and which is described in Table 5.1 as MESFET #2, is forced into a transition from the electrical state at V_d=0V and V_g=0V to the next state at V_d=3V and V_g=-0.5V. As the TLM simulation of the entire channel region is computationally quite expensive, only two representative TLM systems will be monitored. The first is chosen to be in the high-field region directly underneath the gate metal edge, and the second is chosen to be the low-field region in the immediate vicinity of the drain electrode. The latter section simulates the electromagnetic fields exiting the channel into the drain.

The non-stationary data requires deriving relationships for the relaxation effects $\tau_w(w)$ and $\tau_p(w)$ presented by Carnez et al. [5.5, 5.6]. The relaxation time constants were derived in Section 5.1 from the dependencies of E_{ss}, m^*_{ss}, and v_{ss} upon the electron energy. This time, however, the analysis requires treatment of the time-dependent velocity suitable for the present doping level, 2.2 x 10^{17} atoms/cm^3. Figure 4.9 is used to obtain the following set of polynomial equations to fit E_{ss} to w:

$E_{ss}(w) = -14.85 + 364.01w$ $\quad 0.04 \le w \le 0.045$

$E_{ss}(w) = 0.15 + 46.30w - 94.00w^2$ $\quad 0.045 \le w \le 0.2$

$E_{ss}(w) = 27.02 - 461.19w + 3419.75w^2 - 10794.50w^3 + 12858.90w^4$ $\quad 0.2 < w \le 0.38$

$E_{ss}(w) = -112.79 + 354.65w$ $\quad w > 0.38$

Figure 4.10 is also used to obtain the following set of equations to fit m^*_{ss} to $E_{ss}(w)$:

$m^*_{ss}(E_{ss}(w)) = 0.063$ $\quad E_{ss}(w) \le 2$

$m^*_{ss}(E_{ss}(w)) = 0.077 - 0.012\, E_{ss}(w) + 0.0027\, E_{ss}^2(w)$ $\quad 2 < E_{ss}() \le 6$

$$m^*_{ss}(E_{ss}(w)) = -0.064 + 0.039\, E_{ss}(w) - 0.0017\, E_{ss}^2(w) \qquad 6 < E_{ss}(w) \leq 10$$

$$m^*_{ss}(E_{ss}(w)) = 0.10 + 0.0050\, E_{ss}(w) \qquad E_{ss}(w) > 10$$

In these equations, the units for the electric field and the electron energy are kV/cm and eV respectively. The normalized electron effective mass is dimensionless. The parameters of the steady-state electron drift velocity versus field are the same as those used by Chang and Day [5.8]. They are listed in Table 5.1 and shown in Figure 5.9. Using the same sample of GaAs used in Example #1 but with $2.2\text{x}10^{17}$ atoms/cm^{-3}, the time-dependent drift velocity responses to the 2/20/2 kV/cm and 2/40/2 kV/cm electric field pulses are obtained and shown in Figure 5.22. In comparison with the time-dependent velocity in the lighter doped layer of Figure 5.7, it is evident that this sample will experience smaller overshoot velocities. This result is consistent with more carrier scattering events in heavier doped layers.

The space and time discretizations for the GaAs MESFET analysis engine are chosen differently from the TLM system. In the analysis engine, the space discretizations are $\Delta x=4$Å and $\Delta z=100$Å, whereas in the TLM system $\Delta x=50$Å. Space discretization in the x-direction is made much finer in the internal engine so that higher accuracy can be attained for the high field region. The results are interfaced into coarser TLM systems to avoid a very large number of time steps and excessive run time caused by a large number of nodes. Variable time discretization algorithms are incorporated into the analysis engine. The time step is directly dependent on the dynamic gate and drain time constants, τ_g, τ_d, and indirectly on the gate and drain charging voltages:

$$V_{g(i)}(t) = V_{app(i)}(t)\left(1 - e^{-\frac{\Delta t}{\tau_g}}\right) + V_{g(i-1)}(t)\left(e^{-\frac{\Delta t}{\tau_g}}\right) \tag{5.9a}$$

$$V_{d(i)}(t) = V_{app(i)}(t)\left(1 - e^{-\frac{\Delta t}{\tau_d}}\right) + V_{d(i-1)}(t)\left(e^{-\frac{\Delta t}{\tau_d}}\right) \tag{5.9b}$$

where $V_{app(i)}(t)$, are the applied drain or gate voltages at time step i; $V_{d(i)}(t)$, $V_{g(i)}(t)$ are the charging drain and gate voltages at the current time step, $V_{d(i-1)}(t)$, $V_{g(i-1)}(t)$ are the charging

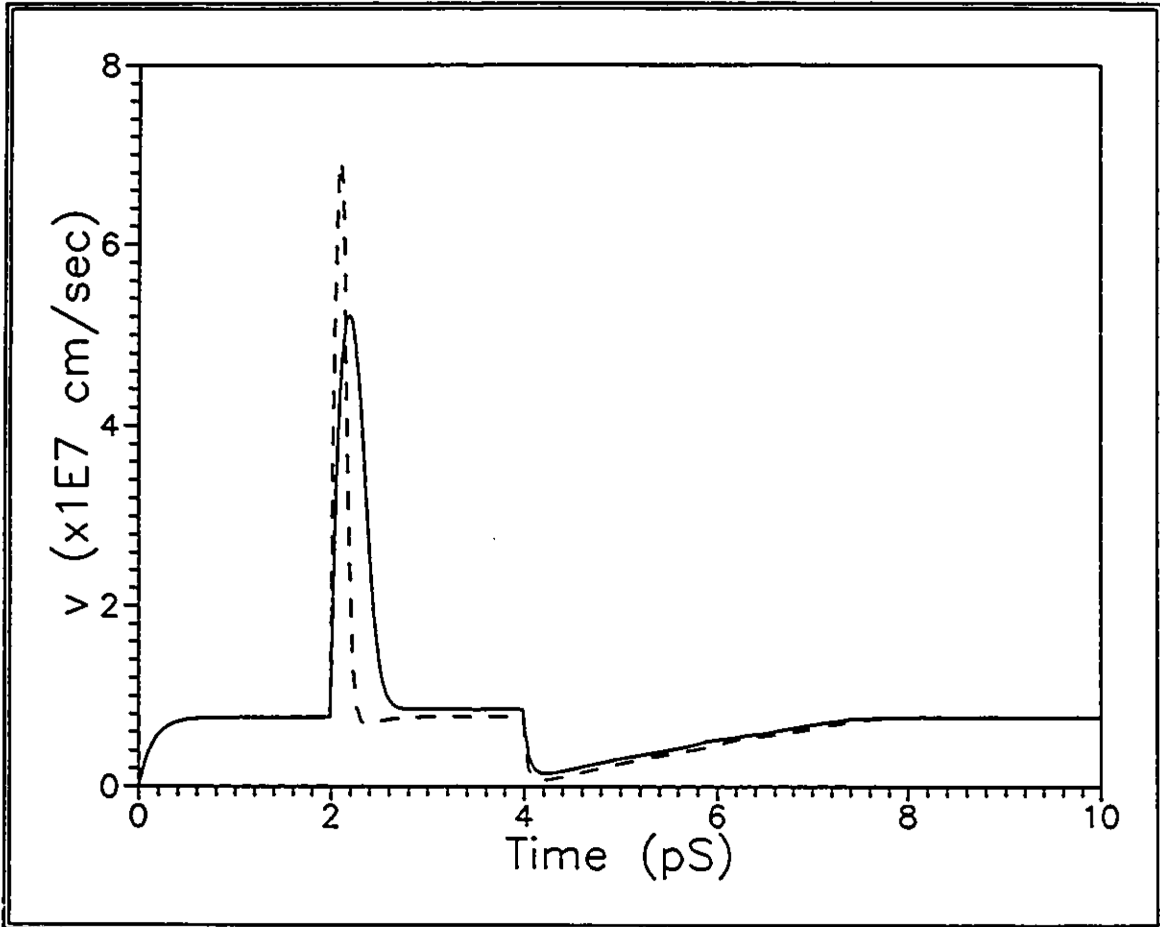

Figure 5.22: Time-dependent velocity response. Solid line: response to a 2/20/2 kV/cm pulse with 2/2/6 pS time duration, dashed line: response to a 2/40/2 kV/cm pulse with 2/2/6 pS time duration.

drain and gate voltages at the previous time step. Since τ_d in the active region is at leastan order of magnitude smaller than τ_g, the device charges to the drain voltage faster than to the gate voltage. Hence, before the drain voltage charges to 98% of the final voltage, $\Delta t=0.025\tau_d$, and thereafter, $\Delta t=0.025\tau_g$. In the TLM system, the time step is linked to the space step, in this case, $\Delta t=6x10^{-17}$ seconds. Since the time step in the internal MESFET analysis engine is coarser, the TLM interface parameters are interpolated at the required TLM time steps.

The charging voltages of the drain and gate circuits are shown in Figure 5.23. The drain circuit charges to the applied voltage in less than 0.26pS, whereas the gate circuit requires 6.65 pS to charge to 98% of the applied gate voltage. During the transition time, the gate and drain time constants vary with time as shown in Figure 5.24. The time constants are initially relatively large indicating a slow carrier velocity. But they both reach a minimum within the first 1pS before they relax to the steady-state. This behavior can be accounted for by examining the carrier velocity at the high and low field regions shown in Figure 5.25. The electrons experience velocity overshoot in the high field section as the electric field quickly exceeds the peak field E_T, and hence the time constants decrease. This condition does not take place in the low field region, and hence the velocity rises monotonically to the steady state. The brief maximum in the velocity in this low-field section arises because of the MESFET's different voltage charging rates: the channel current increases quickly as the drain circuit charges to the final voltage, but soon decreases as the charging gate voltage becomes more negative. The electron concentration, which remains constant in the low field channel section, undergoes carrier depletion in the high field region as shown in Figure 5.26 during the carrier overshoot event, but soon after undergoes carrier accumulation to ensure current continuity.

The calculated TLM interface parameters versus time are shown in Figures 5.27 to 5.29. The TLM pulse energies for the high and low field channel sections are the same since the channel current is identical in both sections. On the other hand, the conductivity of the TLM nodes in the two sections are different since the effective carrier mobility is far lower in the high field section. As for the channel length, Figure 5.29 shows that it decreases very little with time in the low field section, but the high field section shows a

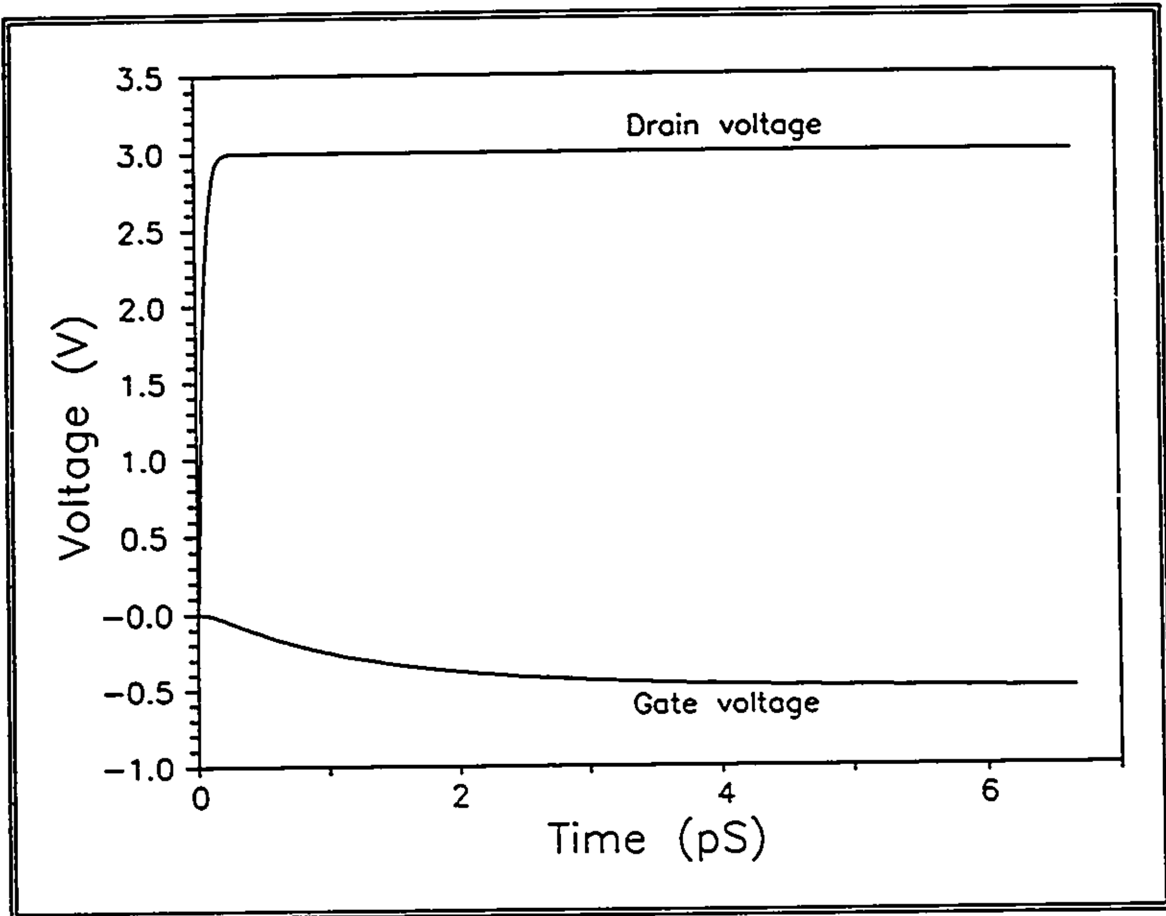

Figure 5.23: Gate and drain circuits charging voltages versus time.

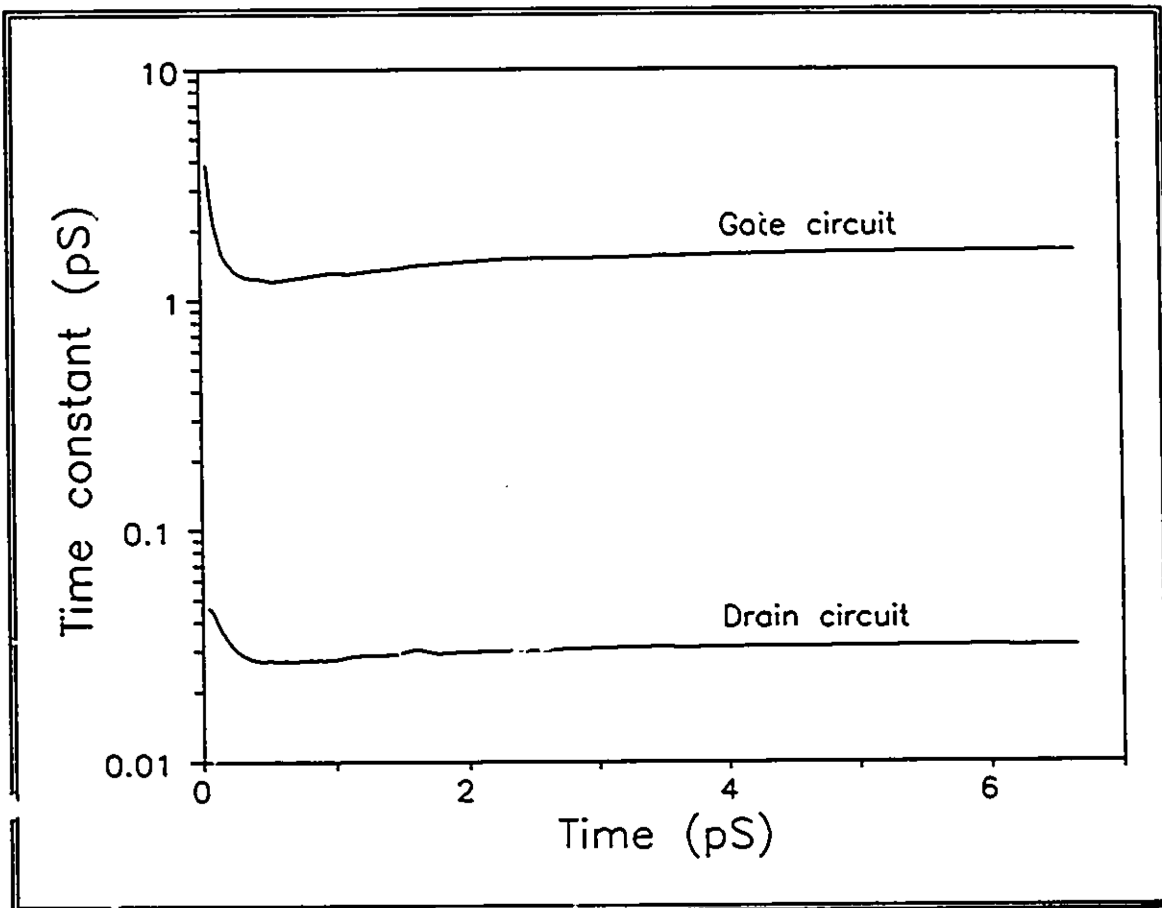

Figure 5.24: Gate and drain time constants versus time.

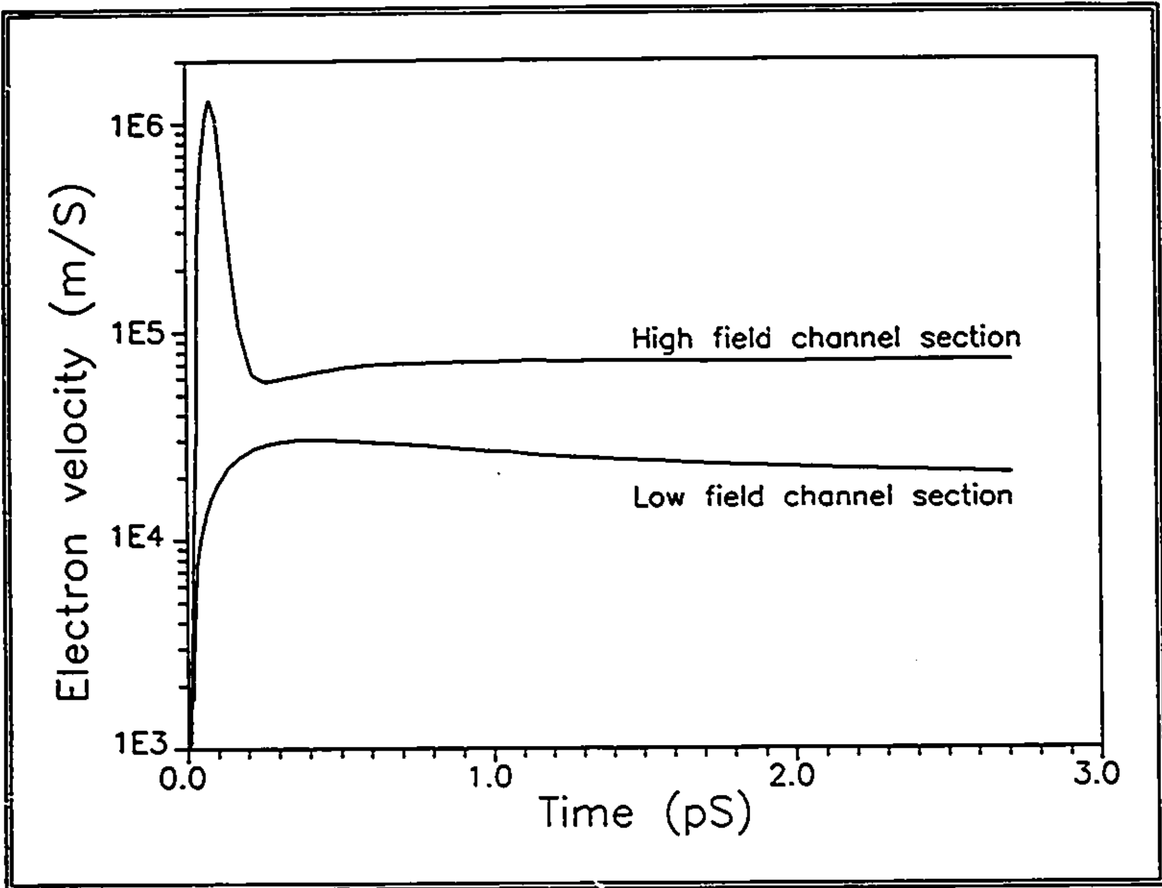

Figure 5.25: Carrier velocity at two channel sections versus time.

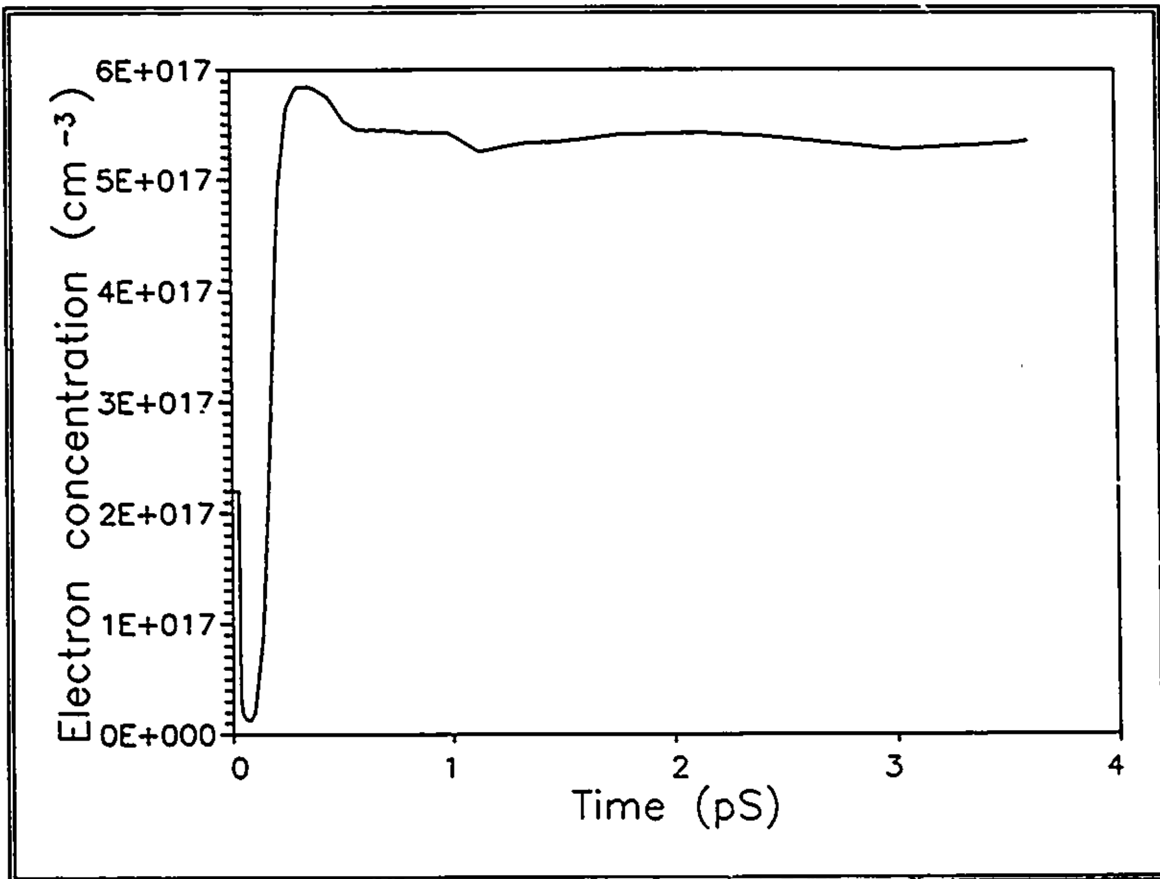

Figure 5.26: Carrier concentration in the high field section versus time.

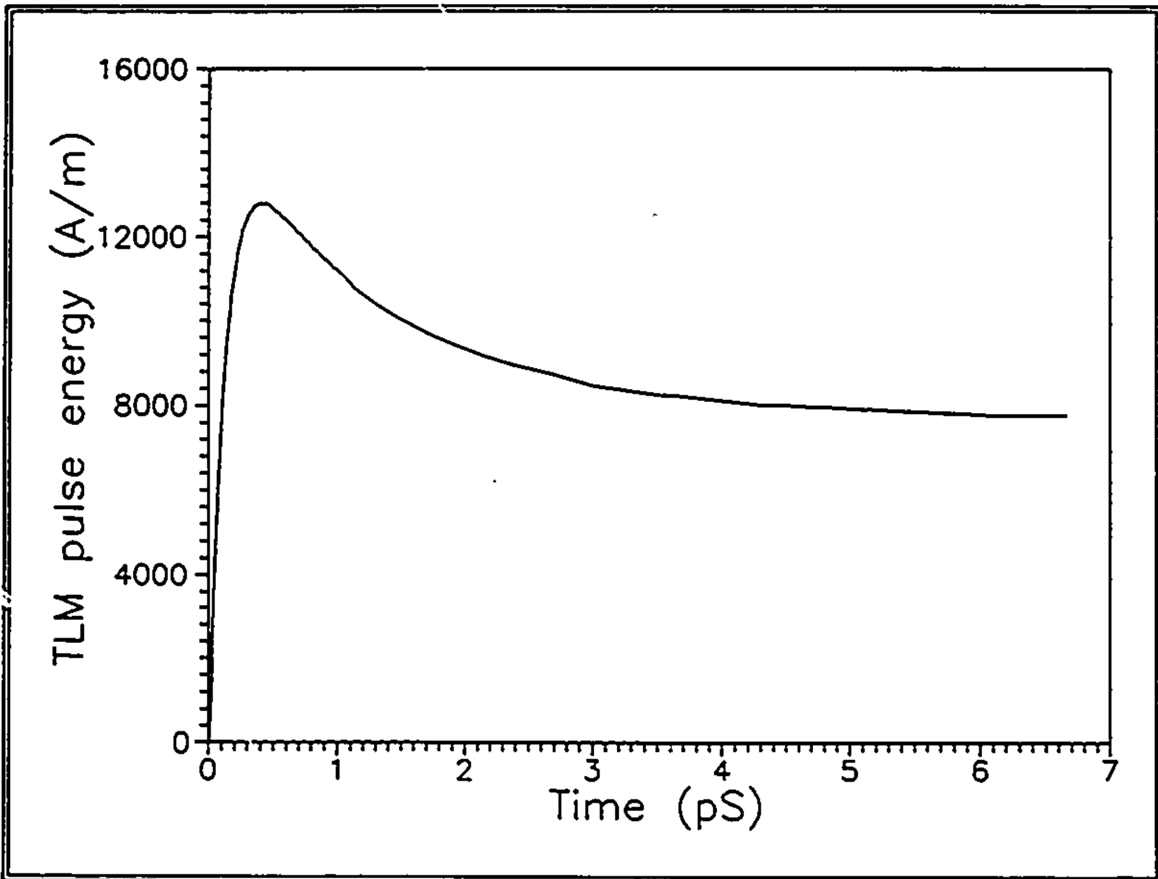

Figure 5.27: TLM pulse energy versus time.

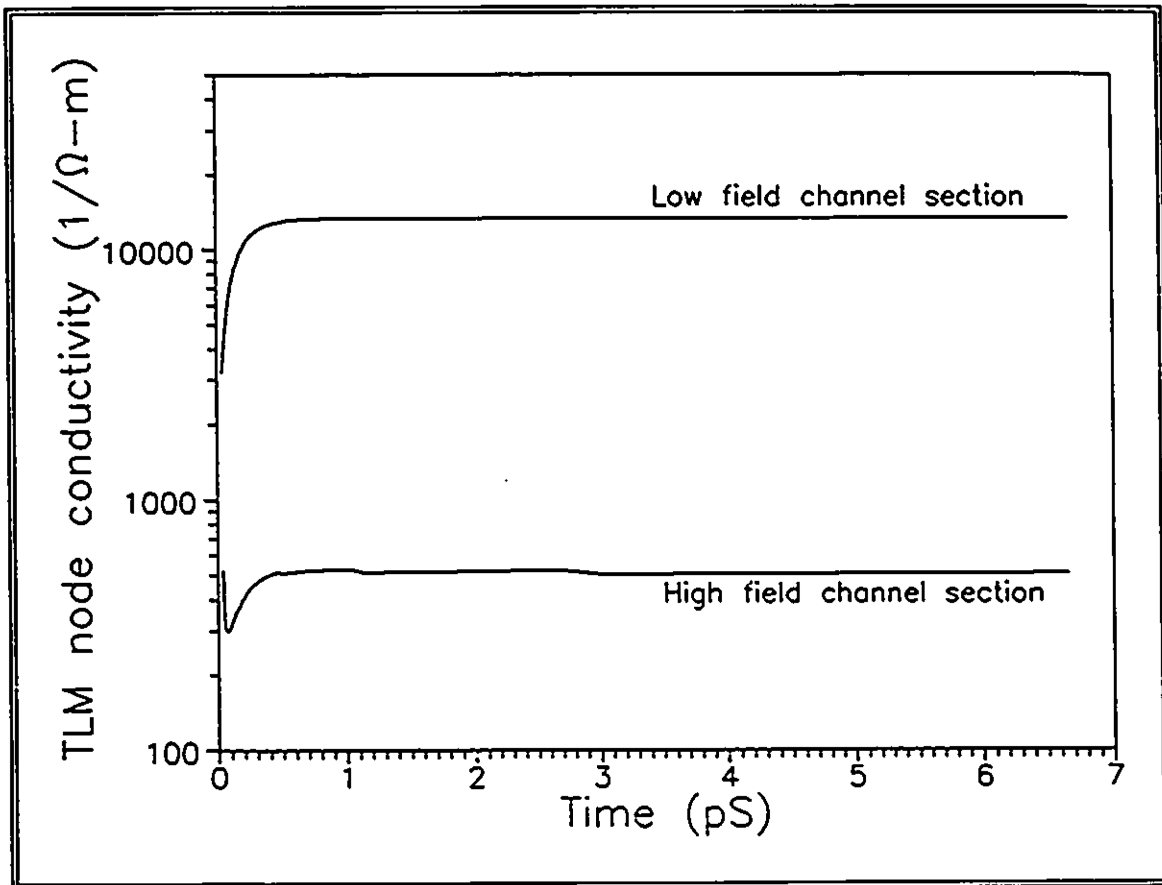

Figure 5.28: TLM nodes conductivity versus time.

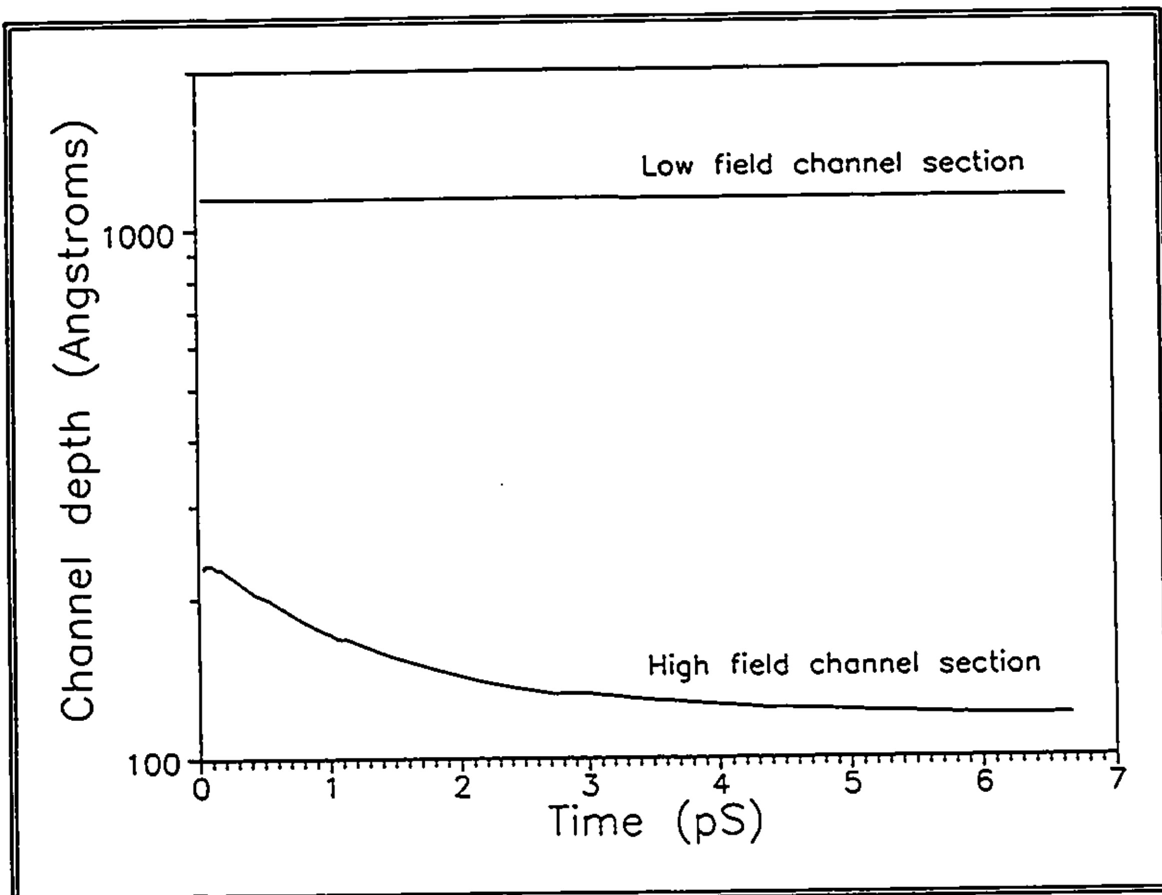

Figure 5.29: Channel depth at two channel sections versus time.

gradual decrease to little more than 100Å. The latter case imposes a moving magnetic boundary condition on the TLM system of the high field region. Finally, since 6.65pS are needed to approach the steady state, approximately 110,240 time iterations will be needed to attain the final response.

Consider the TLM response for the electromagnetic fields in the low field channel section. The response of the electric field in any one of the TLM nodes is the same, and is shown in Figure 5.30 where it is compared with the theoretical response provided by the GaAs MESFET analysis engine. The TLM response initially lags behind the theoretical response, but then rises to the same magnitude. A close-up shown in Figure 5.31 shows that the TLM computed electric field response requires less than 0.1pS to reach the required theoretical response. This behavior is governed by the dielectric relaxation time constant of the TLM system material. The TLM computed magnetic field response is shown in Figure 5.32 for each of the nodes in the system. The maximum magnetic field occurs at the bottom of the channel (x=1200Å), while it is zero at the conducting channel-depletion interface. The spatial distribution at any given instant in time is linear since the doping is uniform. To verify the characteristics of the magnetic field response, we extract the channel current from $H_{y(max)}$ and (5.8). The TLM computed versus the theoretical channel current in Figure 5.33 show good agreement. Furthermore, no time lag is observed, indicating that the transient magnetic field response closely models the theoretical response. Another important observation can be made. The steady-state current, I_c=21.7mA, arrived by the present non-stationary analysis is higher than that arrived by non time-domain approach used in Section 5.3, where the calculated steady-state current is I_c=19.2mA. This is not inconsistent with the findings of other workers [5.5].

Now consider the TLM response for the high-field channel section. The response of the electric field in any one of the TLM nodes is also the same, and is shown in Figure 5.34 where it is compared with the theoretical response provided by the GaAs MESFET analysis engine. The TLM response now initially lags behind the theoretical response by about 1pS. Compared with the previous case, the dielectric relaxation time constant of the TLM system material is now different since the conductivity is several times smaller. The TLM computed magnetic field response shown in Figure 5.35 for each of the TLM

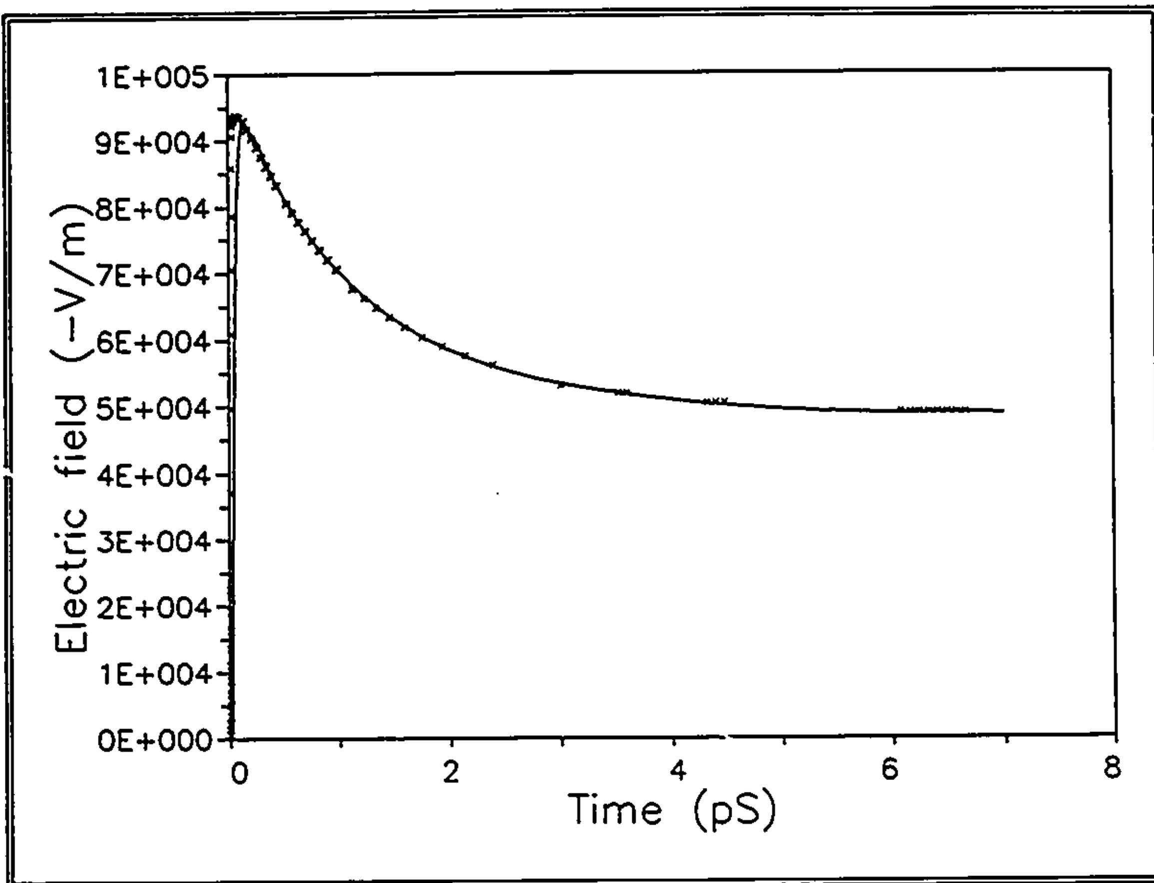

Figure 5.30: Electric field versus time. Solid line: TLM computed, x symbols: theoretical calculations.

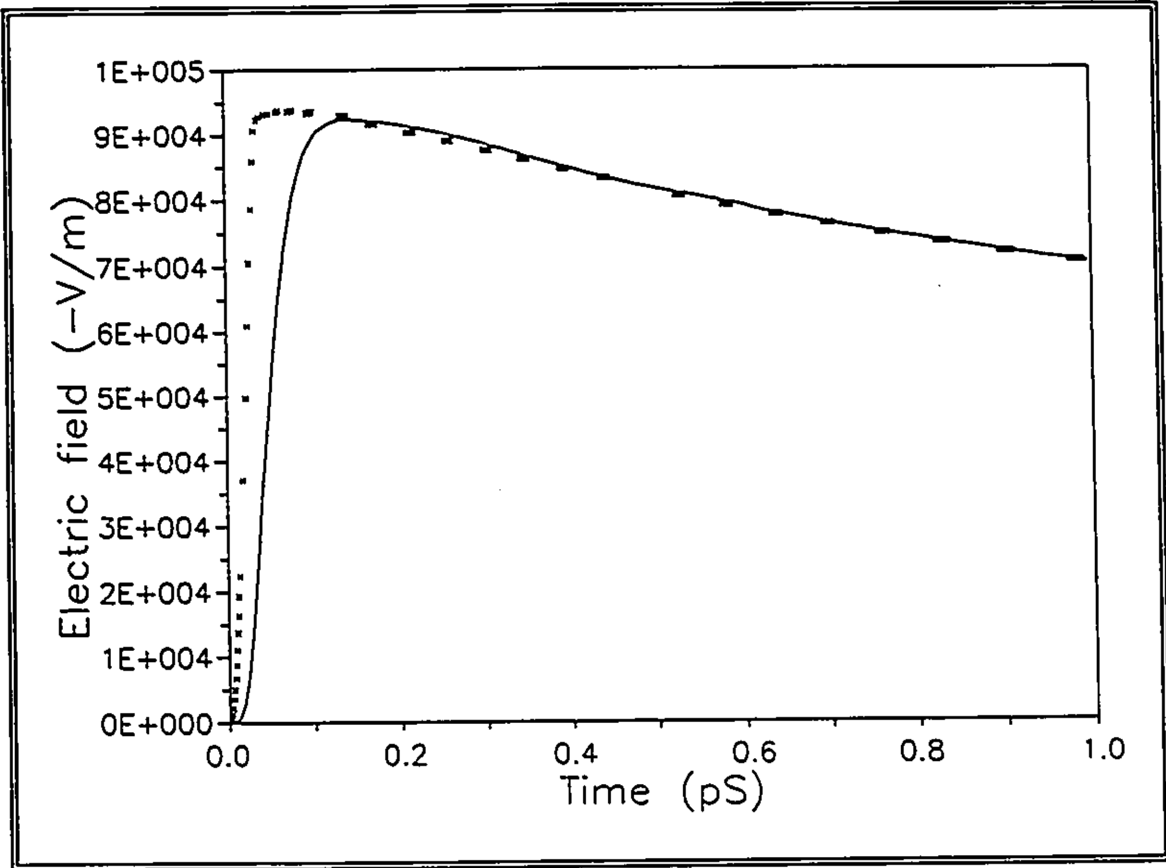

Figure 5.31: Close-up of the electric field versus time. Solid line: TLM computed, x symbols: theoretical calculations.

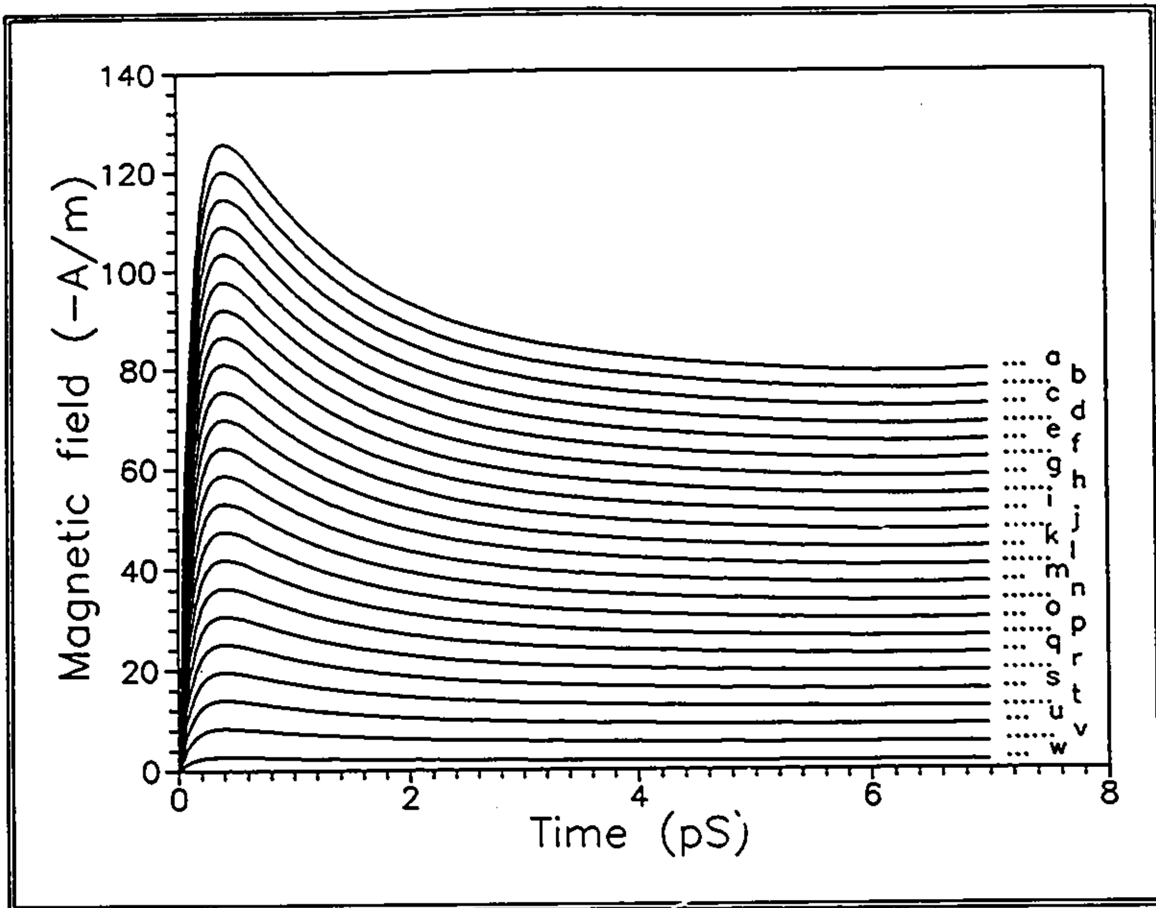

Figure 5.32: TLM computed magnetic field versus time. The TLM nodes are located at a(x=1175Å), b(x=1125Å), c(x=1075Å), d(x=1025Å), e(x=975Å), f(x=925Å), g(x=875Å), h(x=825Å), i(x=775Å), j(x=725Å), k(x=675Å), l(x=625Å), m(x=575Å), n(x=525Å), o(x=475Å), p(x=425Å), q(x=375Å), r(x=325Å), s(x=275Å), t(x=225Å), u(x=175Å), v(x=125Å), w(x=75Å).

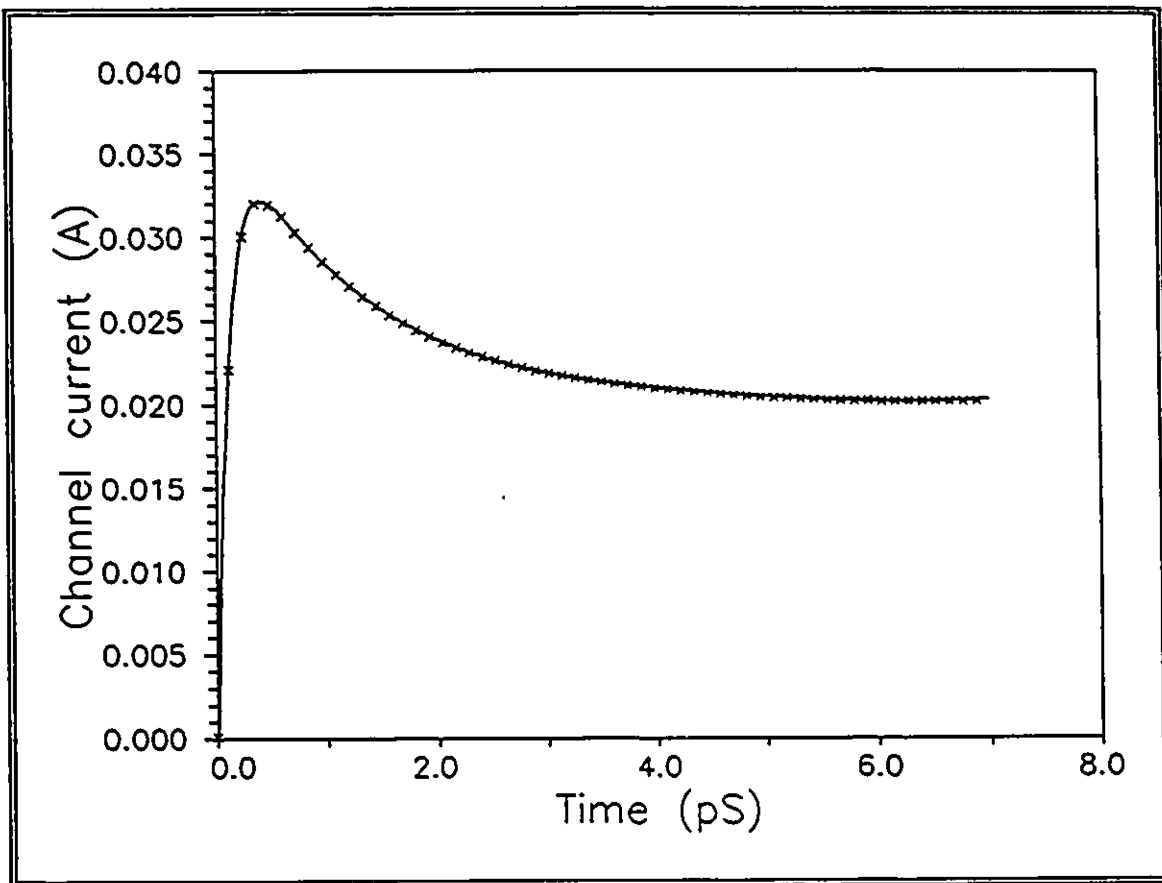

Figure 5.33: Channel current versus time. Solid line: TLM computed, x symbols: theoretical calculations.

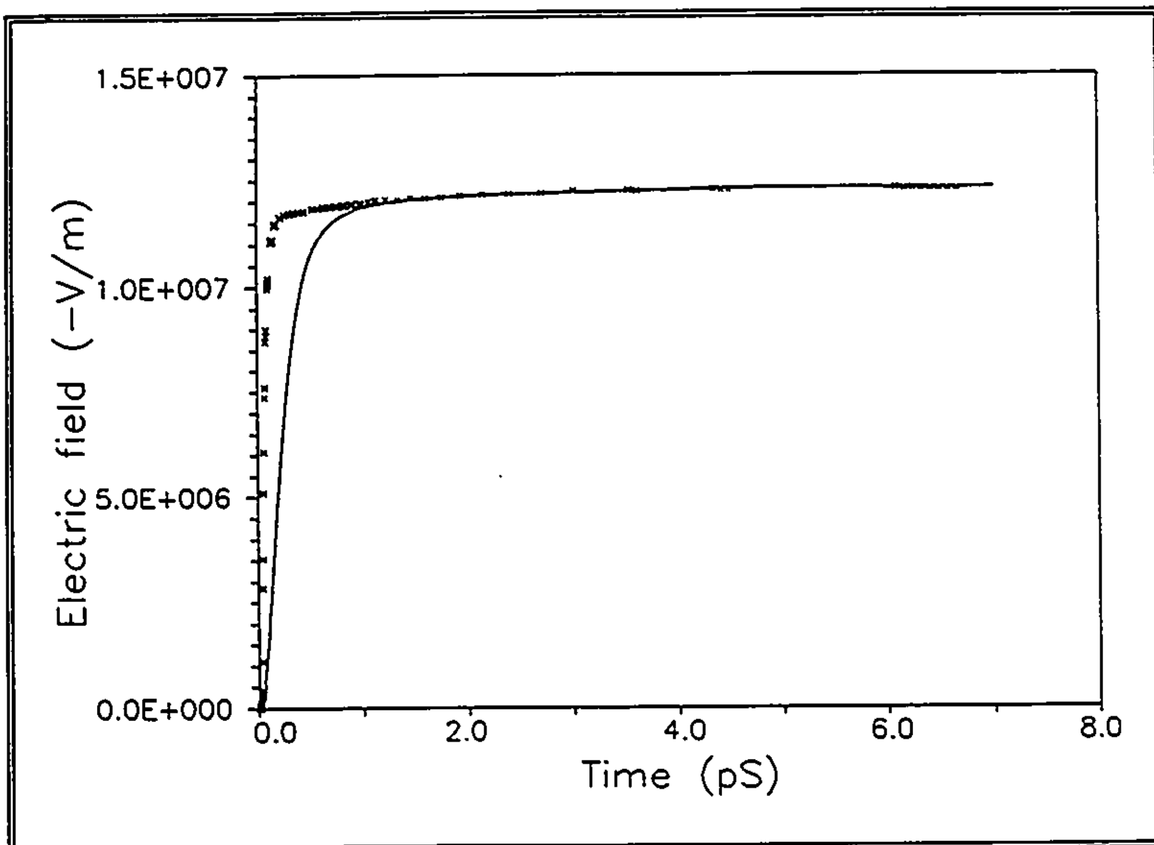

Figure 5.34: Electric fields versus time. Solid line: TLM computed, x symbols: theoretical calculations.

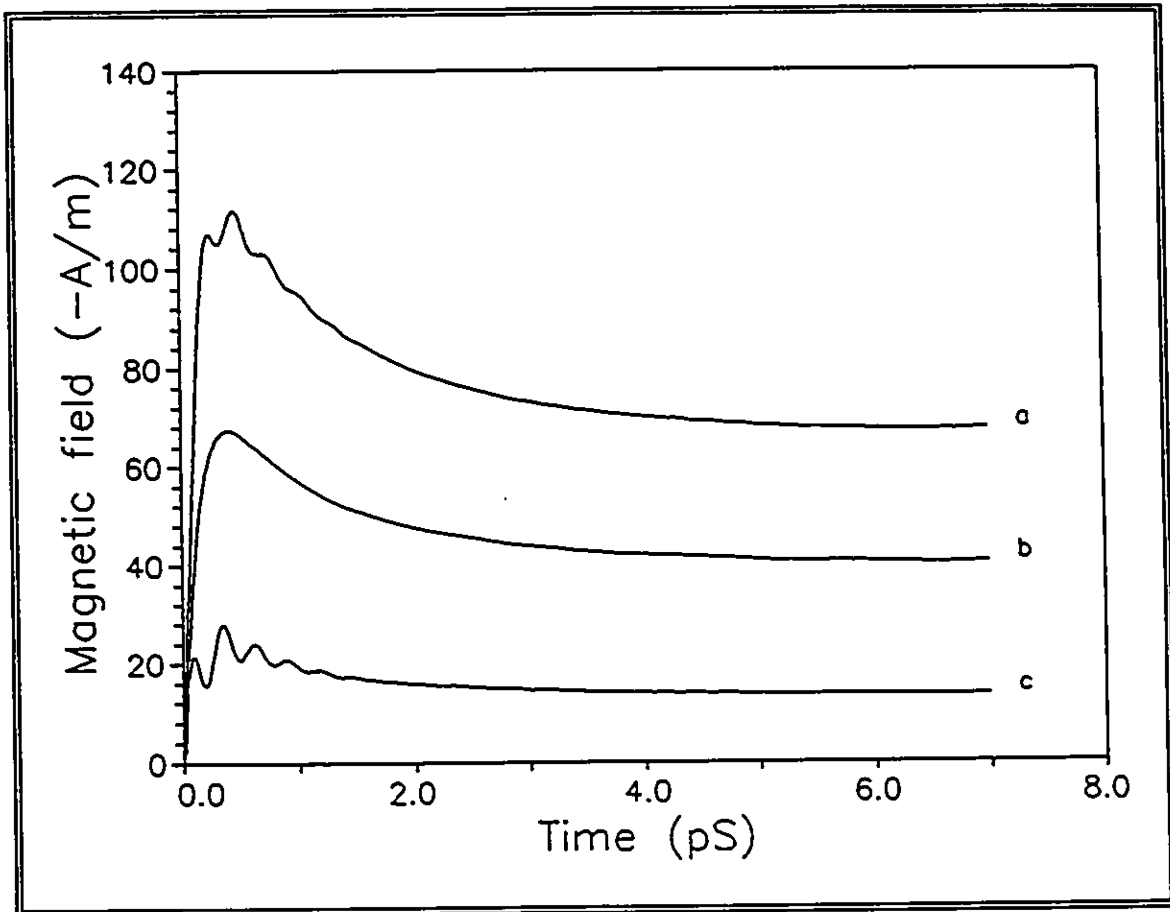

Figure 5.35: TLM computed magnetic field versus time. The TLM nodes are located at a(x=1175Å), b(x=1125Å), c(x=1075Å).

nodes in this system now exhibits decaying oscillations in the first 1 pS. This response is attributed directly to the movement of the magnetic boundary as the channel height decreases in time to its steady-state length. The TLM computed versus the theoretical channel current is shown in Figure 5.36. Good agreement is found, and furthermore, the oscillations are sufficiently small in magnitude that they can be filtered out. Also, no time lag is observed in the response, indicating that the transient magnetic field response closely models the theoretical response.

5.6 Examples #3: GaAs MESFET Transient Response to a Sinusoidal Field

This example demonstrates the current and electromagnetic transient responses of a GaAs MESFET to an impressed 10 GHz sinusoidal electric field waveform. The device and the final conditions arrived at in Example #2 will be used as initial conditions. The same spatial and time discretization schemes will be applied. The experiment is therefore a continuation of the previous example which proceeds 6.65pS after the biases, V_d=3V and V_g=-0.5V, are applied. Since the simulation of the 10 GHz waveform requires 100 pS, approximately 1,657,737 TLM time iterations will be required to attain the complete response. This presents considerable stress on computer storage and time resources, and hence only the low field channel section in the vicinity of the drain electrode will be simulated in a TLM system.

The signal shown in Figure 5.37 represents an x-directed electric field resulting from a 0.4 V peak to peak waveform of the form:

$$V_{signal} = 0.2 \sin(2\pi f(t - 6.65)) \tag{5.10}$$

where f=10 GHz, and t ranges from 6.65pS to 106.65pS. This signal can be classified as medium to large since it is equivalent to -4 dBm RF power. The gate circuit of the MESFET charges to the applied signal as shown in Figure 5.38. Close examination of the charging voltage reveals that, when the effects of time lag are taken into account, the negative peak of the charging voltage is smaller than the positive counterpart. The difference between the positive peaks are 0.71mV while the negative peaks differ by

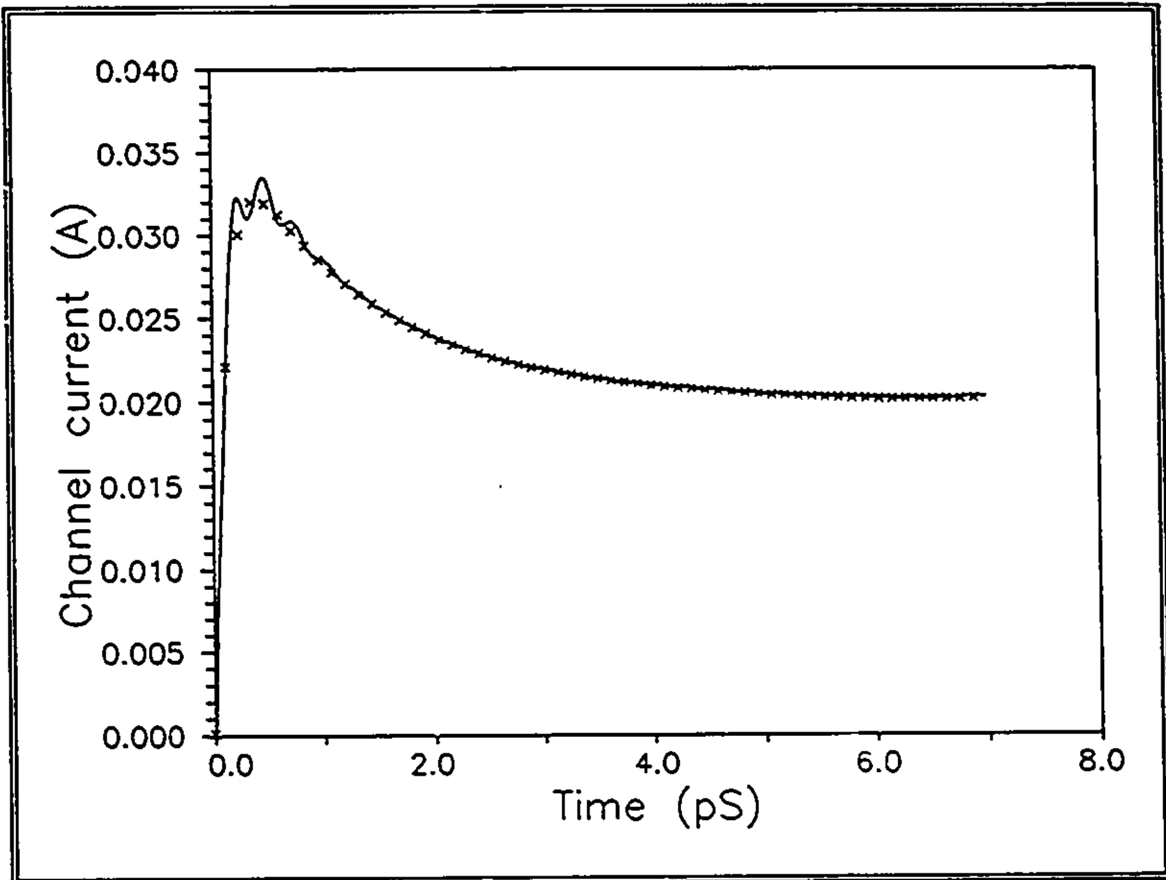

Figure 5.36: Channel current versus time. Solid line: TLM computed, x symbols: theoretical calculations.

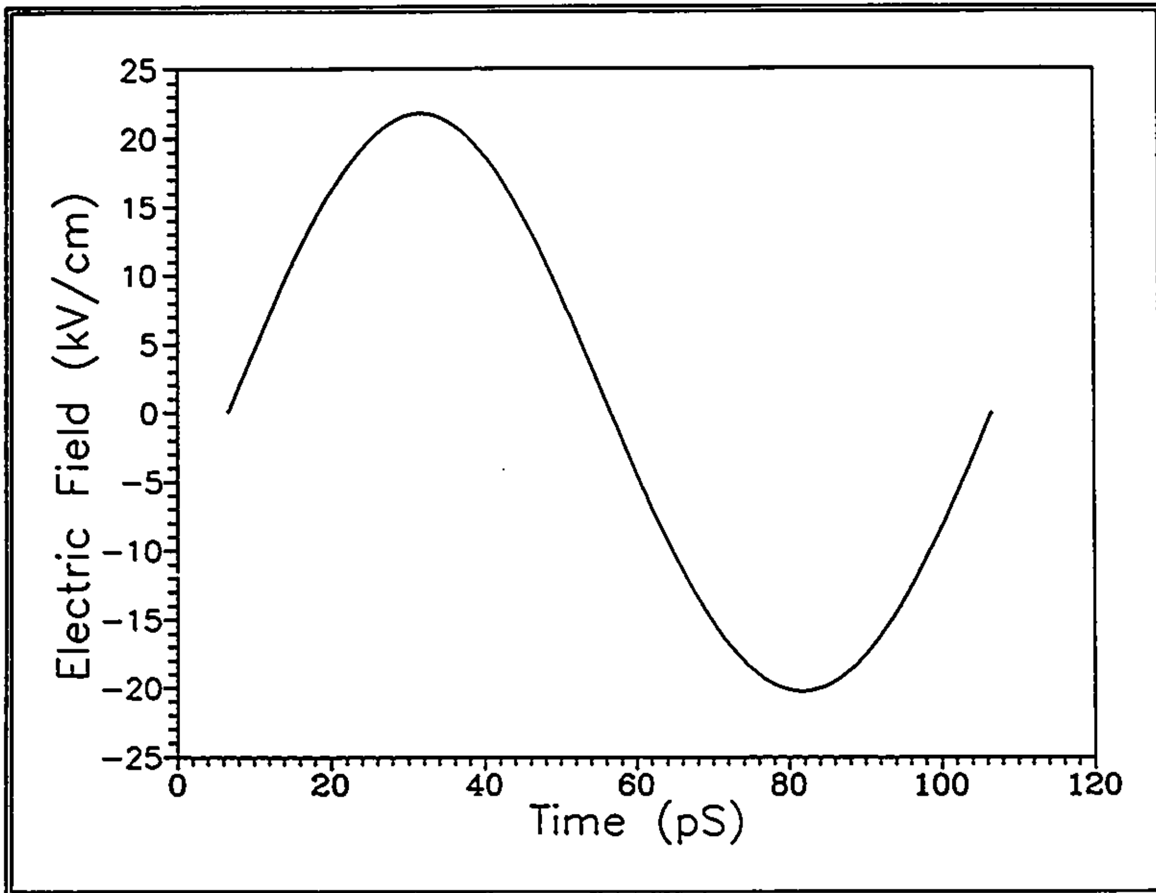

Figure 5.37: The applied electric field signal E_x versus time.

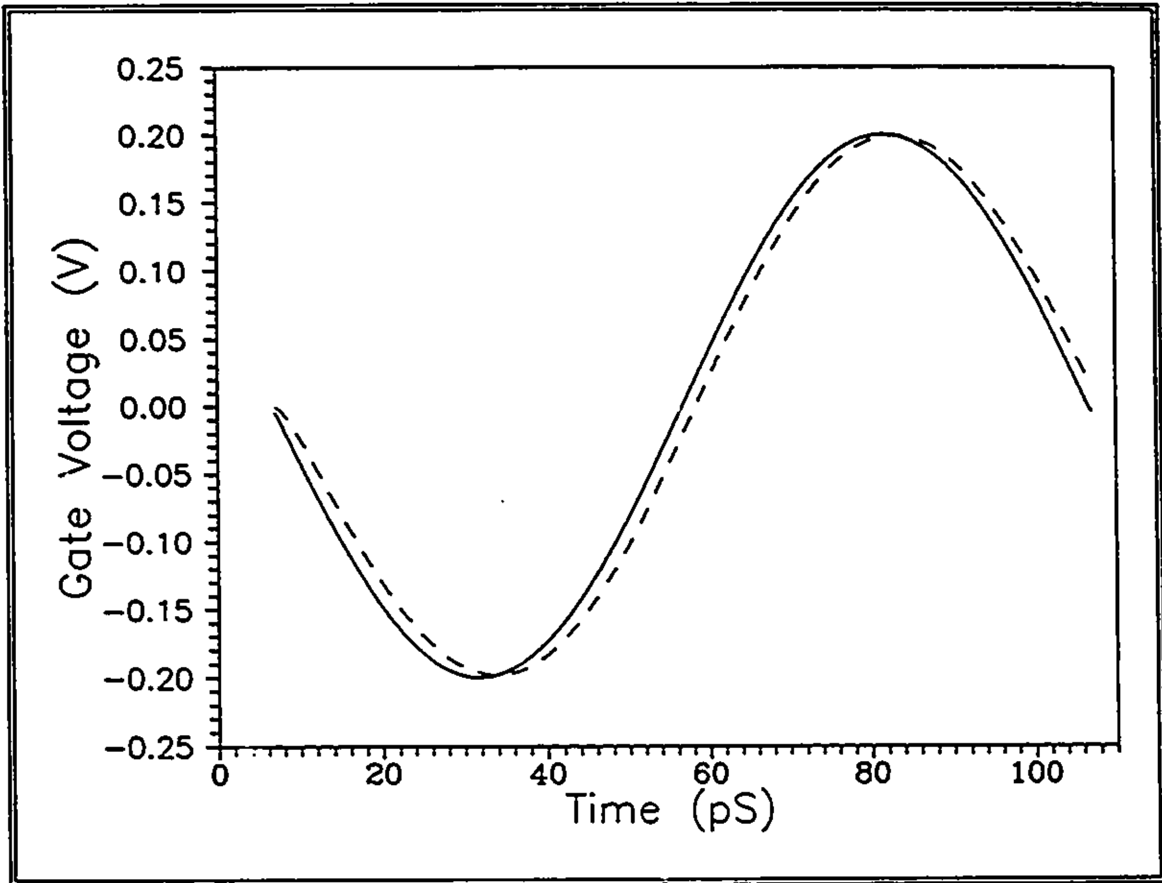

Figure 5.38: The applied and charged gate voltage versus time. The DC components have been removed. Solid line: applied voltage, dashed line: charging voltage.

1.78mV. The signal attenuates at the input by a mere 0.054 dB. This reveals that the device can be modulated at this frequency (10 GHz) since the gate time constant is small enough. But the difference in magnitude of the peaks suggests underlying nonlinearity. The charging voltage lags behind the signal by the gate time constant, which itself varies with time as shown in Figure 5.39. Furthermore the positive-going half cycle is considerably larger in area than the negative going counterpart. The uneven increase of the time constant in the first half of the cycle is attributed to the nonlinear increase of the gate-source capacitance. As to the response in the output channel section, the electric field response is predictably sinusoidal as shown in Figure 5.40, and both the theoretical and TLM computed results show good agreement. The dividing lines in the same figure meet at t=6.65pS when the sinusoidal wave is injected. The magnetic field, which represents the modulation of the channel in response to the input electric field modulation at the gate, is computed by TLM and is shown in Figure 5.41. The spatial distribution at any time step is uniform; however, it can be seen that the magnetic field distribution is relatively more widely spaced at the positive peaks, again indicating a nonlinear response. Extrapolating the maximum magnetic field at the base of the channel, the channel current is computed and compared with the theoretical results in Figure 5.42. In this figure, the DC component has been removed to reveal the induced 10-GHz current waveform. Both the TLM and theoretical channel current show agreement, and as expected, the positive cycle is larger than the negative counterpart. The amplification of the input signal can be evaluated by computing the device transconductance. Using the available gate voltage swing, this measure is evaluated and compared with computations performed by purely steady state analysis in Figure 5.43. The figure reveals that the transconductance computed in the time domain is larger and somewhat steeper than steady-state analysis. This example shows the advantage of using non-stationary time domain analysis for more accurate transient and steady-state prediction of GaAs MESFETs.

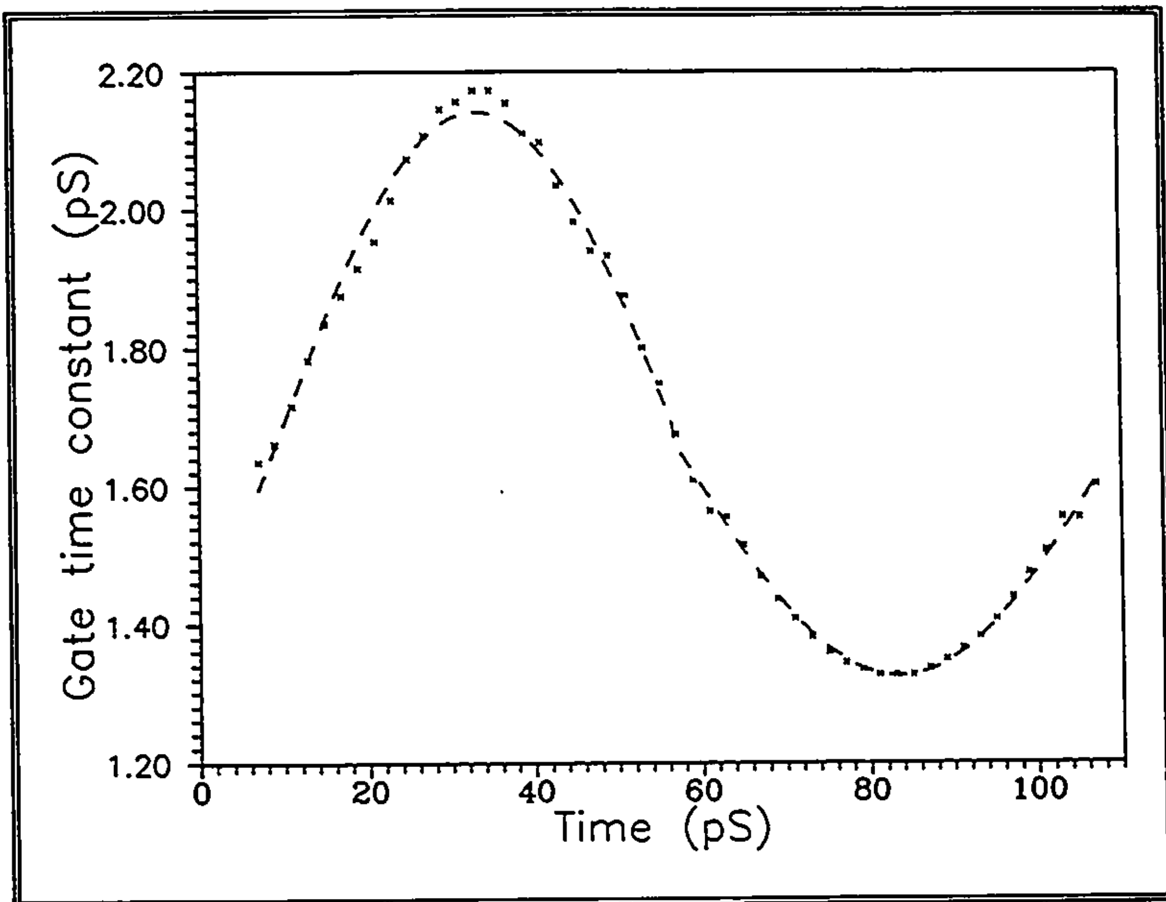

Figure 5.39: The variation of the gate circuit time constant vs time. x symbols: MESFET analysis results, dashed line: fitted function.

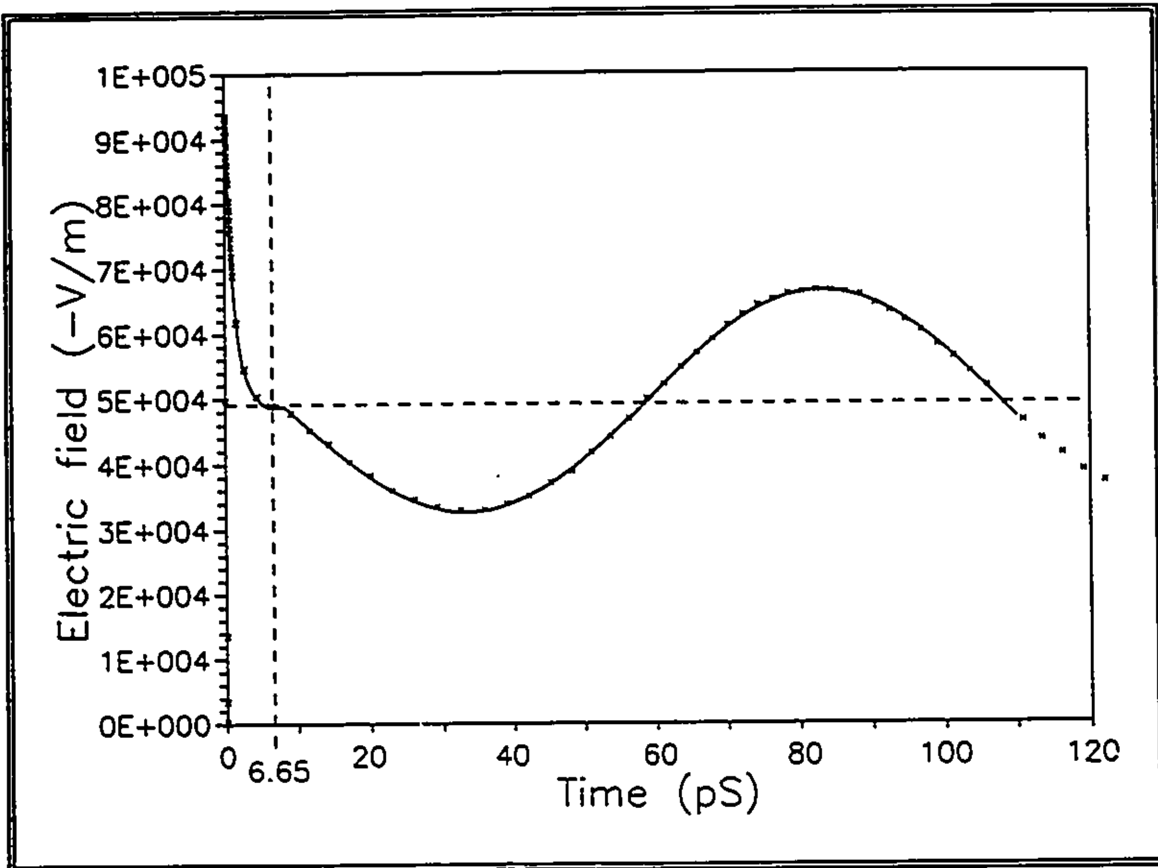

Figure 5.40: The electric field versus time in the low field channel section. Solid line: theoretical analysis, x symbols: TLM computed.

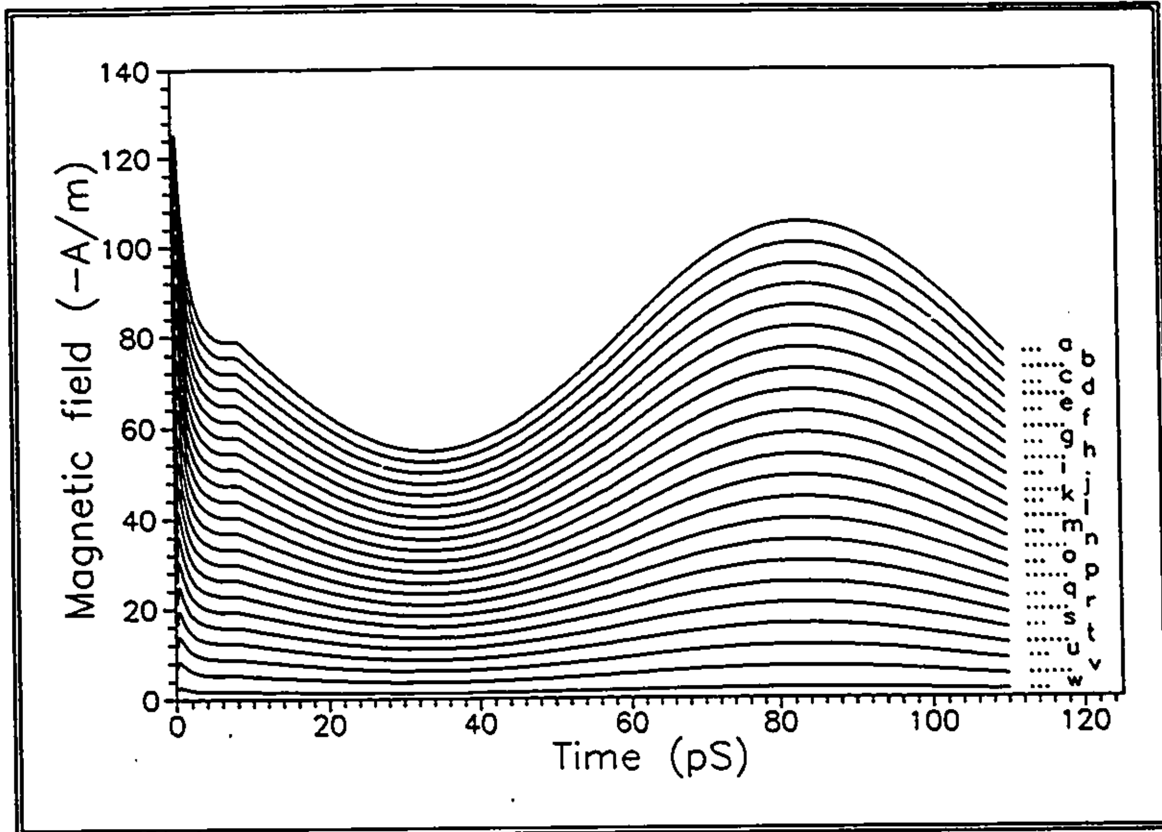

Figure 5.41: TLM computed magnetic field versus time. The TLM nodes are located at a(x=1175Å), b(x=1125Å), c(x=1075Å), d(x=1025Å), e(x=975Å), f(x=925Å), g(x=875Å), h(x=825Å), i(x=775Å), j(x=725Å), k(x=675Å), l(x=625Å), m(x=575Å), n(x=525Å), o(x=475Å), p(x=425Å), q(x=375Å), r(x=325Å), s(x=275Å), t(x=225Å), u(x=175Å), v(x=125Å), w(x=75Å).

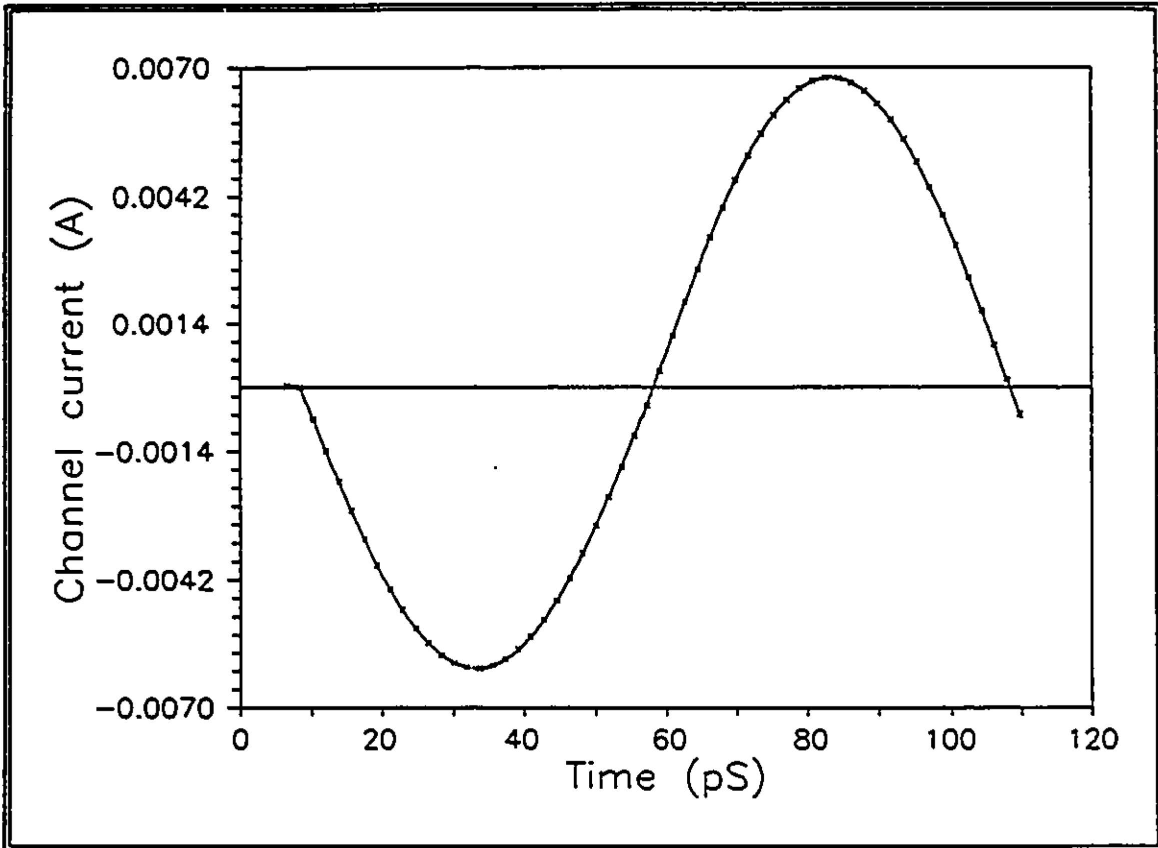

Figure 5.42: The channel current versus time. Solid line: theoretical analysis, x symbols: TLM computed.

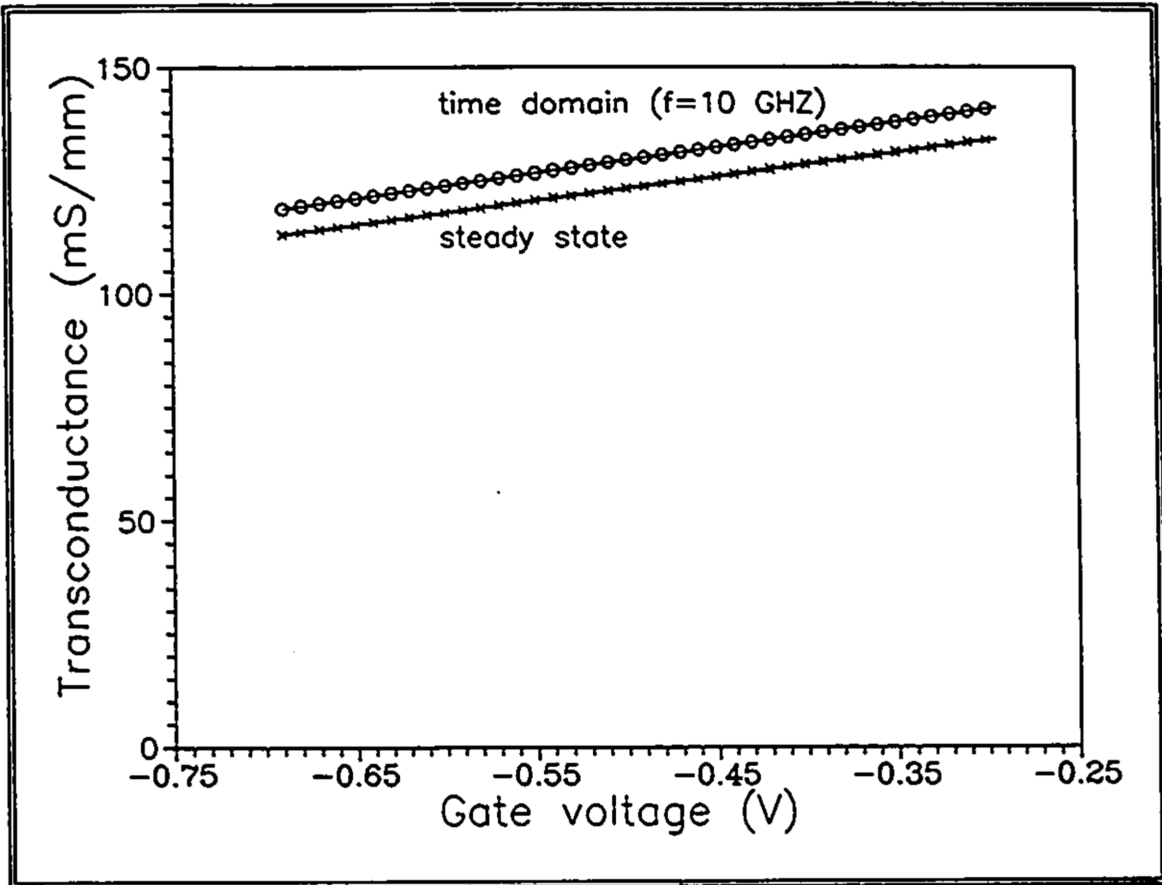

Figure 5.43: Comparison between time domain and steady-state computed transconductances of the same device.

5.6 References

5.1 C. Snowden and D. Loret, "Two-Dimensional Hot-Electron Models for Short Gate Length GaAs MESFETs," IEEE Trans. Electron Devices, Vol. 34, No. 2, pp. 212-223 February 1987.

5.2 Y. Feng and A. Hitz "Simulation of Submicrometer GaAs MESFETs Using a Full Dynamic Transport Model," IEEE Trans. Electron Devices, Vol. 35, No. 9, pp. 1419-1431 September 1988.

5.3 S. El-Ghazaly and T. Itoh, "Two-Dimensional Numerical Simulation of Short Gate Length GaAs MESFETs and Application to the Travelling Gunn Domain Phenomenon," International Journal of Numerical Modeling, Vol. 1, pp. 19-30, 1988.

5.4 S. Yoganathan, and S. Banerjee, "A New Decoupled Algorithm for Non-stationary Transient Simulation of GaAs MESFETs," IEEE Trans. Electron Devices, Vol. 39, No. 7, pp. 1578-1587, July 1992.

5.5 B. Carnez, A. Cappy, A. Kaszynski, E. Constant, and G. Salmer, "Modeling of a Submicrometer gate FET Including Effects of Non-Stationary Electron Dynamics," J. Appl. Phys. 51(1), January 1980, pp. 784-790.

5.6 B. Carnez, A. Cappy, G. Salmer, and E. Constant, "Modelisation de Transistors a Effete de Champ a Grille Ultra-courte," Acta Electronica 23(2), 1980, pp. 165-183.

5.7 S.F. Dindo, M.M. Ney, and R.G. Harrison, "A New Steady-State Formulation For Current-Voltage Characteristics of GaAs MESFETs Using the Voltage Balance Method," Submitted for publication to the IEEE Trans. Electron Devices.

5.8 C. Chang and D. Day, "Analytic Theory for Current-Voltage Characteristic and Field Distribution of GaAs MESFET's," IEEE Trans. Electron Devices, Vol. 36, No. 2, pp. 269-280, February 1989.

5.9 R. A. Pucel, H. A. Haus, and H. Statz, "Signal and Noise Properties of GaAs Microwave FETs," in Advances in Electronics and Electron Physics, vol. 38. New York: Academic, 1975, pp. 195-265.

5.10 H. Morkoç, T. Drummond, and M. Omori, "GaAs MESFET's by Molecular Beam Epitaxy," IEEE Trans. Electron Devices, Vol. 29, No. 2, pp. 222-224, February 1982.

5.11 S.F. Dindo, M.M. Ney, and R.G. Harrison, "Transmission-Line Matrix (TLM) Formulation of the Non-Stationary Transient Electromagnetic Fields in a Thin GaAs Sample," IEEE MTT-S International Microwave Symposium, San Diego, May (1994).

5.12 S.F. Dindo, M.M. Ney, and R.G. Harrison, "A New Two-Dimensional Transmission Line Matrix (TLM) Node Formulation For Thin Semiconductor Samples," Submitted for publication to the International Journal For Numerical Modelling.

CHAPTER 6

Conclusions

6.1 Introduction

The work presented in this thesis was directed toward interfacing into the two-dimensional TLM method the simulation of the GaAs MESFET's active layer. The ultimate goal of such research is to extend the TLM method into the full simulation of monolithic microwave integrated circuits.

Of particular interest was the approach used in this work to implement a physics-based active device model. Compared with lumped element models which are unrealistic and artificial at best, physical models can treat broad range of devices and input signals and are more compatible with the concept of TLM. The implementation of this type of model and the examples in this work were therefore aimed at demonstrating the viability of realizing the overall goal, which is to simulate by electromagnetic techniques both active and passive devices in the same substrate. In this chapter the results of this work are summarized, the original contributions are noted, and suggestions are made for future work.

6.2 Conclusions

In this work, a new approach is used to model GaAs MESFETs in TLM. Since the TLM method cannot undertake their physical modelling, an indirect approach is used where the MESFET is treated as a two-port structure, and a background solver is incorporated into a new TLM formulation which calculates MESFET parameters that the TLM method cannot directly model. The new TLM formulation models a field-linearized discrete section of the MESFET conducting channel, and hence a collection of these systems are used to fit the entire conducting channel. The background solver employs a time domain quasi-two-dimensional GaAs MESFET model capable of simulating non-stationary electron dynamics which are necessary to account for the transient response.

An interface was also designed to assist the linkage between the new TLM method and the background solver. One of the advantages of this approach is that the tight linkage between space and time in TLM, which slows down electromagnetic computations, is decoupled. The background solver can adopt finer spatial meshes and coarser time steps than the TLM method. The linkage between the two systems is done via spatial and time interpolation. It was demonstrated that the new TLM method is capable of simulating the electric and magnetic fields in GaAs MESFETs as well as the channel current for various type of input stimuli.

6.3 Original Contributions

The incorporation of physical GaAs MESFET modelling into the TLM method is the first of its kind. To bring the objectives of this thesis into reality, several new analyses methods had to be researched. For example, the formulation of the two-dimensional TLM method to model the electromagnetic fields in a discretized section of the conducting MESFET channel is new. The GaAs MESFET analysis method also contains several novel aspects. Whereas previous treatments consisted of using non-stationary velocity calculation and fixed time steps, this analysis incorporates the calculation of the dielectric time constants and charging effects in addition to non-stationary electron dynamics to attain a variable time step. Finally, the Voltage Balance Method used to solve the Poisson and current continuity equations is also novel.

6.4 Recommendations for Future Work

The most important undertaking would be to incorporate the effects of the MESFET parasitics into the analysis. These parasitics are due to the gate, drain, and source microstrip lines, and they are best taken into account using three-dimensional analysis. The TLM technique has been demonstrated to be quite suitable in simulating the electromagnetic fields in microstrip structures [6.1-6.4], and presumably coupled lines such as those in the MESFET metallizations can be treated as well. The treatment is envisaged such that the gate, drain, and source microstrip line are discretized along their width. The active layer cross-section at each node would be treated by a separate GaAs

MESFET analysis engine. The electric field of the wave propagating along the gate electrode serves as the input at each node, and the magnetic field emerging from the active layer towards the drain electrode is added to the fields in the surface. The electromagnetic fields propagating on the outer drain microstrip line must be formulated. This must take into account the load terminations as well as the characteristic impedances of the microstrip lines. Also, the field interactions and parasitics of the MESFET electrodes must also be incorporated into the active layer.

Though spatial discretization is the dominant factor in determining the accuracy of the final results, it would still be useful to enhance the accuracy of the intrinsic MESFET model. The present model did not involve diffusion processes and temperature effects since Monte Carlo results were not available. It is suggested that in the absence of published data, Monte Carlo simulations should be conducted to investigate carrier transport properties at various doping levels and temperatures. The GaAs MESFET analysis engine can incorporate these results via look-up tables.

Finally, there are little data on time domain physical modelling of MESFET devices. The analysis engine can be used in the present form to conduct nonlinear analysis, for example, on the effect of gate recess, gate length variations, and channel material on MESFET characteristics. It would be useful to study the extent of distortion of high frequency signals and device limitations. The results can be used to design optimal MESFETs for low-noise and power applications.

6.5 References

6.1 G.E. Mariki and C. Yeh, "Dynamic Three-Dimensional TLM Analysis of Microstriplines on Anisotropic Substrate," IEEE Trans. Microwave Theory Tech., Vol. 33, No. 9, pp. 789-799, September 1985.

6.2 J.H. Thompson and T.R. Apel, "Simplified Microstrip Discontinuity Modeling Using the TLM Method Interfaced to Microwave CAD," Microwave Journal, pp. 79-88, July 1990.

6.3 P.P.M. So, Eswarappa, and W.J.R. Hoefer, "A Two-Dimensional TLM Microwave Field Simulator Using New Concepts and Procedures," IEEE Trans. Microwave Theory Tech., Vol. 37, No. 12, pp. 1877-1884, December 1989.

6.4 P.P.M. So and W.J.R. Hoefer, "A Three-Dimensional TLM Time Domain Electromagnetic Wave Simulator for Microwave Circuit Modeling," IEEE MTT-S Digest 1991, pp. 631-634.

Appendix A

Monte Carlo Methods

The Monte Carlo Method is a technique for simulating many chance experiments and drawing inferences from the results of simulated experiments. Historically, the technique was first used in 1773 by a French scientist to estimate the value of π using chance experiments. By tossing a stick of length L into a large flat piece of paper ruled with straight lines a distance 2L apart, π is computed from the ratio of the total number of tosses to the number of tosses where the stick crosses a line. The results are considered accurate only if large number of experiments are used and the outcome of any given toss is truly random. The technique was given its first systematic development by Von Neumann and Ulam who simulated random neutron diffusion in fissionable material for the development of the atomic bomb at Los Alamos scientific Laboratory in New Mexico. Since then the use of these methods extended with the advent of computers. Beginning in the sixties the Monte Carlo method was actively employed to the investigation of hot electron transport in semiconductors to shed light into the Gunn effect. Soon after the results were used to obtain statistical models of electron velocity-electric field-time behavior in compound semiconductors to quantify non-stationary electron transport. In this thesis, the results of one-dimensional Monte Carlo simulation of hot electron transport in a GaAs sample under steady state electric field are used to derive the electron momentum and energy relaxation behavior under various doping and electric field levels. These parameters are obtained by generating a sample history of an electron by computer using pseudo-random numbers to select the final states of scattering processes, as well as the initial states in which the path terminates by scattering. Many thousands flight histories of electrons are generated in this process to provide a statistical behavior.

The use of Monte Carlo methods in hot electron transport within semiconductors can best be illustrated in an over simplified experiment. Suppose that we wish to model

the transport of the electrons in a conducting semiconductor sample. The latter would have many billions of electrons moving about and colliding with other particles as well as the nuclei of the constituent atoms. Each collision can result in the emission of new particles, in a change in direction and energy of the electron, in the absorption of the electron by the nucleus, and many other effects. We can think of the travel of each electron as a series of experiments. With a certain probability it strikes another particle, and with certain other probabilities the different physical phenomena described above will occur. Some of these phenomena may actually unleash another electron and thus initiate a new set of experiments. At any given point in time there are billions of electrons scattered randomly throughout the conducting sample. They are moving in various directions with a variety of energies. If we could trace the history of these electrons we could determine the energy and other properties of the sample at any given time. This can only be accomplished with reasonable accuracy using the law of large numbers. By scattering a large enough number of electron at random throughout the sample and starting them in random directions and random energies, the histories can be closely traced. Typical Monte Carlo calculations involve generating several sequences of random numbers. Let one sequence describe the position of the electron using cartesian coordinates. The next sequence might specify the direction in which the electron begins to move. The next also represents the starting energy. If the electron collides with another particle the next random sequence can decide whether another particle is released. And the succeeding numbers determine the directions and energies of electrons after a collision. The process continues until any given state or time occurs.

The actual Monte Carlo methods used in electron transport in GaAs is much more involved. The parameters of the Monte Carlo experiment involve the density of the semiconductor, energy band gap, dielectric constant, detailed energy band structure, effective mass, lattice properties, diffusion, impact ionization. carrier-carrier scattering, absorption of light, and many others. This task requires tremendous volume of calculations which is most suited for computers. The central notion in these simulations is that the duration of the electron sample history is long enough to sample the domain of electron variables, and that the numbers generated are truly random. These

requirements can partly be satisfied by using large enough number of trials with a reasonable economy in computer time. Generally, these experiments are repeated as often as necessary and eventually the scientist draws a trend line through the large number of data points in a graph, and a statistical model emerges.

References

P. J. Price, "Calculation of Hot Electron Phenomena," Solid State Electronics, Vol. 21, 1978, pp. 9-16.

S. N. Chamoun, R. Joshi, E. N. Arnold, and R. O. Grondin, "Theoretical and Experimental Investigation of Subpicosecond Photoconductivity," Journal of Applied Physics, Vol. 66, No. 1, July 1989, pp. 236-246.

W. S. Dorn and H. J. Greenberg, Mathematics and Computing with FORTRAN Programming, John Wiley & Sons, pp. 470-473, 1967.

Appendix B

Computer Programming of the TLM MESFET Model

The technique for TLM simulation of GaAs MESFETs developed in this thesis is outlined in the flow-charts shown in Figures 4.5, 4.6, and 4.12. Computer programming of the technique requires the development of three distinct subprograms: 1) the TLM analysis module, 2) the GaAs MESFET analysis engine, and 3) the TLM-MESFET engine interface. Due to the time chronicle of this research the first two modules has been developed separately using different programming objectives, while the third module has been implemented as a series of sub-programs for generation of the look-up tables.

The TLM analysis module was developed under the requirement of very large memory storage. For example, each TLM node requires allocation into memory of 1) four voltage numbers corresponding to the branches, 2) three electromagnetic field components, 3) Cartesian coordinates, and 4) the number of time iterations. It has been seen in the examples of Chapter 5 that the number of TLM time iterations is in the order of hundred of thousands to several millions. Such storage requirements preclude the use of the computer's fast accessing but volatile random access memory because of the latter's storage limits. A program is written in QuickBasic language which instead stores the TLM node information in the computer's non-volatile but slow accessing hard disk memory system because of the latter's vast storage capacity. The program has been adapted to accept the values of the TLM energy, conductivity, and system dimensions at run-time from look-up tables. The program can solve for one TLM system at a time and can accommodate tens of millions of iterations. The penalty paid of such a programming implementation is in terms of the execution speed. The examples in this thesis were simulated using a personal computer based on an Intel 80486 microprocessor running under a 33 MHz clock speed. As a relative benchmark, the computation of the electromagnetic response of the 46 node TLM system described in Chapter 5, Example #3 required 52 hours of run-time to execute 1,657,737 time iterations. It is important to

note that the run-time does not scale linearly with number of TLM nodes. The program slows down considerably with increasing number of nodes. The main reason is the look-up tables reading time and the file writing time required by the computer to store the TLM information. It is for this reason that the program was designed to execute one TLM system at a time.

The memory storage requirements for the GaAs MESFET analysis engine is also quite severe. Unlike the TLM analysis program which solves for one TLM system at a time, the entire MESFET space has to be simulated by the engine. Each node requires allocation into memory of: 1) doping, 2) electron velocity), 3) electron energy, 4) electron momentum, 4) electron energy and momentum relaxation times, 5) two electric field components, 6) voltage, 7) cartesian coordinates, and 8) time steps. Similar to the TLM analysis program, the computer's non-volatile random access memory is used for node information storage. A program is written in Visual Basic for Windows, an event-driven programming language, to execute the simulations reported in this thesis. Using the same computing platform, this programming language enables access to larger amounts of volatile random access memory for analysis requirements. Unlike TLM analysis which requires the execution of few and simple closed loop equations per time step, the GaAs MESFET analysis requires vast and extensive analysis memory as it undergoes hundreds of optimization processes to obtain a MESFET solution per one time step. On the other hand, using a variable time step, the number of time iterations, and consequently file writing time is considerably shortened in comparison to the TLM analysis. As a relative benchmark, using the same computer platform the computation of the transient response of the MESFET in Chapter 5, Example #3 required sixteen hours of run-time.

The TLM interface parameters were generated from the node locations and time steps of the MESFET analysis engine. Using stand-alone computer subroutines, the interface parameters were spatially and time interpolated to fit the TLM analysis node and time step requirements. These were then converted into look-up tables using polynomial functions and stored into computer files. The TLM analysis proceeds for the entire time length to generate the electromagnetic response.